JUNE, 2025

Academic Research in Engineering Sciences

Editor
Prof. Özlem Sallı Bideci, Ph.D.

DOI: 10.5281/zenodo.15762188

Academic Research in Engineering Sciences

Editor

Prof. Özlem Sallı Bideci, Ph.D.

Publisher
Platanus Publishing®

Editor in Chief
Prof. Özlem Sallı Bideci, Ph.D.

Cover & Interior Design
Platanus Publishing®

The First Edition
June, 2025

ISBN

979-828-9992-83-3

Platanus Publishing®
Address: Natoyolu Cad. Fahri Korutürk Mah. 157/B, 06480, Mamak, Ankara, Turkey.

Phone: +90 312 390 1 118
web: www.platanuspublishing.com
e-mail: platanuskitap@gmail.com

Platanus Publishing®

CONTENTS

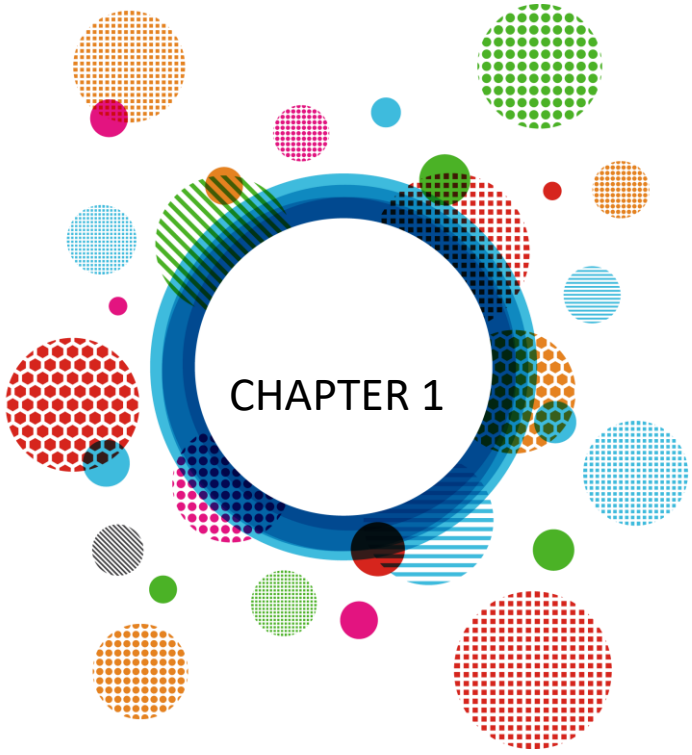

Consumers' Sustainability At-Titudes and Purchasing Be-Haviors Towards Ready-Made Clothing Products

Ceren Gürlek[1] & Damla Durak Uşar[2] & Mehmet Ali Taş[3]

1. Introduction

Since humans are dynamic beings, the order of importance of their needs, preferences and values changes from time to time throughout their lifes. Today, technological developments and globalization affect human beings' decisions in every field. In addition, population growth and industrialization cause an increase in consumption and accelerate the destruction of natural resources. With the effects of climate change being felt more by people, the concept of sustainability has started to be on the agenda of different stakeholder groups such as governments, local governments, the private sector, NGOs and individuals. According to the general opinion, consumers have become more conscious and have started to consider not only their personal needs but also environmental and social impacts when making purchasing decisions.

This consumption trend towards an environmentally friendly attitude has led to the term green marketing. Green marketing includes all activities that aim to create and facilitate all kinds of exchanges aimed at satisfying people's needs and desires so that these needs and desires are met in a way that minimizes damage to the natural environment (Polonsky, 2011). In a more comprehensive definition, the American Marketing Association uses the term to describe efforts to produce, promote, package and recycle goods in an environmentally friendly manner. Green marketing activities can also increase consumers' willingness to purchase (Chen and Chang, 2012). Ecologically compatible products that impose less burden on nature during the production and use phase are increasingly preferred by consumers and the tendency of consumers to pay a price premiumfor environmentally friendly or ecological products is increasing (Laroche *et al*., 2001; Singh and Pandey, 2012). The textile sector, which contributes significantly to the economic development and growth of a country and meets the need for cholting, which is one of the basic physiological needs of every human being, is one of the sectors that keeps the issue of sustainability on its agenda. While there are environmental problems such as the use of many chemicals in textile production, the release of wastes to nature, the intensive consumption of natural resources and water, on the other hand, the presence of social problems related to employee and public health has led the public and private sector to take action. In order to provide the best service to consumers who are interested in environmentally friendly and sustainable products, textile companies resort to

[1] Turkish-German University, ORCID: 0009-0002-8458-9045
[2] Asst. Prof. Dr., Turkish-German University, ORCID: 0000-0001-8402-3856
[3] Re. Asst. Turkish-German University, ORCID: 0000-0003-3333-7972

various practices. Using organic/natural dyes and renewable energy sources in the production process, recycling waste materials, respecting employee rights, and improving working conditions can be given as examples of these practices. Since companies must allocate resources for sustainable practices, for feasibility the consumers' willingness to pay a price premium for environmentally friendly and socially responsible items gains importance.

This study aims to examine the effects of consumers' attitudes towards sustainability on their purchasing behavior in the textile sector. Although the term textile is used wherever fibers, yarns, and fabrics are available, this study focuses on the ready-to-wear sector. 472 consumers were reached through a questionnaire survey. Using structural equation modeling (SEM), the relationship between sustainability attitude and purchasing behavior is examined within the framework of the effects of environmental, social and economic sustainability attitude, which are the three pillars of sustainability, on the first purchase decision, repeat purchase decision and purchase frequency for various consumer groups. A comprehensive literature review is provided in Section 2. Section 3 summarises the model and methodology of the study. Section 4 analyses the descriptive findings. In Section 5, groupings for SEM are determined. In Section 6, the relationship between sustainability attitude and purchasing behavior is estimated by SEM. In Section 7, theoretical and practical implications, limitations of the study, and the conclusion section including future studies are given.

2. Literature Review

The literature examining purchasing behavior generally collects information through survey methods and examines the factors affecting the purchasing decision with different techniques such as cluster analysis (e.g. Yeniçeri, 2009), factor analysis (e.g. Yeniçeri and Özbezek, 2016), choice-based conjoint analysis (e.g. Abreu et al., 2022; Fuchs and Hovemann, 2022; Riesgo et al., 2023), hypothesis tests (e.g. Portakalcı, 2017; Rahman and Koszewska, 2020) and SEM (e.g. Jacobs et al, 2018; Lang and Armstrong, 2018; Lin and Chen, 2022).

According to a survey of 1063 Spanish consumers, 31.9% of consumers attach importance to price, while only 8.65% regularly purchase sustainable fashion products (Riesgo et al., 2023). Klein et al. (2020) stated that environmental awareness, product experience and price are the most important factors affecting the purchase decision. While fit and comfort, price-performance ratio, quality and design are more important for consumers than sustainable features, the most important features of sustainable clothing are the durability of the garment, fair wages and working conditions, as well as the environmentally friendly production process (Rausch et al., 2021). According to Rahman and Kharb (2022) fit, comfort and price-performance ratio are more important than sustainability, while the least important factors are brand and country of origin. Similarly, Abreu

et al. (2022) observed that while price is the most important factor, environmental and social sustainability are more important than brand and country of origin. Boufous et al. (2023) found that the most important factors affecting purchasing behavior are price, toxin-free paint and country of origin. According to Fuchs and Hovemann (2022) product function and social sustainability are have more effect on the purchase decision than the circularity of the product, while durability and recycled material ratio are important among circular features. Bizuneh et al. (2022) observed that environmental factors are more important than social factors. In the literature, inferences regarding demographics do not show a consensus. According to Abreu et al. (2022) income, gender, education level and age affect purchase behavior. On the one hand, according to Rausch et al. (2021), female consumers make more sustainable decisions. Female consumers are more informed and younger consumers attach more importance to sustainability than older consumers (Rahman and Kharb, 2022). According to Boufous et al. (2023), gender and educational level affect purchasing behavior, especially female consumers are willing to pay a price premium. On the other hand, it was also observed that older and male consumers are willing to pay a price premium for sustainable products (Abreu et al., 2022). Guo and Kim (2023) observed that the number of products used by men is less than by women and that they use the products for a long time, while young people have fewer product types and use the products for a short time, and older people use few types of products for a long time. Bizuneh et al. (2022) observed that age and educational level are statistically effective on purchasing behavior, while gender is not effective. Rahman and Koszewska (2020) observed that young consumers and women attach more importance to price than older consumers and men. According to Colasante and D'Adamo (2021), the intention to purchase second-hand products is higher in women than in men, while no difference between genders was observed for biobased products. Generation Z is the generation that buys second-hand clothes the most, Baby-boomer, Generations X and Z are the generations that prefer biobased products the most, but the observation regarding the preference of the older generation may be related to high income (Colasante and D'Adamo, 2021).

In the national literature, there are case studies examining good practices in the sustainable textile and fashion sector (e.g. Can and Ayvaz, 2017; Halaçeli Metlioğlu and Yakın, 2021; Çakır and Sünter Eroğlu, 2023), general purchasing behavior (e.g. Yeniçeri and Özbezek, 2016; Portakalcı, 2017), sustainable product purchasing behavior (e.g. Yeniçeri, 2009; Yeniçeri and Özbezek, 2016; Portakalcı, 2017; Aydın and Tufan, 2018) and textile purchasing behavior (Ercan, 2010). However, there is no econometric study on sustainable textile product purchasing behavior. In a survey study conducted with 399 university students, the most important factors affecting general purchasing behavior were

determined as brand awareness, variety, latest fashion orientation, familiarity, perfectionism and price consciousness. In a survey study conducted with 644 migrants, the factors affecting general purchasing behavior were determined as perfectionism-quality consciousness, innovation, fashion orientation, confusion of choice, price-value consciousness, brand consciousness, entertainment-pleasure orientation, impulsive shopping, and habit-brand loyalty. Female and male consumers differ in terms of perfectionist-quality consciousness and entertainment-pleasure orientation factors (Yeniçeri and Özbezek, 2016). In the survey study conducted with 402 individuals, when consumers were clustered according to their sustainable product purchasing behavior, it was determined that there were statistically significant differences between the clusters in terms of gender, education level and monthly net income. It was determined that consumers with high environmental awareness and environmentally sensitive purchasing behavior are predominantly female, and have high education levels and relatively high income levels (Yeniçeri, 2009). In a survey study conducted with 251 people born after 1980, it was observed that individuals included in the Y generation, although they live consumption-oriented, are sensitive to the environment they live in and reflect this in their purchasing behavior (Aydın and Tufan, 2018). In the survey study conducted with 319 people on textile purchasing behavior, consumers preferred that the designer is from a developed country rather than from a developing country, and if the country is an important producer, the effect of consumer nationalism on the country's image is important. The country's image affects the purchasing tendencies of consumers, who place significant importance on the perception of others regarding themselves. It was found that the country where the product is produced has no effect on the country's image perception of the consumer (Ercan, 2010).

3. Methodology

Based on the studies in the literature, the hypotheses of the study were formed as:

Hypothesis-1: Consumers' environmental sustainability attitudes positively affect their sustainable textile product purchasing behavior.

Hypothesis-2: Consumers' social sustainability attitudes positively affect their sustainable textile product purchasing behaviors.

Hypothesis-3: Consumers' economic sustainability attitudes positively affect their sustainable textile product purchasing behaviors.

Hypothesis-4: Consumers' sustainability attitudes and sustainable textile product purchasing behaviors show a significant difference according to gender.

Hypothesis-5: Consumers' sustainability attitudes and sustainable textile product purchasing behaviors show a significant difference according to generation.

Hypothesis-6: Consumers' sustainability attitudes and sustainable textile product purchasing behaviors show a significant difference according to educational level.

Hypothesis-7: Consumers' sustainability attitudes and sustainable textile product purchasing behaviors show a significant difference according to their monthly income.

Hypothesis-8: Consumers' sustainability attitudes and sustainable textile product purchasing behaviors show a significant difference according to the number of households.

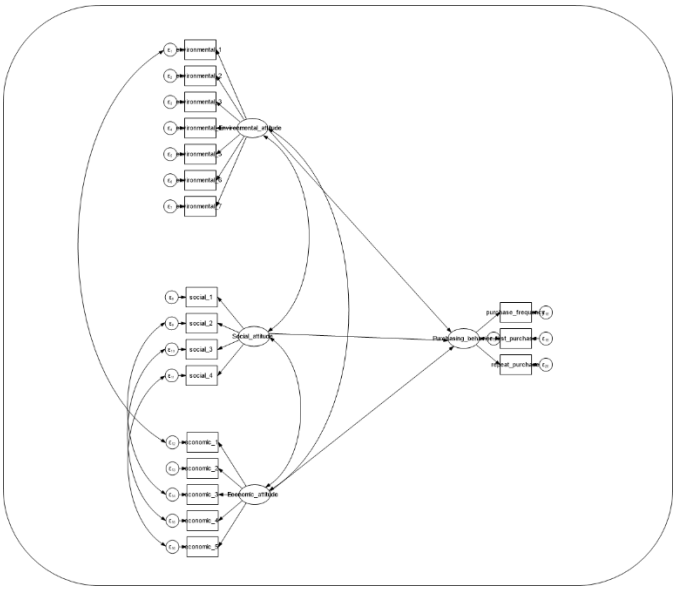

Figure 1. Structural equation model

SEM is an appropriate method for testing research hypotheses with the help of statistical information derived from empirical measurements. SEM represents research hypotheses in terms of a small number of structural parameters defined by an assumed base model with the help of observed means, variances and covariances of a set of variables derived from empirical measurements (Bowen and Guo, 2012). Figure 1 shows the SEM used in the study.

In this study, the survey method was used to collect data and participation in the survey was voluntary. Since all people living in the society are consumers,

the survey was designed to reach participants of different generations, different educational backgounds and income levels. Participants were contacted through social media. Therefore, the data were obtained through a convenient sampling method. Factors affecting sustainability attitude and purchasing behavior and related survey questions are shown in Table 1.

Table 1: Factors affecting sustainability attitude and purchasing behavior and related survey questions

Factors	Survey Questions
Environmental_1	It is important for me to buy sustainable products to contribute to nature.
Environmental_2	It is important for me that the brands I choose to shop from use cardboard or paper for packaging instead of plastic bags.
Environmental_3	It is important for me that the brands I choose to shop from recycle clothes in their stores.
Environmental_4	It is important for me that the brands I choose to shop from do not destroy/destroy less natural resources during production.
Environmental_5	It is important for me that the brands I choose to shop from use less water during production and carry out their production in a way that reduces their carbon footprint.
Environmental_6	It is important to me that the brands I choose to shop from sell recycled products.
Environmental_7	It is important for me that the raw materials of the brands I choose to shop from are sustainable.
Social_1	I prefer brands that publish annual sustainability reports.
Social_2	It is important for me that the brands I choose to shop with disclose their suppliers transparently and establish safe relationships with them.
Social_3	It is important for me that the brands I choose to shop from have a fair and equitable approach to their employees.
Social_4	It is important for me that the brands I choose to shop with help and donate to social responsibility projects.
Economical_1	It is important for me to buy the product that is sustainable, even if the price is higher than two products of the same quality.
Economical_2	It is important for me to buy the product that lasts longer, even if the price of two products of the same quality is higher.
Economical_3	Even though the products of some brands are more expensive than the market, I prefer the brands because they disclose their suppliers transparently and establish safe relationships with them.
Economical_4	Although some brands' products are more expensive than the market, I prefer the brands because they have a fair and egalitarian approach to their employees.

Economical_5	Although the products of some brands are more expensive than the market, I prefer the brands because they provide more aid and donations to social responsibility projects.

4. Findings

472 people responded to the questionnaire. 326 of the participants were female and 146 were male. When the participants were grouped according to their generations, it was determined that 62 of them were Baby-boomers (generation with birth year 1946-1964), 131 of them were members of Generation X (generation with birth year 1965-1979), 124 of them were members of Generation Y (generation with birth year 1980-1994) and 155 of them were members of Generation Z (generation with birth year 1995-2009). When the participants were grouped according to their education level, it was found that 12 participants were primary school graduates, 60 participants were high school graduates, 266 participants were undergraduate graduates and 134 participants were postgraduate graduates. When the participants were grouped according to their monthly income, it was found that 135 of them had a monthly income of one minimum wage or less, 77 of them had a monthly income of one to two minimum wages, 113 of them had a monthly income of two to three minimum wages, 33 of them had a monthly income of three to four minimum wages and 114 of them had a monthly income of four minimum wages or more. Of the participants, 102 live with their parents, 52 live alone, 43 live with their friend(s), 92 live with their spouse, and 183 live with their spouse and child/children. Figure 2 summarises the descriptive findings of the participants.

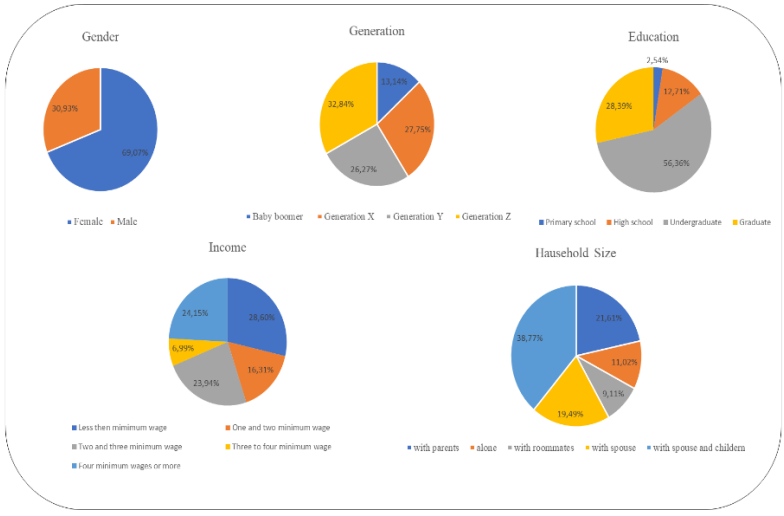

Figure 2. Descriptive findings about the participants

When the participants were examined in terms of purchasing behaviors, 6 participants stated that they purchased textile products several times a week, 9 participants once a week, 51 participants once every two weeks, 123 participants

once a month, 231 participants once every three months (seasonal shopping), while 52 participants stated that they almost never purchase textile products. When the three main factors affecting the first purchase decision were analyzed, it was found that 441 times the quality of the product, 367 times the price of the product, 212 times the sustainability of the product, 161 times the brand's attitude towards the environment, 137 times the social values of the brand and 98 times on recommendation. When the three main factors affecting the repeat purchase decision were analyzed, it was found that 434 times the quality of the product, 342 times the price of the product, 209 times the emotions felt while using the product, 195 times the sustainability of the product, 142 times the brand's attitude towards the environment and 94 times the brand and the brand's social values. Figure 3 summarises the findings regarding the purchasing behaviors of the participants.

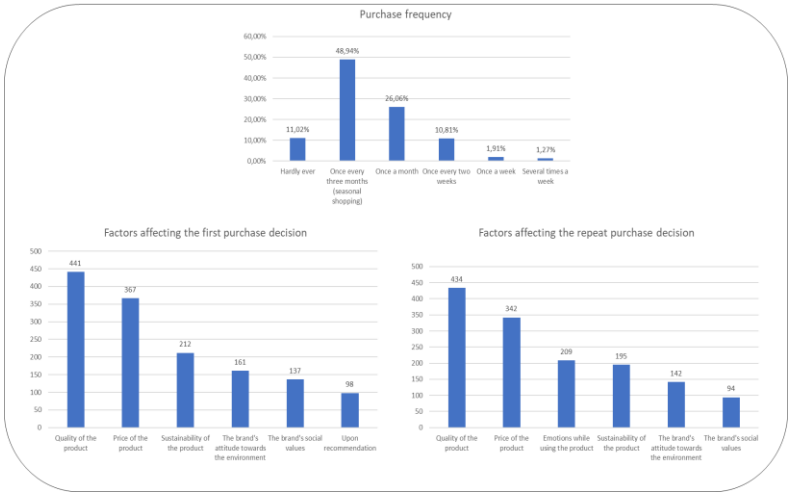

Figure 3. Findings on participants' purchasing behavior

5. Determination of groupings for SEM

To identify groupings in the structural equality model, it must be determined whether groups according to gender, generation, educational level, monthly income and household size differ in terms of purchase frequency, first purchase decision and repeat purchase decision, factors affecting purchasing behavior. When it is suspected that there are more than two main populations within the sample, the non-parametric Kruskal-Wallis Test is applied. The Kruskal-Wallis Test is based on the ordinal numbers of the sample observations and the null hypothesis to be tested is that the three main population means are the same (Newbold, 2000, pp. 684-686). When it is suspected that there are two main populations within the sample, a special case of the Kruskal-Wallis Test, the non-parametric Mann-Whitney Test, is used (Newbold, 2000, pp. 442-444).

In Table 2, when there are K=2 clusters, the null hypothesis that the purchase frequency is the same in the gender groups is rejected even at a 0.5% significance level. When K=2 clusters $x^2(1)=23.689$ the null hypothesis that the first purchase decision is the same in the gender groups is clearly rejected even at a 0.5% significance level. When K=2 clusters, $x^2(1)=12.120$ the null hypothesis that the first purchase decision is the same in the gender groups is clearly rejected even at 0.5%. When K=2 clusters, $x^2(1) = 12.120$ the null hypothesis that the first purchase decision is the same in the gender groups is clearly rejected even at 0.5% The difference between the mean rankings of the gender groups was found to be statistically significant and these groupings are to be considered in the SEM. When K=4 clusters, $x^2(3) = 35.148$, the null hypothesis that the purchase frequency is the same in the four main populations is rejected even at a 0.5% significance level. When K=4 clusters, $x^2(3)=23.103$ the null hypothesis that the first purchase decision is the same in the four main populations is clearly rejected even at a 0.5% significance level. When K=4 clusters, $x^2(3)=23.103$ the null hypothesis that the first purchase decision is the same in the four main populations is clearly rejected even at a 0.5% significance level (Newbold, 2000, pp. 684-686). The difference between the mean rankings of the generation groups was found to be statistically significant and these groupings were considered in the SEM.

When K=4 clusters, $x^2(3)=15.904$ the null hypothesis that the purchase frequency is the same in the four main populations is rejected even at a 0.5% significance level. When K=4 clusters, $x^2(3)=8.668$, the null hypothesis that the first purchase decision is the same in the four main populations is accepted at a 0.5% significance level. When K=4 clusters, $x^2(3)=2.304$, the null hypothesis that the repeat purchase decision is the same in the four main populations is accepted at a 0.5% significance level. Regarding purchase frequency, the difference between the mean rankings of the groups according to educational level was found to be statistically significant and these groupings were considered in the SEM. When K=5 clusters, $x^2(4) = 5.141$ the null hypothesis that the purchase frequency is the same in the five main populations is accepted at a 0.5% significance level. When K=5 clusters, $x^2(4)=23.817$ the null hypothesis that the first purchase decision is the same in the five main populations is clearly rejected even at a 0.5% significance level. When K=5 clusters, $x^2(4)=21.141$ the null hypothesis that the repeat purchase decision is the same in the five main populations is clearly rejected even at a 0.5% significance level. Regarding the first purchase decision and repeat purchase decision the difference between the mean rankings of the monthly income groups was found statistically and these groupings were considered in the SEM.

When K=5 clusters, in terms of purchase frequency $x^2(4)=12.760$ and in terms of the first purchase decision, $x^2(4)=10.160$, the null hypotheses are accepted at a 0.5% significance level. However, when K=5 clusters, $x^2(4)=15.043$, the null hypothesis that the repeat purchase decision is the same in the five main populations is rejected even at a 0.5% significance level (Newbold, 2000, pp. 684-686). Regarding repeat purchase decisions the difference between the mean rankings of the household groups was found to be statistically significant and these groupings were considered in the SEM.Table 2: Kruskal-Wallis Test results

Purchasing Frequency														
Gender			Generation			Education			Monthly Income			Household		
	Sample	Rank Sum (RS)		Sample	RS		Sample	Rank Sum		Sample	RS		Sample	RS
Women	326	83765.5	Baby-boomer	62	10888.00	Primary education	12	1308.50	A minimum wage or less	135	33589.50	I live with my parents.	102	27778.50
Men	146	27862.5	X-Generation	131	27600.50	High school	60	12600.50	Between one and two minimum wage	77	18558.50	I live alone.	52	12074.50
			Y-Generation	124	29257.00	Bachelor degree	266	66737.00	Between two and three minimum wage	113	27653.50	I live with my friend/friends.	43	11300.00
Chi2(1)=23.689			Z-Generation	155	43882.50	Postgraduate	134	30982.00	Between three and four minimum wage	33	7574.50	I live with my wife.	92	20252.50
Prob=0.0001									Four minimum wages or more	114	24252.00	I live with my wife and child/children.	183	40222.50
			chi2(3) = 35.148 Prob = 0.0001			chi2(3) = 15.904 Prob = 0.0012			chi2(4) = 5.141 Prob = 0.2731			chi2(4) = 12.760 Prob = 0.0125		
First Purchase Decision														
Gender			Generation			Education			Monthly Income			Household		
	Sample	RS		Sample	RS		Sample	RS		Sample	RS		Sample	RS
Women	326	81867.50	Baby-boomer	62	15435.00	Primary education	12	1489.00	A minimum wage or less	135	25783.00	I live with my parents.	102	22623.50
Men	146	29760.50	X-Generation	131	35511.50	High school	60	13829.50	Between one and two minimum wage	77	19425.50	I live alone.	52	11230.00
			Y-Generation	124	30318.50	Bachelor degree	266	63932.50	Between two and three minimum wage	113	29927.50	I live with my friend/friends.	43	8453.50
chi2(1) = 12.120			Z-Generation	155	30363.00	Postgraduate	134	32377.00	Between three and four minimum wage	33	9114.00	I live with my wife.	92	23967.50
Prob = 0.0005									Four minimum wages or more	114	27378.00	I live with my wife and child/children.	183	45353.50
			chi2(3) = 23.103 Prob = 0.0001			chi2(3) = 8.668 Prob = 0.0340			chi2(4) = 23.817 Prob = 0.0001			chi2(4) = 10.160 Prob = 0.0378		
Repurchase Behavior														
Gender			Generation			Education			Monthly Income			Household		
	Sample	RS		Sample	RS		Sample	RS		Sample	RS		Sample	RS
Women	326	81925.50	Baby-boomer	62	15857.50	Primary education	12	2301.00	A minimum wage or less	135	26706.00	I live with my parents.	102	23694.50
Men	146	29702.50	X-Generation	131	35930.00	High school	60	15097.50	Between one and two minimum wage	77	18641.50	I live alone.	52	11415.50
			Y- Generation	124	29561.00	Bachelor degree	266	63314.00	Between two and three minimum wage	113	30075.50	I live with my friend/friends.	43	7761.00
chi2(1) = 12.417			Z- Generation	155	30279.50	Postgraduate	134	30915.50	Between three and four minimum wage	33	9517.50	I live with my wife.	92	25186.00
Prob = 0.0004									Four minimum wages or more	114	26687.50	I live with my wife and child/children.	183	43571.00
			chi2(3) = 25.415 Prob = 0.0001			chi2(3) = 2.304 Prob = 0.5118			chi2(4) = 21.141 Prob = 0.0003			chi2(4) = 15.043 Prob = 0.0046		

6. Estimating the relationship between sustainability attitude and purchasing behavior with Structural Equation Modeling

6.1. Grouping by gender

326 of the participants were female and 146 were male.

6.1.1. Testing model goodness of fit

In the literature, there is no consensus on which index should be reported in determining the goodness of fit of SEM and different indices are used (Innami and Koizumi 2011). The most common of these indices is the chi-square statistic and p>chi2<0.05 indicates that the model fit is not good, but this statistic is sensitive to sample size (Fan *et al*., 1999; McDonald and Ho, 2002; Iacobucci, 2010). Many alternative indices have been proposed such as unbiased relative fit index (URFI), comparative fit index (CFI), goodness of fit index (GFI), Tucker-Lewis index (TLI), Normed fit index (NFI), Root mean square error of approximation (RMSEA), and Standardised root mean square error (SRMR). Since these indices are based on different theoretical justifications, there is no agreement on the ideal fit index in the literature (McDonald and Ho, 2002).

Hu and Bentler (1999) suggest evaluating fit indices such as root mean square error of approximation (RMSEA), comparative fit index (CFI), Tucker-Lewis index (TLI) and the square root of standardised errors (SRMR) together. If CMIN/DF is less than 3, there is an acceptable fit. The CFI value is between 0 and 1 and the closer the value is to 1, the better the model fits (Fan, *et al*., 1999). A TLI value greater than 0.90 is an indicator of a good fit (Marsch, *et al*., 2004). Some researchers believe that a 'good' fit occurs when RMSEA is less than 0.05 and an 'acceptable' fit occurs when RMSEA is less than 0.08. If the RMSEA value is greater than 0.1, the fit is considered poor. For SRMR, values less than 0.08 are considered appropriate (MacCallum *et al*., 1996). However, Marsch *et al*. (2004) stated that according to the acceptance limit values suggested in the literature, the goodness of fit for all indices is largely unobtainable for most practical applications. McDonald and Ho (2002) argued that the appropriate index should be selected depending on the purpose of the study, i.e. the measurement model, path analysis or both. A holistic approach should be used when examining various indices. According to Table 3, the CMIN/DF value is less than the recommended value of 3 and indicates an acceptable fit. The CFI value is 0.891 and the TLI value is 0.882, indicating that the model fit is good (Schumaker and Lomax, 2015). The SRMR value is within the recommended range [0;0,10) (Pituch and Stevens, 2015). Based on the values of the comparative fit indices and model data fit indices, the goodness of fit of the measurement model is at an acceptable level.

Table 3: SEM goodness of fit values when grouped by gender

Goodness of Fit Criteria	Goodness of Fit Values
CMIN	921.221
DF	317
CMIN/DF	2,9061
P-Value	***
CFI	0.891
TLI	0.882
RMSEA	0.090
SRMR	0.076

6.1.2. Analysis results and evaluation

According to Table 4, a statistically significant and positive relationship was observed between environmental sustainability attitudes and sustainable textile product purchasing behavior of both female and male consumers. No significant relationship was observed between social sustainability attitudes and sustainable textile product purchasing behavior of both female and male consumers. For both genders, a statistically significant and positive relationship was observed between consumers' economic sustainability attitudes and sustainable textile product purchasing behavior. This observation means that consumers are willing to pay a price premium for sustainable products.

Table 4: SEM results when grouped by gender

Structural			Estimate	S.E.	C.R.	P
Women						
Purchasing Behavior	<--	Environmental Attitude	1.036506	.29982	3.46	0.001
Purchasing Behavior	<--	Social Attitude	-.4568863	.5400185	-0.85	0.398
Purchasing Behavior	<--	Economic Attitude	.5265086	.1631489	3.23	0.001
Environmental_1	<--	Environmental Attitude	1			
Men						
Purchasing Behavior	<--	Environmental Attitude	.6647969	.215052	3.09	0.002
Purchasing Behavior	<--	Social Attitude	-.1739769	.3138516	-0.55	0.579
Purchasing Behavior	<--	Economic Attitude	.7539914	.1990798	3.79	0.000
Measurement						
Environmental_2	<--	Environmental Attitude	1.31057	.0931904	14.06	***
Environmental_3	<--	Environmental Attitude	1.4442	.100681	14.34	***
Environmental_4	<--	Environmental Attitude	1.332119	.0920667	14.47	***
Environmental_	<--	Environmental Attitude	1.41289	.0974276	14.50	***
Environmental_6	<--	Environmental Attitude	1.424076	.0986077	14.44	***
Environmental_7	<--	Environmental Attitude	1.426409	.0970531	14.70	***
Social_1	<--	Social Attitude	1			
Social_2	<--	Social Attitude	1.644732	.1898517	8.66	***
Social_3	<--	Social Attitude	1.365815	.1630793	8.38	***
Social_4	<--	Social Attitude	1.649713	.1873659	8.80	***
Economic_1	<--	Economic Attitude	1			
Economic_2	<--	Economic Attitude	.422744	.0622678	6.79	***
Economic_3	<--	Economic Attitude	1.167106	.0946278	12.33	***
Economic_4	<--	Economic Attitude	1.153437	.0937644	12.30	***
Economic_5	<--	Economic Attitude	1.189611	.0938663	12.67	***
First Purchase	<--	Purchasing Behavior	1			
Repurchase Behavior	<--	Purchasing Behavior	.9649592	.04746	20.33	***
Purchase Frequency	<--	Purchasing Behavior	.0032819	.0421679	0.08	0.938

***: $p < 0{,}001$

6.2. Grouping by generation

When the participants were grouped according to their generations, it was found that 62 of them were Baby-boomers (born between 1946-1964), 131 of

them were members of Generation X (born between 1965-1979), 124 of them were members of Generation Y (born between 1980-1994) and 155 of them were members of Generation Z (born between 1995-2009).

6.2.1. Testing the goodness of model fit

According to Table 5, the CMIN/DF value is less than the recommended value of 3 and shows that the model fit is acceptable. CFI value is 0.855 and TLI value is 0.850, indicating that the model fit is good. The RMSEA value is greater than the recommended value of 0.1 and the SRMR value is not within the recommended range [0;0.10). However, based on the values of other indices, the goodness of fit of the measurement model is at an acceptable level.

Table 5: SEM goodness of fit values when grouped by generation

Goodness of Fit Criteria	Goodness of Fit Values
CMIN	1495.571
DF	665
CMIN/DF	2,249
P-Value	***
CFI	0.855
TLI	0.850
RMSEA	0.103
SRMR	0.104

6.2.2. Analysis results and evaluation

According to Table 6, the effect of environmental sustainability attitudes on sustainable textile product purchasing behavior of Generation Y and Generation Z consumers is statistically significant and positive. There is no statistically significant relationship between the environmental sustainability attitudes and sustainable textile product purchasing behavior of Baby-boomers and Generation X consumers. There is no significant relationship between the social sustainability attitudes and sustainable textile product purchasing behavior of Baby-boomer, X, Y and Z generation consumers. This observation is contrary to the expectation. Firms publishing sustainability reports, establishing safe relationships with their suppliers, showing a fair approach to their employees and making donations to social responsibility projects do not affect consumers' sustainable textile product purchasing behavior. A statistically significant and positive relationship was observed between the economic sustainability attitudes of Generation Y consumers and their sustainable textile product purchasing

behavior. A statistically positive relationship has been observed between Generation Z consumers' economic sustainability attitudes and their sustainable textile product purchasing behavior at a significance level of 0.1. This observation means that consumers are willing to pay a price premium for sustainable products. Generation Z consumers give more importance to environmental sustainability than Generation Y consumers, but it is noteworthy that Generation Y consumers are more willing to pay a price premium than Generation Z consumers.

Table 6: SEM results when grouped by generation

Structural			**Estimate**	**S.E.**	**C.R.**	**P**
Baby-boomer						
Purchasing Behavior	<--	Environmental Attitude	-.6556626	1.109055	-0.59	0.554
Purchasing Behavior	<--	Social Attitude	1.014583	1.491567	0.68	0.496
Purchasing Behavior	<--	Economic Attitude	.6508114	.4207979	1.55	0.122
X-Generation						
Purchasing Behavior	<--	Environmental Attitude	-1.800576	8.158447	-0.22	0.825
Purchasing Behavior	<--	Social Attitude	3.555383	11.78464	0.30	0.763
Purchasing Behavior	<--	Economic Attitude	.2091785	1.63663	0.13	0.898
Y-Generation						
Purchasing Behavior	<--	Environmental Attitude	.831508	.3623019	2.30	0.022
Purchasing Behavior	<--	Social Attitude	-.570629	.5571322	-1.02	0.306
Purchasing Behavior	<--	Economic Attitude	.5990956	.1949842	3.07	0.002
Z-Generation						
Purchasing Behavior	<--	Environmental Attitude	.9704115	.177459	5.47	0.000
Purchasing Behavior	<--	Social Attitude	.1541955	.263137	0.59	0.558
Purchasing Behavior	<--	Economic Attitude	.2923845	.1606308	1.82	0.069
Measurement						
Environmental_1	<--	Environmental Attitude	1			
Environmental_2	<--	Environmental Attitude	1.368314	.0984421	13.90	***
Environmental_3	<--	Environmental Attitude	1.461762	.1039354	14.06	***
Environmental_4	<--	Environmental Attitude	1.337927	.094623	14.14	***
Environmental_5	<--	Environmental Attitude	1.442378	.10141	14.22	***
Environmental_6	<--	Environmental Attitude	1.444798	.1019299	14.17	***

Environmental_7	<-- Environmental Attitude	1.474004	.101976	14.45	***
Social_1	<-- Social Attitude	1			
Social_2	<-- Social Attitude	1.584223	.1754604	9.03	***
Social_3	<-- Social Attitude	1.305823	.149117	8.76	***
Social_4	<-- Social Attitude	1.584358	.1699502	9.32	***
Economic_1	<-- Economic Attitude	1			
Economic_2	<-- Economic Attitude	.4451123	.0611996	7.27	***
Economic_3	<-- Economic Attitude	1.164591	.0931587	12.50	***
Economic_4	<-- Economic Attitude	1.126351	.09239	12.19	***
Economic_5	<-- Economic Attitude	1.149836	.0915836	12.56	***
First Purchase	<-- Purchasing Behavior	1			
Repurchase Behavior	<-- Purchasing Behavior	.9631354	.0456901	21.08	***
Purchase Frequency	<-- Purchasing Behavior	-.0043456	.0454648	-0.10	0.924

***: $p < 0,001$

6.3. Grouping according to education level

When the participants were grouped according to their education level, it was found that 12 participants were primary school graduates, 60 participants were high school graduates, 266 participants were undergraduate graduates and 134 participants were postgraduate graduates. Primary school graduates were not taken into consideration since they were relatively few.

6.3.1. Testing the goodness of model fit

According to Table 7, the CMIN/DF value is less than the recommended value of 3 and shows that the model fit is acceptable. The CFI value is 0.855 and the TLI value is 0.880, indicating that the model fit is good. The RMSEA value is less than the recommended value of 0.1 and the SRMR value is within the recommended range of [0;0.10). Based on these values, the goodness of fit of the measurement model is at an acceptable level.

Table 7: SEM goodness of fit values when grouped by generation

Goodness of Fit Criteria	Goodness of Fit Values
CMIN	1157.482
DF	491
CMIN/DF	2,357
P-Value	***
CFI	0.885
TLI	0.880
RMSEA	0.094
SRMR	0.096

6.3.2. Analysis results and evaluation

According to Table 8, a statistically significant and positive relationship was observed between environmental and economic sustainability attitudes and sustainable textile product purchasing behavior for all consumer groups. No significant relationship was observed between consumers' social sustainability attitudes and sustainable textile product purchasing behavior. This observation is contrary to the expectation.

Table 8: SEM results when grouped according to educational level

Structural	**Estimate**	**S.E.**	**C.R.**	**P**
Highschool				
Purchasing Behavior <-- Environmental Attitude	1.158705	.5292341	2.19	0.029
Purchasing Behavior <-- Social Attitude	-.4271399	.6929911	-0.62	0.538
Purchasing Behavior <-- Economic Attitude	.5085208	.2118753	2.40	0.016
Bachelor				
Purchasing Behavior <-- Environmental Attitude	.8330674	.2351932	3.54	0.000
Purchasing Behavior <-- Social Attitude	-.324717	.4965407	-0.65	0.513
Purchasing Behavior <-- Economic Attitude	.5764544	.2007721	2.87	0.004
Postgraduate				
Purchasing Behavior <-- Environmental Attitude	.6150622	.2780164	2.21	0.027
Purchasing Behavior <-- Social Attitude	-.0078973	.455989	-0.02	0.986
Purchasing Behavior <-- Economic Attitude	.688186	.2678539	2.57	0.010

Measurement					
Environmental_1	<-- Environmental Attitude	1			
Environmental_2	<-- Environmental Attitude	1.352677	.097045	13.94	***
Environmental_3	<-- Environmental Attitude	1.457324	.1039275	14.02	***
Environmental_4	<-- Environmental Attitude	1.32151	.093656	14.11	***
Environmental_5	<-- Environmental Attitude	1.42646	.1002427	14.23	***
Environmental_6	<-- Environmental Attitude	1.469402	.1024381	14.34	***
Environmental_7	<-- Environmental Attitude	1.459443	.1007653	14.48	***
Social_1	<-- Social Attitude	1			
Social_2	<-- Social Attitude	1.637184	.1908736	8.58	***
Social_3	<-- Social Attitude	1.324321	.1582511	8.37	***
Social_4	<-- Social Attitude	1.64987	.1859586	8.87	***
Economic_1	<-- Economic Attitude	1			
Economic_2	<-- Economic Attitude	.4091696	.0608742	6.72	***
Economic_3	<-- Economic Attitude	1.146473	.09280	12.35	***
Economic_4	<-- Economic Attitude	1.107565	.090807	12.20	***
Economic_5	<-- Economic Attitude	1.157708	.0911	12.71	***
First Purchase	<-- Purchasing Behavior	1			
Repurchase Behavior	<-- Purchasing Behavior	.9865114	.0449519	21.95	***
Purchase Frequency	<-- Purchasing Behavior	-.0222331	.0450216	-0.49	0.621

6.4. Grouping by monthly income

When the participants were grouped according to their monthly income, it was found that 135 people had a monthly income of one minimum wage or less, 77 people had a monthly income of one to two minimum wages, 113 people had a monthly income of two to three minimum wages, 33 people had a monthly income of three to four minimum wages and 114 people had a monthly income of four minimum wages or more.

6.4.1. Testing model goodness of fit

According to Table 9, the CMIN/DF value is less than the recommended value of 3 and shows that the model fit is acceptable. CFI value is 0.848 and TLI value is 0.845, indicating that the model fit is good. RMSEA and SRMR values are not

within the recommended range [0;0,10). Based on the Chi-Square test and comparative fit indices, the goodness of fit of the measurement model is at an acceptable level.

Table 9: SEM goodness of fit values when grouped according to monthly income

Goodness of Fit Criteria	Goodness of Fit Values
CMIN	1730.533
DF	839
CMIN/DF	2,0626
P-Value	***
CFI	0.848
TLI	0.845
RMSEA	0.106
SRMR	0.112

6.4.2. Analysis results and evaluation

According to Table 10, the effect of environmental sustainability attitudes of consumers with a monthly income of one minimum wage or less on sustainable textile product purchasing behavior is statistically significant and positive. There is no significant relationship between social sustainability attitudes and sustainable textile product purchasing behavior. A positive relationship was observed between economic sustainability attitudes and sustainable textile product purchasing behavior at a 0.1 significance level. No significant relationship was observed between environmental and social sustainability attitudes and sustainable textile product purchasing behavior of consumers with a monthly income between one and two minimum wages and between two and three minimum wages. The effect of economic sustainability attitudes on sustainable textile product purchasing behavior is statistically significant and positive. Although these consumers do not particularly seek sustainable products, they are open to pay a price premium for a sustainable product. The effect of environmental sustainability attitudes of consumers with a monthly income between three and four minimum wages on their sustainable textile product purchasing behavior is statistically significant and positive. No significant relationship was observed between social sustainability attitudes and sustainable textile product purchasing behavior. A positive relationship was observed between economic sustainability attitudes and sustainable textile product purchasing behavior at a 0.1 significance level. The effect of economic sustainability attitudes of consumers with a monthly income of four minimum

wages or more on sustainable textile product purchasing behavior is statistically significant and positive. These consumers are willing to pay a price premium for a sustainable product. No significant relationship was observed between the environmental and social sustainability attitudes and sustainable textile product purchasing behavior of consumers with a monthly income of four minimum wages or more

Table 10: SEM results when grouped according to monthly income

Structural	**Estimate**	**S.E.**	**C.R.**	**P**
A minimum wage or less				
Purchasing Behavior <-- Environmental Attitude	.669267	.195878	3.42	0.001
Purchasing Behavior <-- Social Attitude	.3293742	.3404963	0.97	0.333
Purchasing Behavior <-- Economic Attitude	.3113074	.1646858	1.89	0.059
Between one and two minimum wage				
Purchasing Behavior <-- Environmental Attitude	.7909814	.4972395	1.59	0.112
Purchasing Behavior <-- Social Attitude	-.9066857	1.060832	-0.85	0.393
Purchasing Behavior <-- Economic Attitude	1.040867	.3607356	2.89	0.004
Between two and three minimum wage				
Purchasing Behavior <-- Environmental Attitude	.0262628	.6656796	0.04	0.969
Purchasing Behavior <-- Social Attitude	.7038898	.8105829	0.87	0.385
Purchasing Behavior <-- Economic Attitude	.6325046	.1745455	3.62	0.000
Between three and four minimum wage				
Purchasing Behavior <-- Environmental Attitude	1.508535	.3206335	4.70	0.000
Purchasing Behavior <-- Social Attitude	-1.352021	.8578068	-1.58	0.115
Purchasing Behavior <-- Economic Attitude	.7824209	.436371	1.79	0.073
Four minimum wages or more				
Purchasing Behavior <-- Environmental Attitude	.6387419	.3983997	1.60	0.109
Purchasing Behavior <-- Social Attitude	-.5987907	.8256266	-0.73	0.468
Purchasing Behavior <-- Economic Attitude	.8006279	.3203004	2.50	0.012
Measurement				
Environmental_1 <-- Environmental Attitude	1			
Environmental_2 <-- Environmental Attitude	1.262257	.0869	14.53	***
Environmental_3 <-- Environmental Attitude	1.367166	.0915408	14.94	***

Environmental_4	<-- Environmental Attitude	1.253744	.0834003	15.03	***
Environmental_5	<-- Environmental Attitude	1.362538	.0891458	15.28	***
Environmental_6	<-- Environmental Attitude	1.369083	.0910511	15.04	***
Environmental_7	<-- Environmental Attitude	1.363873	.0884082	15.43	***
Social_1	<-- Social Attitude	1			
Social_2	<-- Social Attitude	1.715338	.1979945	8.66	***
Social_3	<-- Social Attitude	1.349131	.1619621	8.33	***
Social_4	<-- Social Attitude	1.682406	.1900842	8.85	***
Economic_1	<-- Economic Attitude	1			
Economic_2	<-- Economic Attitude	.4211793	.0601889	7.00	***
Economic_3	<-- Economic Attitude	1.178588	.0922424	12.78	***
Economic_4	<-- Economic Attitude	1.100297	.0880393	12.5	***
Economic_5	<-- Economic Attitude	1.141561	.0888939	12.84	***
First Purchase	<-- Purchasing Behavior	1			
Repurchase Behavior	<-- Purchasing Behavior	.9820843	.0461757	21.27	***
Purchase Frequency	<-- Purchasing Behavior	.0008034	.0451316	0.02	0.986

***: $p < 0{,}001$

6.5. Grouping according to households

Of the participants, 102 live with their parents, 52 live alone, 43 live with their friends/colleagues, 92 live with their spouse and 183 live with their spouse and child/children. Participants living with friends/colleagues were not taken into consideration since they were few.

6.5.1. Testing the goodness of model fit

According to calculations, the CMIN/DF value is less than the recommended value of 3 and shows that the model fit is acceptable. The CFI value is 0.839 and the TLI value is 0.835, indicating that the model fit is good. The RMSEA value is greater than the recommended value of 0.1, but the SRMR value is within the recommended range [0;0.10). Based on the Chi-Square test and comparative fit indices, the goodness of fit of the measurement model is at an acceptable level.

6.5.2. Analysis results and evaluation

According to Table 11, the effect of environmental sustainability attitudes of consumers living with their parents and single consumers on their sustainable textile product purchasing behavior is statistically significant and positive, but

there is no statistically significant and positive relationship between economic sustainability attitudes and sustainable textile product purchasing behavior. Although these consumers are sensitive to the environment, they exhibit a more utilitarian approach and are not willing to pay a price premium. No statistically significant relationship was observed between environmental sustainability attitude and sustainable textile product purchasing behavior for consumers living with their spouse and spouse and child/children. A statistically significant and positive relationship was observed between economic sustainability attitudes and sustainable textile product purchasing behavior of consumers living with their spouse and spouses and child/children. This observation means that consumers living with their spouse and spouse and child/children are willing to pay a price premium for sustainable products. For all consumer groups, no significant relationship was observed between social sustainability attitudes and sustainable textile product purchasing behavior.

Table 11: SEM results when grouped by households

Structural	**Estimate**	**S.E.**	**C.R.**	**P**
With Parents				
Purchasing Behavior <-- Environmental Attitude	.9080001	.2576012	3.52	0.000
Purchasing Behavior <-- Social Attitude	.3846515	.4310742	0.89	0.372
Purchasing Behavior <-- Economic Attitude	.2271547	.1901504	1.19	0.232
Single				
Purchasing Behavior <-- Environmental Attitude	1.459732	.2471142	5.91	0.000
Purchasing Behavior <-- Social Attitude	-.2605644	.4566392	-0.57	0.568
Purchasing Behavior <-- Economic Attitude	.1976277	.2960552	0.67	0.504
With Wife/Husband				
Purchasing Behavior <-- Environmental Attitude	.7476895	.5351071	1.40	0.162
Purchasing Behavior <-- Social Attitude	-.1761166	.6192206	-0.28	0.776
Purchasing Behavior <-- Economic Attitude	.648301	.2036592	3.18	0.001
With Wife/Husband and Child(ren)				
Purchasing Behavior <-- Environmental Attitude	.4847479	.6945176	0.70	0.485
Purchasing Behavior <-- Social Attitude	-.046827	1.033935	-0.05	0.964
Purchasing Behavior <-- Economic Attitude	.8071755	.219418	3.68	0.000
Measurement				
Environmental_1 <-- Environmental Attitude	1			

Environmental_2	<-- Environmental Attitude	1.293786	.1017868	12.71	***
Environmental_3	<-- Environmental Attitude	1.459549	.1127229	12.95	***
Environmental_4	<-- Environmental Attitude	1.334332	.1023121	13.04	***
Environmental_5	<-- Environmental Attitude	1.401557	.1071309	13.08	***
Environmental_6	<-- Environmental Attitude	1.419199	.107877	13.16	***
Environmental_7	<-- Environmental Attitude	1.441308	.1077696	13.37	***
Social_1	<-- Social Attitude	1			
Social_2	<-- Social Attitude	1.535592	.1869118	8.22	***
Social_3	<-- Social Attitude	1.392118	.1706087	8.16	***
Social_4	<-- Social Attitude	1.566854	.1848261	8.48	***
Economic_1	<-- Economic Attitude	1			
Economic_2	<-- Economic Attitude	.4235822	.0636231	6.66	***
Economic_3	<-- Economic Attitude	1.171438	.0971656	12.06	***
Economic_4	<-- Economic Attitude	1.166411	.097107	12.01	***
Economic_5	<-- Economic Attitude	1.157125	.0955525	12.11	***
First Purchase	<-- Purchasing Behavior	1			
Repurchase Behavior	<-- Purchasing Behavior	.9342192	.0469389	19.90	***
Purchase Frequency	<-- Purchasing Behavior	.0132328	.0462415	0.29	0.775

***: $p < 0{,}001$

7. Conclusion

Due to various environmental and social problems, sustainability has become an important issue that needs to be addressed. On the one hand, environmental problems such as intensive water consumption in textile production, consumption of natural resources, the release of wastes to nature, and the disposal of unused products bring great burden on the environment. On the other hand, the intensive use of chemicals in production processes creates various social problems in the sector as it affects both employee health and public health. For this reason, the public and private sectors need to take various measures. In addition to taking steps for environmental and social sustainability by improving production processes and employee working conditions, to ensure economic sustainability and to be able to adapt the product range to consumer demands, the private sector should investigate the consumers' purchase intention towards sustainable textile products. In this study, a survey was conducted on 472 people to determine

consumers' perspectives on environmental, social and economic sustainability and to measure the impact of these factors on their purchasing behavior.

The SEM results indicate that consumers attach importance to economic and environmental sustainability, but not to social sustainability. When grouped according to gender, it is seen that female consumers attach more importance to environmental factors than male consumers while male consumers are more willing to pay a price premium for sustainable products than female consumers. While Baby-boomers and Generation X consumers do not attach importance to environmental sustainability, Generation Y and Generation Z consumers attach importance to environmental sustainability. In addition, while Generation Y consumers are willing to pay a price premium for sustainable textile products, Generation Z consumers are partially willing to pay a price premium for sustainable textile products, Baby-boomers and Generation X consumers are not willing to pay a price premium for sustainable textile products. It has been observed that educational level has no significant effect on sustainability attitudes and purchasing behaviour. Environmental sustainability is important for consumers living with their parents and single consumers, but this group is not willing to pay a price premium for sustainable products. Consumers living with their spouse and spouse and child/children are willing to pay a price premium for sustainable products. However, the reason for this observation may also be related to income level. It is observed that monthly income groups with one to two minimum wages, two to three minimum wages and four minimum wages or more are willing to pay a price premium. The monthly income groups of one minimum wage or less and three to four minimum wages are partially willing to pay price premiums.

In terms of practical and social implications, this study highlights which issues marketing and corporate communication should focus on and what they should do for different consumer groups. It can be seen that consumers are very sensitive about environmental issues, but not as sensitive in social terms. This may be because they have less information about the social dimension of sustainability. For this reason, companies can conduct campaigns to create public opinion about social sustainability efforts in the apparel sector. In the literature, there are studies targeting mostly female consumers but according to the results, male consumers can also be specifically targeted. It is observed that young consumers are more likely to prefer sustainable products but it is thought that they do not have the resources to pay a price premium. On the other hand, while middle-aged and older consumer groups have the resources to pay a price premium, it can be assumed that they do not have as much understanding about sustainability. Companies can prioritize content and the appropriate marketing tools and channels to appeal to this age group while designing their marketing strategies.

This study has some limitations. Participants with primary education were not taken into consideration due to their limited representation. In groupings according to household size, participants living with friends/colleagues were not taken into consideration because of the low number of participants. In future studies, the number of participants can be increased and analyses can be made for groups that could not be included. This study can be repeated by reaching consumers with different education and income levels from various geographies, and comparative analyses can be made.

Acknowledgement

The authors declare that they have no conflict of interest and that they have the ethics committee decision of the Turkish-German University.

References

Abreu, M.C.S.d, Ferreira, F.N.H. and Silva, J.F.B.A. (2022), "To be or not to be sustainable in an emerging market? Conjoint analysis of customers' behavior in purchasing denim jeans", *Journal of Fashion Marketing and Management*, Vol. 26 No. 3, pp.452-472.

Aydın, T.F., Tufan, F. (2018), "Sürdürülebilirlik Ve Yeşil Kavramlari Bağlaminda Y Kuşağinin Satin Alma Davranişlari", *Journal of Selcuk Communication*, Vol. 11 No. 2, pp.397- 420.

Bizuneh, B., Hailemariam, S.S., and Tsegaye, S. (2022), "A study of consumers' pre-purchase evaluation of apparel products in Ethiopia", *Journal of Fashion Marketing and Management*, Vol. 26 No. 5, pp.776-791.

Boufous, S., Hudson, D., and Carpio, C. (2023), "Consumer willingness to pay for production attributes of cotton apparel", *Agribusiness*, Vol. 39, pp.1026-1048.

Bowen, N. K. and S. Guo (2012), *Structural Equation Modeling*, Oxford University Press, NY.

Can, Ö. and Ayvaz, K.M. (2017), "Tekstil ve Modada Sürdürülebilirlik", *Akademia Sosyal Bilimler Dergisi*, Vol. 1 No. 3, pp.110-119.

Chen, Y. and Chang, C. (2012), "Enhance green purchase intentions: The roles of green perceived value, green perceived risk, and green trust", *Management Decision*, Vol. 50 No. 3, pp.502-520.

Colasante, A., and D'Adamo, I. (2021), The circular economy and bioeconomy in the fashion sector: Emergence of a "sustainability bias", *Journal of Cleaner Production*, Vol. 329, 129774.

Çakır, H. and Eroglu, N.S. (2023), "Tekstil Ve Hazir Giyim Markalarina Ait Seçilen Bazi Ürünlerin Sürdürülebilirlik Açisindan Değerlendirilmesi", *Turkish Journal of Fashion Design and Management*, Vol. 5 No. 2, pp.47-66.

Ercan, E. (2010), "Giysi satınalmada tüketicinin kararına etkili olan faktörler giysi satınalmada tüketicinin kararına etkili olan faktörler", *Electronic Journal of Social Sciences*, Vol. 9 No. 33, pp.1-17.

Fan, X., Thompson, B., and Wang L. (1999), "Effects of Sample Size, Estimation Methods, and Model Specification on SEM Fit Indexes", *Structural Equation Modeling: A Multidisciplanary Journal*, pp.56-83.

Fuchs, M. and Hovemann, G. (2022), "Consumer preferences for circular outdoor sporting goods: An Adaptive Choice-Based Conjoint analysis among residents of European outdoor markets", *Cleaner Engineering and Technology*, Vol. 11, 100556.

Guo, W. and Kim, E. (2023), “Categorizing Chinese Consumers’ Behavior to Identify Factors Related to Sustainable Clothing Consumption”, *Sustainability*, Vol. 15 No. 7, 6126.

Metlioğlu, H.H. and Yakın, V. (2021), “Tekstilde Sürdürülebilirlik: Hızlı Moda Markalarının Sürdürülebilirlik Stratejileri”, *OPUS Uluslararası Toplum Araştırmaları Dergisi*, Vol. 18, pp.1883-1908.

Hu, L.T. and Bentler, P.M. (1999), “Cutoff criteria for fit indexes in covariance structure analysis: Conventional criteria versus new alternatives”, *Structural Equation Modeling: A Multidisciplinary Journal*, Vol. 6 No. 1, pp.1–55.

Innami, Y. and Koizumi, R. (2011), “SEM in Language Testing and Learning Research: A Review”, *Language Assessment Quarterly*, Vol. 8 No. 3, pp.250-276.

Iacobucci, D. (2010), “Structural equations modeling: Fit Indices, sample size, and advanced topics”, *Journal of Consumer Psychology*, Vol. 20 No. 1, pp.90-98.

Jacobs, K., Petersen, L., Hörisch, J., and Battenfeld, D. (2018), “Green thinking but thoughtless buying? An empirical extension of the value-attitude-behaviour hierarchy in sustainable clothing” *Journal of Cleaner Production*, Vol.203, pp.1155-1169.

Klein, F.F., Emberger-Klein, A., and Menrad, K. (2020), “Indicators of Consumers’ Preferences for Bio-Based Apparel: A German Case Study with a Functional Rain Jacket Made of Bioplastic”, *Sustainability*, Vol. 12 No. 2, 675.

Lang, C. and Armstrong, C.M.J. (2018), “Fashion leadership and intention toward clothing product-service retail models”, *Journal of Fashion Marketing and Management*, Vol. 22 No. 4, pp.571-587.

Laroche, M., Bergeron, J., and Barbaro-Forleo G. (2001), “Targeting Consumers Who Are Willing to pay a price premiumfor Enviromentally Friendly Products”, *Journal of Consumer Marketing*, Vol. 18 No. 6, pp.503-520.

Lin, P.H. and Chen, W.H. (2022), “Factors That Influence Consumers’ Sustainable Apparel Purchase Intention: The Moderating Effect of Generational Cohorts”, *Sustainability*, Vol. 14 No. 14, 8950.

MacCallum, R.C., Browne, M.W., and Sugawara, H.M. (1996), “Power Analysis and Determination of Sample Size for Covariance Structure Modeling”, *Psychological Methods*, Vol. 1 No. 2, pp.130-149.

Marsch, H.W., Hau K. and Wen, Z. (2004), “In Search of Golden Rules: Comment on Hypothesis-Testing Approaches to Setting Cutoff Values for Fit Indexes and Dangers in Overgeneralizing Hu and Bentler's (1999) Findings”, *Structural Equation Modeling: A Multidisciplinary Journal*, Vol. 11 No. 3, pp.320-341.

McDonald, R.P. and Ho, M.H.R. (2002), "Principles and Practice in Reporting Structural Equation Analyses", *Psychological Methods*, Vol. 7 No. 1, pp.64–82.

Newbold, P. (2000), *İşletme ve İktisat İçin İstatistik*, Translated by Ümit Şenesen, Literatür Publishing, İstanbul.

Pituch K.A., Stevens J.P. 2015. Applied multivariate statistics for the social sciences: Analyses with SAS and IBM's SPSS. Routledge.

Polonsky, M.J. (2011), "Transformative green marketing: Impediments and opportunities", *Journal of Business Research*, Vol. 64 No. 12, pp.1311-1319.

Portakalcı, M. (2017), "Ürün Özelliklerinin Bireylerin Tutumları Üzerindeki Etkisi", *Karabük Üniversitesi Sosyal Bilimler Enstitüsü Dergisi*, Vol. 7 No. 1, pp.189-202.

Rahman, O. and Kharb, D. (2022), "Product Choice: Does Eco-Labeling Play an Important Role in Apparel Consumption in India?", *Fashion Practice*, Vol. 14 No. 2, pp.266-291.

Rahman, O. and Koszewska, M. (2020), "A study of consumer choice between sustainable and non-sustainable apparel cues in Poland", *Journal of Fashion Marketing and Management*, Vol. 24 No. 2, pp. 213-234.

Rausch, T.M., Baier, D., and Wening, S. (2021), "Does sustainability really matter to consumers? Assessing the importance of online shop and apparel product attributes", *Journal of Retailing and Consumer Services*, Vol. 63, 102681.

Riesgo, S.B., Codina, M., and Sádaba, T. (2023), "Does Sustainability Matter to Fashion Consumers? Clustering Fashion Consumers and Their Purchasing Behavior in Spain", *Fashion Practice*, Vol. 15 No. 1, pp.36-63.

Schumaker, R. and Lomax, R. (2015), *A Beginner's Guide to Structural Equation Modeling*, Routledge, USA.

Singh, P.B. and Pandey, K.K. (2012), "Green Marketing: Policies and Practices for Sustainable Development", *Integral Review- A Journal of Management*, Vol. 5 No. 1, pp.22-30.

Yeniçeri, T. (2009), "Tüketicilerin Çevre Bilinci Ve Çevreye Duyarli Satinalma Davranişlarina Yönelik Bir Pilot Araştirma", Sosyal Ekonomik Araştırmalar Dergisi, Vol. 9 No. 17, pp.310-326.

Yeniçeri, T. and Özbezek, B. (2016), "Cinsiyet Tüketici Karar Verme Tarzlarini Farklilaştirir Mi?", Atatürk Üniversitesi İktisadi ve İdari Bilimler Dergisi, Vol. 30 No. 3, pp.591-608.

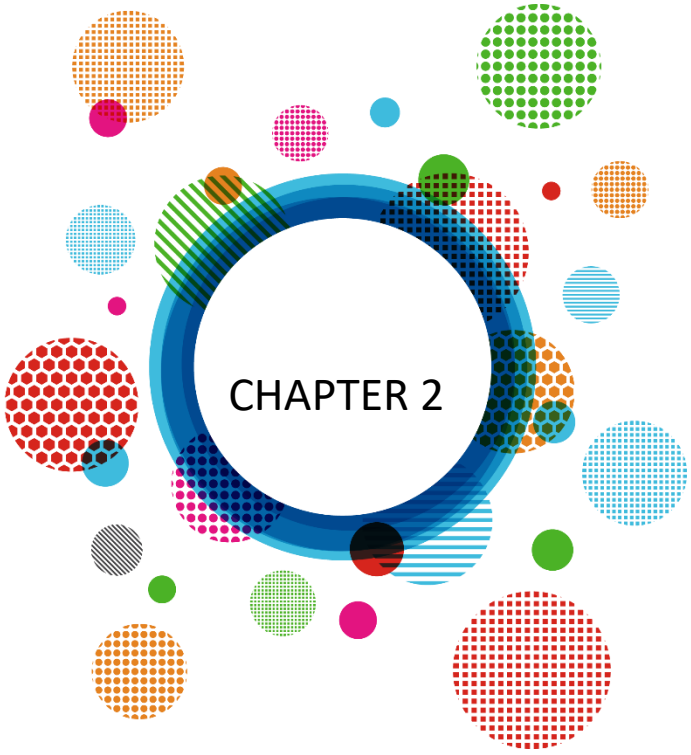

A Bibliometric Analysis of Research on Cyberbullying and Hate Speech in Social Media Content (2018–2025)

Elif Sarıgıl Kara[1] & Murat Koklu[2]

1. Introduction

With the widespread use of digital technologies and internet access, social media platforms have become the main digital channels through which individuals express their thoughts, react to social events, and interact. However, these channels are not only for communication and information sharing; they also pave the way for the spread of negative digital behaviors such as hate speech, cyberbullying, discrimination, and psychological violence. Especially on platforms that generate user-generated content, and its impact on the masses makes it difficult to protect individual rights and freedoms in the digital environment. In this context, the detection and control of harmful content has become a critical necessity for both individual psychological health and social peace. Among the techniques developed to solve this problem, machine learning (ML), natural language processing (NLP), and deep learning (DL) methods have come to the fore in recent years. Thanks to these techniques, posts containing hate speech and online bullying can be classified more effectively and detected automatically. In addition to models such as BERT, GPT, and BiLSTM, Multimodal (text, audio, image) approaches also increase the success of detection systems, especially considering the rich data diversity of social media platforms. However, the methodologically wide range of studies and the use of a large number of different data sets, labeling methods, and model combinations make it difficult to evaluate existing research holistically.

In this context, it is important to understand not only the technical competencies of studies on hate speech and cyberbullying but also their historical development, research trends, and interdisciplinary orientations. The technical depth of the field, as well as its scientific productivity and collaborative structures, will enable the development of more systematic and sustainable approaches to the analysis of social media content.

Therefore, analyzing the scientific literature on hate speech from both a technical and bibliometric perspective offers significant benefits not only for

[1] Graduate School of Natural and Applied Sciences, Selcuk University, Konya, Türkiye
ORCID: 0009-0004-7014-8630
[2] Department of Computer Engineering, Selcuk University, Konya, Türkiye;
ORCID: 0000-0002-2737-2360

academic knowledge production but also for policymakers, content moderators, and technology developers.

1.1. Machine Learning Based Studies on Hate Speech Detection

Boishakhi et al. Pointed out the inadequacy of detecting hate speech with text alone and developed a multimodal-based system that extracts images, audio, and text from video content. They collected 1051 videos from YouTube and movie /series sources and extracted data with OpenCV, MoviePy, and Google Speech Recognition. Feature selection for each modality was performed with RFE and mRMR methods. Separate machine learning models were trained and the decisions were combined with hard voting. They achieved 87% accuracy with the Adaboost model (Boishakhi et al., 2021).

To mitigate the disadvantages of manual annotation, Saifullah et al. developed an automatic annotation system based on semi-supervised learning. In the dataset of 13,169 YouTube comments on political and legal issues in Indonesia, texts were subjected to stemming with Sastrawi. Features were extracted with TF-IDF and Word2Vec methods. In their experiments with SVM, DT, KNN, and NB Algorithms, they achieved 97.1% accuracy with the TF–IDF–supported Decision Tree model using 5% labelled data and threshold value of 0.9. In addition, the KNWord2Vwc and SVM-Word2Vec models achieved 96.9% and 96.8% accuracy, respectively. Interestingly, the authors observed that model performance improved as the proportion of labeled data decreased, highlighting the efficiency of their semi-supervised annotation strategy (Saifullah et al., 2024)

Irfan et al. Developed a multimodal hate speech detection system by processing text and audio data together. In a dataset of 22,083 tweets from Kaggle, they divided the data into three classes and applied various preprocessing steps. They separately processed the text and audio data with a multilingual, pre-trained BERT model and then classified them with CNN and MLP. They achieved 92% accuracy with the multimodal BERT model compared to text-only models. This rate was higher than CNN (85%) and BiLSTM–Attention (88%). They demonstrated that the use of BERT-based multimodality is effective in online hate speech detection. (Irfan et al., 2024).

Nasir et al. Developed a two-stage classification method for detecting hate speech in Roman Urdu. Using a 5000-tweet HS-RU-20 dataset, they first categorized the content into “neutral” and “hostile”, then “insulting” and “hate speech”. They tested six different models by feature extraction with word and character-level n-gram vectors. They obtained the highest accuracy values with the Logistic Regression model at both stages (81%, 87%). They stated that

characther n-grams were particularly effective in the first stage, while the second level classification gave more successful results. However, they also identified limitations such as data imbalance and computational cost (Nasir et al., 2024).

1.2. Studies on Hate Speech Analysis with Natural Language Processing Methods

Fortuna et al. stated that problems such as context-agnostic definitions, biased labeling, and low inter-annotator agreement(IAA) limit model generalization in NLP-based hate speech detection. In some studies, the IAA was as low as 0.3. Although accuracy rates were high, models that failed to perceive context made critical misclassifications (e.g., "Women's place is in the cemetery" was not recognized as hate speech with 99.96% probability). They emphasized that data sampling strategies often failed to capture contextual diversity and that rare but harmful instances of hate speech are missed. Therefore, they advocated for the development of context-aware and community-informed annotation methods (Fortuna et al., 2022).

Jahan et al. evaluated data augmentation methods for hate speech detection and compared WordNet, FastText, BERT-mask, Back-Translation, and GPT-3 techniques on five different datasets. They found that methods such as WordNet and BERT-mask lead to a 5% label flipping. However, they managed to reduce this rate to 0.4% with their proposed BERT-cosine similarity–based filtering method. With the GPT-3 method, they achieved the highest contextual similarity score (96%) and achieved a 1.4% increase in model performance. They also showed that the data augmentation ratio increased by up to 20 times with GPT-3. In their research, they demonstrated that GPT-3 and BERT cosine filtering methods provide effective results by preserving label integrity and increasing model performance (Jahan et al., 2024).

In order to detect anti-semitic hate speech more effectively, Halevy developed 'KnowledJe', a knowledge graph consisting of 618 conceptual elements. This graph was applied to the Echo Corpus of 4,630 tweets and tested with Logistic Regression (LR) and DistilBERT models. After knowledge integration, the F1 score of the LR model increased from 0.321 to 0.336. On the other hand, a marginal decrease was observed in the distilBERT model; the F1 Score decreased from 0.680 to 0.657, and the AUCROC value decreased from 0.929 to 0.924. Despite the slight decline in transformer-based performance, the knowledge graph significantly enhanced the detection of coded and indirect hate expressions, highlighting its utility in the semantic enrichment of classification models (Halevy, 2023).

Ilhan et al. conducted a comparative analysis of Bi-LSTM and Bi-LSTM + GRU models for hate speech classification, using a dataset of 27,406 tweets categorized into six classes: racism, sexism, neutrality, anti-government, anti-religion, and aggression. Texts were vectorized using Word2Vec embeddings, and models were trained with the Adam optimizer. The Bi-LSTM model achieved an F1 score of 97.85% in the neutrality class and 90.02% in the sexism class. The Bi-LSTM +GRU model obtained F1 scores of 97.88% and 85.96% in the same classes, respectively. Overall classification accuracy was reported as 94% for Bi-LSTM and 95% for Bi-LSTM+GRU. The authors concluded that the Bi-LSTM + GRU model was more effective in capturing long-term dependencies and identifying complex hate speech patterns (Ilhan et al., 2024).

Faruqe et al. used deep learning and transducer-based natural language processing methods for hate speech detection on a dataset of 4,978 examples generated from Bangla social media data . They divided the data into two classes as “hate” and “not hate” and applied preprocessing steps such as translation, cleaning, and vectorization. In their experiments, they achieved 98.87% accuracy and 99% F1 score with the GRU model. While 98% accuracy was achieved with the Attention-based model, the BERT model was 95% accurate, and the Bi-LSTM was 71.68% accurate. The authors highlighted that GRU outperformed other models in Bangla due to its fast and efficient architecture, making it particularly suitable for low-resource language settings (Faruqe et al., 2023).

1.3. Studies on Hate Speech Analysis Using Deep Learning Approaches

Pookpanich ve Siriborvornratanakul compared five different BERT-based models for hate speech detection on 2,028,434 messages collected from football-related YouTube content in Thailand. In experiments using both automatically labelled data (WangchanBERTa) and manually annotated datasets, the XLM-RoBERTa model achieved the highest success with 96.69% recall and 95.30% F1 score. However, it was stated that the DistilBERT model is preferred in practical applications due to its low hardware cost and speed advantage. The entire training process was conducted in a GPU environment using the SimpleTransformers library (Pookpanich & Siriborvornratanakul, 2024).

Kibriya et al. proposed a Conv-BiRNN-BiLSTM-based model for hate speech detection and evaluated its performance on a total of 82,702 tweets drawn from three different datasets. The classification task was performed in two stages: a binary classification in the first stage, followed by a multi-class classification in the second. The model achieved 93.3% accuracy (F1 score: 0.93) in the binary task and 98.5% accuracy (F1 score: 0.99) in the multi-class task. The proposed

architecture was described as lightweight, consisting of only 2 million parameters. To enhance model interpretability, SHAP and LIME techniques were applied. The study also emphasized that the model delivered comparable performance to large-scale models such as BERT Large, while requiring significantly lower computational resources (Kibriya et al., 2024)

Toktarova et al. conducted a comparative analysis of traditional machine learning and deep learning-based approaches for hate speech detection on social media data. The dataset consisted of three classes: “hate speech”, “offensive language”, and “neutral”. Features were extracted using Bag of Words, TF-IDF, and Word2Vec techniques. A variety of models were evaluated, including SVM, Naive Bayes, CNN, LSTM, and BiLSTM. Among these, the BiLSTM model achieved the highest performance with 90.2% accuracy and an F1 score of 89.9%, while the Decision Tree model demonstrated the lowest performance (Toktarova et al., 2023).

Alshalan et al. compared CNN, GRU, CNN+GRU, and BERT models 4 4 Arabic hate speech detection in their binary classification experiments conducted on 8.964 tweets collected from Saudi Arabia. The CNN model achieved the best performance with an F1 score of 0.79% and an AUROC value of 0.89%. The BERT model, on the other hand, yielded the weakest results, showing relatively low AUROC values. Out-of-domain testing also confirmed the superiority of the CNN model, which consistently outperformed others. Moreover, in comparison with character n-gram-based SVM and Logistic Regression models, the CNN model delivered the highest scores in terms of overall accuracy and recall for the hate class (Alshalan & Al-Khalifa, 2020).

Badjatiya et al. explored deep learning architectures for the automatic classification of hate speech on X (Twitter), specifically targeting racist, sexist, and neutral categories. Aiming to go beyond traditional n-gram-based approaches, they utilized a benchmark dataset containing 16,000 labeled tweets. Semantic word embeddings were learned through various deep learning models, and these approaches were found to be more effective in capturing the complex structure of natural language. According to the results, deep learning methods yielded approximately an 18% improvement in F1 score compared to conventional character or word-level n-gram-based techniques. The study concluded that deep architectures significantly outperform traditional methods in the task of hate speech classification (Badjatiya et al., 2017).

Zhou et al. performed hate speech detection using a classifier fusion approach that combined ELMo, BERT, and CNN-based models. Their study employed a

balanced dataset from SemEval-2019 Task 5, consisting of 9,000 training tweets, 1,000 development tweets, and 3,000 test tweets (with 42% labeled as hate, 58% as non-hate). In experiments conducted on the SemEval-2019 dataset, the fusion method achieved an accuracy of 87.17% and an F1 score of 81.39%. Compared to individual models, the fusion approach yielded an accuracy improvement of 2.5%–6.9% and an F1 score increase of 0.86%–13.0% (Y. Zhou et al., 2020).

Miran and Yahia conducted A systematic review to examine the use of CNN ve CNN-paste models for hate speech detection on Twitter. Do you study evaluated 565 articles published between 2010 and 2021, and 20 studies were selected for in-depth analysis based on specific inclusion criteria. The reviewed models included CNN, CNN+LSTM, CNN+GRU, and CNN+BERT classifier fusion techniques. These models were tested on tweets in various languages, including English, Arabic, Korean, Portuguese, Russian, and Urdu. Key findings indicated that CNN-based models generally achieved accuracy scores between 81% and 96%, and the FPS codes ranging from 0,78% and 0,93%. Notably, combinations such as CNN+GRU and CNN+LSTM yielded 2%-5% higher accuracy than stand-alone CNN models in some studies. Furthermore, several studies employed large-scale datasets containing over 100,000 tweets and addressed multi-class classification tasks involving categories such as racism, sexism, and religious hate. Despite these advancements, the researchers highlight several limitations, including a lack of cross-lingual generalization, inattention to user-to-user conversational context, and context sensitivity in certain models (Miran & Yahia, 2023).

1.4. Bibliometric Review of Hate Speech Studies

Tontodimamma et al. conducted a bibliometric analysis of 1,614 studies published between 1992 and 2019, evaluating hate speech research in terms of topics, trends, and country-level contributions. Using Latent Dirichlet Allocation (LDA), they identified 12 distinct themes, which were grouped under three main categories. Notably, topic 12, which focused on machine learning approaches, showed the fastest growth, with a 20.5% increase after 2018. While the United States and the United Kingdom led in overall publication volume, Italy and India emerged as prominent contributors in the area of automated detection. The study emphasized the disciplinary shift in hate speech research, highlighting its evolution from the social science toward computer science and its increasingly interdisciplinary nature (Tontodimamma et al., 2021).

Gangurde et al. conducted a bibliometric study analyzing 321 publications released between 2013 and 2021, with a focus on research trends in hate speech

detection on social media. The most frequently occurring keywords were identified as “hate speech”, “machine learning”, and “social media”, and it was found that 75% of the publications were in the form of conference proceedings. The year 2020 stood out as the most productive in terms of publication volume, and a notable increase in machine-learning-focused studies was observed over the last four years. Furthermore, the presence of only 27 publications in Hindi revealed a significant gap in multilingual hate speech research (Gangurde et al., 2022).

Mutanga et al. conducted a bibliometric analysis of 358 articles published between 2016 and 2022, focusing on deep learning based research related to hate speech detection on social media. The study identified India as the most productive country, while Norway and the United Kingdom were found to have the highest average citation rates. The most highly cited paper was attributed to Badjatiya, receiving 552 citations. Keywords such as “Deep learning”, “LSTM”, “BERT”, and “transfer learning” were found to be dominant, whereas traditional approaches appeared to be used less frequently. The authors also highlighted several research gaps, including the lack of interpretability, limited linguistic diversity, and underutilization of visual and audio modalities in hate speech detection studies (Mutanga et al., 2023).

Ramírez-García et al. conducted a bibliometric analysis of 638 Scopus-indexed publications from 2001 and 2020 containing “hate speech” and “social media”. The authors reported that 67.1% of these publications had received at least one citation, and the Field-Weighted Citation Impact (FWCI) was 173% above the global average. The majority of the publications were in the form of conference papers (50.23%) and journal articles (39.28%), with “computer science” and “social sciences” emerging as dominant disciplines. Technical terms such as “Machine learning,” “text mining,” and “detection” appeared most frequently across the dataset. A significant rise in publication output was observed after 2017, with a noticeable acceleration beginning in 2019. This study emphasized that the field holds substantial importance both socially and scientifically (Ramírez-García et al., 2022).

Antona Jimeno et al. conducted a bibliometric study analyzing 153 publications released between 2021 and 2023 in Spain and Latin America (LATAM). The authors reported that 69% of the publications originated from these regions. Rosso was identified as the most prolific author, while Gámez-Guadix and Wachs were the most highly cited researchers. Frequently used keywords included “Hate speech”, “social media”, and “Twitter”. Additionally, topics related to natural language processing (NLP), deep learning, and machine

learning emerged as dominant research themes. Co-authorship and keyword Co-occurrence analysis revealed a strong presence of social issues such as politics, migration, LGBTQ+ rights, and freedom of expression (Antona Jimeno et al., 2024).

This study aims to provide a comprehensive mapping of the growing academic interest in online hate speech and cyberbullying, systematically uncovering the current body of knowledge in the field. Although existing studies in the literature demonstrate a remarkable diversity of technical achievements and modeling approaches, research efforts remain largely limited to scientific languages, geographies, and platforms. Critical aspects such as cross-cultural generalization, multilingual analysis, explainability, and ethical considerations are still insufficiently addressed. Moreover, the lack of standardization in datasets, methodological inconsistencies, and the tendency to evaluate models solely based on accuracy metrics represent major obstacles to the maturation of the field. In this context, the present thesis offers a structural contribution by making visible the prevailing trends, strengths, and limitations in the literature. By adopting a bibliometric analysis approach covering a recent period (2018 and 2025), this study not only delivers a retrospective evaluation but also aims to serve as a guiding resource for future researchers, policymakers, and technology developers interested in the field. In this regard, the study fills a significant gap by helping to understand the trajectory of scientific production on socially impactful issues such as hate speech, to build interdisciplinary bridges, and to inform more deliberate research strategies for the future.

2. Methodological Framework and Application Steps

This section provides a detailed account of the bibliometric analysis process carried out within the scope of this study. First, the data collection strategies and sources used are described, followed by the steps taken to process, clean, and prepare the data for analysis. Subsequently, the bibliometric techniques employed in the analysis are systematically presented under relevant subheadings. The methodological steps are presented in the Figure below.

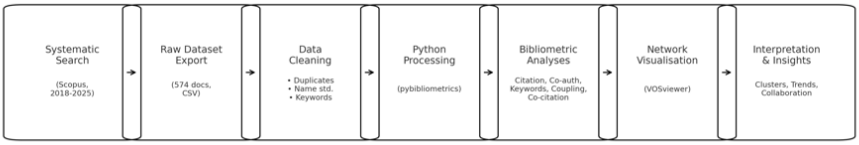

Figure: Implementation Steps

2.1. Data Collection

The primary dataset of this study comprises academic publications on online hate speech and content moderation, published between 2018 and 2025. The data was obtained through a systematic search conducted in March 2025 using the Scopus database. The literature search was structured around 3 main dimensions: Topical keywords (e.g., toxic language detection, hate speech classification, abusive language identification), technological approaches (e.g., BERT, transformers, contrastive learning, few-shot learning), application domains(e.g., social media, automatic moderation, speech-to-text, video analysis)

These keywords were combined to form a multi-dimensional query structure, and the results were exported in CSV format for further processing.

A total of 574 documents were included in the scope of the analysis. As shown in Figure 1, a clear increase in the number of publications over the years has been observed. This upward trend reflects the growing academic interest in the field. While there was only one publication in 2018, the number increased to 38 in 2020, 65 in 2021, and 95 in 2022. The most significant growth occurred in 2023 (n=133) and 2024 (n=208). This pattern highlights the intensifying global interest in AI-based content filtering solutions in recent years. Although the year 2025 is not yet complete and the current data is limited (n=28), the upward trajectory from previous years suggests that high publishing output is likely to continue. In addition, Figure 2 presents the annual publication counts alongside the total number of citations per year, demonstrating that academic attention has increased not only quantitatively but also qualitatively.

An analysis of publication types revealed that, consistent with the dynamic and technology-driven nature of the topic, the majority of the documents were published as conference papers (n=379, 66%). This was followed by research articles (n=160, 27.9%). A smaller number of publications consisted of conference reviews(n=23), Book chapters(n=6), review articles(n=4) , short surveys (n=1), and notes(n=1). The distribution of document types is presented in Figure 3.

Two publications were produced by a total of 532 unique authors, with an average of 1.00 author per document. This suggests that most of the studies were conducted individually or by small-scale research teams. The documents were published across 275 different journals and conference proceedings, with an average of 2.09 publications per source. This reflects the multidisciplinary nature of the field and its broad representation across diverse publication venues.

According to the country-wise distribution, India had the highest number of publications (n=326), followed by the United States (n=89), China (n=51), Indonesia, and Germany. These results indicate a particularly strong interest in online content analysis among Asia-based research communities.

An analysis of institutional productivity revealed that institutions such as Vietnam National University, L3Cube (Pune and India), and Mangalore University stood out as leading contributors. These institutions were found to be particularly active in natural language processing (NLP)-based research and contributed to a substantial number of publications. The inter-institutional collaboration analysis showed that authors were predominantly clustered within regional networks, although a growing trend toward international collaboration has been observed in recent years.

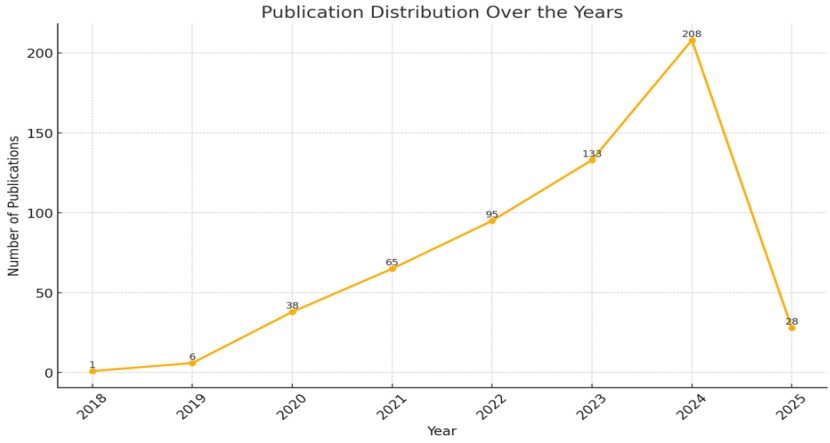

Figure 1. Annual distribution of publications between 2018 and 2025

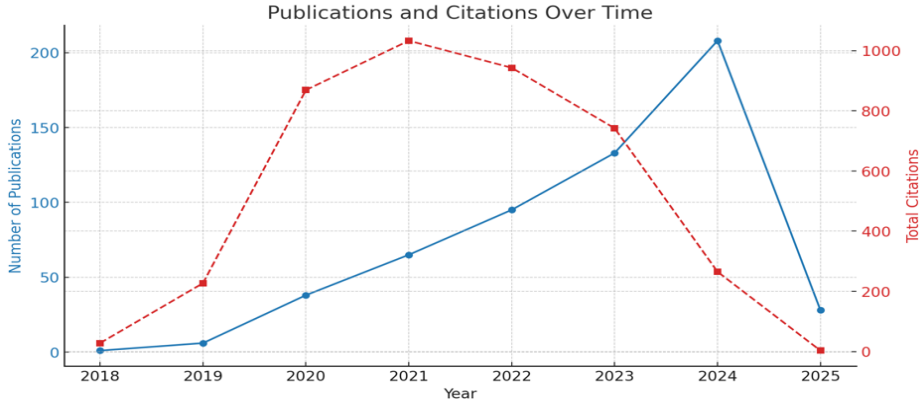

Figure 2. Number of publications per year (blue line), and total number of citations (red dashed line)

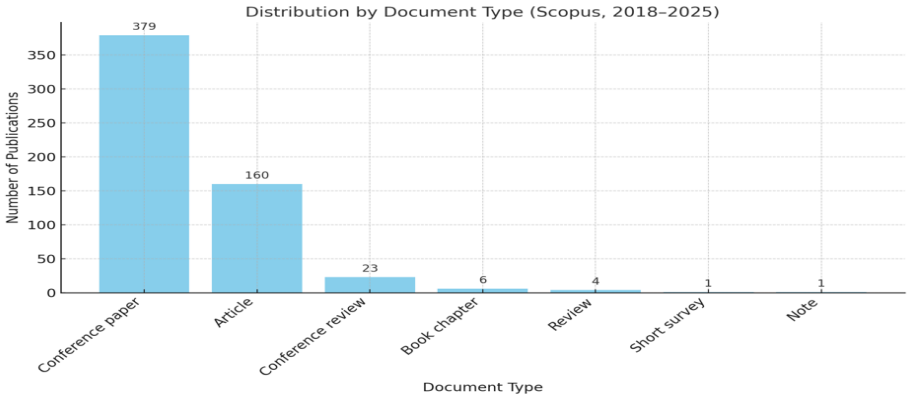

Şekil 3. Distribution of publications by document type between 2018 and 2025 (Scopus data)

2.2. Data Processing

The data processing stage was carried out systematically to clean, organize, and prepare the data set for bibliometric analysis. In the initial phase, raw data exported from the Scopus database in CSV format was processed using the Python programming language. Duplicate records were identified and removed based on key metadata fields such as title, author name, Publication year, and DOI. Next, only peer-reviewed full-text journal articles and international academic conference papers were retained for analysis. In contrast, book chapters, short notes, early access records, and editorial content were excluded from the dataset. During the standardization phase, variations in the spelling of author and institution names were resolved to merge entries referring to the same individuals or organizations, thereby preventing potential errors caused by name

variants. Additionally, keywords associated with each publication were separated into two distinct categories: Author Keywords and Indexed Keywords. These were integrated into the dataset for use in thematic analyses. Columns containing information such as citation counts, country of origin, and publication source were also cleaned and standardized. Incomplete, corrupted, or inconsistent records were identified and removed to ensure that all bibliometric indicators used in the analysis would be reliable and comparable. The automation of the data processing workflow was achieved using open-source scientific libraries in Python. In particular 'pybliometrics' library -designed to interface with Scopus data- was employed to calculate core bibliometric indicators such as citation counts, number of authors, and h-index. For visualization purposes, the 'VOSviewer' software was used to graphically represent collaboration networks among authors, as well as institutional, national, and keyword-based relationships. Notably, keyword co-occurrence analyses, source coupling maps, and thematic clustering visualizations allowed for a clear and interpretable representation of structural properties of the literature.

2.3. Bibliometric Analysis Techniques

Bibliometric analysis is a systematic method used to evaluate the processes of knowledge production, dissemination, and impact within the scientific literature through quantitative indicators (Bahar et al., 2024; Zupic & Čater, 2015) . It's widely employed to understand the structural characteristics of academic fields, identify core research focuses, and map intellectual interactions(Weinberg, 1974; Zupic & Čater, 2015). This approach enables researchers to track the intensity, influence, and collaboration patterns of scholarly activity over time (Chen, 2006; Donthu et al., 2021; Wallin, 2005). In this study, the applied bibliometric analysis techniques are categorized into three main groups: Citation-based analyses, Co-occurrence and collaboration analyses, and bibliographic coupling and Co-citation analyses. Each technique is described in detail under the corresponding subsections.

2.3.1. Citation-Based Analyses

Citation-based analysis is considered one of the fundamental bibliometric methods for measuring scientific impact within a research field (Ho et al., 2017; Yasin et al., 2024). This approach evaluates the visibility and influence of publications quantitatively based on the number of citations they receive. The citation count is widely interpreted as a strong indicator of how well a study has been recognized, utilized, and referenced by other researchers (Hamou-Lhadj & Hamdaqa, 2009; Van Eck & Waltman, 2010). This type of analysis can be applied

not only at the level of individual publications but also across authors, journals, institutions, and countries, thus revealing the source of academic contribution in a detailed manner.

- **Citation Analysis:** Citation analysis is an evaluative process based on the total number of citations received by a given publication. This method enables the identification of the most influential works within a specific research area. Through citation analysis, it's also possible to draw content-based inferences about the dominant themes and research focuses of highly cited publications. Moreover, this technique systematically highlights seminal works that serve as key references within the academic literature (Passas, 2024).
- **Author Citation Analysis:** Author citation analysis enables the identification of the most highly cited researchers, thereby facilitating the mapping of academic leaders and centers of expertise within the field. This type of analysis not only assesses the impact of individuals who have made substantial contributions to scientific knowledge production, but also helps to reveal how research domains are shaped around specific influential figures (Osareh, 1996; Ugurlu & Aktar Ugurlu, 2024).
- **Journal Citation Analysis:** This analysis examines the total number of citations received by the academic journals or conference series in which the documents were published. The resulting data allow for the identification of the most prestigious and frequently cited publication venues within the field. Additionally, this information provides valuable guidance for publication strategies, helping researchers choose the most impactful outlets for disseminating their work (Zhang et al., 2024).
- **Institutional and Country-Level Citation Analysis:** Ü citation analysis at the country and institutional levels reveal the geographic and structural dimensions of scientific impact. As a result, it becomes possible to construct a quantitative and qualitative map of global academic production (Gokhale & Pillai, 2024).

2.3.2. Co-occurrence and Collaboration Analyses

This group of analyses encompasses methods aimed at exploring the conceptual relationships between themes in the literature and the social network structure of scientific production. Keyword co-occurrence analysis reveals how specific topics are clustered and involved over time, while co-authorship analysis

makes visible the patterns of scientific collaboration among researchers, institutions, and countries (Acedo et al., 2006; Klarin, 2024; Schweiggart, 2024).

- **Keyword Co-occurrence Analysis:** This method is based on the frequency and co-occurrence probabilities of keywords appearing within the same documents in the literature. Keyboard occurrence analysis reveals which concepts are commonly discussed together, which research topics are prominent, and how thematic clusters are structured. Through this analysis, it becomes possible to visualize the core conceptual frameworks and emerging trends within the research field(Mehdipour et al., 2024; Zhang & Feng, 2024).
- **Co-authorship Analysis:** This author-level analysis aims to measure the interactions among researchers who have co-authored publications. The co-authorship network, constructed based on authors appearing in the same documents, reveals the academic connections between individuals and highlights the social dimension of scientific production. Through this analysis, it becomes possible to identify prominent collaboration clusters and academic hubs within specific research domains (Sjuchro et al., 2025).
- **Country Co-authorship Analysis:** This international-level analysis measures the extent of collaborative publication efforts among researchers from different countries. It provides insights into the geographical distribution of scientific interaction, enabling the identification of strong collaborative ties as well as more isolated research profiles between countries. In this context, the dynamics of the global scientific network can be systematically analyzed(Hassan & Duarte, 2024; Koklu & Sulak, 2024).
- **Institution Co-authorship Analysis:** Institution-level co-authorship analysis evaluates collaborative relationships between universities and research centers. This method provides insights into which institutions occupy more central positions and which ones are highly connected to multiple other organizations. To contribute to a deeper understanding of the organizational structure of academic collaborations (Dagli et al., 2024; Kurulgan, 2024) .

2.3.3. Bibliographic Coupling and Co-citation Analyses

This group of analysis consists of structural mapping techniques designed to identify theoretical and conceptual proximities between publications in the literature. These methods focused on the extent to which studies cite one another or share common references, thereby enabling the mapping of knowledge

clusters, academic interactions, and intellectual linkages. In this sense, such analyses have the potential to uncover not only thematic similarities, but also methodological and theoretical foundations shared across different studies (Boyack & Klavans, 2010; Ferreira, 2018; Kessler, 1963; Sulak & Koklu, 2024).

- **Bibliographic Coupling:** Bibliographic coupling is based on the assumption that when two publications cite the same sources, there is a conceptual or theoretical similarity between them. This analytical method enables the clustering of studies that rely on a shared body of literature. For instance, research adopting similar methodologies or referencing the same theoretical background can be grouped using this technique. It is particularly effective in revealing the current structural configuration of knowledge clusters in the literature, as the data used in the analysis are derived from already published works, allowing the structure to remain dynamic and responsive to changes over time (Glänzel & Czerwon, 1996; Luc, 2024; Zhao & Strotmann, 2008).
- **Co-citation Analysis:** Co-citation analysis is based on the assumption that when two different publications are cited together by a third publication, there is a conceptual or theoretical connection between them. This method is particularly useful for analyzing the historical development of intellectual clusters formed around specific topics and how they relate to each other. Publications that are frequently co-cited over time tend to represent the foundational works and core knowledge structures of a field. This analysis is highly valuable for revealing how past academic influences shape current knowledge production (Karanam et al., 2024; Martyn, 1964; Small & Griffith, 1974).

3. Findings

This section presents the findings of a systematic bibliometric analysis of academic studies published between 2018 and 2025 on online bullying and hate speech in social media content. The primary objective of the study is to understand how toxic content produced on social media platforms has been addressed at the academic level, and to reveal the structure, trends, and impact areas of scientific output in this field. The analysis includes citation-based metrics, publication types and trends, geographical and institutional distribution, keyword co-occurrence frequencies, and co-authorship networks among researchers. In addition, conceptual proximities and intellectual clusters within the literature are visualized through bibliographic coupling and co-citation

analysis. All analyses conducted as part of the study titled "Bibliometric Analysis of Online Bullying and Hate Speech in Social Media Platforms (2018–2025)" were carried out using data processed with the Python programming language, and the numerical results were visualized through relationship maps and interaction networks generated with VOSviewer. In this way, the structural and thematic dynamics of the field have been comprehensively analyzed both quantitatively and visually.

3.1. Citation Analysis

In this study, citation analysis was conducted based on the "Cited by" variable in the Scopus dataset. The findings indicate that the most cited works in the field of online toxic language and hate speech detection largely focus on transfer learning, BERT-based models, and bias mitigation strategies. The publication with the highest number of citations is the study by Mozafari et al. (2020), titled "A BERT-Based Transfer Learning Approach for Hate Speech Detection in Online Social Media" (Mozafari et al., 2019), which has received a total of 260 citations and is considered one of the seminal references in the literature. At the author level, Farahbakhsh R. (434 citations), Crespi N. (434 citations), and Mozafari M. (422 citations) are among the most cited researchers. Their works have made significant contributions to the development of deep learning–based methods for toxic content classification and have gained reference status in the field. In terms of journals, IEEE Access, Studies in Computational Intelligence, PLOS ONE, and Computer Speech and Language are among the most cited publication venues. These sources appear to serve as important platforms for publishing research on toxic content analysis, automated classification of social media texts, and deep learning–based natural language processing applications.

3.1.1. Author Citation Analysis:

Based on the Scopus data, the most highly cited authors in the field of online toxic language detection and hate speech analysis have been identified. As shown in Figure 4, Farahbakhsh R. and Crespi N. lead the list, each with 500 citations. They are followed by Mozafari M., who has received 467 citations and is recognized as one of the prominent academic figures in the field. His work on BERT-based deep learning architectures, in particular, has gained significant attention in the literature. Other notable researchers within the top 15 include Basile V. (184), Patti V. (180), Li W. (144), Liu P. (144), Zou L. (144), Chakravarthi B.R. (143), and Kovács G. (125). A common feature among these authors is their focus on thematic areas such as automated classification of social media texts, multilingual content analysis, and hate speech detection in low-

resource languages. These findings indicate that the field has a decentralized structure and that contributions are internationally distributed across various regions.

.

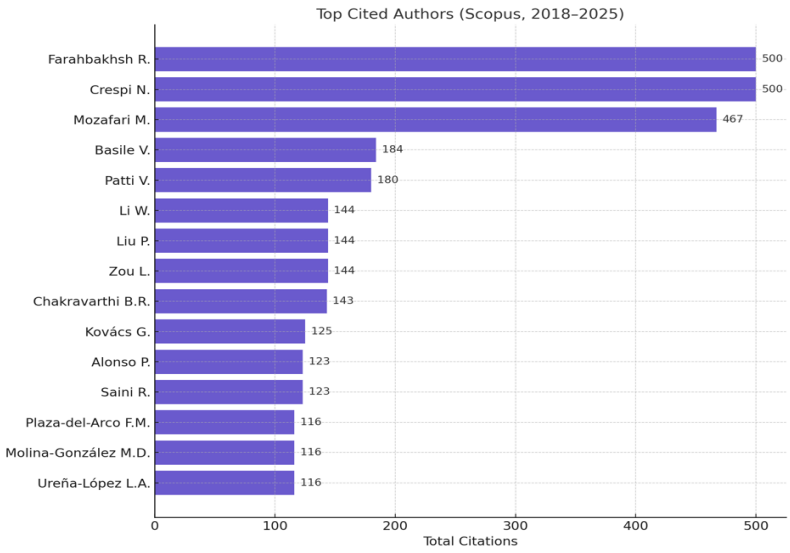

Figure 4. Most cited authors in the field of online hate speech between 2018 and 2025 (Scopus data)

The bar chart in Figure 4 displays the top 15 most cited authors in the field during the specified period. Upon examining the chart, it is evident that the top three authors stand out significantly compared to the others. Notably, the total number of citations for the top three authors (Farahbakhsh R., Crespi N., Mozafari M.) is approximately three times higher than that of the fourth-ranking author. This indicates that certain studies and researchers in the literature have generated substantial academic impact, and that such impact can be meaningfully assessed not only by publication volume but also through citation metrics

3.1.2. Sources Citation Analysis:

The analysis based on the Scopus dataset reveals which academic publication venues have received the highest number of citations in the field of online toxic language analysis and content classification. As shown in Figure 5, the most highly cited platforms are IEEE Access (291 citations) and Studies in Computational Intelligence (260 citations), ranking first and second, respectively. These are followed by Computer Speech and Language (201), Expert Systems with Applications (191), and NAACL HLT 2019 – SemEval Workshop (182).

This distribution indicates that the field is strongly represented in both applied engineering–oriented and natural language processing–focused scientific publication venues. The high citation counts of open-access and broadly interdisciplinary journals such as IEEE Access suggest that technological advancements in the field are rapidly disseminated and reach a wide community of researchers. On the other hand, conference series such as SemEval and COLING also demonstrate significant influence through their high citation figures, guiding both theoretical and applied contributions in the literature.

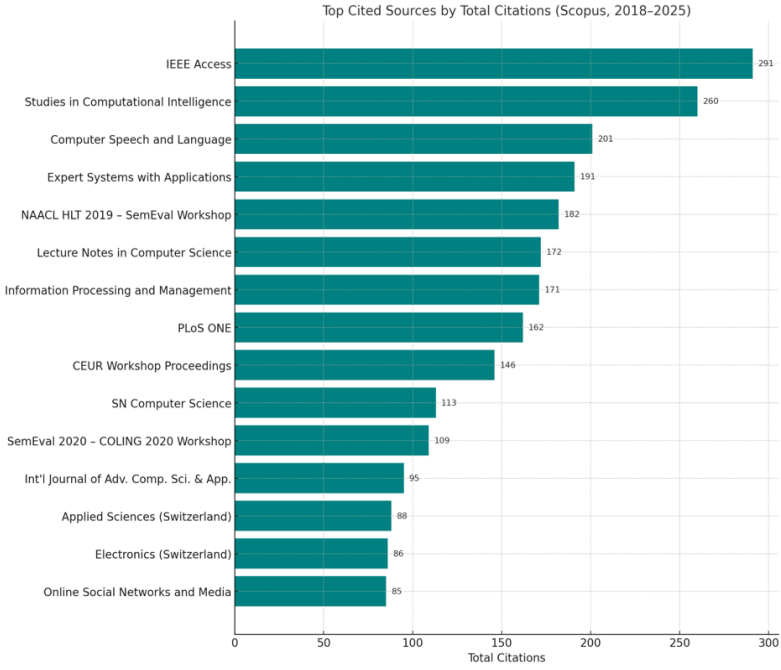

Figure 5. Most cited publication sources in the field of online hate speech and toxic content detection between 2018-2025 (Scopus data)

The bar chart in Figure 5 displays the top 15 publication venues ranked by total number of citations. Upon examining the chart, it becomes clear that the top four sources stand out significantly compared to the others. It is also noteworthy that the list includes not only academic journals but also conference proceedings such as SemEval, COLING, and CEUR, which hold a prominent place. This highlights the fact that in fast-evolving fields, cutting-edge findings are often first presented at conferences and later leave a lasting impact in the literature. The strong citation performance of interdisciplinary journals and multilingual language technology conferences indicates that research on online content analysis spans a broad domain, encompassing both technical and socio-linguistic dimensions.

3.1.3. Citation of Documents

This section identifies the most frequently cited academic publications in the field of online toxic language and hate speech and visualizes the impact levels of these documents. The visualization presented in Figure 6 is a citation network map generated using the VOSviewer tool (Arruda et al., 2022). In the map, each node represents a single document, and the size of the node indicates the total number of citations that document has received. The lines between nodes reflect citation-based connections between documents, revealing patterns of knowledge flow and conceptual proximity within the literature (Bukar et al., 2023; Kumar et al., 2024; Van Eck & Waltman, 2017).

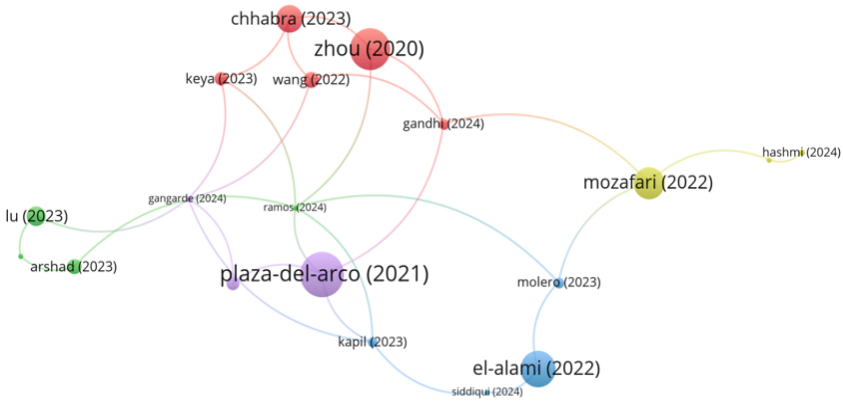

Figure 6. Connections between the most cited documents in the literature between 2018 and 2025 (VOSviewer visualization)

According to the findings obtained from the visualization, the study (Plaza-del-Arco et al., 2021) stands out as the most frequently cited publication, with a total of 79 citations. This document has been widely referenced, particularly in research focused on multilingual toxic content detection and sentiment analysis. The works by (Y. L. Zhou et al., 2020) and (El-Alami et al., 2022) have also secured significant positions in the literature, with 70 and 55 citations respectively. These highly cited documents appear to offer both theoretical contributions and practical guidance for applied modeling processes.

The connection lines visible in the map indicate that these documents stand out not only due to their individual contributions but also because of their relationships with other frequently co-cited publications within specific thematic clusters. In particular, the red cluster comprising studies such as (Y. L. Zhou et al., 2020) and (Chhabra & Vishwakarma, 2023) represents more methodologically focused research, while the blue and purple nodes surrounding

(Plaza-del-Arco et al., 2021) indicate a body of literature closely interacting on topics such as multilingual datasets and semantic modeling. This demonstrates that the flow of knowledge occurs not only through individual documents but also through structured clusters of content.

3.2. Geographical Distribution of Publications by Country

Based on the analysis conducted using the Scopus dataset, the countries of origin for academic literature on online hate speech and toxic language analysis have been identified. As shown in Figure 7, India leads by a wide margin, with 192 publications, making it the most productive country in this field. India is followed by the United States (n = 53) and China (n = 26). These three countries rank among the primary academic hubs driving the field at a global level.

Among the top 15 countries, other notable contributors include Indonesia (n = 24), Spain (n = 23), Germany (n = 21), Turkey (n = 18), and Bangladesh (n = 18). This distribution demonstrates that the research topic is not limited to the Anglo-American academic sphere; rather, research groups based in various regions such as Asia, Europe, and South America have made significant contributions to the field. The increasing visibility of low- and middle-income countries in the literature confirms that online hate speech is recognized as a global issue and is being addressed across diverse socio-cultural contexts.

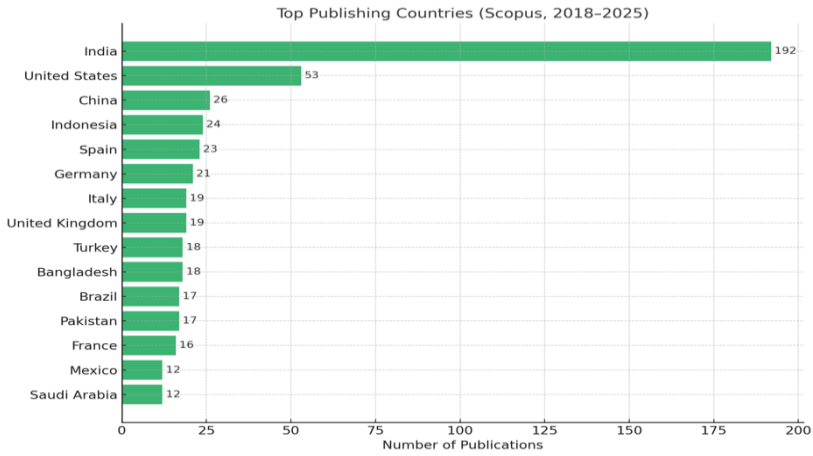

Figure 7. Distribution of publications on online hate speech by country between 2018 and 2025 (Scopus data)

3.3. Institutional Distribution of Publications

The institutional analysis based on Scopus data aims to identify the institutions that have produced the highest volume of academic output on online toxic language, hate speech, and content moderation. As shown in Figure 8, Vietnam National University (Ho Chi Minh City) stands out as the leading institution during the analysis period, with a total of 6 publications. It is followed by other Asia-based technical universities such as the University of Information Technology (Vietnam), Chittagong University of Engineering & Technology (Bangladesh), and L3Cube, Pune (India).

These findings demonstrate that the literature is actively produced not only by Western academic institutions but also by universities in regions such as Southeast Asia, South Asia, and Latin America. In particular, institutions like L3Cube and Mangalore University have made notable contributions, with a strong focus on technical themes such as natural language processing (NLP), multilingual data analysis, and toxic content classification. A significant portion of these studies has been conducted within laboratories affiliated with faculties of engineering and computer science, reflecting the solution- and system-oriented nature of the field.

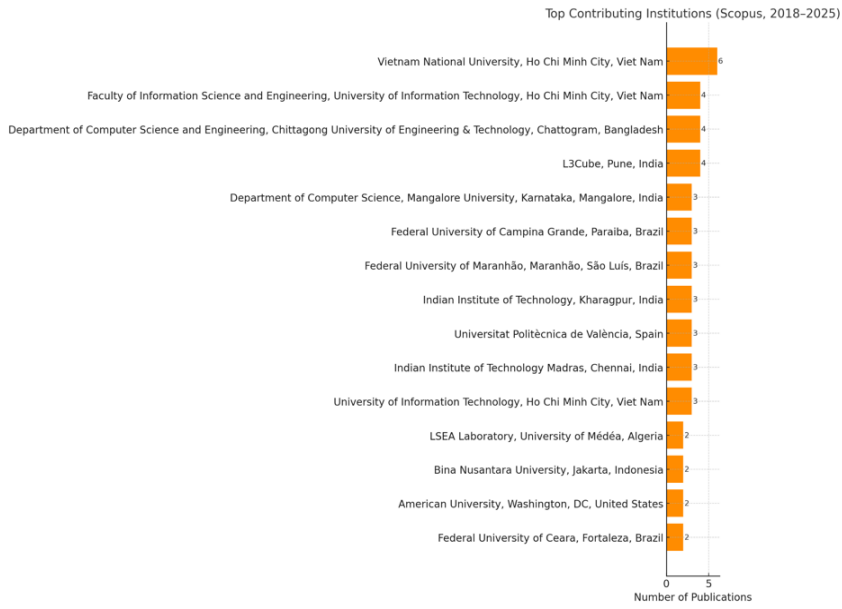

Figure 8. Top publishing institutions in the field of online hate speech between 2018 and 2025 (Scopus data)

An examination of the chart reveals that the majority of the top 15 most productive institutions are located in countries such as Vietnam, India, Brazil,

Indonesia, and Bangladesh. This indicates that scientific output on online hate speech is globally distributed and fueled by contributions from a wide range of institutions across different continents, rather than being concentrated in a few dominant centers. It is also noteworthy that some American and European institutions, while contributing a smaller number of publications, have made highly impactful contributions. This suggests that regional diversity contributes not only to the quantitative but also to the qualitative richness of the field.

3.3.1. Institutional-Level Contribution and Impact Analysis

This analysis evaluates the top contributing institutions in the field of online toxic language detection and content classification based on bibliometric indicators such as the number of publications, total citation count, and total link strength within the collaboration network. The multidimensional bar chart presented in Figure 9 illustrates a comparative performance assessment of institutions across these three criteria.

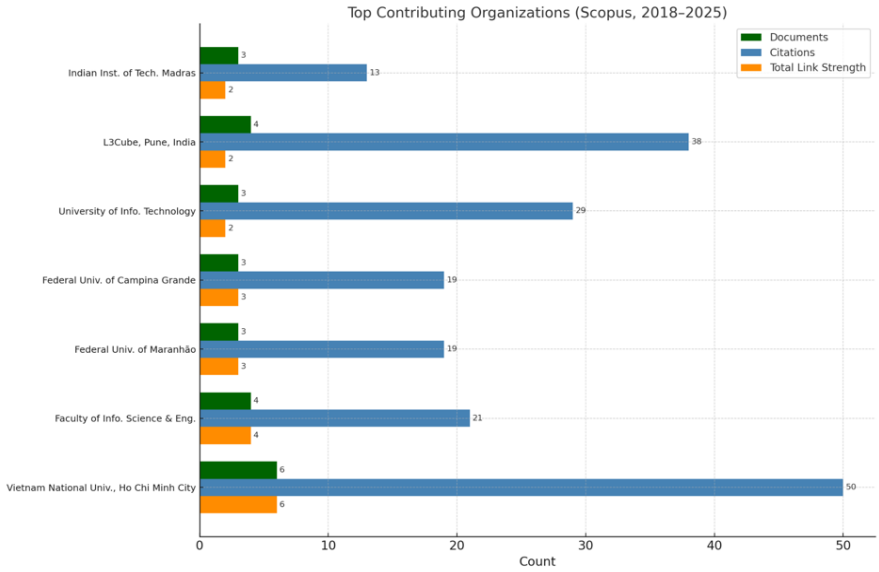

Figure 9. Distribution of the top contributing institutions by number of publications, citations, and total link strength (Scopus data, 2018–2025)

As seen in the chart, Vietnam National University – Ho Chi Minh City stands out as the clear leader with 6 publications, 50 citations, and a total link strength of 6. This institution appears to be the most influential academic center in the field, not only in terms of publication count but also with respect to its citation impact. Similarly, L3Cube (Pune, India) and the University of Information

Technology (Vietnam) are among the prominent institutions, distinguished by their high citation counts and strong collaboration networks.

On the other hand, Brazil-based institutions such as the Federal University of Campina Grande and the Federal University of Maranhão display a more balanced and moderate contribution profile. While their number of publications is comparable to others, they show relatively modest figures in terms of citation count and total link strength. This indicates that some institutions are able to achieve meaningful scientific visibility even with a limited number of publications.

Overall, this analysis highlights regional diversity, institutional areas of expertise, and the evolving dynamics of international scientific collaboration. The active involvement of institutions from Asia and South America in particular demonstrates the emergence of a globally expanding and technically evolving academic field focused on combating online hate speech.

3.4. Co-occurrence and Collaboration Findings

It is important to evaluate the development of online hate speech and toxic language research not only through content but also in terms of conceptual contexts and academic interactions. In this regard, co-occurrence and collaboration analyses reveal the thematic trends of the field, methodological focuses, and the dynamics of collaboration among researchers and institutions. In the following subsections, keyword clusters, author partnerships, international collaborations, and institutional production networks are presented in detail, and the structural organization patterns in the literature are visualized.

3.4.1. Keyword Co-occurrence:

Figure 10 presents the numerical distribution of the most frequently co-occurring keywords in the Scopus database between 2018 and 2025. According to the data, concepts such as “speech recognition” (n = 286), “speech detection” (n = 249), and “social media” (n = 277) stand out. This result shows that, in recent years, analytical approaches have expanded beyond text-based analyses to include audio and multimodal content. In addition, terms such as “deep learning” (n = 179), “natural language processing systems” (n = 126), and “hate speech detection” (n = 134) indicate that the technical aspect of the field is shaped around machine learning and natural language processing techniques.

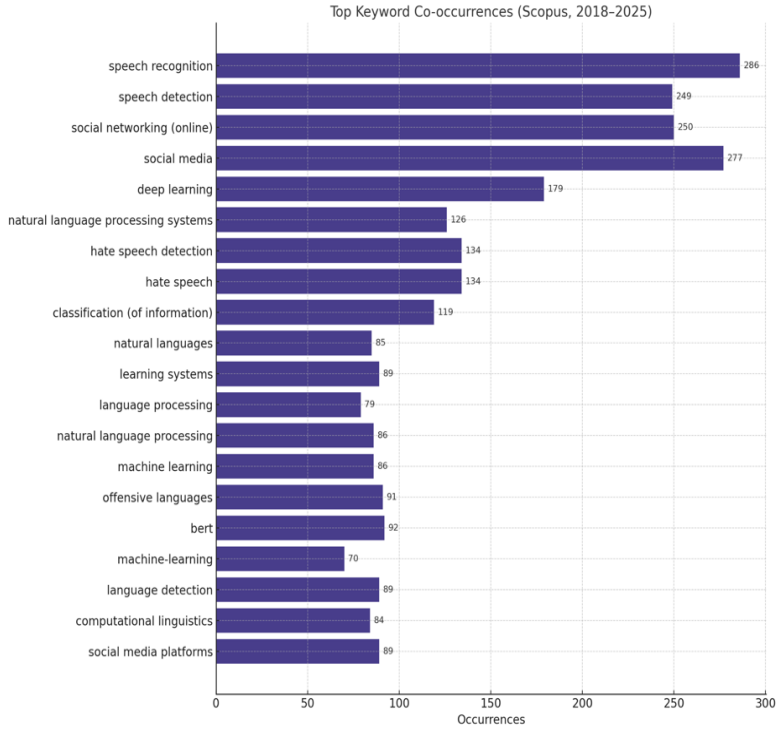

Figure 10. Most frequently co-occurring keywords between 2018 and 2025 (Scopus data)

However, keyword frequency alone is not sufficient to fully reflect the influence of concepts. Therefore, Figure 11 presents a keyword network visualization created using the VOSviewer tool. This graph represents the intensity of each keyword's connections with others (Total Link Strength) and the conceptual clusters they form.

According to the analyses, the concept with the highest total link strength is "speech recognition" (1489), followed by "speech detection" (1284), "social networking (online)" (1283), and "social media" (1273). This indicates that user interaction, content classification, and multimodal analysis approaches are widely adopted in the research field. Additionally, the strong connection strength of technical terms such as "deep learning" (879) and "natural language processing systems" (776) confirms that these technologies form the methodological core of the field

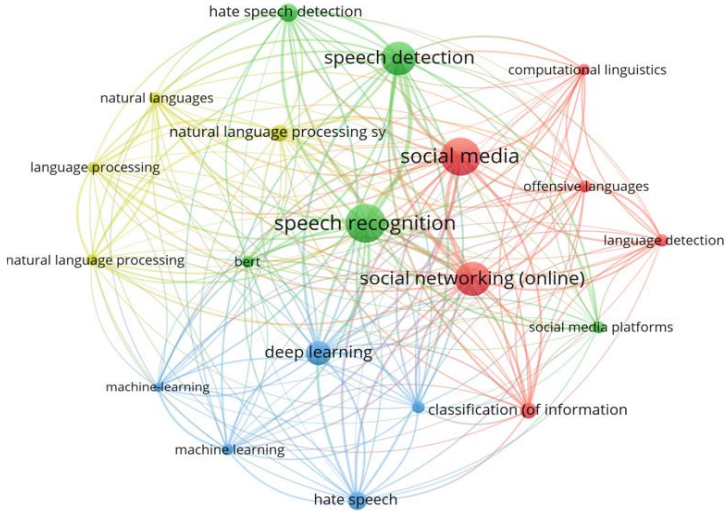

Figure 11. Visualization of relational links between keywords (VOSviewer, 2018–2025)

Overall, the keyword co-occurrence analysis has revealed both the technical foundations (deep learning, NLP, speech recognition) and the content-related targets (hate speech, offensive language, social media) of the online hate speech literature in a comprehensive manner. Additionally, these visualizations clearly show that research trends are increasingly shifting toward multimodal, interaction-focused, and AI-based approaches.

3.4.2. Co-authorship Analysis

According to the analysis results, the most frequently co-authoring pair is Crespi N. and Farahbakhsh R., with a total of 8 joint publications. Their collaboration plays a significant role in the literature, particularly in deep learning and content classification–based approaches. Similarly, the duo of Mukherjee A. & Saha P. stands out with 6 joint publications, while researchers such as Mozafari M., Mnassri K., and Sidorov G. are also prominent for their frequently repeated co-authorship connections. These findings show that highly impactful publications often stem not from individual efforts but from sustained academic collaborations.

Figure 12 presents the distribution of the author pairs with the highest number of co-authored publications between 2018 and 2025. This chart visually reflects the intensity of productive academic partnerships and contributes to identifying the main axes of collaboration within the literature.

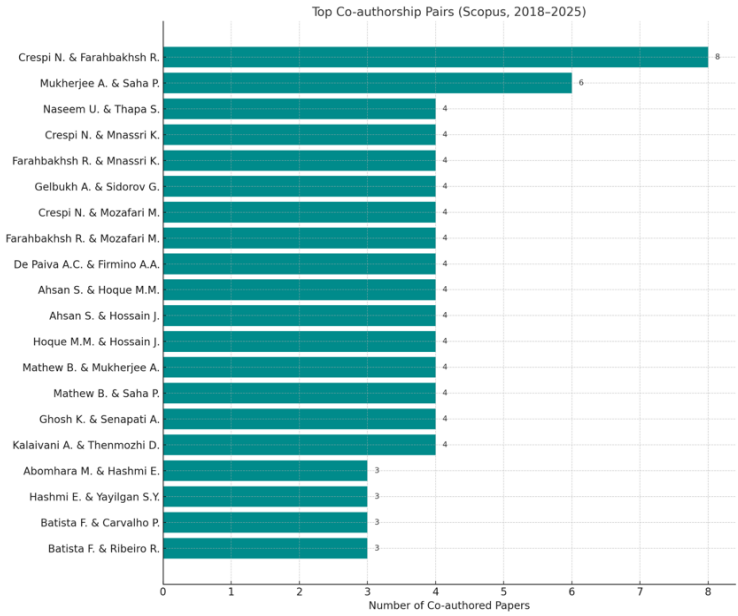

Figre 12. Author pairs with the highest number of co-authored publications between 2018 and 2025 (Scopus data)

In addition, Figure 13 presents the author collaboration network visualization created using the VOSviewer tool. In this analysis, only publications with fewer than 25 authors were included to minimize the dominant effect of mass authorship on the network. In the visualization, each node represents an author, and the lines indicate collaboration relationships between authors. The size of the nodes is proportional to the total number of citations received by the authors, while the colors represent different thematic clusters.

When examining the network structure, it is observed that figures such as Crespi, Noel, and Farahbakhsh, Reza occupy central positions and are in close collaboration with many different researchers. They are followed by other productive researchers such as Mozafari (Marzieh), Sidorov (Grigori), and Plaza-del-Arco (Flor Miriam). The dense connections between nodes reveal that the field is organized around specific research groups and that these groups form structures that shape the direction of the literature.

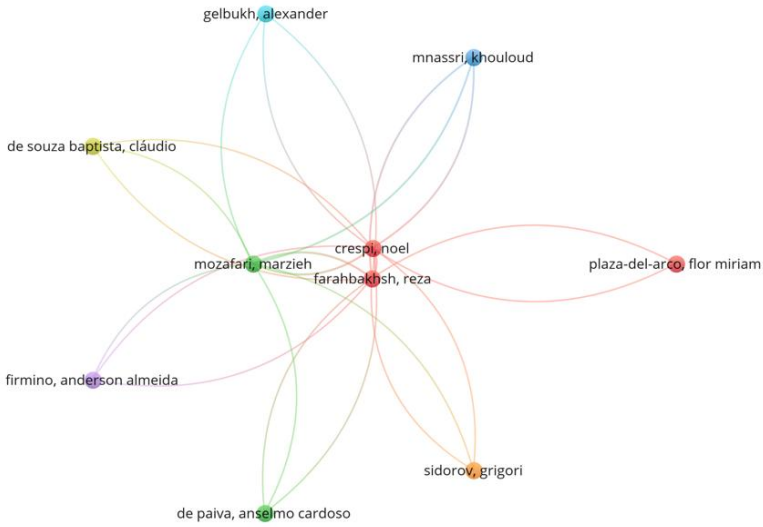

Figure 13. Author collaboration network visualization (VOSviewer, 2018–2025)

As a result of these analyses, it is understood that the structures generating strong academic impact in the field of online hate speech research have largely developed through collective forms of production, and that the key figures at the center of these efforts play a guiding role in the literature.

3.4.3. Co-authorship of Countries

Collaboration between authors from different countries in scientific publications is a key indicator representing the global dissemination and diversity of academic knowledge. In this context, the co-authorship analysis reveals which countries are more actively engaged in collaboration in the field of online toxic language detection and content moderation. Figure 14 visualizes the number of publications by country based on the Scopus dataset. This chart presents the quantitative distribution of the countries from which publications originated between 2018 and 2025.

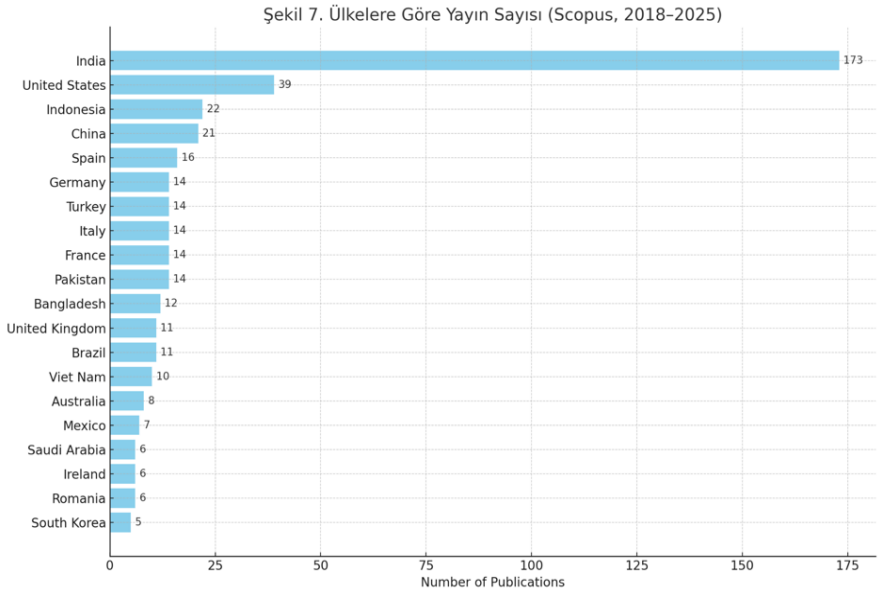

Figure 14. Number of publications by country (Scopus, 2018–2025)

According to the analysis results, India ranks as the country with the highest publication output by a wide margin (n = 173). It is followed by the United States (n = 39), Indonesia (n = 22), and China (n = 21). These countries contribute significantly to the field both in terms of publication volume and interdisciplinary approaches.

The high-frequency co-authorships between India and the United States indicate that these two countries maintain an active international collaboration network, particularly in natural language processing (NLP) and social media analytics. Among European countries, Spain, Germany, Italy, and France have made comparable contributions, especially through multi-centered co-authorship networks. Developing countries such as Turkey, Pakistan, and Bangladesh have enriched the diversity of the field by contributing at both technical and content analysis levels. From the Asia-Pacific region, Vietnam, Australia, South Korea, and Indonesia stand out with their open academic profiles that promote international collaboration.

This distribution shows that multinational research structures are becoming increasingly central in the field of online content analysis, and that collaborative scientific production is gaining importance. This trend highlights the need to strengthen cross-country academic cooperation on digital security and content filtering, which have been evolving in parallel with global social media usage.

Figure 15 presents the country-based co-authorship network generated using the VOSviewer tool. Each node represents a country, and the lines represent co-

authored publications between countries. The size of the nodes indicates the total number of publications for each country, while the colors reflect clustered collaboration groups.

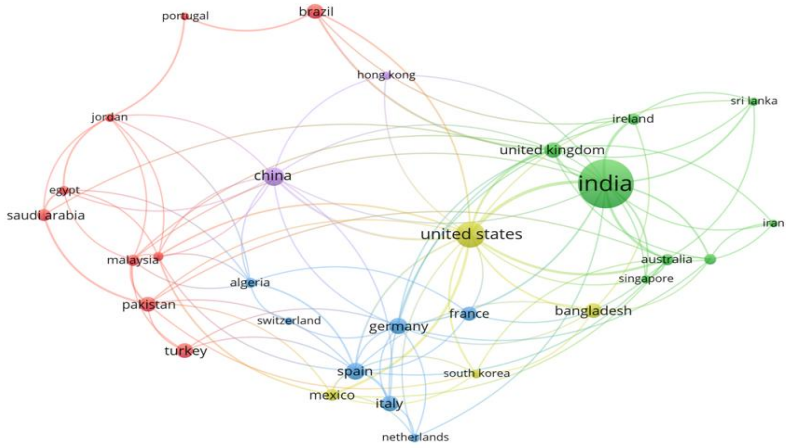

Şekil 15. International co-authorship network visualization by country (VOSviewer, 2018–2025)

3.4.4. Co-authorship of Institutes

According to the analyzed Scopus dataset, the institution with the highest number of co-authored publications is Vietnam National University, Ho Chi Minh City. With a total of 6 collaborative publications, this institution has become a hub of cooperation not only at the regional level but also globally. Known for its work in natural language processing (NLP) and automated content moderation, the university shows strong coordination, particularly with other academic units in Vietnam.

As shown in Figure 16, Vietnam National University is followed by institutions such as L3Cube (Pune, India), Chittagong University of Engineering & Technology (Bangladesh), and the Faculty of Information Science and Engineering (Vietnam). Each of these institutions ranks among the top in the analysis, with 4 publications, and stands out as a focal point for concentrated research networks in the Asian region.

Technical research institutions such as the Indian Institute of Technology (IIT Madras and IIT Kharagpur), the Federal University of Maranhão, and the Federal University of Campina Grande have each contributed to this collaboration network with three co-authored publications. This structure shows that technical universities in developing countries such as India and Brazil play active roles in the field.

From Europe, only Universitat Politècnica de València (Spain) appears in the analysis with three co-authored publications. This indicates that Europe-based academic institutions currently have a limited number of collaborative studies, but they are nonetheless represented in international research networks.

This distribution reveals that Asia-Pacific countries hold a central position in the research field, with countries such as Vietnam, India, and Bangladesh taking the lead in collaboration. It also indicates the emergence of multi-centered, cross-continental partnerships and highlights the growing importance of institutional coordination, particularly in addressing global issues such as content moderation.

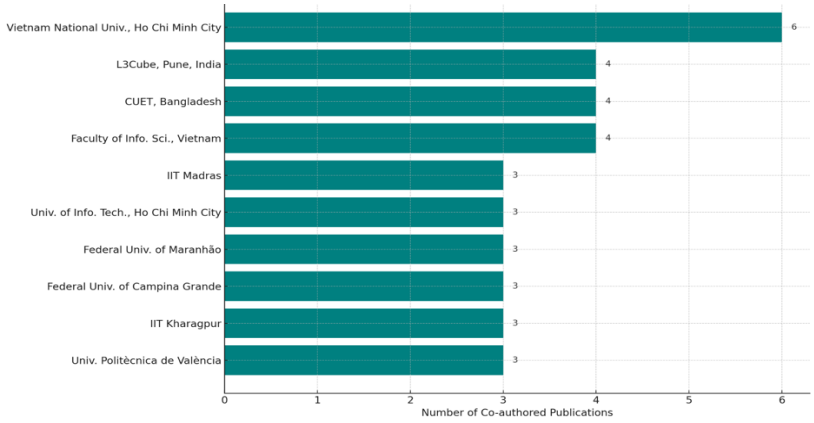

Figure 16. Top institutions by number of co-authored publications (Scopus, 2018–2025)

3.5. Bibliographic Coupling and Co-citation Findings

The analyses presented under this heading aim to gain a deeper understanding of the intellectual structure, thematic clusters, and research agendas of a given academic field by examining the conceptual and structural relationships among its publications (Glänzel & Czerwon, 1996).

3.5.1. Bibliographic Coupling Results

Bibliographic coupling is based on the assumption that when two different publications cite the same references, there is a thematic or methodological similarity between them. This method is an effective analytical tool for identifying studies with similar trends in the literature. In this study, document-level couplings were calculated based on the “References” column obtained from the Scopus dataset, and the ten articles with the highest bibliographic similarity were identified.

The analysis results are presented in Figure 17. The chart shows a comparative display of each article's number of references (blue bars) and citation count (orange bars). The study with the highest number of references is the article titled "A literature survey on multimodal and multilingual automatic hate speech identification," with 171 sources. This is followed by "Hate Speech Detection Using Large Language Models: A Comprehensive Review" (n=143) and "A comprehensive review on automatic hate speech detection in the age of the transformer" (n=129). These publications are review articles that provide a comprehensive evaluation of multilingual and multimodal approaches.

Although some articles contain a high number of references, they have not yet received citations (e.g., reviews based on transformer models), indicating that these studies are very recent and that their academic impact will likely become more evident in the medium term. In contrast, publications such as "Challenges of Hate Speech Detection in Social Media: Data Scarcity, and Leveraging External Resources" have both a high number of references (n=104) and a high citation count (n=93). This shows that the publication is based on an extensive body of literature and is also frequently cited within the academic community.

These publications, particularly clustered around technical topics such as Multilingual-BERT, self-supervised learning, and adversarial example testing, provide strong insights into how current technological approaches are reflected in the literature. Through bibliographic coupling, the extent to which these publications overlap has been identified, and knowledge clusters within the literature have been mapped.

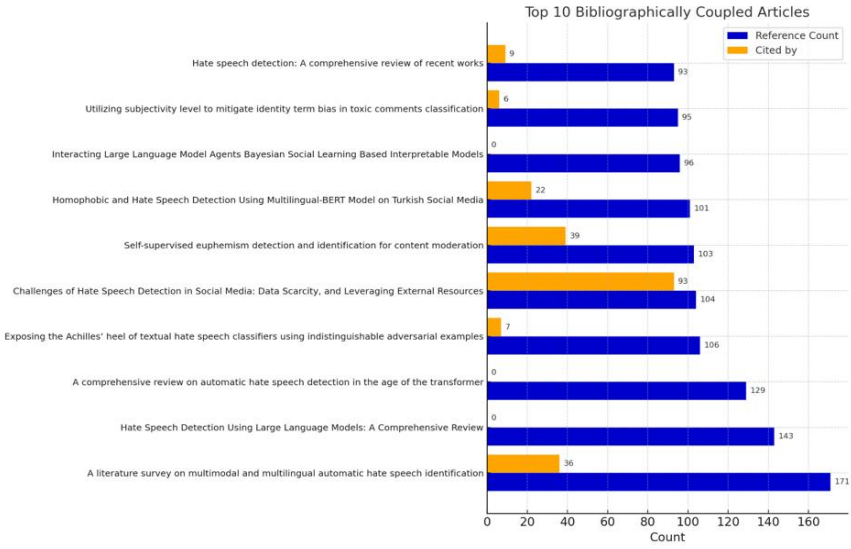

Figure 17. Top 10 articles with the highest bibliographic coupling (Scopus, 2018–2025)

Bibliographic Coupling Deep Dive:

Bibliographic coupling is a key bibliometric analysis technique that assumes a conceptual or methodological similarity between two academic studies if they cite the same sources. This method enables the identification of studies clustered around a specific topic in the literature and allows overlapping structures in research agendas to be revealed. Especially in interdisciplinary areas such as online hate speech, toxic language, and content moderation, this analysis is effective in uncovering knowledge clusters based on shared references and in identifying thematic continuity within the literature (Aria & Cuccurullo, 2017).

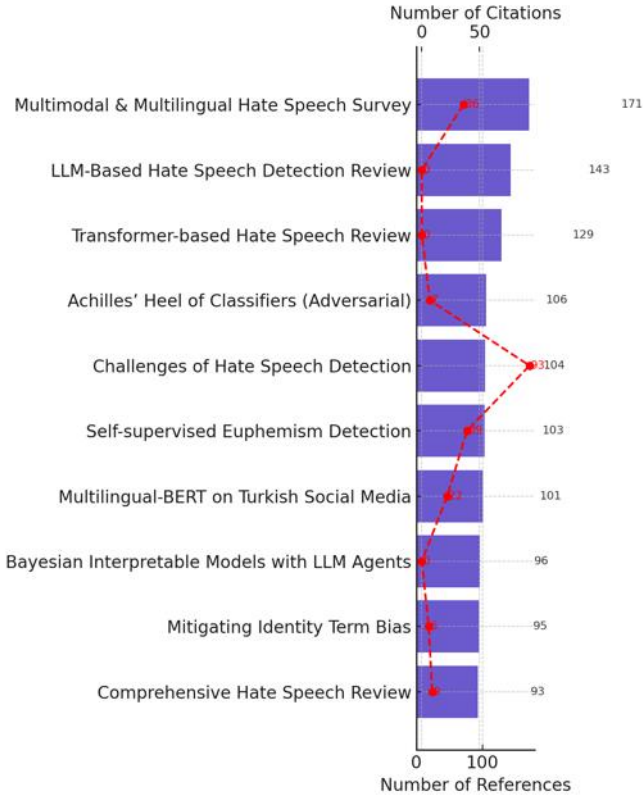

Şekil 18. Kaynak Paylaşımına Dayalı En Etkili 10 Makale (Scopus, 2018–2025)

According to the analysis results, the study titled "A literature survey on multimodal and multilingual automatic hate speech identification" has cited a total of 171 different sources and has been cited 36 times (Chhabra & Vishwakarma, 2023). This indicates that the study is based on an extensive literature review and that research focused on multilingual and multimodal approaches is receiving significant attention in the current literature.

Other studies with a high number of references include "Hate Speech Detection Using Large Language Models: A Comprehensive Review" (n=143) (Albladi et al., 2025) and "A comprehensive review on automatic hate speech detection in the age of the transformer" (n=129) (Ramos et al., 2024) The fact that these studies have been published only recently suggests that their citation counts will increase over time. This also shows that systematic reviews continue to serve as key reference sources in the field.

On the other hand, the study titled "Challenges of Hate Speech Detection in Social Media" (Kovács et al., 2021) has both a rich reference base with 104 sources and has proven to be a valuable contribution to the literature with 93

citations. Similarly, studies such as “Self-supervised euphemism detection” (Zhu et al., 2021), “Homophobic and Hate Speech Detection” (Karayigit et al., 2022) and “Utilizing subjectivity level to mitigate identity term bias in toxic comments classification” (Zhao et al., 2022) have presented high-value outputs in terms of both technical content and proposed solutions.

These findings show that topics such as transformer-based models, BERT architectures, multilingual datasets, and explainable artificial intelligence (XAI) constitute common research interests in the field. The results of the bibliographic coupling analysis reveal that methodological and thematic clusters in the literature are becoming increasingly distinct and that these structures provide strong signals regarding the future directions of the field.

3.5.2. Co-citation Results

Figure 19 shows the document pairs with the highest co-citation counts from publications indexed in the Scopus database between 2018 and 2025. The graph uses horizontal bars to represent the number of shared references in which the co-cited document pairs appear together. The most highly co-cited document pair consists of two studies published by Premjith B. (2024) and Premjith B. (2023). These documents have been co-cited in 13 different sources, indicating a high level of conceptual connection. Similarly, the studies by Narayan N. (2023) and Farooqi Z.M. (2021) have also been co-cited 13 times.

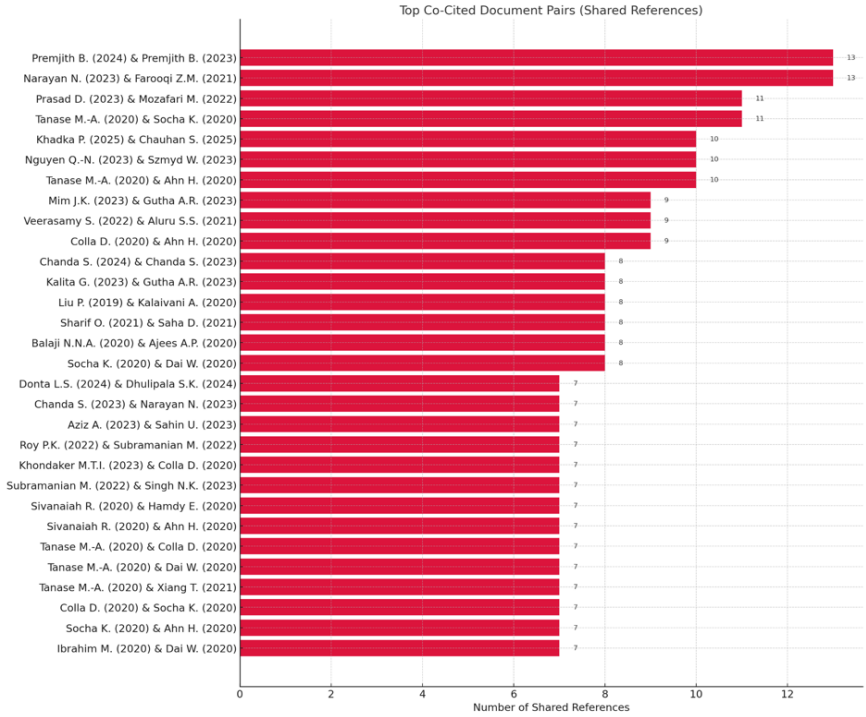

Şekil 19. En Yüksek Ortak Atıf Alan Belge Çiftleri (Scopus, 2018–2025)

These document pairs are followed by Mozafari M. & Prasad D., and Tanase M.-A. & Socha K., each with 11 shared co-citations. It is noteworthy that most of these pairings, involving authors such as Tanase, Mozafari, and Socha, share common technological themes such as deep learning, BERT-based models, and social media analytics.

The findings show that certain research groups or topics tend to be co-cited together in the literature and that these structures represent intellectual clusters within the field. Publications focused on themes such as multimodal analysis, toxic content classification, and data augmentation strategies have been particularly prominent in the co-citation analysis.

Figure 20 presents the co-citation network visualization generated using VOSviewer. Each node represents an author, and the lines between nodes indicate the existence of a co-citation relationship. Central figures in the network—such as Zampieri M., Davidson T., Devlin J., Lee K., and Waseem Z.—stand out as key researchers who are frequently cited and influential in shaping the field. The colors surrounding the nodes represent specific thematic clusters and research directions. These clusters point to areas such as deep learning applications, social bias detection, hate speech analysis on social media, and multilingual content processing.

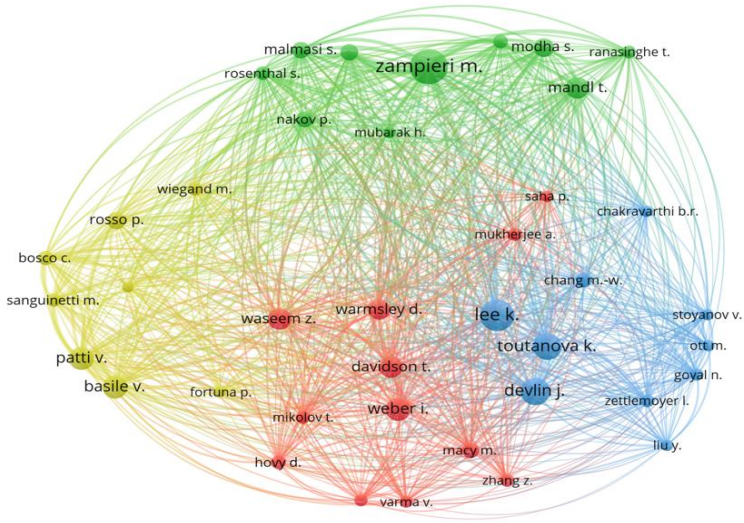

Figure 20. Co-citation Network Visualization (VOSviewer, 2018–2025)

3.6. Distribution of Scientific Subject Areas

The literature examined in this study reveals that topics related to online toxic language detection and content moderation are predominantly addressed within the discipline of Computer Science. Figure 21 presents the top five research disciplines with the highest number of publications between 2018 and 2025. According to the data, approximately 64.3% of the total publications are computer science–based, clearly reflecting the field's focus on technical requirements and the development of algorithmic solutions.

The second most common research area is linguistics and natural language processing (Linguistics/NLP), accounting for 21.1% of the publications. This percentage highlights the importance of topics such as semantic analysis of text-based social media content, interpretation of syntactic structures, and addressing linguistic diversity in multilingual contexts within the literature.

Other contributing fields include engineering (8.1%), social sciences (4.9%), and electrical/electronic engineering (1.6%). Although these percentages appear lower, they indicate a growing inclusion of interdisciplinary approaches to the topic. Contributions from the social sciences help in understanding the sociological and cultural backgrounds of toxic content, while engineering and electronics-based studies provide a foundation for applications such as audio data processing, hardware-based filtering, and integration into real-time systems.

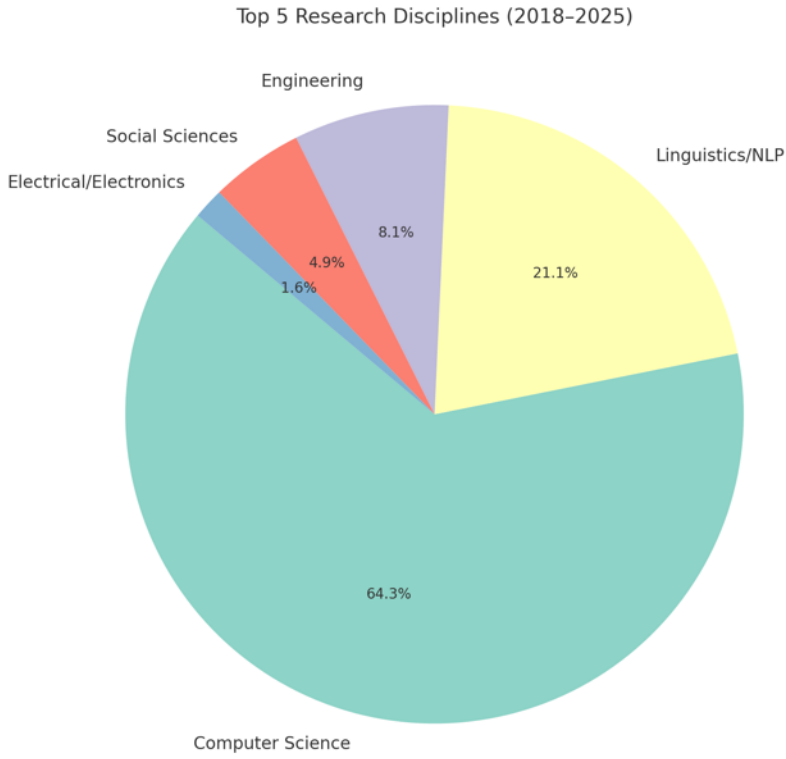

Figure 21. Top five research disciplines with the highest number of publications between 2018 and 2025 (Scopus data)

4. Discussion

This study provided a comprehensive bibliometric analysis of academic publications focused on the detection of online bullying and hate speech on the YouTube platform between 2018 and 2025. The findings revealed the thematic focuses, technical trends, academic collaborations, and regional productivity in the literature from a multidimensional perspective.

The analyses revealed a significant increase in the number of publications, particularly after 2020. This rise is believed to have developed in parallel with the growing number of social media users and the increasing responsibility of platforms in content moderation. In this context, Transformer-based deep learning models—especially BERT and its variants—have become the dominant methods in the literature. Highly cited studies by authors such as Mozafari (2020), Plaza-del-Arco (2021), and Chakravarthi (2022) confirm the academic impact of this approach..

Bibliometric network analyses have shown that countries such as India, the United States, and Indonesia hold leading positions in the field, while institutions like Vietnam National University and L3Cube play a strong central role in terms of publication output and academic collaborations. These institutions have contributed to the literature not only quantitatively but also in terms of academic impact.

As a result of the collaboration analyses, it is observed that academics such as Crespi N. and Farahbakhsh R. have become key figures in the field through regular co-authored publications. This clearly demonstrates the structural impact of interdisciplinary and international collaborations within the literature.

As a result of this study, it is understood that research on online hate speech detection is shaped not only by technical advancements but also by international academic collaboration. The data obtained indicate that this field should be approached from both engineering and social science perspectives.

5. Conclusion

The bibliometric analyses conducted within the scope of this thesis have provided a multidimensional evaluation of scientific output in the field of online bullying and hate speech detection in YouTube content. Publication trends, technical focuses, author and institutional analyses, keyword clusters, and bibliographic relationships have been visualized in detail. In this way, the scientific structure of the field has been effectively mapped.

The analyses show that studies in this field have gained significant momentum, especially with the advancement of deep learning and natural language processing techniques. Transformer architectures, multilingual datasets, and explainable artificial intelligence approaches have emerged as the main trends in the literature.

The high citation levels of publication sources such as IEEE Access indicate that open-access and interdisciplinary publishing increase the impact of research in the field. Additionally, the growing contributions from low- and middle-income countries, particularly from Asia and Latin America, confirm the global expansion of the field.

This study serves not only to understand the current state of the field but also as an important reference for identifying future research opportunities and encouraging scientific collaboration.

6. Future Recommendations

Based on the findings obtained in this thesis, the following recommendations are presented in order to sustain progress in the field and make knowledge production more inclusive:

- The number of hate speech detection studies conducted in low-resource languages and culturally diverse societies should be increased. In particular, the development of multilingual datasets will help fill a significant gap in the field.
- The integration of transformer-based models (e.g., BERT, RoBERTa, LLaMA, etc.) into real-time content classification systems should be made more widespread in both academic and industrial applications.
- Encouraging interdisciplinary studies (such as those involving sociology, psychology, law, and computer engineering) will allow hate speech to be addressed not only from a technical perspective but also in terms of its ethical, cultural, and social dimensions.
- Increasing collaborations between institutions and countries is of great importance, particularly in terms of knowledge sharing, the use of common datasets, and the development of joint projects.
- Repeating bibliometric analyses at regular intervals will be beneficial for monitoring research trends and forming strategic research policies. Additionally, sharing these analyses through open access will enhance transparency in the literature and promote academic engagement.

References

Acedo, F. J., Barroso, C., Casanueva, C., & Galán, J. L. (2006). Co-authorship in management and organizational studies: An empirical and network analysis. *Journal of management studies*, *43*(5), 957-983. https://doi.org/10.1111/j.1467-6486.2006.00625.x

Albladi, A., Islam, M., Das, A., Bigonah, M., Zhang, Z., Jamshidi, F., Rahgouy, M., Raychawdhary, N., Marghitu, D., & Seals, C. (2025). Hate Speech Detection using Large Language Models: A Comprehensive Review. *IEEE Access*. https://doi.org/10.1109/ACCESS.2025.3532397

Alshalan, R., & Al-Khalifa, H. (2020). A deep learning approach for automatic hate speech detection in the saudi twittersphere. *Applied Sciences*, *10*(23), 8614. https://doi.org/10.3390/app10238614

Antona Jimeno, T., Mayagoitia-Soria, A., & Đorđević, J. (2024). Research on Hate Speech. A Proposal of bibliometric analysis in Spain and LATAM during 2021 and 2022. *Icono 14*, *22*(1). https://doi.org/10.7195/ri14.v22i1.2128

Aria, M., & Cuccurullo, C. (2017). bibliometrix: An R-tool for comprehensive science mapping analysis. *Journal of informetrics*, *11*(4), 959-975. https://doi.org/10.1016/j.joi.2017.08.007

Badjatiya, P., Gupta, S., Gupta, M., & Varma, V. (2017). Deep learning for hate speech detection in tweets. Proceedings of the 26th international conference on World Wide Web companion,

Bahar, S. S., Yildiz, M. B., Yasin, E. T., Goktas, A., & Koklu, M. (2024). Bibliometric Analysis of Logistics and Artificial Intelligence Research Trends in the Last 10 Years. *International Journal of Applied Methods in Electronics and Computers*, *12*(4), 119-128. https://doi.org/10.58190/ijamec.2024.112

Boishakhi, F. T., Shill, P. C., & Alam, M. G. R. (2021). Multi-modal hate speech detection using machine learning. 2021 IEEE International Conference on Big Data (Big Data),

Boyack, K. W., & Klavans, R. (2010). Co-citation analysis, bibliographic coupling, and direct citation: Which citation approach represents the research front most accurately? *Journal of the American Society for Information Science and Technology*, *61*(12), 2389-2404. https://doi.org/10.1002/asi.21419

Bukar, U. A., Sayeed, M. S., Razak, S. F. A., Yogarayan, S., Amodu, O. A., & Mahmood, R. A. R. (2023). A method for analyzing text using VOSviewer. *MethodsX*, *11*, 102339. https://doi.org/10.1016/j.mex.2023.102339

Chen, C. (2006). CiteSpace II: Detecting and visualizing emerging trends and transient patterns in scientific literature. *Journal of the American Society for*

Information Science and Technology, *57*(3), 359-377. https://doi.org/10.1002/asi.20317

Chhabra, A., & Vishwakarma, D. K. (2023). A literature survey on multimodal and multilingual automatic hate speech identification. *Multimedia Systems*, *29*(3), 1203-1230. https://doi.org/10.1007/s00530-023-01051-8

Dagli, N., Haque, M., & Kumar, S. (2024). Exploring the Bacteriophage Frontier: A Bibliometric Analysis of Clinical Trials Between 1965 and 2024. *Cureus*, *16*(3). https://doi.org/10.7759/cureus.56266

Donthu, N., Kumar, S., Mukherjee, D., Pandey, N., & Lim, W. M. (2021). How to conduct a bibliometric analysis: An overview and guidelines. *Journal of business research*, *133*, 285-296. https://doi.org/10.1016/j.jbusres.2021.04.070

El-Alami, F. Z., Alaoui, S. O. E., & Nahnahi, N. E. (2022). A multilingual offensive language detection method based on transfer learning from transformer fine-tuning model. *Journal of King Saud University-Computer and Information Sciences*, *34*(8), 6048-6056. https://doi.org/10.1016/j.jksuci.2021.07.013

Faruqe, O., Jahan, M., Faisal, M., Islam, M. S., & Khan, R. (2023). Bangla hate speech detection system using transformer-based nlp and deep learning techniques. 2023 3rd Asian Conference on Innovation in Technology (ASIANCON),

Ferreira, F. A. (2018). Mapping the field of arts-based management: Bibliographic coupling and co-citation analyses. *Journal of business research*, *85*, 348-357. https://doi.org/10.1016/j.jbusres.2017.03.026

Fortuna, P., Dominguez, M., Wanner, L., & Talat, Z. (2022). Directions for NLP practices applied to online hate speech detection. The 2022 Conference on Empirical Methods in Natural Language Processing,

Gangurde, A., Mankar, P., Chaudhari, D., & Pawar, A. (2022). A systematic bibliometric analysis of hate speech detection on social media sites. *Journal of Scientometric Research*, *11*(1), 100-111. https://doi.org/10.5530/jscires.11.1.10

Glänzel, W., & Czerwon, H.-J. (1996). A new methodological approach to bibliographic coupling and its application to the national, regional and institutional level. *Scientometrics*, *37*, 195-221. https://doi.org/10.1007/BF02093621

Gokhale, M., & Pillai, D. (2024). Institutional framework of earnings management in emerging economies–a systematic literature review using bibliometric analysis. *Journal of Economic and Administrative Sciences*. https://doi.org/10.1108/JEAS-08-2023-0208

Halevy, K. (2023). A group-specific approach to nlp for hate speech detection. *arXiv preprint arXiv:2304.11223*. https://doi.org/10.48550/arXiv.2304.11223

Hamou-Lhadj, A., & Hamdaqa, M. (2009). Citation analysis: an approach for facilitating the understanding and the analysis of regulatory compliance documents. 2009 Sixth International Conference on Information Technology: New Generations,

Hassan, W., & Duarte, A. E. (2024). Bibliometric analysis: a few suggestions. *Current problems in cardiology*, 102640. https://doi.org/10.1016/j.cpcardiol.2024.102640

Ho, M. H.-C., Liu, J. S., & Chang, K. C.-T. (2017). To include or not: the role of review papers in citation-based analysis. *Scientometrics*, *110*, 65-76. https://doi.org/10.1007/s11192-016-2158-0

Ilhan, S. S., Sivakumar, S., Ramesh, S., Sreeram, N., & Rajalakshmi, R. (2024). Hate Speech Detection and Classification Using NLP. 2024 Second International Conference on Advances in Information Technology (ICAIT),

Irfan, A., Azeem, D., Narejo, S., & Kumar, N. (2024). Multi-modal hate speech recognition through machine learning. 2024 IEEE 1st Karachi Section Humanitarian Technology Conference (KHI-HTC),

Jahan, M. S., Oussalah, M., Beddia, D. R., & Arhab, N. (2024). A comprehensive study on nlp data augmentation for hate speech detection: Legacy methods, bert, and llms. *arXiv preprint arXiv:2404.00303*. https://doi.org/10.48550/arXiv.2404.00303

Karanam, M., Krishnanand, L., Manupati, V. K., & Nudurupati, S. S. (2024). Emerging themes and future research directions in the cold supply chain: a bibliometric and co-citation analysis. *Benchmarking: An International Journal*. https://doi.org/10.1108/BIJ-11-2023-0771

Karayigit, H., Akdagli, A., & Aci, C. (2022). Homophobic and Hate Speech Detection Using Multilingual-BERT Model on Turkish Social Media. *Information Technology and Control*, *51*, 356-375. https://doi.org/10.5755/j01.itc.51.2.29988

Kessler, M. M. (1963). Bibliographic coupling between scientific papers. *American documentation*, *14*(1), 10-25. https://doi.org/10.1002/asi.5090140103

Kibriya, H., Siddiqa, A., Khan, W. Z., & Khan, M. K. (2024). Towards safer online communities: Deep learning and explainable AI for hate speech detection and classification. *Computers and Electrical Engineering*, *116*, 109153. https://doi.org/10.1016/j.compeleceng.2024.109153

Klarin, A. (2024). How to conduct a bibliometric content analysis: Guidelines and contributions of content co-occurrence or co-word literature reviews.

International Journal of Consumer Studies, *48*(2), e13031. https://doi.org/10.1111/ijcs.13031

Koklu, N., & Sulak, S. A. (2024). Recent Developments in Educational Data Mining: A Four-Year Bibliometric Analysis. *Advances in Education Sciences, M. Dalkılıç and O. Soslu, Eds. Platanus Publishing*, 5-29. https://doi.org/10.5281/zenodo.14582661

Kovács, G., Alonso, P., & Saini, R. (2021). Challenges of Hate Speech Detection in Social Media. *SN Computer Science*, *2*(2), 95. https://doi.org/10.1007/s42979-021-00457-3

Kumar, R., Saxena, S., Kumar, V., Prabha, V., Kumar, R., & Kukreti, A. (2024). Service innovation research: a bibliometric analysis using VOSviewer. *Competitiveness Review: An International Business Journal*, *34*(4), 736-760. https://doi.org/10.1108/CR-01-2023-0010

Kurulgan, M. (2024). A bibliometric analysis of research on dropout in open and distance learning. *Turkish Online Journal of Distance Education*, *25*(4), 200-229. https://doi.org/10.17718/tojde.1355394

Luc, P. T. (2024). Social Entrepreneurial Intention: A Review Based on Bibliographic Coupling Analysis. *The Journal of Entrepreneurship*, *33*(4), 815-838. https://doi.org/10.1177/09713557241306882

Martyn, J. (1964). Bibliographic coupling. *Journal of documentation*, *20*(4), 236-236. https://doi.org/10.1108/eb026352

Mehdipour, M., Chitsaz, E., & Etemadi, M. (2024). A Perspective on Human Interaction and Artificial Intelligence: Bibliometric Analysis with Co-occurrence Technique. https://doi.org/10.48301/KSSA.2024.428257.2778

Miran, A. Z., & Yahia, H. S. (2023). Hate Speech Detection in Social Media (Twitter) Using Neural Network. *Journal of Mobile Multimedia*, *19*(3), 765-798. https://doi.org/10.13052/jmm1550-4646.1936

Mutanga, R. T., Olugbara, O., & Naicker, N. (2023). Bibliometric analysis of deep learning for social media hate speech detection. *Journal of Information Systems and Informatics*, *5*(3), 1154-1176. https://doi.org/10.51519/journalisi.v5i3.549

Nasir, S., Seerat, A., & Wasim, M. (2024). Hate speech detection in roman urdu using machine learning techniques. 2024 5th International Conference on Advancements in Computational Sciences (ICACS),

Osareh, F. (1996). Bibliometrics, citation analysis and co-citation analysis: A review of literature I. https://doi.org/10.1515/libr.1996.46.3.149

Passas, I. (2024). Bibliometric analysis: the main steps. *Encyclopedia*, *4*(2). https://doi.org/10.3390/encyclopedia4020065

Plaza-del-Arco, F. M., Molina-González, M. D., Urena-López, L. A., & Martín-Valdivia, M. T. (2021). Comparing pre-trained language models for Spanish hate speech detection. *Expert Systems with Applications*, *166*, 114120. https://doi.org/10.1016/j.eswa.2020.114120

Pookpanich, P., & Siriborvornratanakul, T. (2024). Offensive language and hate speech detection using deep learning in football news live streaming chat on YouTube in Thailand. *Social Network Analysis and Mining*, *14*(1), 18. https://doi.org/10.1007/s13278-023-01183-9

Ramírez-García, A., González-Molina, A., Gutiérrez-Arenas, M.-d.-P., & Moyano-Pacheco, M. (2022). Interdisciplinarity of Scientific Production on Hate Speech and Social Media: A Bibliometric Analysis. *Comunicar: Media Education Research Journal*, *30*(72), 123-134. https://doi.org/10.3916/C72-2022-10

Ramos, G., Batista, F., Ribeiro, R., Fialho, P., Moro, S., Fonseca, A., Guerra, R., Carvalho, P., Marques, C., & Silva, C. (2024). A comprehensive review on automatic hate speech detection in the age of the transformer. *Social Network Analysis and Mining*, *14*(1), 204. https://doi.org/10.1007/s13278-024-01361-3

Saifullah, S., Drężewski, R., Dwiyanto, F. A., Aribowo, A. S., Fauziah, Y., & Cahyana, N. H. (2024). Automated text annotation using a semi-supervised approach with meta vectorizer and machine learning algorithms for hate speech detection. *Applied Sciences*, *14*(3), 1078. https://doi.org/10.3390/app14031078

Schweiggart, N. (2024). Mapping the role of animal welfare in tourism: examining discourses in tourism research and beyond using a bibliometric co-occurrence analysis of author keywords. *Journal of Ecotourism*, *23*(4), 740-767. https://doi.org/10.1080/14724049.2024.2319221

Sjuchro, D. W., Rahmatullah, T., & Nurfauziah, I. (2025). Community Radio Research Trends in Communication Science: A Co-Authorship Bibliometric Analysis. *Jurnal Kajian Jurnalisme*, *8*(2), 115-128. https://doi.org/10.24198/jkj.v8i2.55978

Small, H., & Griffith, B. C. (1974). The structure of scientific literatures I: Identifying and graphing specialties. *Science studies*, *4*(1), 17-40. https://doi.org/10.1177/030631277400400102

Sulak, S. A., & Koklu, N. (2024). Bibliometric Analysis of Publications Related to Augmented Reality in Education in The Last 20 Years. Advances in Education Sciences. *Advances in Education Sciences, M. Dalkılıç and O.*

Soslu, Eds. Platanus Publishing, 31-58. https://doi.org/10.5281/zenodo.14582661

Toktarova, A., Syrlybay, D., Myrzakhmetova, B., Anuarbekova, G., Rakhimbayeva, G., Zhylanbaeva, B., Suieuova, N., & Kerimbekov, M. (2023). Hate speech detection in social networks using machine learning and deep learning methods. *International Journal of Advanced Computer Science and Applications*, *14*(5), 396-406.

Tontodimamma, A., Nissi, E., Sarra, A., & Fontanella, L. (2021). Thirty years of research into hate speech: topics of interest and their evolution. *Scientometrics*, *126*, 157-179. https://doi.org/10.1007/s11192-020-03737-6

Ugurlu, B. N., & Aktar Ugurlu, G. (2024). Exploring trends and developments in cholesteatoma research: a bibliometric analysis. *European Archives of Oto-Rhino-Laryngology*, *281*(10), 5199-5210. https://doi.org/10.1007/s00405-024-08749-z

Van Eck, N., & Waltman, L. (2010). Software survey: VOSviewer, a computer program for bibliometric mapping. *Scientometrics*, *84*(2), 523-538. https://doi.org/10.1007/s11192-009-0146-3

Van Eck, N. J., & Waltman, L. (2017). Citation-based clustering of publications using CitNetExplorer and VOSviewer. *Scientometrics*, *111*, 1053-1070. https://doi.org/10.1007/s11192-017-2300-7

Wallin, J. A. (2005). Bibliometric methods: pitfalls and possibilities. *Basic & clinical pharmacology & toxicology*, *97*(5), 261-275. https://doi.org/10.1111/j.1742-7843.2005.pto_139.x

Weinberg, B. H. (1974). Bibliographic coupling: A review. *Information Storage and Retrieval*, *10*(5-6), 189-196. https://doi.org/10.1016/0020-0271(74)90058-8

Yasin, E. T., Erturk, M., Bulut, M. T., & Koklu, M. (2024). Bibliometric analysis of deep learning applications in dentistry. *International Dental Journal*, *74*, S216. https://doi.org/10.1016/j.identj.2024.07.044

Zhang, H., Lv, Y., Zhang, S., & Liu, Y. D. (2024). Digital supply chain management: a review and bibliometric analysis. *Journal of Global Information Management (JGIM)*, *32*(1), 1-20. https://doi.org/10.4018/JGIM.336285

Zhang, N., & Feng, G. (2024). Analysis of Big Data Research Hotspots Based on Keyword Co-occurrence. 2024 IEEE 9th International Conference on Data Science in Cyberspace (DSC),

Zhao, D., & Strotmann, A. (2008). Evolution of research activities and intellectual influences in information science 1996–2005: Introducing author bibliographic-coupling analysis. *Journal of the American Society for*

Information Science and Technology, *59*(13), 2070-2086. https://doi.org/10.1002/asi.20910

Zhao, Z. X., Zhang, Z. Q., & Hopfgartner, F. (2022). Utilizing subjectivity level to mitigate identity term bias in toxic comments classification. *Online Social Networks and Media*, *29*, Article 100205. https://doi.org/10.1016/j.osnem.2022.100205

Zhou, Y., Yang, Y., Liu, H., Liu, X., & Savage, N. (2020). Deep learning based fusion approach for hate speech detection. *IEEE Access*, *8*, 128923-128929. https://doi.org/10.1109/ACCESS.2020.3009244

Zhou, Y. L., Yang, Y. Y., Liu, H., Liu, X. F., & Savage, N. (2020). Deep Learning Based Fusion Approach for Hate Speech Detection. *Ieee Access*, *8*, 128923-128929. https://doi.org/10.1109/access.2020.3009244

Zhu, W. Z., Gong, H. Y., Bansal, R., Weinberg, Z., Christin, N., Fanti, G., Bhat, S., & Ieee Computer, S. O. C. (2021, May 24-27). Self-Supervised Euphemism Detection and Identification for Content Moderation.*IEEE Symposium on Security and Privacy* [2021 ieee symposium on security and privacy, sp]. 42nd IEEE Symposium on Security and Privacy (SP), null, ELECTR NETWORK.

Zupic, I., & Čater, T. (2015). Bibliometric methods in management and organization. *Organizational research methods*, *18*(3), 429-472. https://doi.org/10.1177/1094428114562629

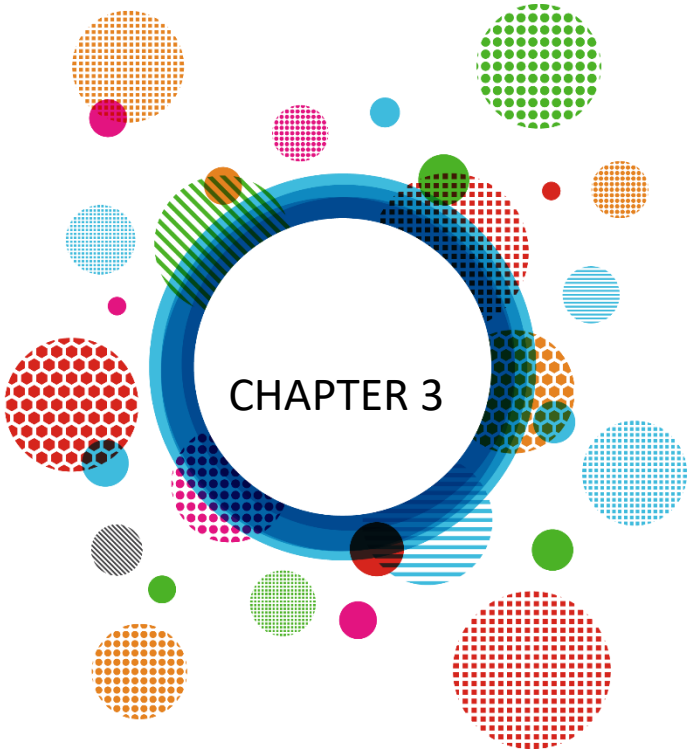

Modulation of Nonlinear Axial Waves of Nanorods Embedded in A Viscoelastic Medium

Guler Gaygusuzoglu[1]

[1] Doç. Dr. Department of Civil Engineering, Tekirdag Namık Kemal University, Turkey
ORCID: 0000-0002-2350-4856

1. INTRODUCTION

Due to the rapid advancement of technology and the shrinking of needs, the demand for nano-scale materials has increased in this direction in order to produce products that require precision. The shrinking of the dimensions has caused engineering problems to be more complex and more detailed. In this study, the investigation of the wave propagation of nanoscale carbon rod is chosen as a theoretical study. When this physical problem is considered, it is seen that the mechanics science is insufficient to obtain accurate results with the classical elasticity theory. In this context, more comprehensive theories have been used to better understand the behaviour of the nanoscale carbon rod representing the problem we have examined. In order to achieve a correct solution to this problem, a solution was sought by using the Nonlocal Elasticity Theory developed by Eringen [6]

Nanotechnology began with the discovery of carbon nanostructures in 1991 [1], which accelerated theoretical and experimental research in this field. When it comes to their mechanical and structural characteristics, carbon nanotubes are one of the best examples of nanoscale materials. Understanding the dynamic behavior of carbon nanotubes has drawn a lot more attention from researchers in recent years. Two categories are used to study the characteristics of carbon nanotubes. Among them is the modeling of atomic/molecular dynamics. The other group includes theories based on various concepts of size-based continuity, such as modified couple stress theory [5], micropolar theory [3], nonlocal elasticity theory [4], and strain gradient theory [2].

In contrast to the traditional theory, the nonlocal elasticity theory takes size effects into account. Eringen [6] assumed that the stress at one point points to distortions at every point in the continuum in order to explain the size effect. Size dependence, particularly at the nanoscale, is greatly influenced by atomic interactions. Using Eringen's nonlocal elasticity theory, the static and dynamic behavior of carbon nanotubes has been thoroughly investigated in the literature. Static evaluation studies have mostly examined bending and torsion, whereas dynamic analysis studies have taken vibration and wave propagation into account. According to recent studies, accurate results are obtained when evaluating the wave propagation and vibration of carbon nanotubes (CNTs) in various media, such as elastic and viscoelastic.

The impact of the scale effect in an elastic medium on the vibration of single-walled carbon nanotubes was examined by Murmu and Pradhan [7]. The axial vibration of a nanorod in an elastic medium was examined by Aydogdu [8] and Yaylı et al. [9] utilizing the theory of nonlocal elasticity. Single-walled carbon nanotubes loaded with a viscous fluid were studied by Lee and Chang [10] in 2009 to see how they vibrated. Using a Pasternak medium, Soltani et al. [11]

examined the thermo-mechanical vibration of single-walled carbon nanotubes in 2010. Single-walled carbon nanotubes' axial vibration under a range of live loads was examined by Khosravi et al. [12] in an elastic medium. The free rotational vibration of single-walled carbon nanotubes in a viscoelastic medium was investigated by Arda and Aydogdu [13], who also looked at how ambient and nonlocal parameters affected vibrational frequencies. Furthermore, Arda and Aydogdu [14] investigated torsional vibration by taking into account the effects of the van der Waals contact between two nanotubes, the stiffness and damping parameters of viscoelastic media, and the nonlocal parameter in double-walled carbon nanotubes in viscoelastic media.

Wave propagation is the method that describes nanostructures the best. It serves as the foundation for nanosensor converters as well. A number of analytical models were examined by Natsuki et al. [15] in order to solve the problem of wave propagation in carbon nanotubes with single and double walls in an elastic medium. Wang et al. [16] investigated how double-walled carbon nanotubes' size affects wave propagation. In order to study wave propagation, Lim and Yang [17] employed size effects and an analytical nonlocal stress model in carbon nanotubes. Ponnusamy and Amuthalakshmi [18] investigated how heat affected the way waves traveled through an acoustic cavity made of double-walled carbon nanotubes.

The propagation of acoustic waves in carbon nanotubes was investigated by Srivastava in 2013 [19]. Viscoelastic wave propagation in viscoelastic single-walled carbon nanotubes was addressed by Tang et al. [20] using the nonlocal strain gradient theory. Zhen [21] looked into how surface and nonlocal factors affected the way waves traveled through fluid-filled, single-walled viscoelastic nanotubes. Using the theory of the nonlocal second-order strain gradient elasticity, Guo and colleagues [22] examined the transverse wave propagation problem in single-walled viscoelastic nanotubes. A recent study by Boyina and Piska [23] examined wave propagation in viscoelastic Timoshenko nanobeams under the influence of magnetic fields and surfaces using strain gradient theory. This work demonstrates the effects of a carbon nanotube's diameter on the shear and flexural wave phase velocities.

Wave propagation is a crucial problem in many scientific and technical domains. The deformation of CNTs has been taken into account in the aforementioned research. Nevertheless, the deformation of CNT is nonlinear [24]. For instance, in many areas of physics and engineering, nonlinear effects have a major impact on water waves, plasma physics, and nonlinear optics. In certain nonlinear vibration and nonlinear wave propagation problems, nonlinear effects in nanotubes have been taken into account. In many of these investigations, Von Kármán geometric nonlinearity has been taken into account.

Yang et al. [25] investigated nonlinear free vibration in single-walled carbon nanotubes using nonlocal Timoshenko beam theory. In 2012, Ke et al. [26] examined the nonlinear vibration of piezoelectric nanobeams using nonlocal theory. Additionally, Sellitto and Di Domenico [27] investigated nonlocal and nonlinear effects on the propagation of thermal and elastic high-frequency waves in nanosystems. The nonlinear vibration of carbon nanobeams with single walls that are clamped and simply supported, with boundary conditions embedded in a multilayer elastic medium, was studied by Sobamowo et al. [28]. Wang et al. [29] conducted one of the few investigations on nonlinear wave propagation in single-walled nonlinearly curved carbon nanotubes by assessing wave propagation using the theory of nonlocal elasticity. Norouzzadeh et al. [30] used nonlinear wave propagation analysis to study strain gradient and nonlocal effects in Timoshenko nanobeams.

Gaygusuzolu and Akdal [31] employed the notion of nonlocal elasticity in an elastic medium to comprehend weak nonlinear wave propagation (solitary waves) in nanorods. Consequently, the governing equation of long waves, the Korteweg-de Vries equation, was obtained. The researchers looked into how the stiffness and nonlocal factors affected the wave profile in an elastic medium. Gaygusuzoglu et al. [32] used the nonlocal elasticity theory to study nonlinear wave modulation in nanorods and found that the nonlinear Schrödinger equation is the governing equation of waves in a nonlocal elastic medium. The researchers also examined linear local and nonlocal and nonlinear local and nonlocal scenarios and discovered amplitude-dependent phase and group velocities and wave frequencies.

This work uses a multiple-scale expansion approach to investigate the nonlinear modulation of axial waves passing through a nanorod in a viscoelastic medium based on nonlocal theory. First, a one-dimensional nonlinear field equation is found. In order to analyze the dispersive nature of the medium, we also provide the linear dispersion relation of waves. We show that the nonlinear modulation of axial waves in a nonlocal viscoelastic medium is governed by the nonlinear Schrödinger equations with complex coefficients.

The current study's organizational chart is shown below. The system's governing equation is covered in Section 2, along with details on nonlocal elasticity theory. The principles of the multiple-scale expansion approach and nonlinear wave modulation are discussed in Section 3. Using this expansion method, the governing equation can be the nonlinear Schrödinger equation, which is a nonlinear Schrödinger equation with complex coefficients. The first equation of this type to appear in the literature is this one.

2. ESSENTIAL FORMULAS AND THEORETICAL INITIATIONS

2.1. Nonlinear Local Viscoelastic Nanorod Model

This section provides the basic formulas for the motion of nanorods in local viscoelastic media. The equation for nonlinear vibration in a nanotube can be derived using the gradient tensor of deformation, which was established by Malvern [33].

$$\mathbf{F} = \nabla \mathbf{U} + \mathbf{I} \tag{1}$$

U is the displacement component of the motion, and **I** is the unit matrix in this case. In a medium subject to finite extension, the equation of motion can be written in terms of material coordinates as follows when the element is not subject to any body forces:

$$\nabla[\mathbf{S}\mathbf{F}^{\mathrm{T}}] + \mathbf{f} = \rho_0 \frac{\partial^2 \mathbf{U}}{\partial t^2} \tag{2}$$

S stands for the second Piola-Kirchoff stress tensor, which is the energy-based conjugate of the Green stress tensor, **f** for the distributed axial force acting on the rod, and ρ_0 for the medium's undeformed density.

The following assumptions about the axial force brought on by the viscoelastic medium are made in this study:

$$\mathbf{f} = -k_e \mathbf{U} - d \frac{\partial \mathbf{U}}{\partial t} \tag{3}$$

where k_e is the elastic medium stiffness and d is the damping coefficient.

Hooke's law can therefore be applied as the governing formula. Consequently, the following is how the equation is expressed:

$$\mathbf{S} = \mathbf{c}\mathbf{E} \tag{4}$$

Here, **c** stands for the fourth-order tensor that illustrates the elastic behavior of the material, and **E** stands for the Green strain tensor, which is expressed as follows:

$$\mathbf{E} = \frac{1}{2}[\mathbf{F}^{\mathrm{T}}\mathbf{F} - \mathbf{1}] \tag{5}$$

A diagonal matrix in Cartesian coordinates is created from the gradient deformation tensor by limiting the rod's boundary conditions and presuming that only radial deformation U(x,t) takes place in the medium:

$$\mathrm{F}_{xx} = 1 + \frac{\partial U}{\partial x} \tag{6}$$

$$\mathrm{F}_{yy} = 1 \tag{7}$$

$$\mathrm{F}_{zz} = 1 \tag{8}$$

Focusing exclusively on the non-zero component of the Green strain tensor yields the following equation:

$$E_{xx} = \left(1 + \frac{1}{2}\frac{\partial U}{\partial x}\right)\frac{\partial U}{\partial x} \tag{9}$$

For isotropic materials with Poisson's ratio ν and elastic modulus E_E, the stress-strain relationships are described by the following equation:

$$\mathrm{S}_{ij} = \frac{E_E}{(1+\nu)}\left[\mathrm{E}_{ij} + \frac{\nu}{1-2\nu}\mathrm{E}_{kk}\delta_{ij}\right] \tag{10}$$

δ_{ij} refers to Kronecker's delta. When Eq. (9) is substituted into Eq. (10), shear stresses are removed, and the normal stress components are shown as follows:

$$\mathrm{S}_{xx} = \frac{E_E(1-\nu)}{(1+\nu)(1-2\nu)}\left(1 + \frac{1}{2}\frac{\partial U}{\partial x}\right)\frac{\partial U}{\partial x} \tag{11}$$

$$\mathrm{S}_{yy} = \mathrm{S}_{zz} = \frac{\nu E_E}{(1+\nu)(1-2\nu)}\left(1 + \frac{1}{2}\frac{\partial U}{\partial x}\right)\frac{\partial U}{\partial x} \tag{12}$$

Eq. (13) can be obtained by rearranging Eqs. (11) and (12) using Eqs. (6), (7), and (8):

$$\left[\frac{3}{2}\left(\frac{\partial U}{\partial x}\right)^2 + 3\frac{\partial U}{\partial x} + 1\right]\frac{\partial^2 U}{\partial x^2} - \frac{k_e(1+\nu)(1-2\nu)}{E_E(1-\nu)}U - \frac{d(1+\nu)(1-2\nu)}{E_E(1-\nu)}\frac{\partial U}{\partial t} = \frac{\rho_0(1+\nu)(1-2\nu)}{E_E(1-\nu)}\frac{\partial^2 U}{\partial t^2} \tag{13}$$

When the viscoelastic medium deforms infinitely, the nonlinear terms in Equation (13) become insignificant, and the equation is simplified to the following:

$$\frac{\partial^2 U}{\partial x^2} - \frac{k_e(1+\nu)(1-2\nu)}{E_E(1-\nu)}U - \frac{d(1+\nu)(1-2\nu)}{E_E(1-\nu)}\frac{\partial U}{\partial t} = \frac{\rho_0(1+\nu)(1-2\nu)}{E_E(1-\nu)}\frac{\partial^2 U}{\partial t^2} \quad (14)$$

The equation will become non-dimensional by adding the following non-dimensional variables:

$$\psi = U / r_0 \quad (15)$$

$$\zeta = x / r_0 \quad (16)$$

r_0 is used here to define the nanorod's radius. Rearranging Eqs. (13) and (14) using Eqs. (15) and (16) yields the following non-dimensional equation:

$$\left[\frac{3}{2}\left(\frac{\partial \psi}{\partial \zeta}\right)^2 + 3\frac{\partial \psi}{\partial \zeta} + 1\right]\frac{\partial^2 \psi}{\partial \zeta^2} - K_e\psi - D\frac{\partial \psi}{\partial t} = \delta\frac{\partial^2 \psi}{\partial t^2} \quad (17)$$

where the coefficients K_e, D, and □ are expressed as shown below:

$$K_e = \frac{k_e r_0^2(1+\nu)(1-2\nu)}{(1-\nu)},\ D = \frac{d r_0^2(1+\nu)(1-2\nu)}{(1-\nu)},\ \delta = \frac{\rho_0 r_0^2(1+\nu)(1-2\nu)}{E_E(1-\nu)} \quad (18)$$

For the local nonlinear nanorod model, Mousavi and Fariborz [34] arrived at Eq. (17) in the following way:

$$\left[\frac{3}{2}\left(\frac{\partial \psi}{\partial \zeta}\right)^2 + 3\frac{\partial \psi}{\partial \zeta} + 1\right]\frac{\partial^2 \psi}{\partial \zeta^2} = \delta\frac{\partial^2 \psi}{\partial t^2} \quad (19)$$

The linear equation of motion is given below:

$$\frac{\partial^2 \psi}{\partial \zeta^2} = \delta\frac{\partial^2 \psi}{\partial t^2}. \quad (20)$$

2.2 Nonlinear Nonlocal Viscoelastic Nanorod Model

The construction of the equations of motion for nanorods in nonlocal viscoelastic media and nonlocal viscoelasticity will be discussed in this section. The constitutive equation for a nanorod was created by Eringen [3] and Aydogdu [35] using nonlocal elasticity theory, and it is written as follows:

$$[1-(e_0 a)^2\nabla^2][\mathbf{SF}^{\mathrm{T}}] = \lambda_L \mathrm{E}_{rr}\delta_{kl} + 2\mu_L \mathrm{E}_{kl} \quad (21)$$

$\mathbf{SF}^{\mathrm{T}}$ stands for the nonlocal stress tensor, $\mathrm{E_{kl}}$ for the strain tensor, a for the internal characteristic length, e_0 for a constant, and λ_L and μ_L for the Lamé constants. The nonlocal parameter must be carefully chosen in order to ensure the accuracy of nonlocal models.

Eringen [3] suggested $e_0 = 0.39$ by comparing the lattice dynamic longitudinal wave frequency data at the end of the first Broullin zone ($k = \pi/a$), where a is chosen as a characteristic length stretch across micro-, meso-, and macroscales and k is the wavelength.

For Rayleigh surface waves, Eringen suggested $e_0 = 0.31$ [6]. Aydogdu [35] asserts that the geometrical and material characteristics of CNTs determine their nonlocal parameter e_0.

To examine the axial modulation of a nanorod, the nonlocal viscoelastic constitutive relation must be established. Therefore, the following method can be used to determine the equation of motion for the nanorod embedded in a viscoelastic medium:

$$\nabla[\mathbf{S}\mathbf{F}^{\mathrm{T}}] + \mathbf{f} = \rho_0 \frac{\partial^2 \mathbf{U}}{\partial t^2} \tag{22}$$

The present study makes the following assumption about the axial force caused by a viscoelastic medium:

$$\mathbf{f} = -k_e \mathbf{U} - d \frac{\partial \mathbf{U}}{\partial t} \tag{23}$$

where the stiffness of the elastic medium is denoted by k_e and the damping coefficient by d. The nanorod model in a viscoelastic medium is schematically depicted in Figure 1.

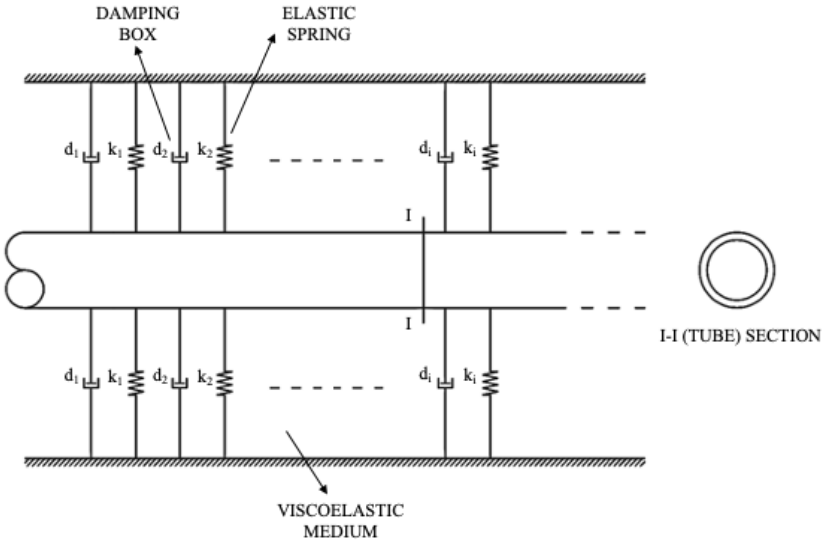

Fig. 1 The nanorod model in a viscoelastic medium is demonstrated.

The following equation can be obtained by taking the gradient of both sides in order to solve Eq. (21) for $\mathbf{SF}^{\mathrm{T}}$:

$$\nabla[\mathbf{SF}^{\mathrm{T}}] = (e_0 a)^2 \nabla^2 \nabla[\mathbf{SF}^{\mathrm{T}}] + \nabla(\lambda_L \mathrm{E}_{rr} \delta_{kl} + 2\mu_L \mathrm{E}_{kl}) \qquad (24)$$

By expressing the gradient of Eq. (22) and multiplying it by a nonlocal parameter, the following equation can be obtained:

$$(e_0 a)^2 \nabla^2 [\mathbf{SF}^{\mathrm{T}}] = (e_0 a)^2 \nabla \left[\rho_0 \frac{\partial^2 \mathbf{U}}{\partial t^2} - \mathbf{f} \right] \qquad (25)$$

When Eq. (24) is inserted into Eq. (25) it takes the following form:

$$\nabla[\mathbf{SF}^{\mathrm{T}}] = (e_0 a)^2 \nabla^2 \rho_0 \frac{\partial^2 \mathbf{U}}{\partial t^2} - (e_0 a)^2 \nabla^2 \mathbf{f} + \nabla(\lambda_L \mathrm{E}_{rr} \delta_{kl} + 2\mu_L \mathrm{E}_{kl}) \qquad (26)$$

The differential equation that results from the combination of Equations (22) and (26) is as follows:

$$\rho_0 \frac{\partial^2 \mathbf{U}}{\partial t^2} = (e_0 a)^2 \nabla^2 \rho_0 \frac{\partial^2 \mathbf{U}}{\partial t^2} - (e_0 a)^2 \nabla^2 \mathbf{f} + \nabla(\lambda_L \mathrm{E}_{rr} \delta_{kl} + 2\mu_L \mathrm{E}_{kl}) + \mathbf{f} \qquad (27)$$

In the setting of nonlocal viscoelasticity, applying non-zero displacement U to a one-dimensional situation results in the following nonlinear non-dimensional equation of motion:

$$\left[\frac{3}{2} \left(\frac{\partial \psi}{\partial \zeta} \right)^2 + 3 \frac{\partial \psi}{\partial \zeta} + 1 \right] \frac{\partial^2 \psi}{\partial \zeta^2} = \delta \left(\frac{\partial^2 \psi}{\partial t^2} - \mu \frac{\partial^4 \psi}{\partial \zeta^2 \partial t^2} \right) + K_e \left(\psi - \mu \frac{\partial^2 \psi}{\partial \zeta^2} \right) + D \left(\frac{\partial \psi}{\partial t} - \mu \frac{\partial^3 \psi}{\partial \zeta^2 \partial t} \right) \qquad (28)$$

where the dimensionless nonlocal parameter, that is □, is $\mu = (e_0 a / r_0)^2$. Setting □ = 0 yields the nonlinear equation of motion for the classical viscoelasticity theory.

3. INVESTIGATION OF NONLINEAR WAVE MODULATION IN NANORODS USING THE MULTIPLE-SCALE EXPANSION METHOD

Finding precise solutions in nonlinear situations may be difficult. Due to the complexity of the governing equations, this is especially true for nonlinear dynamics under the nonlocal elasticity theory. However, when nonlinearity is appropriately weak, handling nonlinear problems is typically not too tough. In this instance, evolution equations from the nonlinearity and dispersion equilibrium may be obtained using the medium's dispersive characteristics. The aforementioned property makes it reasonable to apply the far-field theory of nonlinear waves, which has been fully developed in several engineering and physics fields, to nonlocal elasticity theory when nonlinearity and dispersion are in equilibrium.

The modulation of strongly dispersive and dissipative waves that are weakly nonlinear in nanorods embedded in a viscoelastic medium is examined in this section. We accomplish this by using the multiple-scale expansion technique [36] and show the coordinate stretching that results:

$$\zeta_n = \varepsilon^n \zeta, \qquad t_n = \varepsilon^n t, \qquad n = 0,1,2,... \qquad (29)$$

Here, the small parameter ε is used to measure the nonlinearity's weakness.

Assumed to be functions of both slow $(\zeta_0, \zeta_1, \zeta_2, ...; t_0, t_1, t_2, ...)$ and fast variables (ζ, t) are the field quantities. Consequently, the derivative expansions mentioned below are acceptable:

$$\frac{\partial}{\partial \zeta} = \sum_{n=0}^{N} \varepsilon^n \frac{\partial}{\partial \zeta_n}, \qquad \frac{\partial}{\partial t} = \sum_{n=0}^{N} \varepsilon^n \frac{\partial}{\partial t_n} \qquad (30)$$

The following illustrates the expansion of the field quantities into an asymptotic series of ε:

$$\psi = \sum_{n=1}^{\infty} \varepsilon^n \psi_n(\zeta_0, \zeta_1, \zeta_2, ...; t_0, t_1, t_2, ...) = \varepsilon\psi_1 + \varepsilon^2\psi_2 + \varepsilon^3\psi_3 + \cdots \quad (31)$$

Equation (28) is obtained by applying the expansion to the following differential equation:

$$\left[\frac{3}{2}\left(\varepsilon\frac{\partial\psi_1}{\partial\zeta_0}\right)^2+3\varepsilon^3\frac{\partial\psi_1}{\partial\zeta_0}\frac{\partial\psi_1}{\partial\zeta_1}+3\varepsilon\frac{\partial\psi_1}{\partial\zeta_0}+3\varepsilon^2\frac{\partial\psi_2}{\partial\zeta_0}+3\varepsilon^2\frac{\partial\psi_1}{\partial\zeta_1}+\cdots+1\right]\times\left[\varepsilon\frac{\partial^2\psi_1}{\partial\zeta_0^2}+\right.$$

$$\left.\varepsilon^2\frac{\partial^2\psi_2}{\partial\zeta_0^2}+\varepsilon^3\frac{\partial^2\psi_3}{\partial\zeta_0^2}+2\varepsilon^2\frac{\partial^2\psi_1}{\partial\zeta_0\partial\zeta_1}+2\varepsilon^3\frac{\partial^2\psi_2}{\partial\zeta_0\partial\zeta_1}+2\varepsilon^3\frac{\partial^2\psi_1}{\partial\zeta_0\partial\zeta_2}+\varepsilon^3\frac{\partial^2\psi_1}{\partial\zeta_1^2}+\cdots\right]=$$

$$\delta\left[\varepsilon\frac{\partial^2\psi_1}{\partial t_0^2}+\varepsilon^2\frac{\partial^2\psi_2}{\partial t_0^2}+\varepsilon^3\frac{\partial^2\psi_3}{\partial t_0^2}+2\varepsilon^2\frac{\partial^2\psi_1}{\partial t_0\partial t_1}+2\varepsilon^3\frac{\partial^2\psi_2}{\partial t_0\partial t_1}+2\varepsilon^3\frac{\partial^2\psi_1}{\partial t_0\partial t_2}+\right.$$

$$\left.\varepsilon^3\frac{\partial^2\psi_1}{\partial t_1^2}+\cdots\right]-\delta\mu\left[\varepsilon\frac{\partial^4\psi_1}{\partial t_0^2\partial\zeta_0^2}+\varepsilon^2\frac{\partial^4\psi_2}{\partial t_0^2\partial\zeta_0^2}+\varepsilon^3\frac{\partial^4\psi_3}{\partial t_0^2\partial\zeta_0^2}+2\varepsilon^2\frac{\partial^4\psi_1}{\partial t_0^2\partial\zeta_0\partial\zeta_1}+\right.$$

$$2\varepsilon^3\frac{\partial^4\psi_2}{\partial t_0^2\partial\zeta_0\partial\zeta_1}+2\varepsilon^3\frac{\partial^4\psi_1}{\partial t_0^2\partial\zeta_0\partial\zeta_1}+\varepsilon^3\frac{\partial^4\psi_1}{\partial t_0^2\partial\zeta_1^2}+2\varepsilon^2\frac{\partial^4\psi_1}{\partial\zeta_0^2\partial t_0\partial t_1}+\varepsilon^3\frac{\partial^4\psi_1}{\partial t_1^2\partial\zeta_0^2}+$$

$$\left.2\varepsilon^3\frac{\partial^4\psi_2}{\partial\zeta_0^2\partial t_0\partial t_1}+4\varepsilon^3\frac{\partial^4\psi_1}{\partial t_0\partial t_1\partial\zeta_0\partial\zeta_1}+2\varepsilon^3\frac{\partial^4\psi_1}{\partial\zeta_0^2\partial t_0\partial t_2}+\cdots\right]+K_e\left[\varepsilon\psi_1+\varepsilon^2\psi_2+\right.$$

$$\left.\varepsilon^3\psi_3+\cdots\right]-K_e\mu\left[\varepsilon\frac{\partial^2\psi_1}{\partial\zeta_0^2}+\varepsilon^2\frac{\partial^2\psi_2}{\partial\zeta_0^2}+\varepsilon^3\frac{\partial^2\psi_3}{\partial\zeta_0^2}+2\varepsilon^2\frac{\partial^2\psi_1}{\partial\zeta_0\partial\zeta_1}+2\varepsilon^3\frac{\partial^2\psi_2}{\partial\zeta_0\partial\zeta_1}+\right.$$

$$2\varepsilon^3\frac{\partial^2\psi_1}{\partial\zeta_0\partial\zeta_2}+\varepsilon^3\frac{\partial^2\psi_1}{\partial\zeta_1^2}+\cdots\Big]+D\left[\varepsilon\frac{\partial\psi_1}{\partial t_0}+\varepsilon^2\frac{\partial\psi_2}{\partial t_0}+\varepsilon^3\frac{\partial\psi_3}{\partial t_0}+\varepsilon^2\frac{\partial\psi_1}{\partial t_1}+\right.$$

$$\left.\varepsilon^3\frac{\partial\psi_2}{\partial t_1}+\varepsilon^3\frac{\partial\psi_1}{\partial t_2}+\cdots\right]-D\mu\left[\varepsilon\frac{\partial^3\psi_1}{\partial t_0\partial\zeta_0^2}+\varepsilon^2\frac{\partial^3\psi_2}{\partial t_0\partial\zeta_0^2}+\varepsilon^3\frac{\partial^3\psi_3}{\partial t_0\partial\zeta_0^2}+\right.$$

$$3\varepsilon^2\frac{\partial^3\psi_1}{\partial t_0\partial\zeta_0\partial\zeta_1}+3\varepsilon^3\frac{\partial^3\psi_2}{\partial t_0\partial\zeta_0\partial\zeta_1}+2\varepsilon^3\frac{\partial^3\psi_1}{\partial t_0\partial\zeta_0\partial\zeta_2}+2\varepsilon^3\frac{\partial^3\psi_1}{\partial t_0\partial\zeta_0\partial\zeta_3}+ \tag{32}$$

$$\left.\varepsilon^3\frac{\partial^3\psi_1}{\partial t_0\partial\zeta_1^2}+\varepsilon^2\frac{\partial^3\psi_1}{\partial t_1\partial\zeta_0^2}+\varepsilon^3\frac{\partial^3\psi_2}{\partial t_1\partial\zeta_0^2}+3\varepsilon^3\frac{\partial^3\psi_1}{\partial t_1\partial\zeta_0\partial\zeta_1}+\varepsilon^3\frac{\partial^3\psi_1}{\partial t_2\partial\zeta_0^2}+\cdots\right]$$

Setting all like powers of coefficients ε to zero results in the following set of differential equations:

The first-order, O(ε), equation:

$$\frac{\partial^2\psi_1}{\partial\zeta_0^2}=\delta\frac{\partial^2\psi_1}{\partial t_0^2}-\delta\mu\frac{\partial^4\psi_1}{\partial t_0^2\partial\zeta_0^2}+K_e\psi_1-K_e\mu\frac{\partial^2\psi_1}{\partial\zeta_0^2}+D\frac{\partial\psi_1}{\partial t_0}-D\mu\frac{\partial^3\psi_1}{\partial t_0\partial\zeta_0^2} \tag{33}$$

The second-order, O(ε^2), equation:

$$3\frac{\partial\psi_1}{\partial\zeta_0}\frac{\partial^2\psi_1}{\partial\zeta_0^2}+\frac{\partial^2\psi_2}{\partial\zeta_0^2}+2\frac{\partial^2\psi_1}{\partial\zeta_0\partial\zeta_1}=\delta\left(\frac{\partial^2\psi_2}{\partial t_0^2}+2\frac{\partial^2\psi_1}{\partial t_0\partial t_1}\right)-\delta\mu\left(\frac{\partial^4\psi_2}{\partial t_0^2\partial\zeta_0^2}+2\frac{\partial^4\psi_1}{\partial t_0^2\partial\zeta_0\partial\zeta_1}+2\frac{\partial^4\psi_1}{\partial\zeta_0^2\partial t_0\partial t_1}\right)+K_e\left(\psi_2-\mu\frac{\partial^2\psi_2}{\partial\zeta_0^2}-2\mu\frac{\partial^2\psi_1}{\partial\zeta_0\partial\zeta_1}\right)+D\left(\frac{\partial\psi_2}{\partial t_0}+\frac{\partial\psi_1}{\partial t_1}-\mu\frac{\partial^3\psi_2}{\partial t_0\partial\zeta_0^2}-3\mu\frac{\partial^3\psi_1}{\partial t_0\partial\zeta_0\partial\zeta_1}\right) \tag{34}$$

The third-order, O(ε^3), equation:

$$\frac{3}{2}\left(\frac{\partial\psi_1}{\partial\zeta_0}\right)^2\frac{\partial^2\psi_1}{\partial\zeta_0^2}+3\frac{\partial\psi_1}{\partial\zeta_0}\frac{\partial^2\psi_2}{\partial\zeta_0^2}+3\frac{\partial\psi_2}{\partial\zeta_0}\frac{\partial^2\psi_1}{\partial\zeta_0^2}+2\frac{\partial^2\psi_1}{\partial\zeta_0\partial\zeta_2}+\frac{\partial^2\psi_3}{\partial\zeta_0^2}+2\frac{\partial^2\psi_2}{\partial\zeta_0\partial\zeta_1}+\frac{\partial^2\psi_1}{\partial\zeta_1^2}+6\frac{\partial\psi_1}{\partial\zeta_0}\frac{\partial^2\psi_1}{\partial\zeta_0\partial\zeta_1}=\delta\left(\frac{\partial^2\psi_3}{\partial t_0^2}+2\frac{\partial^2\psi_2}{\partial t_0\partial t_1}+2\frac{\partial^2\psi_1}{\partial t_0\partial t_2}+\frac{\partial^2\psi_1}{\partial t_1^2}\right)-\delta\mu\left(\frac{\partial^4\psi_3}{\partial t_0^2\partial\zeta_0^2}+2\frac{\partial^4\psi_2}{\partial t_0^2\partial\zeta_0\partial\zeta_1}+2\frac{\partial^4\psi_1}{\partial t_0^2\partial\zeta_0\partial\zeta_2}+2\frac{\partial^4\psi_2}{\partial\zeta_0^2\partial t_0\partial t_1}+4\frac{\partial^4\psi_1}{\partial t_0\partial t_1\partial\zeta_0\partial\zeta_1}+2\frac{\partial^4\psi_1}{\partial\zeta_0^2\partial t_0\partial t_2}+\frac{\partial^4\psi_1}{\partial t_0^2\partial\zeta_1^2}+\frac{\partial^4\psi_1}{\partial t_1^2\partial\zeta_0^2}\right)+K_e\psi_3-K_e\mu\left(\frac{\partial^2\psi_3}{\partial\zeta_0^2}+2\frac{\partial^2\psi_2}{\partial\zeta_0\partial\zeta_1}+2\frac{\partial^2\psi_1}{\partial\zeta_0\partial\zeta_2}+\frac{\partial^2\psi_1}{\partial\zeta_1^2}\right)+D\left(\frac{\partial\psi_3}{\partial t_0}+\frac{\partial\psi_2}{\partial t_1}+\frac{\partial\psi_1}{\partial t_2}\right)-D\mu\left(\frac{\partial^3\psi_3}{\partial t_0\partial\zeta_0^2}+3\frac{\partial^3\psi_2}{\partial t_0\partial\zeta_0\partial\zeta_1}+2\frac{\partial^3\psi_1}{\partial t_0\partial\zeta_0\partial\zeta_2}+2\frac{\partial^3\psi_1}{\partial t_0\partial\zeta_0\partial\zeta_3}+\frac{\partial^3\psi_1}{\partial t_0\partial\zeta_1^2}+\frac{\partial^3\psi_2}{\partial t_1\partial\zeta_0^2}+3\frac{\partial^3\psi_1}{\partial t_1\partial\zeta_0\partial\zeta_1}+\frac{\partial^3\psi_1}{\partial t_2\partial\zeta_0^2}\right) \tag{35}$$

where the slow and fast variables both affect ψ_1.

3.1. The Field Equations Solution

We shall solve the field equations governing different terms in the perturbation expansion of varying order in this section.

3.1.1. The O(ε)-order equation's solution:

The linear version of the differential equation in Equation (33) can be used to provide the following solution:

$$\psi_1=\varphi e^{i\theta}+c.c. \tag{36}$$

where the field equations' solution will yield the unknown complex amplitude φ, the phasor θ is defined by $\theta=\omega t_0-k\zeta_0$. The pair ($\omega$, k) here

represents the wave number and the angular frequency that satisfies the dispersion relation;

$$\mathcal{D}(\omega,k)=k^2-\delta\omega^2(1+\mu k^2)+K_e(1+\mu k^2)+i\omega D(1+\mu k^2)=0 \quad (37)$$

Here, $\varphi(\zeta_1,\zeta_2,...;t_1,t_2,...)$ is unknown function whose governing equations will be discovered later.

3.1.2. The O(ε^2)-order equation's solution:

Eq. (36) can be introduced into Eq. (34) to solve the *O(ε^2)*-order problem (34) and obtain

$$\frac{\partial^2\psi_2}{\partial\zeta_0^2}-\delta\frac{\partial^2\psi_2}{\partial t_0^2}-\delta\mu\frac{\partial^4\psi_2}{\partial t_0^2\partial\zeta_0^2}=\left\{2ik\left[1-\delta\mu\omega^2+\mu(K_e+i\omega D)\right]\frac{\partial\varphi}{\partial\zeta_1}+ i\left[2\delta\omega(1+\mu k^2)-iD\right]\frac{\partial\varphi}{\partial t_1}\right\}e^{i\theta}-2ik^3\varphi^2e^{2i\theta}+c.c. \quad (38)$$

According to the form of Eq. (38) we should look for the following kind of solution for ψ_2

$$\psi_2=\psi_2^{(1)}e^{i\theta}+\psi_2^{(2)}e^{2i\theta}+...+c.c. \quad (39)$$

Here $\psi_2^{(1)},\psi_2^{(2)}...$ are a few slow variable functions. Equation (38) yields the following equations when these solutions are entered:

$$\left[k^2-\delta\omega^2(1+\mu k^2)+K_e(1+\mu k^2)+i\omega D(1+\mu k^2)\right]\psi_2^{(1)}+ 2ik\left[1-\delta\mu\omega^2+\mu(K_e+i\omega D)\right]\frac{\partial\varphi}{\partial\zeta_1}+i\left[2\delta\omega(1+\mu k^2)-iD\right]\frac{\partial\varphi}{\partial t_1}=0 \quad (40)$$

$$\frac{2}{3}\left[4k^2-4\delta\omega^2(1+4\mu k^2)+K_e(1+4\mu k^2)+i\omega D(1+4\mu k^2)\right]\psi_2^{(2)}-2ik^3\varphi^2=0 \quad (41)$$

In this case, the coefficient of $\psi_2^{(1)}$ in Eq. (40) represents the dispersion relation, and it needs to be zero. Using the dispersion relation we discover;

$$2k\left[1-\delta\mu\omega^2+\mu(K_e-i\omega D)\right]\frac{\partial\varphi}{\partial\zeta_1}+\left[2\delta\omega(1+\mu k^2)-iD(1+\mu k^2)\right]\frac{\partial\varphi}{\partial t_1}=0 \tag{42}$$

In order for φ to have a non-zero solution and satisfy Eq. (40), it must look like this form:

$$\varphi=\varphi(\xi,\zeta_2,...;t_2,...),\qquad \xi=\zeta_1-\lambda t_1 \tag{43}$$

Here, λ is group velocity, is defined by

$$\lambda=\frac{2k\left[1-\delta\mu\omega^2+\mu(K_e-i\omega D)\right]}{(1+\mu k^2)\left[2\delta\omega-iD\right]} \tag{44}$$

The higher-order expansion of the field quantities yields the governing equation of the function $\psi_2^{(2)}$. Solving Eq. (41) for the α = 2 mode yields

$$\psi_2^{(2)}=\frac{3ik^3}{4k^2+(1+4\mu k^2)\left[-4\delta\omega^2+K_e+2i\omega D\right]}\varphi^2=\frac{3ik^3}{\mathcal{D}(2k,2\omega)}\varphi^2 \tag{45}$$

where $\mathcal{D}(lk,l\omega)\neq 0$ for l=2,3,…

3.1.3. The O(ε³)-order equation's solution:

To complete the solution, we require the equation regulating $\psi_3^{(1)}$. The solution for this order can be expressed using the phasor as

$$\psi_3=\sum_{\alpha=1}^{3}\psi_3^{(\alpha)}e^{i\alpha\theta}+...+c.c. \tag{46}$$

By including Equations (39) and (46) into Equation (35), we have

$$\left[k^2-\delta\omega^2(1+\mu k^2)+K_e(1+\mu k^2)+i\omega D(1+\mu k^2)\right]\psi_3^{(1)}=2ik\left[1-\delta\mu\omega^2+\mu(K_e+i\omega D)\right]\frac{\partial\psi_2^{(1)}}{\partial\zeta_1}$$
$$+i\left[(1+\mu k^2)(2\delta\omega-iD)\right]\frac{\partial\psi_2^{(1)}}{\partial t_1}+i\left[(1+\mu k^2)(2\delta\omega-iD)\right]\frac{\partial\varphi}{\partial t_2}+2ik\left[1-\delta\mu\omega^2+\right.$$
$$\left.\mu(K_e+i\omega D)\right]\frac{\partial\varphi}{\partial\zeta_2}-\left[(1-\delta\mu\omega^2)+\mu(K_e+i\omega D)\right]\frac{\partial^2\varphi}{\partial\zeta_1^2}+\mu k(3iD-4\delta\omega)\frac{\partial\varphi}{\partial\zeta_1\partial t_1}+$$
$$\left[(1+\mu k^2)\left(\delta+\frac{iD}{2\omega}\right)\right]\frac{\partial^2\varphi}{\partial t_1^2}+\frac{3}{2}k^4|\varphi|^2\varphi+6ik^3\psi_2^{(2)}\varphi^* \tag{47}$$

Here, the dispersion relation's coefficient, $\psi_3^{(1)}$, needs to equal zero. Rearranging the Eq. (47) that we already have

$$\left[(1+\mu k^2)(2\delta\omega - iD)\right]\times\left[\left(\frac{\partial\psi_2^{(1)}}{\partial t_1}+\lambda\frac{\partial\psi_2^{(1)}}{\partial\zeta_1}\right)+i\left(\frac{\partial\varphi}{\partial t_2}+\lambda\frac{\partial\varphi}{\partial\zeta_2}\right)\right]-\left[1-\delta\mu\omega^2+\right.$$

$$\left.\mu(K_e+i\omega D)\right]\frac{\partial^2\varphi}{\partial\zeta_1^2}+\mu k(3iD-4\delta\omega)\frac{\partial\varphi}{\partial\zeta_1\partial t_1}+(1+\mu k^2)(\delta-iD)\frac{\partial^2\varphi}{\partial t_1^2}+\frac{3}{2}k^4|\varphi|^2\varphi$$

$$+6ik^3\psi_2^{(2)}\varphi^*=0 \tag{48}$$

In this instance, the dependence of φ on ξ has already been used. Furthermore, if we assume that t_1 and ζ_1 rely on $\psi_2^{(1)}$ via ξ, then the initial terms in Eq. (48) vanish.

The second term in Eq. (48) can be recast by including a new variable, τ: $t_2 = \tau$ $\zeta_2 = \varepsilon\xi + \lambda\tau$.

$$\frac{\partial\varphi}{\partial t_2}+\lambda\frac{\partial\varphi}{\partial\zeta_2}=\frac{1}{\varepsilon}\frac{\partial\varphi}{\partial\xi}-\frac{1}{\varepsilon}\frac{\partial\varphi}{\partial\xi}+\frac{\partial\varphi}{\partial\tau}=\frac{\partial\varphi}{\partial\tau} \tag{49}$$

We obtain the nonlinear Schrödinger equation by first introducing the expressions of $\psi_2^{(2)}$ into Eq. (48).

$$i\frac{\partial\varphi}{\partial\tau}+\frac{1}{2}\frac{\partial\lambda}{\partial k}\frac{\partial^2\varphi}{\partial\xi^2}+\frac{1}{(2\delta\omega-iD)(1+\mu k^2)}\times$$

$$\left\{\frac{3}{2}k^4|\varphi|^2\varphi+6ik^3\frac{3ik^3}{4k^2+(1+4\mu k^2)\left[-4\delta\omega^2+K_e+2i\omega D\right]}|\varphi|^2\varphi\right\}=0 \tag{50}$$

Rearranging Equation (50) yields the following:

$$i\frac{\partial\varphi}{\partial\tau}+\nu_1\frac{\partial^2\varphi}{\partial\xi^2}+\nu_2|\varphi|^2\varphi=0 \tag{51}$$

where the coefficients ν_1 and ν_2 are defined by

$$\nu_1=\frac{1}{2}\frac{\partial\lambda}{\partial k}=\frac{1}{2}\left\{\frac{[1-\delta\mu\omega^2+\mu(K_e+i\omega D)]-4\delta\omega k\mu\lambda-\delta(1+\mu k^2)\lambda^2}{(2\delta\omega-iD)(1+\mu k^2)}\right\} \tag{52}$$

$$\nu_2=\frac{k^4}{(2\delta\omega-iD)(1+\mu k^2)}\left\{\frac{3}{2}-\frac{18k^2}{\left[4k^2+(1+4\mu k^2)\right](-4\delta\omega^2+K_e+2i\omega D)}\right\} \tag{53}$$

When its real and imaginary components of ν_1 are separated, the following equations result:

$$\alpha_1 = \mathrm{Re}\,\nu_1 = \left\{ \frac{\delta\omega - \delta^2\lambda^2\omega - D^2\mu\omega/2 + \delta\mu K_e\omega - \delta^2k^2\lambda^2\mu\omega - 4\delta^2k\lambda\mu\omega^2 - \delta^2\mu\omega^3}{(1+\mu k^2)(D^2+4\delta^2\omega^2)} \right\} \tag{54}$$

$$\beta_1 = \mathrm{Im}\,\nu_1 = \frac{D}{2}\left\{ \frac{1 - \delta\lambda^2 + K_e\mu - \delta k^2\lambda^2\mu - 4\delta k\lambda\mu\omega + \delta\mu\omega^2}{(1+\mu k^2)(D^2+4\delta^2\omega^2)} \right\} \tag{55}$$

Similarly, by separating ν_2 into its real and imaginary parts

$$\alpha_2 = \mathrm{Re}\,\nu_2 = \frac{k^4}{(1+\mu k^2)(D^2+4\delta^2\omega^2)}\left\{ 3\delta\omega + \frac{144\delta^2k^2\omega^3 - 36D^2k^2\omega - 36\delta k^2\omega K_e}{(1+4\mu k^2+4k^2)[4D^2\omega^2 + (K_e - 4\delta\omega^2)^2]} \right\} \tag{56}$$

$$\beta_2 = \mathrm{Im}\,\nu_2 = \frac{Dk^4}{(1+\mu k^2)(D^2+4\delta^2\omega^2)}\left\{ \frac{3}{2} + \frac{144\delta k^2\omega^2 - 18k^2K_e}{(1+4\mu k^2+4k^2)[4D^2\omega^2 + (K_e - 4\delta\omega^2)^2]} \right\} \tag{57}$$

are obtained. In this case the NLS equation can be written in the following form;

$$i\frac{\partial\varphi}{\partial\tau} + (\alpha_1 + i\beta_1)\frac{\partial^2\varphi}{\partial\xi^2} + (\alpha_2 + i\beta_2)|\varphi|^2\varphi = 0 \tag{58}$$

The resulting equation is a nonlinear Schrödinger equation with complex coefficients. This is the first equation of its kind to be found in the literature.

REFERENCES

Iijima, S (1991) Helical microtubules of graphitic carbon, Nature 354 pp 56-58

Aifantis EC (1999), Strain gradient interpretation of size effects, Int J Fracture 95 pp 1-4

Eringen AC (1972) Nonlocal polar elastic continua Int J Eng Sci 10 pp 1-16

Eringen AC, Edelen DGB (1972) On nonlocal elasticity, Int J Eng Sci 10 pp 233-248

Ma HM, Gao XL, Reddy JN (2008) A microstructure-dependent Timoshenko beam model based on a modified couple stress theory, J Mech Phys Solids 56(12) pp3379-3391

Eringen AC (1983) On Differential Equations of Nonlocal Elasticity and Solutions of Screw Dislocation and Surface Waves, Princeton University, Technical Report no58

Murmu T, Pradhan SC (2009) Buckling analysis of a single-walled carbon nanotube embedded in an elastic medium based on nonlocal elasticity and Timoshenko beam theory and using DQM; Physica E 41 pp1232-1239

Aydogdu M (2012) Axial vibration analysis of nanorods (carbon nanotubes) embedded in an elastic medium using nonlocal theory, Mechanics Research Communications 43 pp34-40

Yaylı MO, Yanık F, Kandemir SY (2015) Longitudinal vibrationof nanorods embedded in an elastic medium with elastic restraints at both ends, Micro and Nano Letters 10 pp641–644

Lee H, Chang W-J (2009) Vibration analysis of a viscous-fluid-conveying single-walled carbon nanotube embedded in an elastic medium, Physica E-Low-dimensional System 41(4) pp 529-532

Soltani P, Dastjerdi HA, Farshidianfar A (2010) Thermo-mechanical vibration of a single-walled carbon nanotube embedded in a pasternak medium based on nonlocal elasticity theory, 18 th Annual International Conference on Mechanical Engineering-ISME2010, Craiova, Romania

Khosravi F, Hosseini SA, Tounsi A (2020) Forced axial vibration of a single-walled carbon nanotube embedded in elastic medium under various moving forces, Journal of Nano Research 63 pp112–133

Arda M, Aydogdu M (2015) Analysis of free torsional vibration in carbon nanotubes embedded in a viscoelastic medium, Advances In Science and Technology-Research Journal 9(26) pp33

Arda M, Aydogdu M (2019) Torsional dynamics of coaxial nanotubes with different lengths in viscoelastic medium, Microsystem Technologies 25(10) pp3943–3957

Natsuki T, Hayashi T, Endo M (2005) Wave propagation of carbon nanotubes embedded in an elastic medium, Journal of Applied Physics 97 044307

Wang Q, Zhou GY, Lin KC (2006) Scale effect on wave propagation of double-walled carbon nanotubes, International Journal of Solids and Structure 43(20) pp6071-6084

Lim CW,Yang YyF (2010) Wave propagation in carbon nanotubes: Nonlocal elasticity-induced stiffness and velocity enhancement effects, Journal of Mechanics of Materials and Structures 5(3) pp459-476

Ponnusamy P, Amuthalakshmi A (2014) Influence of Thermal and Longitudinal Magnetic Field on Vibration Response of a Fluid Conveying Double Walled Carbon Nanotube Embedded in an Elastic Medium, Journal of Computational and Theoretical Nanoscience 11(12) pp 2570-2577(8)

Srivastava S (2013) Propagation of Acoustic Wave inside the Carbon Nanotube: Comparative Study with Other Hexagonal Material, Open Journal of Acoustics 03(03) pp53-61

Tang Y, Liu Y, Zhao D (2016) Viscoelastic wave propagation in the viscoelastic single walled carbon nanotubes based on nonlocal strain gradient theory, Physica E: Low-dimensional Systems and Nanostuctures 84 pp 202-208

Zhen Y-X (2017) Wave propagation in fluid-conveying viscoelastic single-walled carbon nanotubes with surface and nonlocal effects, Physica E: Low-dimensional Systems and Nanostuctures 86 pp 275-279

Guo H, Shang F, Li C (2021) Transverse wave propagation in viscoelastic single-walled carbon nanotubes with surface effect based on nonlocal second-order strain gradient elasticity theory Microsystem Technologies 27(9) pp 1-10

Boyina K, Piska R 2023 Wave propagation analysis in viscoelastic Timoshenko nanobeams under surface and magnetic field effects based on nonlocal strain gradient theory Applied Mathematic and Computation 439 127580

Cho H, Yu MF, Vakakis AF, Bergman LA, McFarland DM (2010) Tunable broadband nonlinear nanomechanical resonator, Nano Letters 10(5) pp1793–1798

Yang J, Ke LL, Kitipornchai S (2010) Nonlinear free vibration of single-walled carbon nanotubes using nonlocal Timoshenko beam theory, Physica E: Low-dimensional Systems and Nanostuctures 42(5) pp 1727-1735

Ke L-L Wang Y-S, Wang Z-D (2012) Nonlinear vibration of the piezoelectric nanobeams based on the nonlocal theory, Composite Structures 94(6) pp 2038–2047

Sellitto A, Di Domenico M (2019) Nonlocal and nonlinear contributions to the thermal and elastic high-frequency wave propagations at nanoscale, Continuum Mechanics and Thermodynamics 31(2) 807-821

Sobamowo MG, Yinusa AA, Popoola OP, Waheed MA (2021) Nonlinear Vibration Analysis of Thermo-Magneto-Mechanical Piezoelectric Nanobeam Embedded in Multi-Layer Elastic Media based on Nonlocal Elasticity Theory, Journal of Materıals and Engıneerıng Structures 8 pp 373–402

Wang B, Deng Z, Ouyang H , Zhou J (2015) Wave propagation analysis in nonlinear curved single-walled carbon nanotubes based on nonlocal elasticity theory, Physica E: Low-dimensional Systems and Nanostuctures 66 pp 283-292

Norouzzadeh A, Ansari R, Rouhi H (2018) Nonlinear wave propagation analysis in Timoshenko nano-beams considering nonlocal and strain gradient effects, Meccanica 53(13) 53 pp 3415–3435

Gaygusuzoglu G, Akdal S (2020) Weakly nonlinear wave propagation in nanorods embedded in an elastic medium using nonlocal elasticity theory, Journal of the Brazilian Society of Mechanical Sciences and Engineering 42 pp 564

Gaygusuzoglu G, Aydogdu M, Gul, U (2018) Nonlinear wave modulation in nanorods using nonlocal elasticity theory, International Journal of Nonlinear Sciences and Simulation 19(7-8) pp 709-719

Malvern LE (1969) Introduction to the Mechanics of a Continuum Medium, Prentice Hall, Englwood Cliffs, New Jersey

Mousavi SM, Fariborz SJ (2012) Free vibration of a rod undergoing finite strain, *Journal of Physics, Conference Series* 382(1)

Aydogdu M (2009) Axial vibration of the nonaroads with the nonlocal continuum rod model, Physica E: Low-dimensional Systems and Nanostructures 41(5) pp 861-864

Jeffrey A and Kawahara T (1982) Asymptotic Methods in Nonlinear Wave Theory, Pitman, Boston

Jeffrey A 1989 Nonlinear Wave Motion, Longman, UK

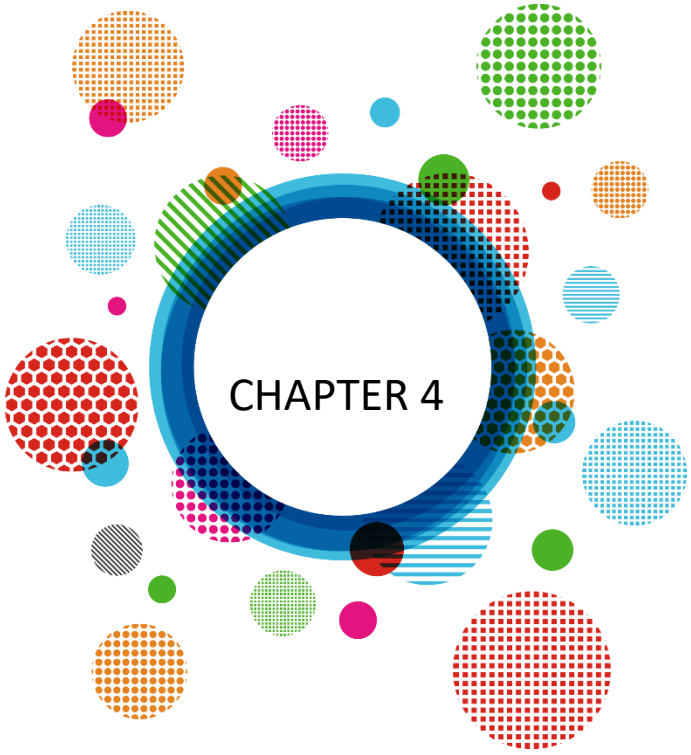

Vitamin, Mineral and Protein Fortification of Milk and Dairy Products

***Fatma Coşkun*[1]**

[1] Assoc. Prof. Dr. Tekirdağ Namık Kemal University, Faculty of Agriculture, Food Engineering Department, Tekirdağ, ORCID: 0000-0001-8889-363X

INTRODUCTION

Nutrition is a process consisting of stages such as the intake, digestion, absorption and elimination of useless parts of the nutrients necessary for sustaining life (Kutluay Merdol et al., 2013). Protein, water, fat, carbohydrate, 14 vitamins, 8 amino acids, 1 fatty acid and 22 mineral requirements should be met with daily foods (Yurttagül, 1995). Health problems caused by malnutrition are inefficiency in daily life due to inadequate nutritional intake, difficulty in learning and understanding, work accidents due to distraction, prolonged treatment of diseases and frequent illnesses, and retarded growth and development (Seidell, 1998).

Nutrient fortification is a public health strategy aimed at preventing or alleviating nutritional deficiencies within a population, particularly among specific groups. This process involves restoring nutrients that are naturally found in a food's composition but are diminished during processing. In contrast, food enrichment refers to adding a nutrient that was not originally present in the food. (Kahyaoğlu & Demirci 2019). Food fortification started to gain momentum in the 1940s and was approved by the US Food and Drug Administration (FDA) in 1980. Fortification practices are under FDA supervision. The fortification application should not exceed the Generally Recognized as Safe (GRAS) amount (Ilgaz et al., 2020; Aksu & Özbey, 2021).

The FDA has associated the Food Fortification Policy, published in 1980, with six basic principles (Dwyer et al., 2015).

- The intake of the food consumed without fortification is considerably lower than the recommended amount: It emphasizes that fortification is necessary, i.e. when a particular nutrient is inadequately supplied in a particular segment of the population or in the population as a whole.

- The fortified food makes a significant contribution to the population's nutrient intake: It is important that the food to be fortified is a food commonly consumed by the target population and that the added nutrient makes a significant contribution to their daily intake.

- The nutrient added by fortification does not disrupt the homeostasis of essential nutrients: The added nutrient should not adversely affect the balance of other essential nutrients in the body and should not lead to excessive or unbalanced intakes.

- Stability of the added nutrient under appropriate storage and use conditions: It is important that the nutrient added to the food maintains its stability during storage, processing and preparation and maintains its effectiveness until it reaches the consumer.

- Physiological availability of the added nutrient from the food (bioavailability): The added nutrient must be easily absorbed by the human body from food and be in a usable form.

- Ensuring that potential toxic intake levels are not observed: It is essential that fortification levels are set to avoid excessive intake levels that could lead to toxic effects. This includes considering both the risk of over-intake of a single nutrient and cumulative intake from different sources (other fortified foods, supplements, etc.).

For successful fortification, nutrients with the highest propensity to be consumed by the population should be selected, consumed in regular and consistent amounts, allow for centralized production, be relatively easy to add using low-cost technology, and be evenly distributed across product groups (Maurya, Bashir & Aggarwal, 2020). Food fortification strategies can increase macro- and micronutrient intake without increasing consumption portions (Cave, Abbey & Capra, 2020; Aksu & Özbey, 2021).

The first examples of food fortification started in 400 BC when Melanpus, King of Pars, ordered the addition of iron to the wine drunk by his soldiers (Panda, Mishra & Mohapatra, 2011). Later, in 1831, French physician Boussingault added iodine to salt and contributed to the prevention of goiter disease. The enrichment of salt with iodine started in Switzerland and the USA in the 1920s. Following World War I and II, food fortification practices were initiated by adding iodine to salt, vitamins A and D to margarine, vitamins D, B_1 and B_2 to milk, and iron to flour and bread to prevent nutritional deficiencies during the war (Dwyer et al., 2015).

In order to perform an effective fortification, fortification should be technically feasible, there should be no negative interaction between the food and the food to be added, it should not adversely affect the texture of the food, the newly formed food should have a positive effect on the consumer, and there should be no tendency to overconsume the food as a result of fortification (Kahraman, 2011).

Food fortification methods are applications of adding nutrients to foods in order to eliminate vitamin and mineral deficiencies. The international approval and standardization of these methods was achieved at the International Congress on Nutrition held in 1992 in cooperation with FAO (Food and Agriculture Organization of the United Nations) and WHO (World Health Organization). At this congress, 159 countries reached a consensus on the elimination of vitamin and mineral deficiencies (Allen, 2006)

There are three types of food fortification.

Bulk fortification; The addition of more than one vitamin and mineral to foods that are highly consumed by the community, such as milk and dairy products, is called bulk fortification,

Targeted Fortification; The society consists of various groups of people such as children, young, old, pregnant. The fortification of foods that these different groups can consume is called targeted fortification. An example is the addition of vitamins or minerals to products consumed by children,

Market-oriented fortification; The aim here is to increase the nutritional value of the food by adding specific vitamins or minerals to packaged products and it is an application made at the initiative of food companies in developed countries and it may cause excessive intake of some nutrients (Dary & Hurrell, 2006).

Food fortification has many advantages. It is acceptable to societies and does not require societies to change their dietary habits. Food fortification is done in such a way that the sensory properties of the food to be consumed, such as taste and smell, are not altered. Food fortification can be implemented quickly and its benefits are quickly seen, it is safe and it is a cost-effective method applied for communities at risk for micronutrient deficiencies (World Health Organization & Food and Agriculture Organization of the United Nations, 2006; Demircioğlu & Aslan, 2023).

FORTIFICATION OF MILK AND DAIRY PRODUCTS

VITAMIN FORTIFICATION

Vitamin D Fortification

Vitamin D added to milk was an early application of nutrient enrichment and fortification, beginning around the 1930s (Food and Agriculture Organization & World Health Organization, 1995). Several developed nations, including the USA, Australia, the UK, and Canada, have since mandated the fortification of foods like milk and yogurt with vitamin D (Gıda, Tarım ve Hayvancılık Bakanlığı, 2013; Kahyaoğlu & Demirci, 2019). Specifically, Canada and the United States introduced vitamin D to milk in the 1930s to combat rickets in children, a condition caused by vitamin D deficiency (Lindsay, Benoist, Dary & Hurrell, 2006; Ritu & Gupta, 2014). While this supplementation significantly improved vitamin D status in these regions, widespread deficiency persists (Ritu & Gupta, 2014), with an estimated one billion people globally affected by varying degrees of vitamin D insufficiency (Nikooyeh et al., 2011; Küçük & Yıbar, 2018).

According to the Institute of Medicine (2011), the recommended daily intake (RDA) for vitamin D ranges from 600 to 800 IU per day, depending on age and

under the assumption of no vitamin D synthesis from sun exposure. The estimated average requirement (EAR) is set at 400 IU daily, while the tolerable upper intake level (UL) for individuals of all ages is 4,000 IU per day (National Institutes of Health, 2011). Vitamin D deficiency is particularly common among individuals with limited sun exposure. This includes those living at higher latitudes, individuals who routinely avoid UV-B exposure, older adults, and people with darker skin pigmentation (Calvo, Whiting & Barton, 2004). Vitamin D daily intake recommendation was reported as 15 µg/day in the TBSA 2019 report (T.C. Sağlık Bakanlığı Halk Sağlığı Genel Müdürlüğü. 2019). The Turkish Society of Endocrinology and Metabolism (TEMD) recommends a daily intake of 1000 mg calcium and 800-1500 IU vitamin D for women aged 18-50 years and 600-800 IU vitamin D for healthy adult men to prevent osteoporosis in young women (Türk Endokrinoloji ve Metabolizma Derneği. 2020). Exposure to sunlight to increase vitamin D levels is recognized as a public health approach, but there are concerns about this (Cashman, 2020). Vitamin D deficiency can be seen even in areas with intense sunshine throughout the year (Maurya, Bashir & Aggarwal, 2020; Aksu & Özbey, 2021).

In the United States, it's standard practice for all liquid pasteurized milk to be fortified with a minimum of 400 IU of vitamin D. This involves adding vitamin concentrates to the milk before pasteurization (Public Health Service/U.S. Food and Drug Administration, 2015). The U.S. Food and Drug Administration (FDA) requires that the amount of vitamins in fortified liquid products falls within 100% to 150% of the declared values on the label (Nichols, 1992). For vitamin D, this corresponds to a concentration between 400 and 600 IU per quart (Public Health Service/U.S. Food and Drug Administration, 2015).

Typically, synthetic vitamin D_3 is used for fortifying liquid milk in the U.S. This synthetic form is produced by irradiating animal fat, commonly derived from lanolin, the waxy substance found on sheepskin (Budvari, 1996; Holick, 1999; S. Smith, personal communication, 2016; Yeh, Barbano & Drake, 2017).

A comparison of vitamins added to milk and milk products across various countries can be found in Table 1 (Titcomb & Tanumihardjo, 2019; Ekşi & Karadeniz, 1996; Kahyaoğlu & Demirci, 2019; Demircioğlu & Aslan, 2023).

Table 1. Vitamins added to milk and milk products in different countries.

Countries	Milk and Dairy Products	Vitamins
Philippines	Milk	Vitamins A and D
Australia	Margarine	Vitamins A and D
USA	Milk	Vitamins A and D
UK	Milk and margarine	Vitamins A and D
Canada	Margarine	Vitamins A and D
Canada	Milk	Vitamin D
Sweden	Margarine	Vitamins A and D
Turkey	Margarine	Vitamins A and D
Taiwan	Margarine	Vitamin A and D
Morocco	Margarine	Vitamins A, D and E
Germany	Dairy products and margarine	Vitamins A, B, C, D, E

Information on the fortification of milk and milk products with vitamin D in the USA is shown in the Table 2. (U.S. Food and Drug Administration, n.d.).

Tablo 2. Fortification of milk and milk products with vitamin D in the USA

Foods	Fortification status	Maximal level allowed**	Usual fortification level
Liquid milk***, acidified milk, cultured milk, condensed milk, dry whole milk	Optional	42 IU·(100 gr)$^{-1}$	400 IU·quart or 946 mL^{-1}
Non-fat dry milk, evaporated milk, dry whole milk enriched with A and D	Required	42 IU·(100 gr)$^{-1}$	400 IU·quart or 946 mL^{-1}
Yogurt, low-fat yogurt, fat-free yogurt	Optional	89 IU·(100 gr)$^{-1}$	40–80 IU·RACC^{-1} *
Margarine	Optional	331 IU·(100 gr)$^{-1}$	40–140 IU·RACC^{-1} *

*RACC, conventionally consumed reference amount or US Food and Drug Administration (FDA) regulatory serving size.
**Maximum level of vitamin D that may be added for the food category in accordance with 21 CFR 184.1(b)(2).
*** Fluid milk is the only dairy product that is routinely fortified.

Under the Canadian Food and Drug Regulations, milk and margarine are designated as foods that must be fortified with vitamin D. Specifically, liquid milk is mandated to include sufficient added vitamin D so that a typical daily intake provides between 300 IU and 400 IU of the vitamin (Health Canada, n.d. -a). In Canada, fluid milk labels indicate that a 250 mL serving provides 44% of the recommended daily intake, which is based on a standard of 400 IU. Additional dairy products that require vitamin D fortification include evaporated milk, powdered milk, and goat milk. Margarine sold in Canada is also enriched with vitamin D, containing 530 IU per 100 grams (Health Canada, n.d.-b). Both Canadian and U.S. regulations allow the use of vitamin D-enriched milk in food

production. However, milk used for industrial purposes—such as in the production of yogurt, cheese, ice cream, or for cooking—is typically not fortified, and there is no obligation to add vitamin D to the final processed foods (Calvo et al., 2004).

Because whole milk naturally contains only small amounts of vitamin D—typically between 0.34 and 0.84 IU per gram of fat (McBean & Speckmann, 1988)—milk that has not been fortified is generally not regarded as a meaningful dietary source of this nutrient. Consequently, removing fat does not diminish milk's nutritional value with respect to vitamin D, making fortification with the vitamin optional for all milk types. When vitamin D is added, it should be at a rate of 400 IU per quart (Public Health Service/U.S. Food and Drug Administration, 2015). The majority of fluid milk in the United States is fortified with vitamin D due to its critical role in human health (Holick, Shao, Liu & Chen, 1992; McBean & Speckmann, 1988; Miller, Jarvis & McBean, 2006). Although fortifying milk and yogurt with vitamin D is not required by regulation, dairy products like cheese and other cultured items that are not fortified are generally poor sources of this vitamin. When vitamin D is added, its concentration should be at least 400 IU per quart, with an acceptable range between 400 and 600 IU per quart (Public Health Service/U.S. Food and Drug Administration, 2015).

Vitamins may be added to milk at various stages of processing, including directly into the pasteurization vat, into the balance tank of the HTST (High-Temperature Short-Time) system, or via continuous dosing into the pipeline after the standardization process. In most cases, vitamin enrichment is performed following cream separation and fat standardization but before pasteurization. After pasteurization, the milk is homogenized to ensure even distribution of the added vitamins (Public Health Service/U.S. Food and Drug Administration, 2015; Yeh et al., 2017).

The amounts of vitamin D contained in yogurts with different fat ratios in different countries are shown in the Table 3 (Küçük & Yıbar (2018).

Tablo 3.The amounts of vitamin D contained in yogurts with different fat ratios in different countries.

Country	Yogurt, plain (100 g)	Vitamin D (µg)	Reference
Germany	10% fat	0.20	Max Rubner-Institut. 2018
	3.5% fat	0.06	
	1.5%fat	0.03	
USA	Full fat	0.1	USDA, 2018
	Low fat	0.0	
	Fat free	0.0	
Denmark	Full fat	0.1	Technical University of Denmark – National Food Institute, 2018
	Low fat (1.5%)	0.05	
	Reduced fat (0.1%)	0.04	
France	Average	0.0-0.8	ANSES, 2018
Turkey	Full fat (≥ 3.8%)	1.1	TürKomp, 2018
	Half fat (> 2% milk fat ≥1.5%)	0.7	

According to the Turkish Food Codex Regulation, both cholecalciferol (vitamin D_3) and ergocalciferol (vitamin D_2) are approved forms of vitamin D that may be added to foods (Republic of Turkey Ministry of Food, Agriculture and Livestock, 2017). However, evidence from studies—including a meta-analysis by Tripkovic et al. (2012)—indicates that vitamin D_3 is more effective than D_2 in increasing serum 25-hydroxyvitamin D [25(OH)D] levels, suggesting that D_3 may be the more suitable option for dietary supplementation.

Studies investigating the stability of vitamin D in fortified milk and dairy products indicate that vitamin D remains unaffected by the heat treatments involved in milk pasteurization and sterilization, and it demonstrates stability during storage (Crevier, Belanger, Vuillemard & St Gelais, 2017). Furthermore, Kazmi, Vieth and Rousseau (2007) and Hanson and Metzger (2010) found that both water-dispersible and fat-dispersible forms of vitamin D_3 have demonstrated stability in yogurt, indicating their effectiveness and suitability for use in fortification.

Jafari et al. (2016) found that both water-dispersible and fat-dispersible forms of vitamin D remained stable during the entire shelf life of yogurt stored in opaque packaging. However, the water-dispersible form showed instability when packaged in transparent containers, exhibiting a significant decrease in vitamin D content at 1, 2, and 3 weeks after storage compared to day 0. In contrast, the fat-dispersible form remained stable for only one week in transparent containers, experiencing a significant decline after two and three weeks (Küçük & Yıbar, 2018).

Whole milk with 3.9% fat (w/w), unfortified, pasteurized, and homogenized, was sourced from Parmalat Canada (London, Ontario, Canada). Two different forms of vitamin D_3 were utilized: crystalline cholecalciferol (Sigma Chemicals, St. Louis, MO, USA) and an emulsified preparation known as Vitex D, containing 205,000 IU·mL^{-1} (approximately 5125 μg·mL^{-1}). To prepare a 400,000 IU·mL^{-1} vitamin D_3 stock solution, 100 mg of crystalline vitamin D_3 was dissolved in 10 mL of 95% ethanol. From this solution, 1 mL was combined with 3 mL of melted anhydrous butterfat (supplied by Gay Lea Foods, Guelph, Ontario, Canada), resulting in a mixture with a concentration of 100,000 IU·mL^{-1}. This fortified blend was then incorporated into the milk designated for processing into specific dairy products, in accordance with the required dosage. The results demonstrated that vitamin D_3-fortified Cheddar-style cheese, yogurt, and ice cream could effectively serve as delivery vehicles for the vitamin. Importantly, no degradation of vitamin D_3 was detected in yogurt or ice cream during processing or throughout their expected shelf life. However, some vitamin loss occurred during the production of Cheddar-type cheese, with approximately 7–9% of the vitamin being lost to the whey. Over a three-month storage period, degradation of vitamin D_3 was observed in cheese, with the emulsified form showing better stability compared to the crystalline form. In contrast, both forms remained stable in the experimental yogurt and ice cream samples throughout their anticipated shelf life. These processed dairy products thus appear suitable for vitamin D_3 fortification. It is crucial to consider this degradation when assessing fortification levels for Cheddar cheese, especially given its typically longer ripening periods, which can extend beyond four years in some instances (Kazmi et al., 2007).

There are a few foods that contain sufficient amounts of vitamin D. Fish species such as sardines, trout, salmon and mackerel, which are high in fat, contain sufficient amounts of vitamin D. Others are meat, milk and eggs (Nowson & Margerison, 2002). Vitamin D is a highly heat-stable vitamin and is used to fortify milk, breakfast cereals, yogurt, cheese and margarine (Moore, Murphy, Keast & Holick, 2004). Fortification of margarine and butter is mandatory. Margarine is also fortified with vitamin A. Children consumed 27 g of vitamin A fortified margarine daily for 6 months and their serum retinol levels were 16% higher than those who did not (Allen, 2006).

The addition of encapsulated vitamin D3 to nonfat yogurt using coacervation of recombined casein micelles was investigated by Levinson and colleagues in 2016. Encapsulated vitamin D proved more resilient to UV radiation, heat treatment, and degradation during three weeks of storage at 4 °C than its unprotected form. This encapsulated version also demonstrated enhanced in vivo bioavailability, suggesting its utility as a practical and efficient delivery system. Moreover, in nonfat yogurt, which is a pseudoplastic substance (exhibiting

decreased viscosity with increased shear), the incorporation of casein led to a desirable increase in viscosity (Levinson, Ish-Shalom, Segal, & Livney, 2016; Adinepour, Pouramin, Rashidinejad & Jafari, 2022).

Another study explored the fortification of ice cream with encapsulated vitamin D using an emulsification technique that involved different milk proteins such as whey protein isolate, skim milk powder, and sodium caseinate. Among these, sodium caseinate proved to be the most effective, producing smaller particle sizes and resulting in a lower creaming index during storage. This effect is explained by the fact that smaller particles improve emulsion stability and minimize cream separation. The encapsulated vitamin D remained stable in the ice cream throughout a 56-day storage period at -20 °C (Tipchuwong, Chatraporn, Ngamchuachit & Tansawat, 2017; Adinepour et al., 2022).

A study conducted a comprehensive search of the PubMed database to investigate the effects of vitamin D-fortified liquid dairy products—including regular milk and fermented variants—on vitamin D intake and serum or plasma 25-hydroxyvitamin D [25(OH)D] concentrations. This review targeted observational research published between 1993 and 2017. The findings consistently demonstrated a positive association between the consumption of vitamin D-enriched milk and improved 25(OH)D levels across various demographic groups. In countries with well-established national vitamin D fortification programs that include a broad range of liquid dairy products—such as Finland, Canada, and the United States—dairy products contributed substantially to overall vitamin D intake, accounting for approximately 28% to 63%. In contrast, countries lacking such a policy, or where supplementation was limited to only a few dairy items (like Sweden and Norway), showed a much lower or negligible contribution from these products (Itkonen, Erkkola & Lamberg-Allardt, 2018)

Systematic vitamin D fortification of certain dairy products, whether mandatory or voluntary, is observed in only a handful of countries: Finland, Norway, Sweden, Canada, and the United States of America (Table 1) (Itkonen et al., 2018). In Finland, the current suggested fortification level for all fluid milks, excluding some organic varieties, is 1 µ /100 g, though products with a concentration of 2 µg·(100 gr)$^{-1}$ are also on the market (National Nutrition Council, 2010; Ministry of Agriculture and Forestry of Finland, 2016). While this fortification is voluntary, all producers consistently adhere to these guidelines. Norway recommends vitamin D fortification for only one type of milk, at a concentration of 0.4 µg·(100 gr)$^{-1}$ (Nasjonalt råd for ernæring, 2006). Sweden recently increased the fortification level for fluid milk products to 1 µg per 100 grams and made vitamin D fortification mandatory for all fluid milks containing less than 3% fat (Livsmedelsverket, 1983; Livsmedelsverket, 2018). Similarly,

Health Canada has recommended raising the required vitamin D content in fluid milks from about 1 μg per 100 grams to 2 μg per 100 grams, citing concerns over inadequate vitamin D intake among the population (Department of Health, 2018). In the United States, although federal regulations permit fortification of fluid milks at approximately 1 μg per 100 grams, it is not a nationwide mandate; however, most states enforce fortification requirements (Calvo & Whiting, 2013). In countries like the United Kingdom, Ireland, Spain, and Australia, vitamin D fortification is not systematically applied, yet various fortified dairy products remain available on the market (Black, Walton, Flynn, & Kiely, 2014; Cribb, Northstone, Hopkins & Emmett, 2015; Hennessy, Browne, Kiely, Walton & Flynn, 2017; González-Rodríguez, Estaire, Peñas-Ruiz, Ortega & UCM Research Group VALORNUT, 2013; Jayaratne, Hughes, Ibiebele, Van den Akker & Van der Pols, 2013).

New starch-based nanoparticles have been created to improve the retention of Vitamin D3. These novel nanocarriers, loaded with VD3, achieved encapsulation efficiencies between 37.06% and 78.11%. Sensory analysis of fortified milk containing these nanoparticles revealed no significant difference compared to control milk samples. This indicates that the developed nanocarriers successfully masked any off-flavors and resolved the issue of vitamin D3's poor solubility. The findings suggest that these nanoparticles hold promise for use in food fortification, potentially enhancing the bioavailability of vitamin D3 and other hydrophobic compounds (Hasanvand, Fathi, Bassiri, Javanmard & Abbaszadeh, 2015).

The countries that have implemented a policy of vitamin D fortification in liquid dairy products are shown in Table 4.

Table 4. Countries with a policy of vitamin D fortification in liquid dairy products

Country	Vitamin D fortified dairy products	Type of fortification	Amount of vitamin D added	New recommended amounts of vitamin D
Finland	Liquid dairy products (milk, yogurt, sour milk)*	Optional	1 μg·(100 gr)$^{-1}$	na****
Norway	Extra low-fat milk (also lactose-free)	Optional	0.4 μg·(100 gr)$^{-1}$	na
Sweden	Low-fat milk (maximum 1.5% fat)	Mandatory	0.38-0.50 μg·(100 gr)$^{-1}$	For milk with less than 3% fat content 0.95-1.10 μg·(100 gr)$^{-1}$ For fermented milk with less than 3% fat content 0.75-1.10 μg·(100 gr)$^{-1}$
Canada	Milk	Mandatory	0.825-1.125 μg·(100 gr)$^{-1}$	2 μg·(100 gr)$^{-1}$
USA	Liquid milk (also acidified milk and cultured milk), yogurt	Optional**	For milk 1.05 μg·(100 gr)$^{-1}$ For yogurt 2.225 μg·(100 gr)$^{-1}$***	na

* For organic dairy products, it is mandatory to add 1 μ /100 g vitamin D to homogenized skim milk (This is not allowed for other organic dairy products)
** For dairy products, only evaporated and skimmed dry milk is mandatorily fortified.
*** Maximum amount
****na: Not applicable

Vitamin A Fortification

Vitamin A is necessary for epidemiological tissue health and general growth. It is effective in reproduction and bone growth. When it is deficient, resistance to diseases decreases. Another function of vitamin A is related to vision. It allows us to see at night by binding to proteins in the retina. Vitamin A or retinol deficiency causes night blindness. The adequacy of vitamin A intake decreases with age. Vitamin A deficiency is common in developed countries. They have limited access to animal-based food sources and foods containing vitamin A (Türker & Yüksel, 2019). The average daily vitamin A intake is 900μg for adult men, 700 μg for women, 800 μg during pregnancy and 1120-1300 μg during breastfeeding (Institute of Medicine, 2001).

Vitamin A supplementation is crucial for low-fat and skim milk products because, unlike whole milk which naturally contains vitamin A palmitate, most of this fat-soluble vitamin is lost along with the fat during processing. Therefore, fortifying these dairy products has become a common strategy to prevent vitamin A deficiency (Parish & Richter, 1979).

Regulations mandate that low-fat and skim milk must be enriched with at least 2000 International Units (IU) of vitamin A, whereas fortification of whole milk remains optional (Public Health Service/U.S. Food and Drug Administration, 2015). It is also noteworthy that vitamin A is sensitive to light exposure and degrades rapidly, with this degradation occurring more quickly in skim milk compared to milk containing fat (Senyk & Shipe, 1981; Whited, Hammond, Chapman & Boor, 2002).

The FDA requires that vitamin levels in fortified liquid products range between 100% and 150% of the amounts stated on the label (Nichols, 1992). For vitamin A, this corresponds to a concentration of 2000 to 3000 IU per quart (Public Health Service/U.S. Food and Drug Administration, 2015). Consequently, vitamin A must be added to skim milk in sufficient quantities to replace what is lost during fat removal.

Since vitamin A is primarily found in the fat fraction of milk—approximately 37.7 IU per gram of fat—unfortified whole milk naturally contains significant amounts of this vitamin (McBean & Speckmann, 1988). However, when fat is removed to produce low-fat and skim milk, the vitamin A content decreases accordingly. With the growing popularity of low-fat and skim milk products in the U.S., concerns arose about this reduction in vitamin A. The 1978 Pasteurized Milk Ordinance (PMO) addressed this by mandating that low-fat and skim milks be fortified with vitamin A to match the nutritional value of whole milk, requiring at least 2000 IU per liter. Fortification of whole milk is optional, but if applied, vitamin A levels must also meet this minimum concentration. In the U.S., synthetic retinyl palmitate is the standard fortificant used for vitamin A enrichment in liquid milk (Public Health Service, 1965). This compound is synthesized by reacting vitamin A acetate with methyl palmitate in the presence of sodium hydroxide (S. Smith, personal communication, 2016; Yeh et al., 2017).

Vitamin E Fortification

Vitamin E protects the general health of the cell and increases the durability of DNA molecules. It reduces the oxygen needs of heart and muscle cells and allows them to work more comfortably. Red blood cells in the blood begin to die in a short time due to vitamin E deficiency. As a result of its insufficiency, it causes the transmission of nerve impulses to weaken and muscle weakness. Vitamin E should be taken at a dose of 400 IU per day (Türker & Yüksel, 2019).

Vitamin E has the ability to form complexes with milk proteins through hydrophobic interactions, which may negatively impact its bioavailability and antioxidant effectiveness, as well as cause undesirable modifications in the final dairy product (Tan et al., 2018). For example, studies examining yogurt fortified with vitamin E have reported a decrease in the yogurt's gel strength, indicating an adverse effect on its textural properties (Dai, Corke & Shah, 2016; Tan et al., 2018). This is likely due to vitamin E complexing with yogurt proteins, which can disrupt the compound balance and decrease the proteins' water absorption capacity. This, in turn, may result in reduced water retention capacity and increased syneresis (Dai et al., 2016; Tan et al., 2018). In contrast, several studies have reported no interaction between **c**arotenoids and tocopherols when added to milk and its components (de Campo et al., 2019; Ningtyas, Bhandari, Bansal & Prakash, 2019; Šeregelj et al., 2021; Adinepour et al., 2022).

Vitamin K Fortification

Epidemiological research has indicated that higher intake of dietary menaquinones (vitamin K2, MK-n) is linked to reduced coronary artery calcification and a lower risk of coronary heart disease, highlighting the possible importance of vitamin K for cardiovascular health (Knapen et al., 2015).

Knapen et al. (2015) investigated the effects of drinking yogurt enriched with 28 µg menaquinone 7 (MK-7 = vitamin K2-7) twice daily for twelve weeks on coronary heart health in 60 healthy women and men with an average age of 56. n-3 polyunsaturated fatty acids (PUFAs), vitamins C and D, Ca and Mg were also added to the MK-7 enriched drinking yogurt to provide 15% of the daily recommended intake. As a result of the study, it was determined that the intake of enriched yogurt increased the vitamin K content in the body.

Folic Acid Fortification

Folic acid plays a role in DNA and RNA synthesis. It provides growth with its role in cell division, ensures the development of the baby's nervous system in the womb, and is involved in the production of white blood cells. It reduces the risk of heart attack, stroke, and dementia. It has also been stated that it reduces the substance that causes atherosclerosis. The daily requirement for adults is 400 micrograms. The need increases from childhood to adulthood (Türker & Yüksel, 2019).

Folate is a water-soluble B vitamin consisting of formyl-tetrahydropteroylglutamates. It is also known as vitamin B_9 (Hill, 1997). The synthetic form of folate is called folic acid (pteroylmonoglutamic acid) and this synthetic form is used in food supplements or enriched cereal products. 120 $\mu g \cdot day^{-1}$ should be taken at the age of 2-3 years, increasing with age to 330 $\mu g \cdot day^{-1}$ for those over 70 years of age. Folate, which is produced in large

quantities by bacteria, is in the form of monaglutamate, which can be absorbed most rapidly. Folate production is mostly carried out by *Lactobacillus* and *Bifidobacterium*. It has been determined that the basic starter culture of yogurt, *Streptococcus thermophilus*, and *Lactobacillus delbrueckii* ssp. *bulgaricus* species have higher production amounts than other species. Another example of *Lactobacillus* bacteria that produce folate is the combination of *S. thermophilus* and *Bifidobacterium animalis*. With this combination, the production of 5 methylene tetrahydrofolate (5-MTHF) in yogurt increased 6-fold after 12 hours of fermentation (LeBlanc et al., 2011). The use of vitamin-producing microorganisms can be considered as a more natural alternative to synthetically produced and supplemented food enrichment. It is known that milk is a poor source of folic acid. However, it is a potential food for enrichment in folic acid through fermentation. In a study, it was determined that the highest folate-producing strain in the environment was *Lactobacillus amylovorius* CRL887. In the study, the folate value in yogurt reached 260 $\mu g \cdot L^{-1}$, which attracted attention as a natural enrichment of this yogurt in terms of folate (Laiño, Valle, Savoy de Giori & LeBlanc, 2014; Demirtaş, Kayahan & Gezmen Karadağ, 2021).

In a study focused on producing bio-yogurt using various probiotic bacteria, including *Lactobacillus acidophilus* LA-5, *Bifidobacterium lactis* BB-12, *Lactobacillus plantarum* 15HN, *Lactococcus lactis* 44Lac, and *Lactobacillus plantarum* LAT BY PL, it was observed that the folate content in yogurts containing *L. plantarum* 15HN reached its peak value on the 7th day. This highlights the ability of certain probiotic strains to produce folate within the yogurt matrix (Khalili, Rad, Khosroushahi, Khosravi & Jafarzadeh, 2019).

Vitamin C Fortification

Vitamin C contributes to increasing the body's resistance to microbes, keeping blood vessels strong, stabilizing vitamin E and folic acid, and transporting fatty acids (Türker & Yüksel, 2019).

Ascorbic acid (vitamin C) plays a vital role in animal iron metabolism (National Research Council, 1993). It promotes intestinal absorption of iron by converting ferric iron into the more soluble ferrous form, which is more efficiently absorbed (Monsen, 1988). Additionally, ascorbic acid aids in the release and reduction of ferric iron from ferritin via adenosine triphosphate (ATP) and facilitates its incorporation into tissue ferritin through iron-binding proteins such as apoferritin and transferrin (Lim, Kiesius, Li & Robinson, 2000). Despite these important functions, ascorbic acid is highly unstable and prone to degradation when exposed to heat, pH changes, oxygen, and UV light during processing. To overcome these limitations, microencapsulation methods have been explored. In one study, L-ascorbic acid and the water-soluble iron compound ferric ammonium sulfate were added to milk in both encapsulated (100

ppm) and unencapsulated (100 ppm) forms to evaluate the efficacy of ascorbic acid fortification in preventing iron-induced lipid oxidation over a 12-day storage period. As anticipated, the control group, without any additions, showed no change in the TBA (Thiobarbituric Acid) value until 8 days of storage, after which it increased slowly to 0.08 by day 12. Groups with iron but no L-ascorbic acid exhibited a proportionally increasing TBA value with storage time. Conversely, groups supplemented with L-ascorbic acid had significantly lower TBA values compared to those without it. The group treated with 100 ppm of unencapsulated iron experienced a significant rise in TBA values, increasing from 0.06 to 0.15 between day 0 and day 12. Although microencapsulated iron was also added, it still contributed negatively to lipid oxidation during the 12-day storage period. In contrast, when 100 ppm of microencapsulated L-ascorbic acid was incorporated into the milk, the sourness score remained similar to the control for up to five days, after which it gradually increased through day 12 (Lee, Ahn, Lee & Kwak, 2004).

A study was conducted to meet the vitamin C needs of individuals by enriching yogurt, which is consumed daily with L-ascorbic acid. In a study by Ilic and Ashoor (1988), 300 mg of ascorbic acid was incorporated into 227 g of yogurt and stored at 3 °C for six weeks. At the end of this period, the remaining vitamin C content in the yogurt was sufficient to meet the entire recommended daily allowance in the USA.

Troise, Vitiello, Tsang, and Fiore (2016) encapsulated ascorbic acid (vitamin C) using a coating made from equal parts palm oil, triolein, and tripalmitin, and then incorporated it into ultra-high temperature (UHT) milk at a laboratory scale. Vitamin C is recognized for its antioxidant properties in fortified milk, helping to minimize the oxidation of unsaturated fatty acids (Teucher, Olivares & Cori, 2004). Beyond this, ascorbic acid supports iron absorption and enhances immune defense. However, when added in its free form—particularly during intense heat treatments—it may promote the formation of undesirable Maillard reaction products. Troise et al. (2016) showed that encapsulating ascorbic acid effectively decreased Maillard reactions and increased lysine levels by 45% (Troise et al., 2016; Adinepour et al., 2022).

In recent years, there has been growing interest in enriching milk and dairy products with vitamins such as D_3, E, C, and B_{12} (Giroux et al., 2013; Tan et al., 2018; Troise et al., 2016). Encapsulating these vitamins provides multiple benefits: it protects them from degradation, masks their characteristic tastes, allows for controlled release, and aids in incorporating fat-soluble vitamins into water-based food matrices (Ghanbari, Saeedi & Mortazavian, 2016; Adinepour et al., 2022).

MINERAL FORTIFICATION

Iron Fortification

Today, iron deficiency is very important for babies, children and women in the fertile period. Iron deficiency can cause health problems such as physical fatigue, decreased pregnancy rates and decreased brain functions (Martinez-Navarrete, Camacho, Martinez-Lahuerta, Martinez-Monzó & Fito, 2002; Yeung, Glahn & Miller 2001; Youdim, 2000).

Milk typically contains approximately 0.2 $mg.kg^{-1}$ of iron. When milk and dairy products are enriched with iron, this added mineral can interact with various milk components, including lipids, casein, minerals, and serum proteins (Gaucheron, 2000; Ünal & Akalın, 2004).

For iron fortification of milk and dairy products, different forms of iron are utilized, such as iron salts (Fe^{+2} and Fe^{+3}), elemental iron (FeO), and iron complexes with proteins or phospholipids. To mitigate oxidation during the fortification process, it has been considered best practice to add iron after homogenization but before pasteurization (Lotfi, Venkatesh Mannar, Merx & Naber-van den Heuvel, 1996).

For the fortification of various food products with iron, different forms of iron are employed. These can be categorized into four main groups (Hurrell, 1997):

1. Highly Water-Soluble Forms: This group includes iron (II) sulfate, iron (II) gluconate, iron (II) lactate, and iron (III) ammonium citrate.
2. Soluble in Dilute Acids: These forms are soluble in weak acids, such as gastric juice. Examples include iron (II) fumarate, iron (II) succinate, and iron (III) saccharate.
3. Water-Insoluble but Dilute Acid-Soluble Forms: This category comprises iron (III) orthophosphate, iron (III) ammonium orthophosphate, iron (III) pyrophosphate, and elemental iron powders.
4. Protected Iron Compounds: This group consists of compounds like Fe-EDTA and hemoglobin, which are designed to enhance stability and reduce interactions with food components.

When it comes to iron fortification, iron (II) sulfate and iron (II) gluconate are commonly found in infant formulas. While iron (II) sulfate boasts high bioavailability, it also exhibits stronger prooxidant properties compared to iron (III) glycinate, iron (II) fumarate, and iron (II) succinate. Conversely, iron (III) glycinate, iron (III)-EDTA, and iron-protein succinate offer superior bioavailability when compared to iron (II) sulfate. On the other hand, inert iron

compounds such as iron (III) pyrophosphate demonstrate considerable stability when added to foods, but their absorption from the diet is notably poor (Kaup, 1998; Kınık, Gürsoy & Gökçe, 2003).

Among the bioactive compounds introduced into dairy products, iron has been shown to interact with milk proteins, particularly casein. This interaction can lead to the formation of an iron-casein complex, which becomes insoluble in the gastrointestinal tract, potentially reducing iron bioavailability. Furthermore, the presence of oxygen in conjunction with these iron-casein complexes accelerates the lipid oxidation reaction in milk, resulting in undesirable flavors and aromas in the product (Gaucheron, 2000; Gupta, Chawla, Arora, Tomar & Singh, 2015; Kwak, Yang & Ahn, 2003; Adinepour et al., 2022)

It can also cause undesirable color changes and vitamin and mineral deterioration due to interaction with anthocyanins, flavonoids and tannins (Mehansho, 2006). Therefore, microencapsulation of iron salts is recommended to prevent these adverse effects. Microencapsulation with liposomes and fatty acid esters (FAE) is a special technique that is more convenient, well characterized, easily made, quite versatile in carrier properties and consists of edible components compared to others.

A study by Abbasi and Azari (2011) revealed that milk fortified with liposomes and fatty acid esters (FAE)-microencapsulated iron closely resembled the control sample, particularly at lower concentrations (7 $mg.L^{-1}$). This method was deemed to be cost-effective, straightforward, rapid, and practical.

The absorption or metabolism of certain food compounds can be influenced by high iron content. Conversely, iron absorption is positively impacted by vitamins A, C, E, and folic acid. In contrast, calcium (Ca), phosphorus (P), magnesium (Mg), malonaldehyde, polyphenols, oxalic acid, and phytic acid inhibit iron absorption. Lactoferrin, a naturally occurring protein in cow and breast milk, possesses the ability to bind and transport iron, delivering it to specific receptor cells in the human intestine. Consequently, lactoferrin is a valuable milk component due to its role in enhancing iron absorption, and it can be incorporated into various iron-enriched products (Aït-oukhatar et al., 1997; Hugunin, 2002; Martínez-Navarrete, Camacho, MartínezLahuerta, Martínez-Monzó & Fito, 2002). The most well-known compound that increases iron absorption is vitamin C (Aykut, Günay & Öztürk 1997; Huang, 2000; Martínez-Navarrete et al., 2002). This effect of vitamin C (for its activity in the form of reduced powder and chelate) is related to the formation of soluble complexes with iron at low pH. The complexes formed here maintain their solubility and absorbability in the duodenum at a more alkaline pH. The effect of vitamin C in increasing the absorption of iron compounds is the same for all iron compounds used for enrichment (Huang, 2000; Martínez-Navarrete et al., 2002).

The food and iron compounds to be used for iron fortification should be in harmony in terms of optimizing iron bioavailability and preventing rancidity in the food. In addition, interactions between the food selected for fortification and micronutrients are a factor that must be taken into account (Martínez-Navarrete et al., 2002). The importance of milk powder for iron fortification is a fact accepted all over the world. For example, there are successful applications in Brazil and Chile (Lysionek et al., 2002). In recent years, new products such as stabilized and microencapsulated iron (II) sulfate (commercial name SFE-171) have been developed for iron delivery to humans. The commercial iron preparation called SFE-171 is used in Argentina and other countries for the iron fortification of milk and dairy products, including milk powder. In the application for milk powder, SFE-171 is added to the milk and the product is subjected to a traditional drying process (production of milk powder in hot air flow at 205oC) and enriched milk powder is obtained. In studies conducted on rats, it was observed that the bioavailability of iron in the product enriched with SFE 171 was not affected by the processing conditions during milk powder production. It is also reported that the obtained product is consumed with pleasure by consumers and that the stability and pleasant taste of the product are preserved even after months of storage (Lysionek et al., 2002). It is known that iron catalyzes lipid oxidation and creates undesirable odor and flavor in products. In a study on the subject, whole cow's milk enriched with iron was evaluated sensorily after being pasteurized at a temperature below 79ºC and it was observed that the Fe+3 compound caused rancid flavor. No relevant defect occurred in the pasteurization process applied at 81ºC. When Fe^{+2} compounds are added to whole milk before pasteurization, they cause an oxidized flavor in the final product (Gaucheron, 2001).

Soluble Ferric Pyrophosphate (SFP) has higher bioavailability than iron (III) pyrophosphate, sodium iron (II) citrate and iron (II) sulphate. It has been determined in preliminary trials that the product can be easily used especially in the enrichment of milk and yoghurt (Juneja, 2001). The use of soy and its products (soy protein, soy milk etc.) in milk and its products brings a new approach to the agenda regarding iron deficiency. In particular, the fact that soy proteins bind iron strongly and prevent intestinal absorption of iron, and that phytic acid, which can be found in soy milk, also exhibits similar effects, necessitates that soy milk and milk and products with added protein should be consumed with caution by people in the risk group for iron deficiency (Kınık et al. 2003).

In a study conducted by Kırımi, Tuncer, Ataş and Ceylan (2004), 6-month-old babies were made to consume breast milk or iron-fortified baby food and the growth and iron status of these babies were investigated. As a result of the study,

it was concluded that babies who received breast milk and babies who consumed iron-fortified baby food were almost equal.

In an additional study focused on iron fortification, ferric ammonium sulfate was utilized (Kwak et al., 2003). When microencapsulating iron for milk fortification, it is crucial that the microcapsules do not create a lumpy texture in the milk or float on its surface. Typically, small microcapsules are preferred to prevent undesirable textural changes in the food system (Kwak et al., 2003). It is well-established that iron catalyzes lipid oxidation, which can lead to spoilage and the development of unpleasant odors and flavors. The primary rationale for employing iron microencapsulation in fortifying dairy products is to mitigate the risk of oxidized flavors (Jackson & Lee, 1991), likely stemming from the lipid prooxidation of milk (Edmondson, Douglas Jr & Avants, 1971). Consequently, the impact of iron microencapsulation on fat oxidation was assessed via the TBA test over a 9-day storage period in this study. The results demonstrated a satisfactory protective effect against lipid oxidation in milk fortified with encapsulated iron, as compared to milk fortified with non-encapsulated iron (Kwak et al., 2003).

In a study where Cheddar cheese was produced from iron-fortified milk, various iron sources and concentrations were utilized (Zhang & Mahoney, 1991). The recovery rates of iron in the resulting cheeses varied depending on the form of iron added: FeCl3 showed 71–81% recovery, iron citrate had 52–53%, the Fe-casein complex ranged from 55–75%, and the ferripolyphosphate-fat protein complex achieved 70–75%. Although a slight increase in TBA (Thiobarbituric Acid) values was observed in the iron-fortified cheeses, these remained within the normal range typically seen in unfortified cheeses. Notably, aging the cheeses for up to three months did not adversely affect TBA results or the sensory scores related to oxidized off-flavors and overall cheese taste. The study concluded that Cheddar cheese can be successfully fortified with 40–50 $mg \cdot kg^{-1}$ of iron—using ferripolyphosphate-fat protein complexes, iron-casein complexes, or ferric chloride—without compromising its quality.

Brown cheese, a traditional Norwegian variety, contains a considerable iron content—approximately 10 mg per 100 g—along with 11 g of protein, 39 g of sugar, 29 g of fat, and 520 mg of calcium. In this cheese, about 90% of the iron is tightly bound to the protein fraction (Gaucheron, 2000). However, the study found no evidence of protein modifications resulting from this iron-protein binding.

Mozzarella cheese was produced using milk fortified with either 25 or 50 mg of iron per kilogram, with iron supplied as casein-chelated iron, whey protein-chelated iron, or ferric chloride ($FeCl_3$). The addition of 25 mg iron per kilogram did not alter the cheese's physical properties. Although the apparent viscosity of

cheese fortified with 50 mg iron per kilogram tended to be slightly higher than the control, this difference was not statistically significant throughout the storage period. Iron fortification also had no impact on the cheese's cooking color. No notable increase in chemical oxidation was observed between control and iron-fortified cheeses. However, a minor rise in metallic and oxidized flavors was noted in the fortified samples. Sensory analysis indicated no significant differences between cheeses fortified with casein- or whey protein-chelated iron compared to those fortified with $FeCl_3$. Consumer panels evaluating the cheeses on pizza found the iron-fortified products comparable to the control (Gaucheron, 2000).

White soft cheese was produced using a pre-cheese retentate fortified with 80 mg $Fe \cdot kg^{-1}$, supplied as electrolytic iron, $FeCl_3$, or $FeSO_4$. The study found that fortification with electrolytic iron or $FeCl_3$ resulted in particularly favorable sensory attributes for the white soft cheese (Gaucheron, 2000).

Skim milk fortified with iron ammonium citrate was used to produce bakery and curd cheeses. Iron retention differed between the two types, with about 14% retained in bakery cheese and a significantly higher 58% in curd cheese. The heat treatment during production was identified as the main factor affecting iron retention. Importantly, the addition of iron did not impair starter culture activity or alter the initial flavor profile. Moreover, no rapid development of off-flavors was detected in the iron-fortified cheeses over a two-month storage period (Gaucheron, 2000).

Jackson and Lee (1992) fortified Harvati cheese with 140 $mg \cdot kg_{-1}$ of $FeCl_3$ and observed that iron microencapsulated within stearin-coated microcapsules improved the product's organoleptic qualities. However, this encapsulation led to reduced iron retention in the cheese, with microencapsulated iron retaining about 70% compared to 90% retention when free $FeCl_3$ was used.

In another study, Hekmat and McMahon (1997) produced low-fat and nonfat yogurts fortified with iron at levels of 10, 20, and 40 mg per kilogram. After 30 days of storage, no increase in chemical oxidation was found. Although the fortified yogurts showed slightly elevated scores for oxidized flavors compared to controls, no rise in metallic, bitter, or other off-flavors was detected. Additionally, consumer panels reported no significant differences in appearance, texture, flavor, or overall quality between fortified and non-fortified flavored yogurts.

A study examined nine commonly used food fortification compounds, focusing on color and flavor changes in chocolate milk fortified with ferripolyphosphate and a ferripolyphosphate-whey protein complex (Douglas Jr, Rainey, Wong, Edmondson & LaCroix, 1981). Sodium ferric pyrophosphate,

ferripolyphosphate, and the ferripolyphosphate-whey protein complex caused little to no color alteration both initially and after two weeks of storage. Conversely, all other compounds tested resulted in noticeable and persistent discoloration. Flavor analysis revealed that ferric compounds produced minimal to no off-flavors in chocolate milk immediately and after 7 and 14 days of storage at 4°C. Ferrous compounds, however, initially generated off-flavors, though these improved following 14 days of refrigeration. Chocolate beverage powders fortified with ferric pyrophosphate were acceptable in terms of color and flavor when reconstituted with cold, hot (80°C), or boiling water or milk. Similarly, powders fortified with ferrous fumarate were acceptable when mixed with cold or hot (80°C) water or milk. However, products fortified with ferrous fumarate and reconstituted using boiling water or milk experienced an undesirable color shift from red/brown to an unacceptable grey. This outcome, unfortunately, suggests that ferrous fumarate is not suitable for use in commercially available chocolate drink powders that might be prepared with boiling liquids (Hurrell, Reddy, Dassenko, Cook & Shepherd, 1991; Gaucheron, 2000).

A study focused on using ferrous sulfate heptahydrate for iron fortification, due to its low cost and high bioavailability. Fresh cow and buffalo milk, blended in equal parts (with 3% fat and 8.5% non-fat solids), was fortified with either ferrous sulfate or iron microcapsules at a concentration of 10 $mg.L^{-1}$ of iron (Gupta et al., 2015). Three types of microcapsules were utilized for fortification:

1. Egg phosphatidylcholine liposomes prepared via freeze-drying.
2. Sodium alginate and modified starch microcapsules produced through an emulsification process.
3. Sodium alginate microcapsules also prepared by emulsification.

Sensory evaluation revealed that milk fortified with sodium alginate and modified starch microcapsules (containing 10 $mg.L^{-1}$ iron) closely resembled the control (non-fortified) milk in taste and appearance. Additionally, the emulsification method achieved the highest encapsulation efficiency at 74.85%. In contrast, milk enriched with liposomes exhibited an oily, off-putting odor and flavor. These low sensory scores were not due to oxidation but rather the inherent taste of phosphatidylcholine. Furthermore, liposome-fortified milk developed a slight yellow-brown tint, which contributed to its lowest overall sensory ratings (Gupta et al., 2015).

Gupta, Chawla, and Arora (2015) explored the microencapsulation of iron using a wall material blend composed of modified starch, maltodextrin, and gum Arabic in a 1:1:4 ratio, applied via a modified solvent evaporation technique. This encapsulated iron was then added to a mixture of buffalo and cow milk. Since iron is known to accelerate fat oxidation in milk, causing off-flavors and

undesirable aromas, the study measured the TBA (Thiobarbituric Acid) values and found that milk fortified with encapsulated iron exhibited significantly lower TBA values compared to milk enriched with free iron. These results suggest that using a combination of modified starch, maltodextrin, and gum Arabic effectively protects iron in milk without compromising sensory quality. Additionally, the encapsulated iron demonstrated higher in vitro bioaccessibility than the non-encapsulated form. Separately, Kwak et al. (2003) investigated iron-fortified milk with iron coated by polyglycerol monostearate through an emulsification process. They observed no negative sensory impacts during 5 days of storage. Iron release was minimal (3–5%) under acidic conditions simulating the stomach environment, but increased substantially (95.7%) at neutral pH, reflecting intestinal conditions. Their findings further emphasized that iron encapsulation can effectively reduce lipid oxidation in milk; the TBA value for milk with non-encapsulated iron was 0.58, compared to 0.35 in milk containing encapsulated iron (Adinepour et al., 2022).

In a separate study, the microencapsulation of iron and vitamin C using polyglycerol monostearate via an emulsification method was explored in drinkable yogurt, with the aim of increasing iron bioavailability**.** This investigation spanned a 20-day storage period. The encapsulation of iron successfully reduced lipid oxidation by preventing the interaction of iron with milk casein, thereby inhibiting the development of unpleasant odors and tastes in the yogurt. Throughout the 20 days of storage (at 4 °C), no significant difference was observed in the viability of the bacterial strains, *Lactobacillus delbrueckii subsp. bulgaricus* and *Streptococcus thermophilus*, in the fortified yogurt drink containing encapsulated vitamin C and iron, when compared to their initial viability on day one. The results indicated that polyglycerol monostearate served as an effective coating material, offering good protection for both vitamin C (with an encapsulation efficiency of 76%) and **iron** (with an encapsulation efficiency of 73%) (Kim, Ahn, Seok, & Kwak, 2003).

Another research group examined the fortification of solid yogurt with **ir**on encapsulated in niosomes (Gutiérrez et al., 2016). Gutiérrez et al. (2016) found that iron release from niosomes remained stable under simulated gastrointestinal conditions, which was attributed to a high retention rate of iron within the niosomes (72–84%). Moreover, the sensory and rheological properties of yogurt fortified with encapsulated iron showed no differences compared to the control yogurt. In another study investigating the fortification of flavored yogurt with liposomal β-carotene, Toniazzo et al. (2014) reported no adverse effects on yogurt structure, phase separation, or rheological characteristics. They also demonstrated that liposomes effectively preserved β-carotene during three months of refrigerated storage, with 88% retention. These findings suggest that

encapsulated β-carotene is a promising option for producing red-colored yogurt (Toniazzo et al., 2014; Adenepour et al., 2022).

Calcium Fortification

Calcium is a mineral that plays a role in many vital functions. Adequate calcium intake has shown many health benefits, including reduced risk of hypertensive disorders in pregnancy, lower blood pressure, especially among adolescents, prevention of osteoporosis and colorectal adenomas, lower cholesterol levels, and lower blood pressure in offspring of mothers who received adequate calcium during pregnancy (Cormick, & Belizán. 2019).

Cow's milk typically contains an average of 1.20 g of calcium per liter. The majority of this calcium exists colloidally as a caseinate-phosphate complex**,** which is readily released during digestion, leading to high potential bioavailability (Guéguen & Pointillart, 2000). The Recommended Dietary Allowance (RDA) for calcium ranges from 400-1300 mg, depending on age and specific physiological conditions. Calcium supplementation is commonly applied to a variety of dairy products, including yogurt, yogurt drinks, ice cream, cottage cheese, sour cream, cream cheese preparations, and desserts (Gerstner, 2002; Pirkul, Temia & Erdem, 1997).

Dried milk and flavored milk powders are also frequently fortified with vitamins A and D, calcium, and iron. Several commercial calcium salts are used for fortification in milk and beverages, such as calcium carbonate, calcium chloride, calcium phosphate, tribasic calcium phosphate, calcium citrate malate, calcium lactate, calcium gluconate, calcium lactate gluconate, and natural milk calcium (Singh et al., 2007).

In one study, cow's milk was fortified with calcium at a concentration of 50 mg per 100 ml using three different calcium salts: calcium chloride, calcium lactate, and calcium gluconate. A metabolic study in mice showed that the calcium bioavailability from phosphate-stabilized cow's milk fortified with calcium lactate and calcium gluconate disodium was slightly higher than that from non-fortified cow's milk (Singh et al., 2007).

In a rat study by Kaushik, Sachdeva, Arora, Kapila, and Wadhwa (2014), different fortified milk preparations were evaluated:

-Calcium-enriched milk: fortified with 600 ppm calcium citrate

-Vitamin D_2-enriched milk**:** fortified with 600 $IU \cdot L^{-1}$ vitamin D_2

-Calcium + vitamin D_2-enriched milk: fortified with both 600 ppm calcium citrate and 600 $IU \cdot L^{-1}$ vitamin D_2

The study found that vitamin D_2 supplementation enhanced both the apparent digestibility coefficient and retention of calcium. Conversely, calcium positively influenced the digestibility and retention of vitamin D_2. Notably, vitamin D_2 supplementation significantly increased the apparent digestibility coefficient of iron, suggesting improved iron absorption, while calcium supplementation decreased iron absorption. For zinc, calcium supplementation reduced both its apparent digestibility coefficient and retention, whereas vitamin D_2 increased these parameters. The inhibitory effects of calcium on zinc absorption have also been reported by Amaro and Camara (2004), and Perales, Barbera, Lagarda, and Farre (2006) similarly noted that calcium from fortified milk can inhibit iron absorption.

Another study evaluated the impact of calcium fortification in milk on the bioavailability of calcium, iron, and zinc. It confirmed that while calcium supplementation increases both the calcium content and its bioavailability in milk, calcium from fortified milk inhibits iron absorption. The effect of calcium on zinc bioavailability varied depending on the in vitro method used, zinc solubility in calcium-fortified milk, and reductions observed in dialysis, though the overall percentage of zinc uptake remained consistent. Therefore, it is advisable to consume iron supplements at different times than milk. Generally, cow's milk is not an ideal vehicle for iron fortification unless specific strategies are employed to enhance iron bioavailability. Excess dietary calcium has also been shown to impair zinc availability (Jovaní, Barberá & Farré, 2001; Cámara & Amaro, 2003; SandstroÈm, 2001), though this interaction appears to be influenced by dietary phytic acid content. The lack of phytate in the studied samples may explain why no negative effect of calcium on zinc bioavailability was observed in this study (Perales et al., 2006).

In the study by Coşkun and Şenoğlu (2011), calcium carbonate ($CaCO_3$) was added to milk at varying concentrations—100, 200, 400, and 600 mg per 100 mL—both before and after pasteurization, prior to yogurt production. The results indicated that calcium carbonate supplementation increased the yogurt's pH and viscosity. Concurrently, it resulted in a decrease in the titratable acidity and the amount of serum separation. Yoghurt samples containing calcium carbonate added before pasteurization and not exceeding 400 $mg \cdot 100mL^{-1}$ were more appreciated than control samples in terms of sensory evaluation.

It has been determined that safe doses are exceeded in men who frequently consume calcium-fortified milk and dairy products and who do not need calcium supplements (Lotfi et al., 1996). Vitamin D toxicity has also been observed as a result of calcium-fortified milk (American Dietetic Association, 2001).

Park, Ahn, and Kwak (2008) investigated the effects of nanoencapsulated calcium in milk on female rats. Their study revealed that rats consuming fortified

milk exhibited a higher total bone/phosphatase ratio (59%) compared to the control group. Furthermore, the nanocalcium particles demonstrated superior biocompatibility in rats when compared to conventional calcium powder (Park et al., 2008).

Zinc Fortification

Zinc holds the distinction of being the body's second most abundant trace element, surpassed only by iron. It plays a crucial role in numerous fundamental physiological processes, including human growth and development, reproduction, immunological defense mechanisms, the perception of taste and smell, and bone mineralization. Primary and secondary factors such as improper dietary practices, poverty, nutritional deficiencies, parasitic infections, genetic diseases such as sickle cell anemia, and even hot and humid climate conditions easily cause zinc levels in the body to decrease (Kahraman, 2011).

The human body possesses a limited capacity for zinc storage (Maret & Sandstead, 2006). Therefore, zinc status is significantly influenced by its bioavailability, as well as an individual's age and physiological condition (World Health Organization, 2001; Aquilanti et al., 2012).

While milk and dairy products are not considered exceptionally rich sources of zinc, their zinc content varies:

- Cream Cheese: 1.4 $mg \cdot (100g)^{-1}$
- Mozzarella: 3.1 $mg \cdot (100g)^{-1}$
- Ricotta: 1.1 $mg \cdot (100g)^{-1}$
- Yogurt: 0.9 $mg \cdot (100g)^{-1}$
- Milk (Chocolate Milkshake): 0.4 $mg \cdot (100mL)^{-1}$
- Cow's milk: 0.3 $mg \cdot (100mL)^{-1}$
- Goat's milk: 0.3 $mg \cdot (100mL)^{-1}$
- Sheep's milk: 0.5-0.7 $mg \cdot (100mL)^{-1}$

While the daily zinc requirement determined by the European Union Commission (European Union, 2008) is 10 mg, this rate varies between 4.7-18.6 mg in different countries. The highest tolerated daily zinc value is 40 mg in adults. It is estimated that dairy products contribute only approximately 19% to 31% of the daily zinc requirement (Hunt & Nielsen, 2009; Kahraman, 2011).

The United States Food and Drug Administration (FDA) generally recognizes five zinc compounds as safe (GRAS): zinc sulfate, zinc chloride, zinc gluconate, zinc oxide, and zinc stearate (Food and Drug Administration, 2011).

Milk and milk-based products are considered suitable candidates for zinc supplementation. However, the impact of calcium, which is abundant in milk, on zinc absorption has been a subject of considerable debate. Some researchers propose that calcium reduces zinc bioavailability (Maret & Sandstead, 2006; Takasugi, Matsui, Omori & Yano, 2007), while others suggest it has no stimulatory effect (Diaz-Castro, Alferez, Lopez-Aliaga, Nestares & Campos, 2009).

The naturally low pH of milk-based products such as yogurt and cheese makes them ideal candidates for zinc supplementation (Rosado, 2003). In cow's milk, zinc is primarily chelated by casein proteins (Al-Awadi & Srikumar, 2001; Drago & Valencia, 2002), which explains its substantial retention in the curd during milk coagulation (Cichoscki, Valduga, Valduga, Tornadijo, & Fresno, 2002). Acidification of milk—whether through bacterial fermentation or the addition of lactic acid—facilitates the dissociation of calcium from casein. This process enhances zinc solubility and improves its bioavailability (Drago & Valencia, 2002; Singh et al., 1989).

In a study examining the response of lactic acid bacteria (LAB) to skim milk fortified with zinc aspartate, zinc sulfate, or zinc gluconate, the acidification activity of 98 different LAB strains was evaluated. The findings revealed that the response varied depending on the bacterial strain, regardless of the zinc source used. The strains exhibiting the highest acidification rates and extents were selected for producing zinc-fortified cheeses. For the production of Italian mg.L-1 *Streptococcus thermophilus* strains (A1, C1, E2, and 9.2) were used in Squacquerone, while a mixture consisting of two Streptococcus thermophilus strains (E2 and 9.2) and two *Lactobacillus helveticus* strains (GS1 and GS4) in a 2:1 ratio was utilized for Caciotta. Zinc supplementation did not affect the main physical or chemical properties of the cheeses. Sensory evaluations confirmed that all three zinc salts were appropriate for fortifying both types of cheese, achieving a final zinc concentration near 140 mg.kg-1. Although previous reports have noted changes in sensory characteristics for foods fortified with zinc sulfate (Boccio & Montiero, 2004; Salgueiro et al., 2002), no off-flavors such as metallic, bitter, or oxidized tastes were detected in the zinc-fortified cheeses in this particular research. This highlights the critical role of selecting suitable starter cultures when developing zinc-enriched dairy products. Moreover, no significant differences in overall quality were perceived between fortified and control cheeses. These results support the feasibility of milk fortification for producing soft and semi-hard cheeses like Squacquerone and Caciotta, especially

for populations vulnerable to zinc deficiency, including women of reproductive age and the elderly (Aquilanti et al., 2012).

Tesan et al. (2009) evaluated the bioavailability of yogurts fortified with two zinc sources: zinc gluconate stabilized with glycine and zinc sulfate, both commonly used in food fortification. Their results demonstrated that zinc gluconate stabilized with glycine serves as an effective option for enriching yogurt. Achanta, Aryana and Boeneke (2007) enriched fat-free yogurt with zinc gluconate and other minerals at a rate of 25% of the daily recommended intake (15 mg zinc). According to the tests, zinc did not cause any change in the final product quality. Turkish white cheese was enriched with zinc sulfate by Gulbas and Saldamlı (2005). In the study, the results were evaluated by adding the zinc compound to both pasteurized milk and cheese brine. A higher recovery rate was observed in the enrichment made by adding the zinc compound to pasteurized milk. After ripening, an increase in the zinc level was observed in the cheese enriched by adding it to the salt water, while a decrease was observed in the zinc level in the white cheese enriched by adding it to pasteurized milk. However, the most effective recovery rate of 87% was obtained by adding zinc to pasteurized milk.

The presence of inhibitors that prevent zinc bioavailability is also a common factor. There are many agents that affect the absorption of zinc from the intestine, such as calcium, metal complexes, proteins and phytate (Maret & Sandstead, 2006; Gibson, Bailey, Gibbs & Ferguson, 2010). In addition, wheat bran, lignin and hemicelluloses reduce zinc bioavailability (Maret & Sandstead, 2006; Harzer & Kauer, 1982). It has also been reported that in fortification with iron, the iron/zinc ratio should not exceed 2 in order not to reduce zinc bioavailability (Biringen Löker, Ugur & Yıldız, 2003; Kahraman, 2011).

PROTEIN SOURCES FORTIFICATION

Soy protein helps lower cholesterol levels; low cholesterol helps protect cardiovascular health. The amount of soy protein in food should be at least 6.25 g.portion^{-1}. According to the Turkish Food Codex (2017), food labels stipulate that for the expected health benefits of soy protein to be realized, daily consumption should be at least 25 g, and the diet should be low in cholesterol and saturated fat.

Dairy yogurts with 5% added soy protein concentrate are considered to meet the requirement of 6.25 g of soy protein per serving. Yogurts containing 2.5% added soy protein concentrate are classified as a "good source" of soy protein (Food and Drug Administration, 1999; Drake, Chen, Tamarapu & Leenanon, 2000).

Soybeans boast a protein content exceeding 50%. After oil extraction, protein ingredients such as soy protein concentrate (SPC), soy protein isolate (SPI), and textured soy protein can be derived from defatted soy flour (Friedeck, Aragul-Yuceer & Drake, 2003).

Soy protein concentrates are recognized for being cost-effective, nutritious, and highly functional ingredients in various food products (Anderson, Johnstone & Cook-Newell, 1995; Zind, 1998; Drake et al., 2000).

Frozen desserts could serve as an effective vehicle for incorporating soy protein. A study investigated the effects of adding soy protein isolate (SPI) to low-fat dairy ice cream, using formulations containing 0%, 2%, and 4% SPI. Sensory testing by consumers revealed no notable differences in texture and appearance between the control (0%) and the highest SPI level (4%) for both vanilla and chocolate varieties. Nevertheless, SPI addition significantly influenced flavor perception. Notably, the 4% SPI chocolate ice cream received higher acceptability ratings than the vanilla versions, indicating that chocolate flavor better concealed the characteristic soy taste. This indicates that fortifying low-fat dairy ice cream with soy protein isolate could be a promising strategy for introducing soy protein positively to a wider consumer base (Friedeck et al., 2003).

In one study, 1%, 2.5%, and 5% soy protein was mixed into yogurt milk. Soy protein-enriched dairy yogurts exhibited higher viscosities and protein contents than control dairy yogurts. Yogurts containing 1% and 2.5% soy protein were found to be most similar to traditional dairy yogurts. However, yogurts with 5% soy protein concentrate developed a mayonnaise-like texture. Soy-enriched yogurt is considered a nutraceutical food. Yogurts fortified with 5% soy protein concentrate fulfill the FDA-approved (Food and Drug Administration, 1999) health claim of "lowering cholesterol" and also provide a sufficient amount of fiber, offering 1 g of dietary fiber per serving. The incorporation of additional sweeteners may assist in masking the inherent soy flavors or in enhancing existing dairy flavors (Drake et al., 2000).

Buttermilk powder, due to its rich protein content of approximately 34% (Smith, 2008), presents a valuable ingredient for enriching various dairy products. Its inclusion can boost the overall protein content, as well as the levels of essential amino acids such as lysine, methionine, isoleucine, and tryptophan, thereby enhancing both the physical and sensory attributes of the fortified products (Madenci, Aktaş & Türker, 2013). Buttermilk powder contains concentrated calcium, lactose and some other important nutrients (Salas-Brıngas, Rukke, Saga, Lekang, & Schuller, 2010). In a study conducted by Shibu, Kumar, Narasımhan ve Pugazhenthi (2000), the effects of using buttermilk powder in ice cream on sensory quality properties were investigated. It was determined that

buttermilk powder did not change the titratable acidity and specific gravity of ice cream, but improved viscosity, structure and texture. As a result of the study, it was recommended to use buttermilk powder in an amount of 25% of the nonfat dry matter of milk (Shibu et al., 2000; Yıldırım & Güzeler, 2013).

The usability of mushrooms as a protein source in the enrichment of ice cream was investigated. Pleurotus ostreatus species was used in the study, and the protein content of mushroom powder in dry matter was found to be 25.59%. During ice cream production, natural protein solutions prepared with water from mushroom powder at different concentrations were added as control (0), 0.1 g·20 mL^{-1}, 0.2 g·40 mL^{-1}, 0.4 g·80 mL^{-1}, 0.8 g·160 mL^{-1} and 1.6 g·320 mL^{-1}. It is thought that 160 ml mushroom powder concentration is the most suitable concentration. At this concentration, the protein content of ice cream increased by approximately 11.73%. At concentrations above 160 ml, a significant decrease in the L* value was observed (Beşir, Kırmızıkaya, Çaylar & Koçer, 2019).

Arthrospira platensis, more commonly known as Spirulina, stands out as the most widely recognized microalgal species. Its popularity stems from its exceptionally high protein content, typically around 65%, and its significant nutritional value. It is known that Spirulina has preventive or therapeutic properties for cancer, renal failure, hypertension and infertility. In addition, it has been stated that it has antibacterial and antifungal effects on some pathogens and supports the development of lactic acid bacteria in milk and its products. It has been emphasized that the addition of Spirulina, rich in dietary fiber and bioactive components, to yoghurts improves the textural structure by maintaining sensory acceptability and increasing mouthfeel, and even its addition at a rate of 0.25% significantly accelerates fermentation and can be an alternative to forms enriched with synthetic chemical components (Barkallah et al., 2017; Altuntaş, 2021).

Fat-free whey powder contains 95.1 $g \cdot kg^{-1}$, half-fat whey powder contains 49 $g \cdot kg^{-1}$ protein (Schuck & Dolivet, 2002). Whey powder is widely used in the production of yogurt and ice cream from dairy products (Andıç, Zorba & Tunçtürk, 2010). The low cost of whey powder compared to other fat-free dry matter amounts of milk is one of the most important factors explaining its widespread use in ice cream and other products (Young, 2007; Yıldırım & Güzeler, 2013).

It is a common practice to fortify yogurt with skimmed milk powder (SMP), but other dried milk protein components like whey products and caseinates are also frequently utilized (Isleten & Karagul-Yuceer, 2006). The addition of these milk proteins contributes to a firmer body in the yogurt and helps to reduce whey separation (Peng, Serra, Horne & Lucey, 2009).

MODERN METHODS OF FORTIFICATION

Traditional fortification methods, such as simply adding nutrients directly to foods, have had limited success in maintaining nutrient stability and absorption. However, newer techniques—including microencapsulation, nanoencapsulation, spray drying, freeze-drying, emulsification, and coacervation—have markedly improved these outcomes. These advanced technologies help protect sensitive nutrients, allow for controlled nutrient release, and preserve the sensory qualities of dairy products. Additionally, strategies like liposomal encapsulation, protein-based delivery systems, and polymer nanoparticles further boost the stability and effectiveness of fortified dairy items. By safeguarding fragile nutrients and extending product shelf life, these encapsulation methods offer lasting health benefits. Given the widespread acceptance of dairy and its nutritional value, fortifying dairy products with these innovative approaches holds great promise in combating global micronutrient deficiencies (Bhtoya, Pradhan, Kumar & Dobhal, 2025).

HARMFUL EFFECTS OF FORTIFICATION OF FOOD

Some health risks may be encountered during food fortification. Toxicity, exposure and concealment of disease symptoms are particularly prominent among these risks. In order to avoid such risks, certain rules must be followed. For example, steps such as defining the problem, increasing the sensitivity of policy makers, obtaining public support and ensuring participation, conducting preliminary studies on technical, economic and other issues, establishing national programs, establishing quality and control mechanisms, establishing packaging-distribution etc. systems, obtaining state support, determining and implementing behavioral change strategies are necessary for successful food fortification studies (Aslan & Köksel, 2003; Demircioğlu & Aslan, 2023).

Benefit/Harm Although fortification practices are implemented in underdeveloped and developing countries to prevent inadequate dietary intake of daily nutrients, they can cause excessive intake of some nutrients in developed countries (Tektunalı Akman & Garipağaoğlu, 2018).

There are risks and risks of overdose as a result of fortification of foods with calcium and consumption of these foods. It has been determined that safe levels are exceeded in men who frequently consume calcium-fortified milk and dairy products (milk, yogurt, cottage cheese) and who do not need any calcium supplements (Lotfi et al., 1996). Vitamin D toxicity has been observed as a result of calcium fortification of milk (American Diabetes Association, 2001).

The benefits of this optional fortification vary depending on which foods are used for fortification, the amount of the nutrient used for fortification, and the extent to which the community consumes that food. Individual differences also

cause fortification to vary from person to person. Various gene polymorphisms can affect digestion and absorption, and can change the response of individuals to nutrients. It is thought that it is necessary to record or monitor the possible side effects of nutrient intakes that are well above tolerable amounts in individuals who use both vitamin-mineral supplements and frequently consume fortified foods (Health Canada, Food Directorate, Health Products and Food Branch, 2018; Tektunalı & Akman Garipoğlu, 2018).

CONCLUSION

As a result, fortification of milk and dairy products with vitamins, minerals and protein sources plays a critical role in improving public health and eliminating nutritional deficiencies. This strategy has great potential in combating vitamin D, calcium, iron and zinc deficiencies, which are particularly prevalent in developing countries. The fortification process not only increases the intake of essential nutrients, but also offers a wide range of benefits, such as strengthening the immune system, supporting bone health and improving cognitive development in children. However, the success of this application depends on raising consumer awareness, increasing investments in this direction by the food industry and strengthening relevant legislation. In the future, the development of more specific fortification approaches for individual nutritional needs and the integration of alternative protein sources will further advance innovations in this area. Fortification of milk and dairy products will remain one of the important steps taken towards building a sustainable nutritional future.

REFERENCES

Abbasi, S., & Azari, S. (2011). Efficiency of novel iron microencapsulation techniques: fortification of milk. International journal of food science and technology, 46(9), 1927-1933.

Achanta K, Aryana K. J., & Boeneke, C. A. (2007). Fat free plain set yogurts fortified with various minerals. LWT- Food Science and Technology, 40, 424–429.

Adinepour, F., Pouramin, S., Rashidinejad, A., & Jafari, S. M. (2022). Fortification/enrichment of milk and dairy products by encapsulated bioactive ingredients. Food Research International, 157, 111212.

Aït-oukhatar, N., Bouhallab, S., Bureau, F., Arhan, P., Maubois, J-L., Drosdowsky, M.A., & Bouglé, D. (1997). Bioavailability of caseinophosphopeptide bound iron in the young rat. Nutritional Biochemistry, 8, 190-197.

Aksu, B. M., & Özbey, F. (2021). D vitamini ile zenginleştirilmiş yoğurt tüketimi ve sağlık üzerine etkileri. Gıda, 46(5), 1171-1182.

Al-awadi, F. M., & Srikumar, T. S. (2001). Trace elements and their distribution in protein fractions of camel milk in comparison to other commonly consumed milks. Journal of Dairy Research, 68(3), 463-469.

Allen, L. H. (2006). New approaches for designing and evaluating food fortification programs. The Journal of Nutrition, 136(4), 1055-1058.

Altuntaş, S. (2021). Yoğurtta zenginleştirme olanaklarının teknolojik yönü ve güncel gelişmeler. Avrupa Bilim ve Teknoloji Dergisi, 22, 230-238.

Amaro M.A., & Camara, F. (2004). Iron availability: An updated review. International Journal of Food Science and Nutrition, 55, 597-606.

American Dietetic Association. (2001). Position of the American Dietetic Association: Food Fortification and Dietary Supplements. *Journal of the American Dietetic Association* 101(1),115-125.

Anderson, J. W., Johnstone, B. M., & Cook-Newell, M. E. (1995). Meta-analysis of the effects of soy protein intake on serum lipids. New england journal of medicine, 333(5), 276-282.

Andıç, S., Zorba, Ö., & Tunçtürk, Y. (2010). Effect of whey powder, skim milk powder and their combination on yield and textural properties of meat patties. International Journal of Agriculture and Biology, 12(6), 871-876.

Türkiye Cumhuriyeti Gıda Tarım ve Hayvancılık Bakanlığı. (2017, March 7). *Türk Gıda Kodeksi Gıdalara Vitaminler, Mineraller ve Belirli Diğer Öğelerin Eklenmesi Hakkında Yönetmelik* (Sayı: 30000). T.C. Resmî Gazete.

T.C. Sağlık Bakanlığı Halk Sağlığı Genel Müdürlüğü. (2019). *Türkiye beslenme ve sağlık araştırması (TBSA)* (Sayı: 1132).

Türk Endokrinoloji ve Metabolizma Derneği. (2020). *Osteoporoz ve metabolik kemik hastalıkları tanı ve tedavi kılavuzu*.

ANSES. (2018). *Ciqual Fransız gıda bileşimi tablosu* .https://ciqual.anses.fr/

Aquilanti, L., Kahraman, O., Zannini, E., Osimani, A., Silvestri, G., Ciarrocchi, F., Garofalo, C., Tekin, E., & Clementi, F. (2012). Response of lactic acid bacteria to milk fortification with dietary zinc salts. International Dairy Journal, 25(1),52-59. https://doi.org/10.1016/j.idairyj.2011.12.006

Aslan, D., & Köksel, H. (2003). Gıda zenginleştirilmesi ve bazı yaklaşımlar. Sürekli Tıp Eğitim Dergisi, 12(11), 418-420.

Aykut, M., Günay, O., & Öztürk, Y. (Trans.). (1997). *Diyet, beslenme ve kronik hastalıkların önlenmesi* (Dünya Sağlık Örgütü Teknik Raporlar Serisi 797). Erciyes Üniversitesi Matbaası.

Barkallah, M., Dammak, M., Louati, I., Hentati, F., Hadrich, B., Mechichi, T., Ayadi, M.A., Fendri, I., Attia, H., & Abdelkafi, S. (2017). Effect of Spirulina platensis fortification on physicochemical, textural, antioxidant and sensory properties of yogurt during fermentation and storage. LWT-Food Science and Technology, 84, 323-330.

Beşir, İ., Kırmızıkaya, E. S., Çaylar, M., & Koçer, F. (2019). Pleurotus ostreatus (Jacq.) P. Kumm. Kullanılarak Dondurmanın Proteince Zenginleştirilmesi. Mantar Dergisi, 10(3), 178-185.

Bhtoya, R., Pradhan, G., Kumar, S., & Dobhal, A. (2025). Advanced fortification techniques in dairy products: enhancement of nutritional value through encapsulation. Nutrire, 50(1), 22.

Biringen Löker, G., Ugur, M., & Yıldız, M. (2003). A partial supplementation of pasteurized milk with vitamin C, iron and zinc. Nahrung/Food 47(1),17-20.

Black, L. J., Walton, J., Flynn, A., & Kiely, M. (2014). Adequacy of vitamin D intakes in children and teenagers from the base diet, fortified foods and supplements. *Public Health Nutrition*, *17*(4), 721–731.

Boccio, J., & Monteiro, J. B. (2004). Food fortification with iron and zinc: pros and cons from a dietary and nutritional viewpoint. Revista de Nutricao-Campinas, 17(1), 71-78.

Budavari, S. (Ed.). (1996). *The Merck index: An encyclopedia of chemicals, drugs and biologicals* (12th ed.). Merck & Co., Inc.

Calvo, M. S., Whiting, S. J., & Barton, C. N. (2004). Vitamin D fortification in the United States and Canada: current status and data needs. The American journal of clinical nutrition, 80(6), 1710S-1716S.

Calvo, M. S., & Whiting, S. J. (2013). Vitamin D fortification in North America: Current status and future considerations. In R. V. Preedy, R. Srirajaskanthan, & V. Patel (Eds.), *The handbook of food fortification from concepts to public health applications* (Vol. 2, pp. 259–271). Springer Science + Business Media..

Cámara, F., & Amaro, M. A. (2003). Nutrional aspect of zinc availability. International Journal of Food Sciences and Nutrition, 54(2), 143-151.

Cashman, K.D. (2020). Vitamin D deficiency: defining, prevalence, causes, and strategies of addressing. Calcified Tissue International, 106(1),14-29. https://doi.org/10.1007/s00223-019-00559-4

Cave, D. P., Abbey, K. L., & Capra, S. M. (2020). Can food services in aged care homes deliver sustainable food fortification strategies? A review. International Journal of Food Sciences and Nutrition, 71(3),267-275, https://doi.org/10.1080/09637486.2019.165872

Cichoscki, A. J., Valduga, E., Valduga, A. T., Tornadijo, M. E., & Fresno, J. M. (2002). Characterization of Prato cheese, a Brazilian semi-hard cow variety: evolution of physico-chemical parameters and mineral composition during ripening. Food Control, 13(4-5), 329-336.

Cormick, G., & Belizán, J. M. (2019). Calcium intake and health. Nutrients, 11(7), 1606. https://doi.org/10.3390/nu11071606

Coşkun, F. & Şenoğlu, C. (2011). The effect of using different levels of calcium carbonate on the physical, chemical and sensory properties of yoghurt. The Journal of Food, 36(3), 129-135.

Crevier, B., Belanger, G., Vuillemard J. C., & St Gelais, D. (2017). Short communication: Production of cottage cheese fortified with vitamin D. Journal of Dairy Sciendce, 100(7),5212-5216. https://doi.org/10.3168/jds.2016-12308

Cribb, V. L., Northstone, K., Hopkins, D., & Emmett, P. M. (2015). Sources of vitamin D and calcium in the diets of preschool children in the UK and the theoretical effect of food fortification. *Journal of Human Nutrition and Dietetics*, *28*(5), 583–592.

Dai, S., Corke, H., & Shah, N. P. (2016). Utilization of konjac glucomannan as a fat replacer in low-fat and skimmed yogurt. Journal of Dairy Science, 99(9), 7063-7074.

Dary, O., & Hurrell, R. (2006). *Guidelines on food fortification with micronutrients*. World Health Organization; Food and Agriculture Organization of the United Nations.

de Campo, C., Assis, R. Q., da Silva, M. M., Costa, T. M. H., Paese, K., Guterres, S. S., de Oliveria Rios, A., & Flôres, S. H. (2019). Incorporation of zeaxanthin nanoparticles in yogurt: Influence on physicochemical properties, carotenoid stability and sensory analysis. Food Chemistry, 301, 125230. https://doi.org/10.1016/j.foodchem.2019.125230

Demircioğlu, E. Ö., & Aslan, D. (2023). Halk sağlığı uygulamalarında gıda zenginleştirilmesi. Sürekli Tıp Eğitimi Dergisi, 32(1), 69-79.

Demirtaş, A., Kayahan, S., & Gezmen Karadağ, M. (2021). Probiyotiklerin doğal folat kaynağıolma potansiyeli. Gazi Sağlık Bilimleri Dergisi, 6(3)135-142.

Department of Health. (2018, February 10). *Regulations amending certain regulations made under the Food and Drugs Act (Nutrition Symbols, Other Labelling Provisions Partially Hydrogenated Oils and Vitamin D.)*. *Canada Gazette*, *152*(6). http://gazette.gc.ca/rp-pr/p1/2018/2018-02-10/pdf/g1-15206.pdf

Díaz-Castro, J., Alférez, M. J. M., López-Aliaga, I., Nestares, T., & Campos, M. S. (2009). Effect of calcium-supplemented goat or cow milk on zinc status in rats with nutritional ferropenic anaemia. International Dairy Journal, 19(2), 116-121.

Douglas Jr, F. W., Rainey, N. H., Wong, N. P., Edmondson, L. F., & LaCroix, D. E. (1981). Color, flavor, and iron bioavailability in iron-fortified chocolate milk. Journal of Dairy Science, 64(9), 1785-1793.

Drago, S. R., & Valencia, M. E. (2002). Effect of Fermentation on Iron, Zinc, and Calcium Availability from Iron-fortified Dairy Products. Journal of Food Science, 67(8), 3130-3134.

Drake, M. A., Chen, X. Q., Tamarapu, S., & Leenanon, B. (2000). Soy protein fortification affects sensory, chemical, and microbiological properties of dairy yogurts. Journal of Food Science, 65(7), 1244-1247.

Technical University of Denmark – National Food Institute. (2018). *Danish food composition database*. Retrieved May 28, 2025, from https://frida.fooddata.dk/QueryFood.php?fn=yogurt

Dwyer, J. T., Wiemer, K. L., Dary, O., Keen, C. L., King, J. C., Miller, K. B., Philbert, M. A., Tarasuk, V., Taylor, C. L., Gaine, P. C., Jarvis, A. B., & Bailey, R. L. (2015). Fortification and health: challenges and opportunities. Advances in Nutrition, 6(1), 124–131, https://doi.org/10.3945/an.114.007443

Edmondson, L. F., Douglas Jr, F. W., & Avants, J. K. (1971). Enrichment of pasteurized whole milk with iron. Journal of Dairy Science, 54(10), 1422-1426.

Ekşi A., & Karadeniz, F. (1996) Gıda Zenginleştirme Yaklaşımı ve Türkiye'de Uygulanma Olanağı. Beslenme ve Diyet Dergisi, 25(2),47-1.

European Union. (2008). *Council Directive 90/496/EEC on nutrition labelling for foodstuffs as regards recommended daily allowances, energy conversion factors and definitions*. Official Journal of the European Union, L 285/9 EN. [Amended by Commission Regulation 2008/100/EC of 28 October 2008].

Food and Agriculture Organization & World Health Organization. (1995). *Development of guidelines on the fortification requirements of lower fat products* (CX/NFSDU 95/9). Food and Agriculture Organization.

Food and Drug Administration. (1999). Food labeling health claims; Soy protein and coronary heart disease. *Federal Register*, *64*(222), 57699–57733.

Food and Drug Administration. (2011). *Code of Federal Regulations, Title 21, Part 182, Subpart I: Nutrients, Substances Generally Recognized as Safe*.

Friedeck, K. G., Aragul-Yuceer, Y. K., & Drake, M. A. (2003). Soy protein fortification of a low-fat dairy-based ice cream. Journal of Food Science, 68(9), 2651-2657.

Gaucheron, F. (2000). Iron fortification in dairy industry. Trends in Food Science & Technology, 11(11), 403-409.

Gerstner, G. (2002). Dairy products: The calcium challenge. International Food Ingredients, 3, 45-48.

Ghanbari, M., Saeedi, M., & Mortazavian, A. M. (2016). Nutraceuticals and functional foods production. Clinical Excellence, 5(1), 1-15.

Gıda, Tarım ve Hayvancılık Bakanlığı. (2013, August 16). *Türk Gıda Kodeksi Takviye Edici Gıdalar Tebliği* (Tebliğ No: 2013/49). *Resmi Gazete*, (28737).

Gibson, R. S., Bailey, K.B., Gibbs, M., & Ferguson, E. L. (2010). A review of phytate, iron, zinc, and calcium concentrations in plant-based complementary foods used in low-income countries and implications for bioavailability. Food and Nutrition Bulletin, 31,134-146.

Giroux, H. J., Constantineau, S., Fustier, P., Champagne, C. P., St-Gelais, D., Lacroix, M., & Britten, M. (2013). Cheese fortification using water-in-oil-in-water double emulsions as carrier for water soluble nutrients. International Dairy Journal, 29(2), 107-114.

González-Rodríguez, L. G., Estaire, P., Peñas-Ruiz, C., Ortega, R. M., & UCM Research Group VALORNUT. (2013). Vitamin D intake and dietary sources

in a representative sample of Spanish adults. *Journal of Human Nutrition and Dietetics*, *26*(1), 64–72.

Guéguen, L., & Pointillart, A. (2000). The bioavailability of dietary calcium. Journal of the American College of Nutrition, 19(sup2), 119S-136S.

Gulbas, S. Y., & Saldamli, I. (2005). The effect of selenium and zinc fortification on the quality of Turkish white cheese. International Journal of Food Sciences and Nutrition, 56(2), 141-146. https://doi.org/10.1080/09637480500082579

Gupta, C., Chawla, P., & Arora, S. (2015). Development and evaluation of iron microencapsules for milk fortification. CyTA-Journal of Food, 13(1), 116-123.

Gupta, C., Chawla, P., Arora, S., Tomar, S. K., & Singh, A. K. (2015). Iron microencapsulation with blend of gum arabic, maltodextrin and modified starch using modified solvent evaporation method–Milk fortification. Food Hydrocolloids, 43, 622-628.

Gutiérrez, G., Matos, M., Barrero, P., Pando, D., Iglesias, O., & Pazos, C. (2016). Iron-entrapped niosomes and their potential application for yogurt fortification. LWT- Food Science and Technology, 74, 550-556.

Hanson, A. L., & Metzger, L. E. (2010). Evaluation of İncreased vitamin D Fortification in high temperature, short-time-processed 2% milk, UHT-processed 2% fat chocolate milk, and low fat strawberry yogurt. Journal of Dairy Science, 93,801-807. https://doi.org/10.3168/jds.2009-2694

Harzer, G., & Kauer, H. (1982). Binding of zinc to casein. The American Journal of Clinical Nutrition, 35, 981-987. https://doi.org/10.1093/ajcn/35.5.981

Hasanvand, E., Fathi, M., Bassiri, A., Javanmard, M., & Abbaszadeh, R. (2015). Novel starch based nanocarrier for vitamin D fortification of milk: Production and characterization. Food and Bioproducts Processing, 96, 264-277.

Health Canada, Food Directorate, Health Products and Food Branch. (2018). *Category specific guidance for temporary marketing authorization: Caffeinated energy drinks*. https://www.canada.ca/en/health-canada/services/food-nutrition/legislation-guidelines/guidance-documents/category-specific-guidance-temporary-marketing-authorization-caffeinated-energy-drinks.html

Health Canada. (n.d. a). *Food and Drug Regulations: B.08.003*. Retrieved from https://www.canada.ca/en/health-canada/services/food-nutrition/legislation-guidelines/regulations/food-drug-regulations-b08003.html

Health Canada. (n.d. b). *Food and Drug Regulations: B.09.016*. Retrieved from http://www.hc-sc.gc.ca/food-aliment/friia-raaii/food_drugs-aliments_drogues/act-loi/pdf/e_b-text-1.pdf

Hekmat, S., & McMahon, D. J. (1997). Manufacture and quality of iron-fortified yogurt. Journal of Dairy Science, 80(12), 3114-3122.

Hennessy, Á., Browne, F., Kiely, M., Walton, J., & Flynn, A. (2017). The role of fortified foods and nutritional supplements in increasing vitamin D intake in Irish preschool children. *European Journal of Nutrition*, *56*(3), 1219–1231.

Hill, M. J. (1997). Intestinal flora and endogenous vitamin synthesis. European Journal of Cancer Prevention, 6(1),43-45.

Holick, M. F. (1999). Vitamin D. In *Modern nutrition in health and disease* (9th ed., pp. 329–345). William & Wilkins.

Holick, M. F., Shao, Q., Liu, W. W., & Chen, T. C. (1992). The vitamin D content of fortified milk and infant formula. New England Journal of Medicine, 326(18), 1178-1181.

Huang, Y. C. (2000). Nutrient intakes and iron status of vegetarians. Nutrition, 16(2),147- 148.

Hugunin, A. (1999). Whey products in yogurt and fermented dairy products. US Dairy Export Council, 1-8.

Hunt, C. D., & Nielsen, F. H. (2009). Nutritional aspects of minerals in bovine and human milk. In P. L. H. McSweeney & P. F. Fox (Eds.), *Advanced dairy chemistry: Vol. 3. Lactose, water, salts and minor constituents* (3rd ed., p. 420). Springer.

Hurrell, R. F., Reddy, M. B., Dassenko, S. A., Cook, J. D., & Shepherd, D. (1991). Ferrous fumarate fortification of a chocolate drink powder. British Journal of Nutrition, 65(2), 271-283.

Hurrell., R. F. 1997. Preventing iron deficiency through food fortification. Nutrition Reviews 55 (6), 210-222.

Ilgaz, Ş., Yardım, N., Çimen, M. Y. B., Kanbur, N., Özmert, E. N., Satman, İ., Tavil, B., Tayfur, M., & Umman, C. (2020). Türkiye'de besinlerin D vitamini, folik asit ve demir ile zenginleştirilmesi: Sağlık bakanlığı önerileri. Turkish Journal of Public Health, 18(3),226-248.

Ilic, D. B., & Ashoor, S. H. (1988). Stability of vitamins A and C in fortified yogurt. Journal of Dairy Science, 71(6), 1492-1498.

Institute of Medicine. (2011). *Dietary reference intakes for calcium and vitamin D*. The National Academies Press.

Isleten, M., & Karagul-Yuceer, Y. (2006). Effects of dried dairy ingredients on physical and sensory properties of nonfat yogurt. Journal of Dairy Science, 89(8), 2865-2872.

Itkonen, S. T., Erkkola, M., & Lamberg-Allardt, C. J. (2018). Vitamin D fortification of fluid milk products and their contribution to vitamin D intake and vitamin D status in observational studies—a review. Nutrients, 10(8), 1054.

Jackson, L. S., & Lee, K. (1991). Microencapsulated iron for food fortification. Journal of Food Science, 56(4), 1047-1050.

Jackson, L. S., & Lee, K. (1992). Fortification of cheese with microencapsulated iron. *Cultured Dairy Products Journal*, 27(2), 4-7.

Jafari, T., Askari, G., Mirlohi, M., Javanmard, S. H., Faghihimani, E., & Fallah, A. A. (2016). Stability of Vitamin D_3 in fortified yoghurt and yoghurt drink (Doogh). Advanced Biomedical Research, 5(1),52. https://doi.org/10.4103/2277-9175.178796

Jayaratne, N., Hughes, M. C., Ibiebele, T. I., Van den Akker, S., & Van der Pols, J. C. (2013). Vitamin D intake in Australian adults and the modeled effects of milk and breakfast cereal fortification. *Nutrition*, *29*(7-8), 1048–1053.

Jovaní, M., Barberá, R., & Farré, R. (2001). Effect of some components of milk-and soy-based infant formulas on mineral bioavailability. Food Science and Technology International, 7(3), 191-198.

Juneja, L. R. (2001, June 23–27). *Improved solubility, safety and bioavailability of superdispersed ferric pyrophosphate-a new concept of iron fortification* [Paper presentation]. 2001 IFT Annual Meeting, New Orleans, LA, United States.

Kahraman, Ö. (2011). Süt ve süt ürünlerinin çinko ile zenginleştirilmesine ilişkin yaklaşımlar. Gıda, 36(4), 241-248

Kahyaoğlu, F., & Demirci, B. D. (2019). The importance of enriched and fortified foods on health and practices in some countries. Bozok Tıp Dergisi, 9(2), 164-169. https://doi.org/10.16919/bozoktip.451123

Kaup, S. M. 1998. Aspects of mineral bioavailability in infant nutrition. International Dairy Journal 8, 435-441. https://doi.org/10.1016/S0958-6946(98)00066-1

Kaushik, R., Sachdeva, B., Arora, S., Kapila, S., & Wadhwa, B. K. (2014). Bioavailability of vitamin D_2 and calcium from fortified milk. Food Chemistry, 147, 307-311.

Kazmi, S.A., Vieth, R., & Rousseau, D. (2007). Vitamin D_3 fortification and quantification in processed dairy products. International Dairy Journal, 17, 753 759. https://doi.org/10.1016/j.dairyyj.2006.09.009

Khalili, M., Rad, A.H., Khosroushahi, A.Y., Khosravi, H., & Jafarzadeh, S. (2019). Application of probiotics in folate biofortification of yoghurt. Probiotics and Antimicrobial Proteins, 12, 756-763.

Kınık, Ö., Gürsoy, O., & Gökçe, R. (2003). Süt ürünlerinin demir ile zenginleştirilmesi. Pamukkale Üniversitesi Mühendislik Bilimleri Dergisi, 9(3), 393-401.

Kırımi, E., Tuncer, O., Ataş, B., & Ceylan, A. (2004). Yaşamın ilk altı ayında yalnızca anne sütü veya demirle zenginleştirilmiş mama ile beslenen süt çocuklarında 5. ve 1. aylarda büyüme ve demir durumu. Turkiye Klinikleri Journal of Medical Sciences 24(6), 608-613.

Kim, S. J., Ahn, J., Seok, J. S., & Kwak, H. S. (2003). Microencapsulated iron for drink yogurt fortification. Asian-Australasian Journal of Animal Sciences, 16(4), 581-587.

Knapen, M.H., Braam, L.A., Teunissen, K.J., Zwijsen, R.M., Theuwissen, E., & Vermeer, C. (2015). Yogurt drink fortified with menaquinone-7 improves vitamin K status in a healthy population. Journal of Nutritional Science, 4(35), 1-8.

Kutluay Merdol, T., Baş, M., Kızıltan, G., Şensoy, F., Şeker, E., Dağ, A., & Acar Tek, N. (2013). *Genel beslenme*. Anadolu Üniversitesi Yayını No: 2768; Açıköğretim Fakültesi Yayını No: 1726.

Küçük, S. C., & Yıbar, A. (2018). D vitamini ile zenginleştirilmiş yoğurdun besin değeri ve metabolik etkileri. Gıda, 43(4), 549-557.

Kwak, H. S., Yang, K. M., & Ahn, J. (2003). Microencapsulated iron for milk fortification. Journal of Agricultural and Food Chemistry, 51(26), 7770-7774.

Laiño, J. E., Valle, M. J., Savoy de Giori, G., & LeBlanc, J. G. (2014). Applicability of a *Lactobacillus amylovorus* strain as co culture for natural folate bio-enrichment of fermented milk. International Journal of Food Microbiology, 191(17),10-16. https://doi.org/10.1016/j.ijfoodmicro.2014.08.031

LeBlanc, J. G., Laino, J. E., Juarez del Valle, M., Vannini, V., Van Sinderen, D.,Taranto, M. P., Font de Valdez, G. , Savoy de Giori, G., & Sesma, F. (2011). B-Group vitamin production by lactic acid bacteria – current knowledge and potential applications. Journal of Applied Microbiology, 111(6),1297-309. https://doi.org/10.1111/j.1365-2672.2011.05157.x

Lee, J. B., Ahn, J., Lee, J., & Kwak, H. S. (2004). L-ascorbic acid microencapsulated with polyacylglycerol monostearate for milk fortification. Bioscience, biotechnology, and Biochemistry, 68(3), 495-500.

Levinson, Y., Ish-Shalom, S., Segal, E., & Livney, Y. D. (2016). Bioavailability, rheology and sensory evaluation of fat-free yogurt enriched with VD_3 encapsulated in re-assembled casein micelles. Food & Function, 7(3), 1477-1482.

Lim, C., Kiesius, P. H., Li, H., & Robinson, E. H. (2000). Interaction between dietary levels of iron and vitamin C on growth, hematology, immune response and resistance on chemical catfish (Ictalurus punctatus) to Edwardsiella ictalun challenge. Aquaculture, 185, 313–327.

Lindsay, A., Benoist, B., Dary, O., & Hurrell, R. (2006). *Guidelines on food fortification with micronutrients*. World Health Organization; Food and Agriculture Organization of the United Nations. https://citeseerx.ist.psu.edu/document?repid=rep1&type=pdf&doi=19d204d5568d78c25c7f3feedeb53c1ae87b5ce2

Livsmedelsverket. (1983). *Food Agency's Order about Fortification of Foodstuffs* (SLVFS 1983:2) [Livsmedelverkets Föreskrifter om Berikning av Vissa Livsmedel]. https://www.livsmedelsverket.se/globalassets/om-oss/lagstiftning/berikn---kosttillsk---livsm-spec-gr-fsmp/slvfs-1983-02-kons.pdf

Livsmedelsverket. (2018). *Food Agency's order about fortification of foodstuffs* (LIVSFS 2018:5) [Livsmedelverkets föreskrifter om berikning av vissa livsmedel]. https://www.livsmedelsverket.se/globalassets/om-oss/lagstiftning/berikn---kosttillsk---livsm-spec-gr-fsmp/livsfs-2018-5_web.pdf

Lotfi, M., Mannar, M.G.V., Merx, R., & Heuvel, P.N. (1996). *Micronutrient Fortification of Foods: Current Practices, Research and Opportunities*. The Micronutrient Initiative & The International Agricultural Centre. Retrieved from http://www.emro.who.int/NFS/FlourFortification-IronFlourFortificationReferences.htm

Lysionek, A. E., Zubillaga, M. B., Salgueiro, M. J., Pineiro, A., Caro, R. A., Weill, R., & Boccio, J. R. (2002). Bioavailability of microencapsulated ferrous sulfate in powdered milk product from fortified fluid milk: A prophylactic study in rats. Nutrition 18, 279- 281.

Madenci, A. B., Aktaş, K., & Türker, S. (2013). Yayıkaltının Sağlıklı Beslenme Açısından Önemi ve Fırıncılık Ürünlerinde Kullanımı. *Uluslararası 2. Helal ve Sağlıklı Gıda Kongresi*, 656–657.

Maret, W., & Sandstead, H. H. (2006). Zinc requirements and the risks and benefits of zinc supplementation. Journal of Trace Elements in Medicine and Biology, 20(1), 3-18.

Martınez-Navarrete, N., Camacho, M. M., Martınez-Lahuerta, J., Martınez-Monzó, J., &Fito, P. (2002). Iron deficiency and iron fortified foods—a review. Food Research International, 35(2-3), 225-231.

Maurya, V.K., Bashir, K., & Aggarwal, M. (2020). Vitamin D microencapsulation and fortification: trends and technologies. The Jourbal of Steroid Biochemistry Moleculer Biology, 196,105489. https://doi.org/10.1016/j.jsbmb.2019.105489

McBean, L. D., & Speckmann, E. W. (1988). Nutritive value of dairy foods. In *Fundamentals of dairy chemistry* (pp. 343–407). Springer US.

Mehansho, H. (2006). Iron fortification technology development: new approaches. The Journal of Nutrition, 136(4), 1059-1063.

Miller, G. D., Jarvis, J. K., & McBean, L. D. (2006). *Handbook of dairy foods and nutrition*. CRC Press.

Ministry of Agriculture and Forestry of Finland. (2016). *Decree on the vitamin D fortification of fat-free homogenized milk* (Maa-ja metsätalousministeriön asetus rasvattoman homogenoidun maidon D-vitaminoinnista). http://www.finlex.fi/fi/laki/alkup/2016/20160754

Monsen, E. R., (1988). Iron nutrition and absorption: dietary factors which impact iron bioavailability. Journal of the American Dietetic Association, 88, 786–790.

Moore, C., Murphy, M. M., Keast, D. R. & Holick, M. F. (2004). Vitamin D intake in the United States. Journal of the American Dietetic Association, 104(6), 980-983.

Max Rubner-Institut. (2018). *The German Nutrient Database*. Retrieved March 29, 2018, from https://www.vitamine.com/lebensmittel

Nasjonalt råd for ernæring. (2006). *Measures to ensure a good vitamin D status in the population* (Tiltak for å Sikre en God Vitamin D-Status I Befolkningen). https://helsedirektoratet.no/Documents/Om%20oss/R%C3%A5d%20og%20utvalg/Nasjonalt%20r%C3%A5d%20for%20ern%C3%A6ring/Tiltak%20for%20%C3%A5%20sikre%20en%20god%20vitamin%20D-status%20i%20befolkningen%20IS-1408.pdf

National Institutes of Health, Office of Dietary Supplements. (2011). *Dietary supplement fact sheet: Vitamin D*. https://ods.od.nih.gov/factsheets/VitaminD-HealthProfessional/

National Nutrition Council. (2010). *Report of vitamin D Working Group* (Valtion Ravitsemusneuvottelukunta D-Vitamiinityöryhmän Raportti). https://www.evira.fi/globalassets/vrn/pdf/d-vitamiiniraportti2010.pdf

Nichols, J. G. (1992, December 22). *Recommended levels of vitamins A & D in milk products* (M-I-92-13). U.S. Food and Drug Administration, Milk Safety Branch. http://vm.cfsan.fda.gov/~ear/prime.html

Nikooyeh, B., Neyestani, T.R., Farvid, M., AlaviMajd, H., Houshiarrad, A., Kalayi, A., Shariatzadeh, N., Gharavi, A., Heravifard, S., Tayebinejad, N., Salekzamani S., & Zahedirad M. (2011). Daily consumption of vitamin D- or vitamin D+ calcium- fortified yogurt drink improved glycemic control in patients with type 2 diabetes: a randomized clinical trial. *The American Journal of Clinical Nutrition,* 93, 764-71. https://doi.org/10.3945/ajcn.110.007336

Ningtyas, D. W., Bhandari, B., Bansal, N., & Prakash, S. (2019). Flavour profiles of functional reduced-fat cream cheese: Effects of β-glucan, phytosterols, and probiotic L. rhamnosus. LWT-Food Science and Technology, 105, 16-22.

Nowson, C. A., & Margerison, C. (2002). Vitamin D intake and vitamin D status of Australians. Medical journal of Australia, 177(3), 149-152.

National Research Council. (1993). *Nutrient requirements of fish*. National Academy Press.

Panda, A. K., Mishra, S. & Mohapatra, S. K. (2011). Iron in ayurvedic medicine. Journal of Advances in Developmental Research, 2(2), 287-293.

Park, H. S., Ahn, J., & Kwak, H. S. (2008). Effect of nano-calcium-enriched milk on calcium metabolism in ovariectomized rats. Journal of Medicinal Food, 11(3), 454-459.

Parrish, D. B., & Richter, E. F. (1979). Determination of vitamin D in foods: a review. Critical Reviews in Food Science & Nutrition, 12(1), 29-57.

Peng, Y., Serra, M., Horne, D. S., & Lucey, J. A. (2009). Effect of fortification with various types of milk proteins on the rheological properties and permeability of nonfat set yogurt. Journal of Food Science, 74(9), C666-C673. https://doi.org/10.1111/j.1750-3841.2009.01350.x

Perales, S., Barberá, R., Lagarda, M. J., & Farré, R. (2006). Fortification of milk with calcium: effect on calcium bioavailability and interactions with iron and zinc. Journal of Agricultural and Food Chemistry, 54(13), 4901-4906.

Pirkul, T., Temiz, A., & Erdem, Y. K. (1997). Fortification of yoghurt with calcium salts and its effect on starter microorganisms and yoghurt quality. International Dairy Journal, 7(8-9), 547-552.

Public Health Service. (1965). *Grade "A" pasteurized milk ordinance, 1965: Recommendations of the Public Health Service* (Public Health Service Publication No. 229). U.S. Government Printing Office.

Public Health Service/U.S. Food and Drug Administration. (2015). *Grade "A" pasteurized milk ordinance* (Revision). Public Health Service. https://www.idfa.org/docs/default-source/d-news/2015-pmo-final.pdf

Public Health Service/U.S. Food and Drug Administration. (1978). *Grade "A" Pasteurized Milk Ordinance* (Public Health Service Publication No. 229). U.S. Government Printing Office.

Ritu, G., & Gupta, A. (2014). Fortification of Foods with Vitamin D in India. Nutrients, 6, 3601-3623. https://doi.org/10.3390/nu6093601

Rosado, J. L. (2003). Zinc and copper: proposed fortification levels and recommended zinc compounds. The Journal of Nutrition, 133(9), 2985S-2989S.

Salas-Brıngas, C., Rukke, E. O., Saga, L., Lekang, O. I., & Schuller, R.B., (2010). Rheological properties of buttermilk pellets manufactured by a new die pelleting rig of a texture analyzer. Annual Transactions of the Nordic Rheology Society, 18, https://nordicrheologysociety.org/Content/Transactions/2010/Poster/Salas-Bringas%20et%20al%20(4)%202010.pdf

Salgueiro, M. J., Zubillaga, M., Lysionek, A., Caro, R., Weill, R., & Boccio, J. (2002). Fortification strategies to combat zinc and iron deficiency. Nutrition reviews, 60(2), 52-58.

SandstroÈm, B. (2001). Micronutrient interactions: effects on absorption and bioavailability. British journal of Nutrition, 85(S2), S181-S185.

Schuck, P., & Dolivet, A. (2002). Lactose crystallization: Determination of α-lactose monohydrate in spray dried dairy products. Lait, 82, 413-421. https://doi.org/10.1051/lait:2002020

Seidell, J. C. (1998). Dietary fat and obesity: an epidemiologic perspective. The American Journal of Clinical Nutrition, 67(3), 546S-550S.

Senyk, G. F., & Shipe, W. F. (1981). Protecting your milk from nutrient losses. Dairy Field, 164(3), 81-82,84-85.

Šeregelj, V., Pezo, L., Šovljanski, O., Lević, S., Nedović, V., Markov, S., Tomić, A., Čanadanović-Brunet, J., Vulić, J., Šaponjac V. T., Ćetković, G., & Ćetković, G. (2021). New concept of fortified yogurt formulation with encapsulated carrot waste extract. LWT-Food Science and Technology, 138, 110732.

Shibu, A. V., Kumar, C. N., Narasımhan, R., & Pugazhenthi, T. R. (2000). Substitution of buttermilk powder in ice cream. Journal of Veterinary and Animal Sciences, 31, 25-27.

Singh, G., Arora, S., Sharma, G. S., Sindhu, J. S., Kansal, V. K., & Sangwan, R. B. (2007). Heat stability and calcium bioavailability of calcium-fortified milk. LWT-Food Science and Technology, 40(4), 625-631.

Singh, H., Flynn, A., & Fox, P. F. (1989). Zinc binding in bovine milk. Journal of Dairy Research, 56(2), 249-263.

Smith S. (2016). Personal communication. DSM Nutritional Products: Parsippany, N.J

Smith, K. (2008). *Dried dairy ingredients*. Wisconsin Center for Dairy Research.

Takasugi, S., Matsui, T., Omori, H., & Yano, H. (2007). Excess calcium increases bone zinc concentration without affecting zinc absorption in rats. Biological Trace Element Research, 116, 311-320.

Tan, P. Y., Tan, T. B., Chang, H. W., Tey, B. T., Chan, E. S., Lai, O. M., Baharin, S. M., Nehdi, I. A., & Tan, C. P. (2018). Effects of storage and yogurt matrix on the stability of tocotrienols encapsulated in chitosan-alginate microcapsules. Food Chemistry, 241, 79-85. https://doi.org/10.1016/j.foodchem.2017.08.075

Tektunalı Akman, C., & Garipağaoğlu, M. (2018). Besin zenginleştirmesi. Sağlık ve Toplum. 3, 3-9.

Tesan, F. C., Collia, N., Arnoldi, S., Fuda, J., Torti, H., Weil,l R., Salgueiro, M. J., & Boccio, J. (2009). Relative bioavailability of zinc in yogurt using body weight gain, femur weight and bone zinc content in rats as markers. The Open Nutraceuticals Journa,l 2,16-19.

Teucher, B., Olivares, M. & Cori, H. (2004). Enhancers of iron absorption: ascorbic acid and other organic acids. International Journal for Vitamin and Nutrition Research, 74(6), 403-419.

Türkiye Gıda Kodeksi. (2017, January 26). Beslenme ve Sağlık Beyanları Yönetmeliği (Sayı: 29960). T.C. Resmî Gazete. https://resmigazete.gov.tr/eskiler/2017/01/20170126M1-5.htm

Tipchuwong, N., Chatraporn, C., Ngamchuachit, P. (2017). Increasing retention of vitamin D_3 in vitamin D_3 fortified ice cream with milk protein emulsifier. International Dairy Journal, 74, 74-79.

Titcomb, T. J., & Tanumihardjo, S. A. (2019). Global Cconcerns with B vitamin statuses: Biofortification, fortification, hidden hunger, interactions, and toxicity. *Comprehensive Reviews in Food Science and Food Safety*, 18(6),1968-1984. https://doi.org/10.1111/1541- 4337.12491

Toniazzo, T., Berbel, I. F., Cho, S., Fávaro-Trindade, C. S., Moraes, I. C., & Pinho, S. C. (2014). β-carotene-loaded liposome dispersions stabilized with xanthan

and guar gums: Physico-chemical stability and feasibility of application in yogurt. LWT-Food Science and Technology, 59(2), 1265-1273.

Tripkovic, L., Lambert, H., Hart, K., Smith, C.P., Bucca, G., Penson, S., Chope, G., Hyppönen, E., Berry, J., Vieth, R., & Lanham-New, S. (2012). Comparison of Vitamin D2 and D3 supplementation in raising serum 25 hydroxyvitamin D status: a systematic review and meta-analysis. *The American Journal of Clinical Nutrition*, 95,1357-64. https://doi.org/10.3945/ajcn.111.031070

Troise, A. D., Vitiello, D., Tsang, C., & Fiore, A. (2016). Encapsulation of ascorbic acid promotes the reduction of Maillard reaction products in UHT milk. Food & Function, 7(6), 2591-2602.

Türker, A., & Yüksel, O. (2019). Beslenmede Vitaminlerin Önemi. Beslenme ve Obezite, 7,7-32.

TürKomp. (2018). *Ulusal Gıda Kompozisyon Veri Tabanı*. http://www.turkomp.gov.tr/main

U.S. Food and Drug Administration. (n.d.). Direct food substances affirmed as generally recognized as safe. Subpart B: Listing of specific substances affirmed as GRAS. Sec. 184.1950 Vitamin D. Retrieved May 29, 2025, from http://www.accessdata.fda.gov/scripts/cdrh/cfcfr/CFRSearch.cfm?fr184.1950

U.S. Department of Agriculture, Agricultural Research Service. (2018). *USDA Branded Food Products Database*. National Agricultural Library. https://fdc.nal.usda.gov/

Ünal, G., & Akalın, A. S. (2004). Demir eksikliği ve süt ürünlerinin demirce zenginleştirilmesi. Gıda, 29(4),317-323.

Whited, L. J., Hammond, B. H., Chapman, K. W., & Boor, K. J. (2002). Vitamin A degradation and light-oxidized flavor defects in milk. Journal of Dairy Science, 85(2), 351-354.

World Health Organization & Food and Agriculture Organization of the United Nations, (2006). *Guidelines on food fortification with micronutrients*. World Health Organization.

World Health Organization. (2001). *Zinc: Environmental health criteria 221*. World Health Organization. https://iris.who.int/handle/10665/42337

Yeh, E. B., Barbano, D. M., & Drake, M. (2017). Vitamin fortification of fluid milk. Journal of Food Science, 82(4), 856-864.

Yeung, A. C., Glahn, R. P. & Miller, D. D. (2001). Dephosphorylation of sodium caseinate, enzymatically hydrolyzed casein and casein phosphopeptides by

intestinal alkaline phosphatase: implications for iron availability. The Journal of Nutritional Biochemistry, 12(5), 292-299.

Yıldırım, Ç., & Güzeler, N. (2013). Peyniraltı suyu ve yayıkaltının toz olarak değerlendirilmesi. Çukurova Üniversitesi Ziraat Fakültesi Dergisi, 28(2), 11-20.

Youdim, M. B. H. (2000). Nutrient deprivation on brain function: Iron. Nutrition 16 (7/8): 504-508.

Young, S. (2007). *Whey products in ice cream and frozen dairy desserts*. U.S. Dairy Export Council.

Yurttagül, M. (1995). Hafif şişman ve şişman kadınların beslenme alışkanlıkları ve zayıflamaya ilişkin tutum ve davranışları. Beslenme ve Diyet Dergisi, 24(1), 59-73.

Zhang, D., & Mahoney, A. W. (1991). Iron fortification of process Cheddar cheese. Journal of Dairy Science, 74(2), 353-358.

Zind, T. (1998). Making the case for soy. Food Processing, 25(7), 31-34.

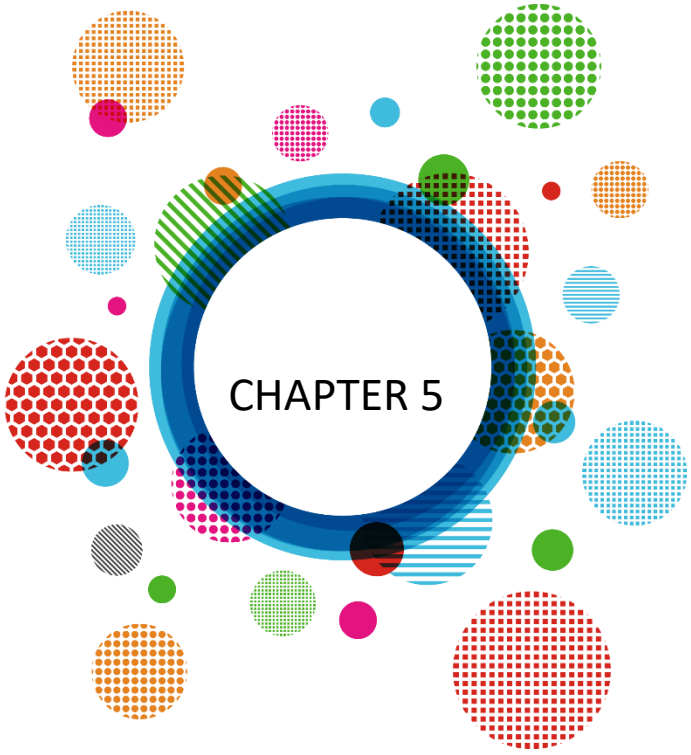

Modeling the Impact of Energy Consumption on Population Forecasting in Türkiye Using Artificial Neural Networks

Cebrail Çiflikli[1] & Ayça Yıldız[2] & Bahatdin Daşbaşı[3]

[1] Prof. Dr., Kayseri University, Vocational School of Technical Sciences, Department of Electronics and Automation, Electronics and Communication Technology Program Kayseri/Turkey. https://orcid.org/0000-0001-7389-3100

[2] Kayseri University, Graduate School of Education, Department of Electrical and Electronics Engineering Kayseri/Turkey. https://orcid.org/0000-0003-1086-0074

[3] Assoc. Prof. Kayseri University, Faculty of Engineering, Architecture and Design, Department of Engineering Basic Sciences, Kayseri/Turkey, https://orcid.org/0000-0001-8201-7495

1. INTRODUCTION

Energy consumption patterns are fundamental indicators of a country's level of development, economic sustainability, and environmental impact. In developing nations such as Turkey, the increasing demand for energy is closely tied to rapid population growth. The types of energy utilized—including natural gas, hydroelectric power, coal and its derivatives, liquid fuels, renewable energy, and waste-based sources—not only reflect the energy strategy of a nation but also serve as key variables for demographic forecasting (Kizilaslan & Karlik, 2009).

Natural gas is considered a cleaner fossil fuel with relatively low carbon emissions, extensively used in heating and power generation (Karimi & Dastranj, 2014). Hydroelectric energy, produced by harnessing the kinetic energy of water, is a renewable source with minimal environmental footprint, playing a significant role in the energy mix of water-rich countries like Turkey (Gunduz & Sahin, 2015). Coal and coal-based derivatives remain primary energy sources, especially for electricity generation, despite their high greenhouse gas emissions and environmental concerns (Yilmaz, Tosunoğlu, Kaplan, Üneş, & Hanay, 2022). Liquid fuels, such as gasoline and diesel, are widely used in the transportation and industrial sectors, given their high energy density and infrastructure compatibility (Günay, 2016).

In contrast, renewable energy sources such as solar, wind, and biomass, along with energy recovery from waste, offer environmentally sustainable alternatives and are critical for reducing dependence on fossil fuels (Gulcu & Kodaz, 2017). The demand for these energy sources tends to rise in parallel with population growth, especially in urbanizing regions, where energy requirements for housing, transportation, and industry increase (Hamzaçebi, Es, & Çakmak, 2017). The interplay between energy consumption and population dynamics is complex and nonlinear. Therefore, traditional statistical models may fall short in capturing these relationships. ANNs, inspired by biological neural systems, offer strong predictive capabilities in datasets with high dimensionality and complex interdependencies (K. Kavaklioglu & Ceylan, 2009).

Artificial Neural Networks (ANNs) are computational models that mimic the functional structure of biological nervous systems, particularly neurons in the human brain, through mathematical representations in a computer environment (Shanmuganathan, 2016). The learning algorithms used in these systems differ from traditional programming approaches in that they resemble biological learning processes, exhibiting intuitive and adaptive properties. As a result, ANNs have attracted significant attention in various disciplines and are effectively used in numerous application areas such as time series analysis, optimization, classification, analysis of relationships between variables, and modeling of nonlinear systems (Daşbaşı, Barak, Taşyürek, & Arslan, 2024;

Singh, Tiwari, & Ajbar, 2025; Wang, Li, Song, & Rong, 2020). Artificial neural networks are composed of three fundamental layers: the input layer, the hidden layer, and the output layer. Each of these layers contains interconnected artificial neurons. The input layer functions as the interface through which external data are introduced into the network. The number of neurons in this layer is determined by the number of parameters influencing the given problem. The output layer, on the other hand, is responsible for transmitting the processed information from the network to the external environment. Positioned between the input and output layers, the hidden layer solely receives signals from the input layer and transmits them to the output layer; it does not have any direct interaction with the external environment. Neurons in the hidden layer play a crucial role in determining the learning capacity and overall performance of the network (Benli, 2002; Warner & Misra, 1996).

In their work in (Murat & Ceylan, 2006), Murat and Ceylan proposed an artificial neural network (ANN) approach based on supervised neural networks for transportation energy demand forecasting using socio-economic and transportation related indicators. Kialashaki and Reisel (Kialashaki & Reisel, 2013) proposed two sets of models for developing energy demand models that can predict future energy demand in the residential sector in the USA. One of these sets uses the artificial neural network (ANN) technique and the other uses the multiple linear regression (MLR) technique. In the study in (Sözen, 2009), Sözen aimed to obtain numerical equations to estimate Türkiye's energy dependency based on basic energy indicators and sectoral energy consumption by using artificial neural network (ANN) technique. In their study (Uzlu, Kankal, Akpınar, & Dede, 2014), Uzlu et al. aimed to apply the ANN (artificial neural network) model together with the TLBO (teaching-learning based optimization) algorithm to estimate the energy consumption in Türkiye. Aydın (Aydın, 2014) modeled Türkiye's PEC using regression analysis (RA) based on population (CP) and gross domestic product (GDP). He also validated the model he proposed using various statistical approaches such as coefficient of determination, t-test, F-test and residual analysis.

In this study, we propose the use of Artificial Neural Networks (ANN) to model the nonlinear interactions between multiple energy sources and population growth in Turkey. Using historical data on energy consumption across six main categories (natural gas, hydro, coal, liquid fuels, renewable energy, and waste) and corresponding population data, the ANN model will be trained to forecast future population levels. This approach not only enables more accurate demographic forecasting but also provides insights into how shifts in energy usage could signal population trends in emerging economies.

2. DATASET

The population of Turkey was estimated using Artificial Neural Networks (ANN) based on the consumption of various energy sources between 1985-2020. For this purpose, data on natural gas, hydroelectric energy, coal and coal derivatives, liquid fuels, renewable energy and waste consumption were considered as input variables for the model. The data from TSI is given in Table 1.

Table 1. Data (TSI)

Natural Gas x_1	**Hydroelectric Energy x_2**	**Coal and Coal Derivatives x_3**	**Liquid Fuel x_4**	**Renewable Energy And Waste x_5**	**Population y**
0	3032800	2824500	2600000	165700	35.605.176
0	2610200	2980200	4028300	162400	36.553.685
0	3204200	2920800	4941400	175500	37.502.193
…	…	…	…	…	…
92482816,5	59938425,6000	113248625,2	329116,1	38802901,6	82.003.882
57288201	88822775,6000	112894124	336003	44556456	83.154.997
70931333,1	78094368,8000	105812004,1	322660,1	51542726,3	83.614.362

The data presented in Table 1 were taken into account for the years 1985-2020. Since some population data were missing, the data were linearly increased. Thus, a dataset of 51x6 size with 5 input and 1 output variable was reached. The data to be analyzed will be the input columns first and then the output column, respectively. Furthermore, for the data given in Table 1, the some following conclusions was achieved in Table 2.

Table 2. Some results for analysis data in Table 1.

	Minimum value (1.0e+07 *)	Maximum value (1.0e+08 *)	Means (1.0e+07 *)	Standart Deviation (1.0e+07 *)
x_1	0	1.2058	3.8449	4.1792
x_2	0.2603	0.8882	3.0974	2.1256
x_3	0.2824	1.1325	3.5411	3.1106
x_4	0.0323	0.1074	0.5153	0.2594
x_5	0	0.5154	0.5026	1.1813
y	0.35605	0.8361	6.0362	1.4385

3. METHODOLOGY

Within the scope of this study, data on energy consumption between the years 1985 and 2020, published by the Turkish Statistical Institute (TSI), were analyzed. In this context, certain variables derived from energy consumption data that influence population estimation were examined using an artificial neural network (ANN) model. Five variables were used as inputs in the model, which aimed to estimate the population as the output. These are $x_i(t)$ for $i = 1,2,\dots,5$ in Table 1.

In artificial neural networks, activation functions are mathematical operations used to determine the output of a neuron. These functions make the network suitable for learning and especially enable modeling of non-linear relationships. Without activation functions, neural networks only work as a linear regression model and cannot learn complex data. Information about some activation functions is presented in Table 3.

Table 3. Equations used in ANN analysis and their explanations

Name	Mathematical Expression $(f(x))$	Activation Equation (y)	Output Range	Key Features
Hyperbolic Tangent Sigmoid	$\frac{e^x - e^{-x}}{e^x + e^{-x}}$	$b_2 + LW\tanh(b_1 + IWx)$	(-1, 1)	Zero-centered; used in hidden layers; may suffer from vanishing gradients.
Log-Sigmoid	$\frac{1}{1+e^{-x}}$	$b_2 + LW\text{logsig}(b_1 + IWx)$	(0, 1)	Output bounded between 0 and 1; used in classification.
Linear	x	$b_2 + LW\text{purelin}(b_1 + IWx)$	(-∞, ∞)	Preserves linearity; limited learning capability.
Positive Linear	$max(0,x)$	$b_2 + LW\text{poslin}(b_1 + IWx)$	[0, ∞)	Efficient; sparse activation; suppresses negatives.
Radial Basis	e^{-x^2}	$b_2 + LW\text{radbas}(b_1 + IWx)$	(0, 1]	Localized; used in RBF networks.
Saturating Linear	$\begin{cases}0, x < 0\\ x, 0 \le x \le 1\\ 1, x > 1\end{cases}$	$b_2 + LW\text{satlin}(b_1 + IWx)$	[0, 1]	Saturates outside [0,1]; limits learning at extremes.
Symmetric Saturating Linear	$\begin{cases}-1, x \le -1\\ x, -1 < x < 1\\ 1, x \ge 1\end{cases}$	$b_2 + LW\text{satlins}(b_1 + IWx)$	[-1, 1]	Zero-centered; symmetric saturation.
Softmax	$\frac{e^{x_i}}{\sum_j e^j}$	$b_2 + LW\text{softmax}(b_1 + IWx)$	(0, 1), sum = 1	Probability output; used in multi-class classification.
Triangular Basis	$\begin{cases}1 - \lvert x\rvert, -1 < x < 1\\ 0, otherwise\end{cases}$	$b_2 + LW\text{tribas}(b_1 + IWx)$	[0, 1]	Peak at center; localized activation.
Hard Limit	$\begin{cases}0, x < 0\\ 1, x \ge 0\end{cases}$	$b_2 + LW\text{hardlim}(b_1 + IWx)$	{0, 1}	Binary step; not differentiable.

Symmetric Hard Limit	$\begin{cases} -1, x < 0 \\ 1, x \geq 0 \end{cases}$	$b_2 + LW\text{hardlims}(b_1 + IWx)$	{-1, 1}	Zero-centered step; non-differentiable.

In here, it is showed Input weights by IW, Layer weights by LW and Bias terms by b1 and b2. Also, each activation function is suitable for different types of neural networks (e.g., RBF, classification, regression).

The main purpose of the Artificial Neural Network analysis is to estimate the population of Turkey using the 5 inputs given above regarding energy consumption. To achieve this, a customized Artificial Neural Network model was developed. The dataset was divided into training (%70), testing (%15) and validation sets (%15). These subsets were used in the relevant stages of the Artificial Neural Network model development. As a result, the modeling process aimed to determine the ANN configuration that can estimate the population of Turkey with minimum error. For this purpose, the data presented in Table 1 were, respectively,

- Directly taken.

- Taken by applying min-max normalization.

- Taken by applying normalization according to Z-score.

Then, for each dataset, the activation function that showed the best performance for estimating the population of Turkey was found using the 11 activation functions mentioned in Table 3.

4. RESULTS and DISCUSSION

The ANN architecture used in this study is the one that showed the best performance in previous experiments and is given in Figure 1. The analysis was conducted using the Matlab R2023a software.

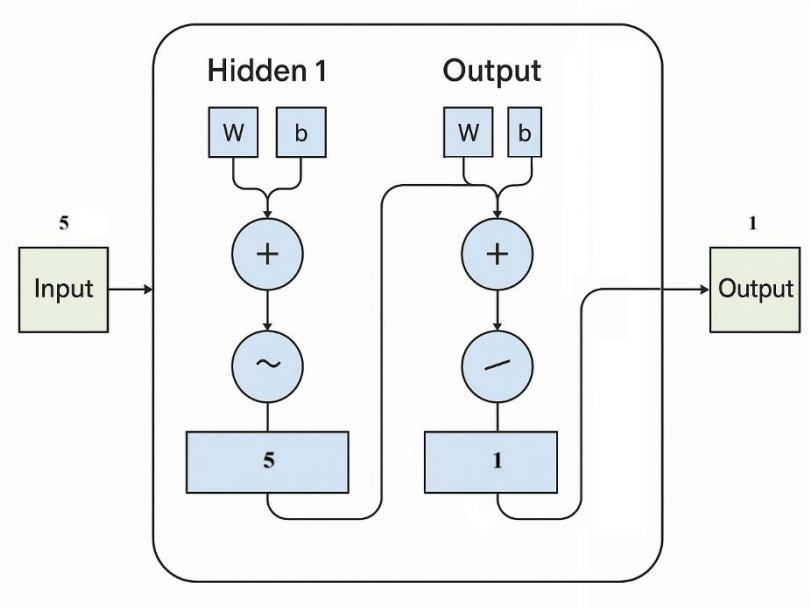

Fig. 1. Used ANN architecture

Some metric results obtained as a result of ANN Analysis are given in Table 4.

Table 4. Some metric results of ANN Analysis

Case1: Normalization process is not applied											
	tanh	**logsig**	**purelin**	**poslin**	**radbas**	**satlin**	**satlins**	**softmax**	**tribas**	**hardlim**	**hardlims**
RMSE	11356521.32	11070677.509	2307153.84	292423022.68	22144735.70	20775526.63	13291986.55	11416123.20	14381879.59	6855547.074	6944137.72
MAPE	15.95	15.22	3.229	46.09	41.69	36.47	18.74	15.15	21.42	10.85	10.35
R	0.614	0.630	0.987	0.315	-0.186	-0.027	0.373	0.837	-0.217	0.8787	0.873
Case2: Min-max normalization process is applied											
	tanh	**logsig**	**purelin**	**poslin**	**radbas**	**satlin**	**satlins**	**softmax**	**tribas**	**hardlim**	**hardlims**
RMSE	1199807.95	351416.21	2317267.56	2889938.92	381892.14	1195751.26	453323.16	134950.71	9581881.36	848168 7.14	8512577.37
MAPE	0.67	0.47	3.44	2.51	0.49	1.55	5.67	1.96	12.44	11.81	12.16
R	0.99648	0.99971	0.98719	0.97970	0.99965	0.99659	0.94846	0.99571	0.82324	0.80684	0.80734
Case3: Normalization process according to z-score is applied											
	tanh	**logsig**	**purelin**	**poslin**	**radbas**	**satlin**	**satlins**	**softmax**	**tribas**	**hardlim**	**hardlims**

RMSE	7664269.50	3110044.34	2535409.33	2168055.56	2202364.37	9263062.30	2090869.77	9152705.98	8834906565774944	12590927.56	62019269.45
MAPE	0.56	0.43	3.37	2.84	1.22	13.12	2.31	1.24	1	18.53	41318741179.34
R	0.9986	0.9997	0.9869	0.9891	0.9880	0.7599	0.9905	0.9981	0.8819	0.4848	0.4789

According to the metric results in Table 3, the activation functions that show the best population estimation performance are seen as purelin for Case 1, logsig for Case 2 and logsig for Case 3, respectively. On the other hand, the coefficients of these functions are given in Table 5.

Table 5. Coefficients of activation functions having best performance

	For Case 1
b_1	$\begin{pmatrix} -113.8532 \\ 141.8877 \\ -527.6034 \\ 406.1819 \\ 19.7275 \end{pmatrix}$
b_2	$(4.3739\mathrm{e}+07)$
IW	$\begin{pmatrix} -9.8521 & -18.8533 & 36.1786 & -14.2142 & -73.9373 \\ 4.9266 & -0.7179 & -17.5471 & 74.1128 & 103.3770 \\ 21.4093 & 5.8757 & -48.3743 & 66.7614 & 96.8599 \\ -7.2220 & 32.9254 & 95.5313 & 429.2975 & -643.6853 \\ -5.5418 & -13.8649 & -21.4315 & 139.7309 & 219.3269 \end{pmatrix}$
LW	$\begin{pmatrix} 0.3973 \\ 0.7686 \\ 1.2777 \\ 1.3463 \\ 3.1585 \end{pmatrix}^t$
	For Case 2
b_1	$\begin{pmatrix} -0.1071 \\ 4.0153 \\ 10.7882 \\ -3.0806 \\ -1.4297 \end{pmatrix}$
b_2	(-1.0922)
IW	$\begin{pmatrix} -8.0643 & 2.1526 & 29.5054 & -1.0753 & -20.7978 \\ -4.7694 & 1.0443 & 1.1774 & 7.2740 & 3.8285 \\ -3.2561 & 1.8476 & -4.7310 & -2.7736 & -1.1439 \\ -3.9172 & -1.8305 & 0.6986 & -0.4565 & 0.3432 \\ -0.2135 & -0.0395 & -0.3367 & -0.1258 & -1.8114 \end{pmatrix}$

LW	$\begin{pmatrix} 0.3246 \\ -0.1098 \\ 1.9873 \\ -10.9071 \\ -2.5735 \end{pmatrix}^t$
	For Case 3
b_1	$\begin{pmatrix} -1.1088 \\ -6.0543 \\ -2.1789 \\ 3.6011 \\ -2.2364 \end{pmatrix}$
b_2	(2.2930)
IW	$\begin{pmatrix} 0.4160 & -1.0764 & -2.9959 & -0.0598 & 6.5093 \\ -0.3984 & 2.3300 & 1.9274 & 0.8113 & -0.1367 \\ 2.0665 & -0.6453 & -1.8279 & -0.4016 & 2.7727 \\ -0.3109 & 0.0014 & -0.2526 & -0.8511 & -4.1696 \\ -2.3183 & -0.5066 & 0.5354 & -0.2688 & 0.4599 \end{pmatrix}$
LW	$\begin{pmatrix} -2.1385 \\ 0.8527 \\ 1.1758 \\ -1.7224 \\ -2.1482 \end{pmatrix}$

Also, the equation that gives the minimum RMSE value for all cases is the equation corresponding to the Case 3. This is the analysis performed by normalizing according to z-score. In this analysis, the best performing activation function is logsig and its coefficients are in Table 5.

4. CONCLUSIONS

In this study, the relationship between Turkey's population growth and its consumption of five major energy types over the 1985–2020 period was successfully modeled using Artificial Neural Networks (ANNs). The goal was to accurately forecast population trends based on consumption data for natural gas, hydroelectric energy, coal and coal derivatives, liquid fuels, and renewable energy and waste.

The results confirmed that energy consumption—often considered a consequence of population growth—can also serve as a predictive variable. The consumption patterns of different energy types are strongly correlated with demographic shifts, particularly in rapidly urbanizing regions. The study tested three data input strategies—raw data, min-max normalization, and z-score normalization. Among these, z-score normalization, when paired with the log-sigmoid activation function, delivered the best population forecasting performance. This underlines the importance of data preprocessing in neural network modeling, as it affects learning efficiency and model accuracy. Among the eleven activation functions evaluated, the log-sigmoid and purelin functions showed superior performance across various preprocessing scenarios. Specifically, the log-sigmoid function applied to z-score normalized data

achieved the lowest RMSE (311004.34) and MAPE (0.43), along with a high correlation coefficient (R = 0.9997), indicating strong predictive accuracy. The ANN model significantly outperformed traditional linear approaches by successfully capturing the nonlinear and complex interdependencies between multiple input variables and population output. This demonstrates the strength of ANN in demographic forecasting tasks involving high-dimensional and interrelated datasets.

The model's ability to predict population changes based on energy consumption trends offers practical value for energy policy, urban planning, and sustainable development strategies. Government agencies and planners can utilize such models to anticipate demographic pressures and align infrastructure investments accordingly. While this study focused solely on energy consumption variables, future models could integrate additional socio-economic indicators such as GDP, employment rates, urbanization ratios, and educational attainment levels. Moreover, exploring deep learning architectures or hybrid models may further enhance forecasting precision.

In conclusion, this study illustrates the feasibility and utility of ANN-based approaches in demographic modeling. It also reinforces the notion that energy consumption is not just a consequence but also a driver and signal of population dynamics. By leveraging the predictive power of neural networks, policymakers and researchers can gain valuable foresight into future population trends, ultimately contributing to more informed decision-making in emerging economies like Turkey.

REFERENCES

Aydın, G. (2014). Modeling of energy consumption based on economic and demographic factors: The case of Turkey with projections. *Renewable and Sustainable Energy Reviews, 35*, 382-389.

Benli, Y. (2002). Finansal Basarisizligin Tahmininde Yapay Sinir Agi Kullanimi ve IMKB'de Uygulama. *Muhasebe Bilim Dünyası Dergisi, 4*(4), 17-30.

Daşbaşı, B., Barak, D., Taşyürek, M., & Arslan, R. (2024). Using an Artificial Neural Networks Approach to Assess the Links Among Environmental Protection Expenditure, Energy use and Growth in Finland. *Journal of the Knowledge Economy*, 1-29.

Gulcu, S., & Kodaz, H. (2017). The estimation of the electricity energy demand using particle swarm optimization algorithm: A case study of Turkey. *Procedia Comput. Sci., 111*, 64-70.

Gunduz, M., & Sahin, H. (2015). An early cost estimation model for hydroelectric power plant projects using neural networks and multiple regression analysis. *J. Civ. Eng. Manag., 21*(4), 470–477.

Günay, M. (2016). Forecasting annual gross electricity demand by artificial neural networks using predicted values of socio-economic indicators and climatic conditions: Case of Turkey. *Energy Policy, 90*, 92-101.

Hamzaçebi, C., Es, H., & Çakmak, R. (2017). Forecasting of Turkey's monthly electricity demand by seasonal artificial neural network. *Neural Comput. Appl., 28*(1), 57-66.

K. Kavaklioglu, H. O., & Ceylan, H. (2009). Modeling and prediction of Turkey's electricity consumption using artificial neural networks. *Energy Convers. Manag., 50*(11), 2719–2727.

Karimi, H., & Dastranj, J. (2014). Artificial neural network-based genetic algorithm to predict natural gas consumption. *Energy Systems, 5*, 571–581.

Kialashaki, A., & Reisel, J. (2013). Modeling of the energy demand of the residential sector in the United States using regression models and artificial neural networks. *Applied Energy, 108*, 271-280.

Kizilaslan, R., & Karlik, B. (2009). Combination of neural networks forecasters for monthly natural gas consumption prediction. *Neural Netw. World, 19*(2), 191-199.

Murat, Y., & Ceylan, H. (2006). Use of artificial neural networks for transport energy demand modeling. *Energy policy, 34*(17), 3165-3172.

Shanmuganathan, S. (2016). Artificial neural network modelling: An introduction. Springer International Publishing.

Singh, S., Tiwari, A., & Ajbar, W. (2025). Optimization and performance enhancement of parabolic trough collectors using hybrid nanofluids and ANN modeling. *Journal of the Taiwan Institute of Chemical Engineers, 169*(105984).

Sözen, A. (2009). Future projection of the energy dependency of Turkey using artificial neural network. *Energy policy, 37*(11), 4827-4833.

TSI. (tarih yok). Turkish Statistical Institute. 5 24, 2025 tarihinde https://biruni.tuik.gov.tr/medas/?kn=95&locale=tr adresinden alındı

Uzlu, E., Kankal, M., Akpınar, A., & Dede, T. (2014). Estimates of energy consumption in Turkey using neural networks with the teaching–learning-based optimization algorithm. *Energy, 75*, 295-303.

Wang, Y., Li, Y., Song, Y., & Rong, X. (2020). The influence of the activation function in a convolution neural network model of facial expression recognition. *Applied Sciences, 10*(5).

Warner, B., & Misra, M. (1996). Understanding neural networks as statistical tools. *The american statistician, 50*(4), 284-293.

Yilmaz, M., Tosunoğlu, F., Kaplan, N., Üneş, F., & Hanay, Y. (2022). Predicting monthly streamflow using artificial neural networks and wavelet neural networks models. *Model. Earth Syst. Environ., 8*, 5547–5563.

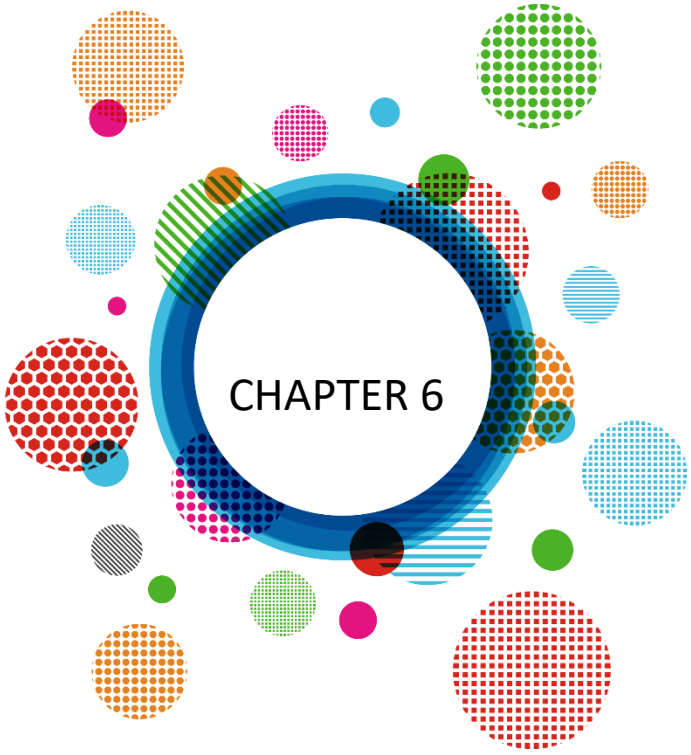

Evaluating the Effect of Roi Masking On Vehicle Detection Performance of Yolov8n to Yolov11n Models

Ufuk Kırbaş[1] *& Akif Akbulut*[2]

[1] Prof. Dr., Ondokuz Mayis University, Engineering Faculty, Department of Civil Engineering, Atakum/Samsun, TURKEY Orcid: 0000-0002-2389-425X
[2] MSc., Ondokuz Mayis University, Engineering Faculty, Department of Civil Engineering, Atakum/Samsun, TURKEY Orcid: 0009-0009-4079-5956

1. Introduction

Object detection emerges as a critical problem that forms the foundation of both academic and industrial studies in the field of computer vision. This problem, which involves determining the locations and classifications of objects in image and video data, has undergone a significant transformation in recent years with the advancement of deep learning-based methods. Especially with the proliferation of real-time applications, the need for algorithms capable of producing fast and accurate results has increased. The models developed in this context offer structures that not only analyze visual data but also enable the simultaneous execution of various tasks. Object detection methods, used in a wide range of fields from transportation systems to healthcare technologies, from security applications to autonomous vehicles, are among the main components that determine the effectiveness of AI-powered solutions.

YOLO is a deep learning-based object detection approach that stands out for its real-time performance. Since its first version, it has simplified the traditional multi-stage processes of object detection, making it possible to perform all operations through a single network. In this way, it has provided significant advantages in both processing time and computational efficiency (Redmon, Divvala, Girshick & Farhadi, 2016). The first version of the model, YOLOv1, was designed to divide the image into a grid structure and predict information such as object presence, class, and location within each cell. Although the detection of small objects was limited in this version, the core approach laid the foundation for subsequent developments. With the following versions, YOLOv2 and YOLOv3, the depth of the model was increased, the anchor box structure was integrated, and accuracy rates were improved in more complex scenes (Redmon & Farhadi, 2017). YOLOv3, in particular, offered stronger performance for the simultaneous detection of objects of different sizes and for multiple objects (Redmon & Farhadi, 2018). With YOLOv4, significant improvements were achieved in the balance between speed and accuracy, and advanced architectures such as CSPDarknet53 were used to enhance both the training process and work performance (Bochkovskiy, Wang, & Liao, 2020). YOLOv5 and YOLOv7, developed later, addressed a broad range of use cases with their lightweight, modular, and user-friendly structures, providing flexibility in terms of training and deployment (Olorunshola, Irhebhude & Evwiekpaefe, 2023). YOLOv8, is designed to support various tasks such as segmentation, pose estimation, tracking, and classification. This version is particularly well-suited for real-time applications due to its ability to deliver high performance even with limited system resources (Reis, Hong, Kupec & Daoudi, 2024).

The latest versions of the YOLO algorithm YOLOv9, YOLOv10, and YOLOv11 have been developed to further advance object detection systems in terms of both accuracy and efficiency. These versions were introduced with the aim of overcoming the limitations of previous models, achieving higher accuracy with fewer resources, and supporting multi-purpose artificial intelligence tasks. YOLOv9 offers a more modular architecture and greater flexibility in deep learning processes compared to its previous version, YOLOv8. One of the notable developments in this model is the integration of dynamic learning strategies in data processing and model optimization. YOLOv9 aims to deliver high accuracy not only in classic object detection but also in tasks such as segmentation and tracking. Furthermore, its ability to perform multiple tasks simultaneously has paved the way for widespread adoption in industrial applications (Yaseen, 2024). With YOLOv10, lightweight versions of the model have been developed to enhance usability on low-cost computing devices. Architecturally, this version is enriched with Transformer-based components, and attention mechanisms have been employed to enhance the model's perception capabilities in complex scenes. Thanks to its structure that unifies different visual tasks under a single network, YOLOv10 has become capable of supporting not only object detection but also multi-object tracking, segmentation, and action recognition. Adaptive learning rates and automatic data augmentation strategies have also been widely utilized during the training process in this version (Wang et al., 2024). YOLOv11, as the latest version, aims to surpass all previous versions in terms of performance, speed, and versatility. In this model, the backbone and head components of the architecture have been redesigned to enable faster information flow and more effective feature extraction. Additionally, semi-supervised learning strategies that require minimal labeled data during the training process have been made more effective in this version. YOLOv11 offers scalable structures optimized to operate efficiently on both cloud systems and edge devices. Its ability to function with low power consumption provides a significant advantage for mobile and embedded systems. Overall, the evolutionary process from YOLOv9 to YOLOv11 has not only improved accuracy rates but also enhanced the model's flexibility, energy efficiency, and multi-tasking capabilities. As a result of these developments, YOLO has further solidified its central role in modern artificial intelligence applications (Khanam & Hussain, 2024).

The working principle of the YOLO algorithm is based on dividing the image into multiple regions and determining whether an object exists in each region. For each cell, the object class, probability, and location coordinates are predicted; this information is obtained through a single deep learning network. The core

elements that enable the model's fast performance include its single-stage structure, CNN architecture, use of anchor boxes, and optimization techniques. With a wide range of applications, YOLO is preferred in many industries, particularly in autonomous systems, security technologies, and smart city applications. Thanks to its high accuracy and processing speed in areas such as real-time video processing, object tracking, and scene analysis, it holds a significant position in the evolution of object detection technologies (Aktaş, Doğan & Demir).The ability of the YOLO algorithm—so widely used—to deliver effective results depends not only on the model's architecture but also on each step of the application process. In this context, the success of the object detection process is directly related to the proper and optimized execution of the preprocessing (which prepares the image for the model), inference (where the model makes predictions on the image), and post-processing (where these predictions are converted into meaningful outputs) stages. The function of each step and its role within the system's overall structure directly influence the detection accuracy and application efficiency.

In the YOLO (You Only Look Once) algorithm, the "preprocess" phase refers to the transformation of raw image data into an appropriate format to ensure the model operates accurately and efficiently. This stage is the preparation phase that takes place before the images are fed into the model. First, the images are resized to fixed dimensions expected by the model (e.g., 640x640 pixels). During this process, padding is often used to preserve the aspect ratio of the image, ensuring that the geometric structure of objects remains intact. Next, pixel values are normalized to a specific range (e.g., between 0 and 1), which facilitates more stable learning and output generation by the model. The color channels are also arranged according to the model's expectations; for example, some models require input in BGR format instead of RGB. Finally, the image data is converted into a tensor format to enable the mathematical computations necessary for the model's operation. The main goal of the preprocessing stage is to prepare input data in line with the structural and numerical requirements of the model, thereby improving both accuracy and computational efficiency (Jeong, Park, & Ha, 2018).

In the YOLO algorithm, the inference process refers to the stage where a trained model performs object detection on a new image and generates output. During this process, the model uses previously learned information to identify objects in the image and determine their locations. When a preprocessed image is fed into the model, the YOLO architecture divides the image into a certain number of grid cells and evaluates the presence of objects in each cell. For each

object candidate, information such as class label, bounding box coordinates, and confidence score is generated. These outputs are not used directly; instead, a non-maximum suppression (NMS) algorithm is applied to filter out multiple predictions that may belong to the same object. This algorithm retains the box with the highest confidence score among overlapping boxes and eliminates the others. As a result, the detected objects become clear, non-redundant, and visually meaningful. The output is then visualized on the image with bounding boxes and labels, making it interpretable for the user. The inference process is effectively used in many fields such as video analytics, security systems, autonomous vehicles, and industrial automation, providing high speed and sufficient accuracy especially for real-time object recognition applications (Wang et al., 2023). In the YOLO algorithm, the post-process stage ensures that the raw data generated by the model during inference is made meaningful, consistent, and usable. At this stage, the class predictions, confidence scores, and bounding box coordinates produced by the model are processed. These coordinates, which are normalized or rescaled according to the model's input dimensions, are converted back to the original image dimensions to provide accurate location information. Then, the NMS algorithm is again applied to eliminate overlapping boxes referring to the same object, retaining only the most reliable detection. This step enhances both the visual integrity and the accuracy of the output.

Additionally, only predictions above a certain confidence threshold (e.g., 30% or 50%) are taken into consideration; thus, low-accuracy and potentially false positives are eliminated from the system. The purpose of the post-process stage is to transform the abstract and raw data produced by the model into a form that is interpretable by the user and can be directly utilized in applications. These outputs are typically presented on the image using class labels and bounding boxes (Portnov, Shubin, & Frolova, 2024).

2. Materials and Methods

In this study, security camera footage of a two-lane road section was used as reference data for vehicle detection and processing time analyses. The video was recorded by a fixed camera at 30 frames per second (FPS) and consists of an uninterrupted 10-minute-long footage. The image frame has a resolution of 900 pixels in width and 800 pixels in height, and all analyses were conducted at this resolution. To perform vehicle detection and temporal performance measurements on the video data, different versions of the YOLO (You Only Look Once) object detection architecture developed by Ultralytics namely YOLOv8n, YOLOv9t, YOLOv10n, and YOLOv11n models were used. Object detection was performed on each video frame for every model. For each detection, the

preprocessing, inference, and post-processing times reported by the model were recorded, and average values were calculated. Additionally, a masking process was applied to ensure that only vehicles within the region of interest (ROI) were detected in the images. This operation was performed using the OpenCV library; a black-and-white mask image created with the same dimensions as the original video frames was applied to the video using the cv2.bitwise_and() function (Figure 1).

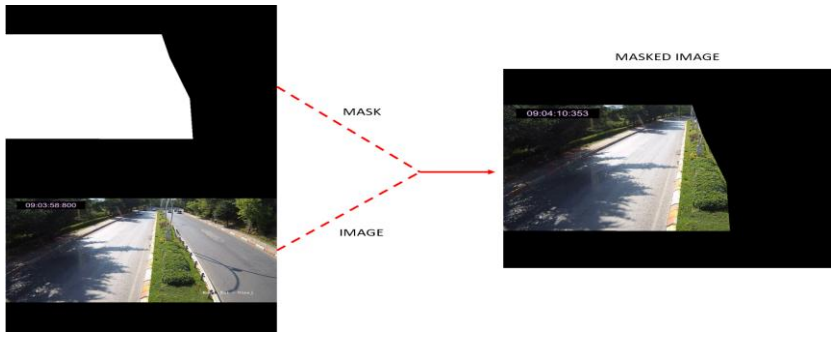

Figure 1. Masking of the Image

Within the scope of this process, exemplified in Figure 1, an image masking technique was applied to focus solely on the targeted road area for analysis. For this purpose, a black-and-white mask with the same dimensions as the video frames was created using the OpenCV library, and this mask was applied to the corresponding video frame using the cv2.bitwise_and() function. As a result, only the vehicles located within the defined region of interest became visible in the image, ensuring that the system performed detection exclusively within this limited area. This approach aimed to exclude non-vehicle objects and off-road regions from the analysis, thereby reducing the model's processing load and enhancing detection accuracy.

Within the scope of this study, the fastest models from different versions of the YOLO architecture YOLOv8n, YOLOv9t, YOLOv10n, and YOLO11n were used. For each model, object detection was performed separately on both the original (unmasked) and masked video frames. The detection process for each frame was analyzed through three main components: preprocessing, inference, and post-processing. The time durations reported by each model for these components were recorded, and average processing times were calculated to evaluate overall performance. This dual analysis provided an opportunity to comparatively assess the effects of masking on both vehicle detection accuracy and total processing time on a per-model basis. Thus, the contribution of masking as a performance-enhancing preprocessing method in object detection processes was demonstrated in detail.

3. Findings and Discussion

The image data used in the study were obtained through a fixed video camera positioned along a two-lane road. The camera is capable of recording at a resolution of 1920x1080 pixels (Full HD) and a frame rate of 30 frames per second (FPS). In this context, the original 1920x1080 pixel video frames were resized to a width of 900 pixels and a height of 800 pixels. This resizing process reduces processing time and allows for more efficient use of system resources.

The total video duration is 10 minutes and was recorded during daylight hours under natural lighting conditions. Traffic on the observed section is bidirectional, and the footage was analyzed for vehicle counting and object detection purposes (Figure 2).

Figure 2. Determination of the mask area and drawing of the counting zone

The developed Python-based software enables the optimization of the analysis region for object detection and vehicle counting processes on video data. The "mask area," defined through the user interface, is used to designate parts of the scene that are irrelevant or intended to be excluded from analysis. This area, marked with a purple line in the image, ensures that the system considers only the objects located within the Region of Interest (ROI). In this way, non-relevant elements such as roadside trees, shadows, or vehicles in the opposite lane are prevented from negatively impacting model performance.

In line with the area defined by the user, the software generates a black-and-white mask image that matches the resolution of the video. This output is automatically created in JPG format and used by the system as an input prior to processing. In the generated mask image, black pixels represent regions excluded

from analysis, while white pixels indicate the areas where analysis will be conducted. This method not only enhances processing efficiency but also contributes to reducing false positive detections. The vehicle detection performance of different versions of the YOLO architecture YOLOv8n, YOLOv9t, YOLOv10n, and YOLOv11n was evaluated using both unmasked and masked image data. In the reference scene used for all models, a total of 189 actual vehicles are present, and this count forms the basis for all comparisons (Table 1).

Table 1. Vehicle detection performance of YOLO models

Feature/Model	YOLOv8n	YOLOv9t	YOLOv10n	YOLO11n
Actual Number of Vehicles	189	189	189	189
YOLO Detection (Unmasked)	151	134	179	186
YOLO Detection (Masked)	187	181	183	188

In the analysis conducted on unmasked images, the YOLOv8n model detected 151 vehicles, achieving a success rate of 79.8%. The YOLOv9t model showed the lowest performance by detecting 134 vehicles with an accuracy of 70.8%. In contrast, the YOLOv10n and YOLOv11n models achieved significantly better results, detecting 179 and 186 vehicles respectively, corresponding to 94.7% and 98.4% accuracy. These results clearly demonstrate that architectural improvements in newer models directly contribute to enhanced detection performance. When detection was performed using masked images, a notable performance increase was observed in all models. The YOLOv8n model correctly detected 187 vehicles in masked images, reaching an accuracy of 98.9%. Compared to its low performance in the unmasked scenario, YOLOv9t achieved a remarkable improvement by correctly detecting 181 vehicles, yielding 95.7% accuracy. YOLOv10n and YOLOv11n exhibited the highest detection rates with 96.8% and 99.5% accuracy, respectively. These findings highlight that applying masking, especially on road sections, effectively focuses detection on relevant vehicles within the scene. This confirms that masking is a highly efficient preprocessing technique. Overall, the implementation of masking significantly improved detection accuracy across all models, and the latest YOLO versions particularly YOLOv10n and YOLOv11n demonstrated high reliability in vehicle detection. The findings of the research reveal that the use of masking in traffic analysis to increase data quality can make a significant contribution.

The vehicle detection performances of the YOLO models were analyzed based on their F1 scores. The F1 score was chosen because it reflects a balanced measure of both precision and recall. Given that the actual number of vehicles in the test environment was 189, F1 scores were calculated for each model under both masked and unmasked conditions (Table 2).

Table 2. F1 Scores for the models

Model	F1-score (Unmasked)	F1-score (Masked)
YOLOv8n	0.8885	0.9945
YOLOv9t	0.8288	0.9773
YOLOv10n	0.9721	0.9837
YOLOv11n	0.9919	0.9974

In unmasked images, the YOLOv8n model demonstrated a balanced performance with an F1 score of 0.89. The YOLOv9t model, on the other hand, exhibited the lowest performance with an F1 score of 0.83, indicating certain challenges in its detection capabilities. Moreover, the YOLOv10n and YOLOv11n models achieved highly successful results in vehicle detection, with impressive F1 scores of 0.97 and 0.99, respectively. These findings highlight that architectural improvements in the models directly enhance detection accuracy. Following the application of masking, a notable improvement in F1 scores was observed across all models. The YOLOv8n model achieved an almost perfect score of 0.995 in the masked scenario. Similarly, the YOLOv9t model's score increased to 0.977. YOLOv10n and YOLOv11n also demonstrated superior performance in masked tests, with F1 scores of 0.984 and 0.997, respectively. This improvement confirms that masking is a highly effective preprocessing technique that allows models to detect vehicles more accurately. Based on the F1 scores, masking contributes to better vehicle detection by reducing false positives and increasing the number of correctly identified objects. This supports the argument that models provide more balanced and reliable results when masking is employed. Additionally, the YOLOv8n and YOLOv11n models, especially when combined with masking, emerge as strong and reliable options for vehicle detection, enhancing the diversity and robustness of the model range.

Additionally, the processing times for the YOLO models were analyzed separately. For each model, the average durations of the three main processing stages (preprocessing, inference, and postprocessing) were measured on both unmasked and masked images. This approach enabled a comparative evaluation of the models' temporal efficiency in both overall performance and individual processing steps (Table 3).

Table 3. Models and processing times

Durations (Millisecond)	YOLOv8n		YOLOv9t		YOLOv10n		YOLO11n	
	Unmasked	Masked	Unmasked	Masked	Unmasked	Masked	Unmasked	Masked
Preprocess	2.74	2.52	2.65	2.53	3.05	2.83	3.41	2.74
Inference	21.42	14.5	23.4	20.27	23.74	17.22	19.94	13.77
Postprocess	1.9	1.05	1.46	1.14	0.82	0.52	2.13	1.22
Total Duration	**26.06**	**18.07**	**27.51**	**23.94**	**27.61**	**20.57**	**25.48**	**17.73**

In terms of preprocessing time, all models were observed to have similar processing durations. The application of masking led to a small but consistent reduction in preprocessing time for each model. For example, in the case of the YOLOv11n model, the preprocessing time decreased from 3.41 ms (without masking) to 2.74 ms (with masking). This indicates that masked images provide a simpler data structure to the model, thereby reducing the preprocessing workload. The inference stage constitutes the most time-consuming and critical part of the entire process across all models. Among them, YOLOv10n and YOLOv9t showed the highest inference times on unmasked images, at 23.74 ms and 23.40 ms respectively, while YOLOv11n achieved a lower duration of 19.94 ms. The application of masking significantly reduced inference times. Notably, YOLOv8n's inference time dropped from 21.42 ms to 14.5 ms, and YOLOv11n's from 19.94 ms to 13.77 ms. This improvement can be attributed to the model needing to focus less on irrelevant areas within the image. Masking also had a clearly observable effect on post-processing times. In all models, post-processing duration decreased following the application of masking. For instance, in the YOLOv10n model, this time was reduced from 0.82 ms to 0.52 ms. Although the YOLOv11n model initially had a relatively higher post-processing time of 2.13 ms in the unmasked case, it dropped to 1.22 ms with masking. When total processing times are considered, it becomes evident that masking significantly reduces the overall processing time across all models. The total time for YOLOv8n dropped from 26.06 ms to 18.07 ms, and for YOLOv11n, from 25.48 ms to 17.73 ms. This demonstrates that masking not only enhances detection accuracy but also offers substantial efficiency gains in terms of processing time. These timing analyses reveal that YOLO models can be optimized for vehicle detection tasks not only in terms of accuracy but also in terms of processing time. Specifically, the masking technique contributes to a reduction in both inference and total durations, allowing the models to operate more efficiently in real-time applications. Among the evaluated models, YOLOv11n stands out as the most balanced and high-performing architecture in terms of both accuracy and processing speed.

4. Conclusion

The conducted analyses comparatively evaluated the performance of different versions of the YOLO algorithm (YOLOv8n, YOLOv9t, YOLOv10n, YOLOv11n) in terms of vehicle detection accuracy and processing time. Based on the obtained findings, the following conclusions were drawn:

- The masking application significantly improved vehicle detection accuracy across all YOLO models. In particular, by excluding irrelevant areas in the images, it contributed both to a reduction in false positive detections and a decrease in processing time.
- The YOLOv11n model demonstrated the highest performance in both accuracy and efficiency, achieving up to 99.5% accuracy and a low total processing time of 17.73 ms. The F1 score analysis revealed that masking enhanced the model's performance and that the YOLOv10n and YOLOv11n versions delivered balanced and reliable results.
- Masking has improved not only detection accuracy but also temporal efficiency at every stage of the processing pipeline, including preprocessing, inference, and postprocessing.
- The integration of masking into object detection processes has been found to provide significant gains in both accuracy and processing speed, especially in real-time applications with limited resources. The use of such preprocessing techniques alongside the newer versions of the YOLO algorithm markedly enhances the model's effectiveness in traffic monitoring and similar image-based analyses.

Based on these results, it is recommended that future studies test model performance under various environmental conditions such as different weather scenarios, day-night variations, and heavy traffic situations. Additionally, investigating the effects of different masking strategies (e.g., dynamic mask generation, deep learning-based ROI estimation) would be beneficial for enhancing the model's adaptive capabilities. Within this scope, conducting field tests and implementing real-time system integrations on edge devices would also represent important steps for advancing practical applications in future work.

Acknowledgments

The research described in this paper was financially supported by Ondokuz Mayıs University under the project titled "Karayolu Ağlarında Kurp Kesimlerinde Şerit Disiplininin Sağlanması ve Yol Kapasitesinin Arttırılması Uygulaması" with the project number PYO.MUH.1906.23.004.

The research described in this paper was financially supported by TÜBİTAK under the project titled *"Karayolu Trafiğinde Şerit İhlallerinin Azaltılmasına Yönelik Bir Çözümün Geliştirilmesi"* with the project number 124M818.

References

Redmon, J., Divvala, S., Girshick, R., & Farhadi, A. (2016). You only look once: Unified, real-time object detection. *Proceedings of the IEEE Conference on Computer Vision and Pattern Recognition (CVPR)*, 779–788. https://doi.org/10.1109/CVPR.2016.91

Redmon, J., & Farhadi, A. (2017). YOLO9000: Better, Faster, Stronger. *Proceedings of the IEEE Conference on Computer Vision and Pattern Recognition (CVPR)*, 6517–6525. https://doi.org/10.1109/CVPR.2017.690

Redmon, J., & Farhadi, A. (2018). YOLOv3: An incremental improvement. *CoRR*, *abs/1804.02767*. https://doi.org/10.48550/arXiv.1804.02767

Bochkovskiy, A., Wang, C.-Y., & Liao, H.-Y. M. (2020). YOLOv4: Optimal speed and accuracy of object detection. *arXiv*. https://doi.org/10.48550/arXiv.2004.10934

Olorunshola, O. E., Irhebhude, M. E., & Evwiekpaefe, A. E. (2023). A comparative study of YOLOv5 and YOLOv7 object detection algorithms. *Journal of Computing and Social Informatics*, *2*(1).

Reis, D., Hong, J., Kupec, J., & Daoudi, A. (2024). Real-time flying object detection with YOLOv8. *arXiv*. https://doi.org/10.48550/arXiv.2305.09972

Yaseen, M. (2024). WHAT IS YOLOV9: An in-depth exploration of the internal features of the next-generation object detector. *arXiv*. https://doi.org/10.48550/arXiv.2409.07813

Wang, A., Chen, H., Liu, L., Chen, K., Lin, Z., Han, J., & Ding, G. (2024). YOLOv10: Real-time end-to-end object detection. *Proceedings of the 38th Conference on Neural Information Processing Systems (NeurIPS 2024)*.

Khanam, R., & Hussain, M. (2024). YOLOV11: An overview of the key architectural enhancements. *arXiv*. https://doi.org/10.48550/arXiv.2410.17725

Aktaş, A., Doğan, B., & Demir, Ö. (2020). Tactile paving surface detection with deep learning methods. *Journal of the Faculty of Engineering and Architecture of Gazi University, 35*(3), 1685-1700. https://doi.org/10.17341/gazimmfd.652101

Jeong, H.-J., Park, K.-S., & Ha, Y.-G. (2018). Image preprocessing for efficient training of YOLO deep learning networks. In *Proceedings of the 2018 IEEE International Conference on Big Data and Smart Computing (BigComp)* (pp. 635-637). https://doi.org/10.1109/BigComp.2018.00113

Wang, M., Lu, H., Blumenstein, M., Cho, S. B., Liu, C. L., Yagi, Y., & Kamiya, T. (2023). Q-YOLO: Efficient inference for real-time object detection. In H. Lu, M. Blumenstein, S. B. Cho, C. L. Liu, Y. Yagi, & T. Kamiya (Eds.),

Pattern recognition. ACPR 2023. Lecture Notes in Computer Science (Vol. 14408, pp. 307–321). Springer. https://doi.org/10.1007/978-3-031-47665-5_25

Portnov, A., Shubin, A., & Frolova, G. (2024). The effect of pre- and post-processing techniques on tree detection in young forest stands from images of snow cover using YOLO neural networks. *European Journal of Forest Engineering, 10*(2), 149–159. https://doi.org/10.33904/ejfe.1462335

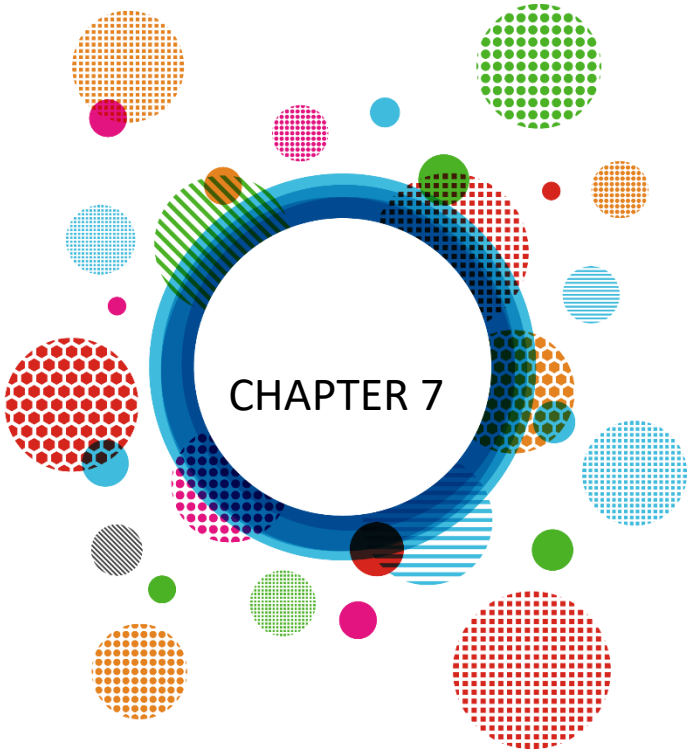

Forecasting the Share of Wind Energy in Total Electric Energy Sources (2024-2030): A Comparative Study Using Linear Regression and Artificial Neural Networks

Mahmut Cengiz[1] & Gokhan Karacoban[2] &

Yagmur Arıkan Yıldız[3]

[1]Sivas Cumhuriyet University, Department of Information Systems and Technologies ORCID: 0000-0001-7089-3172

[2] Sivas University of Science and Technology, Department of Astronautical Engineering ORCID: 0000-0001-5155-8360

[3] Dr, Sivas University of Science and Technology, Department of Electrical and Electronic Engineering, ORCID: 0000-0003-0947-2832

1 Introduction

The increasing global energy demand has significantly reinforced the interest in other energy sources, while the financing has continued (Ndubuisi & FNisafetyE, 2025). Wind energy, which stands out thanks to its low carbon footprint and economic opportunities, accounted for only 0.2% of global electricity production in 2000, while this share increased to 7.8% in 2023 (International Energy Agency, 2023). Such a development clearly shows that the weight of the change in the global energy portfolio is rapidly increasing and the energy transformation process is gaining momentum (Gielen et al., 2019). The rise of wind energy is supported by factors such as technological advances, the decline in the rise and increasing environmental awareness (Kara and Şahin, 2023). However, the growth dynamics in the production payment of wind compared to other sources such as coal, natural gas, hydroelectric and solar differ regionally and globally.

Wind energy in Türkiye provides significant contributions to the diversification of the energy portfolio and sustainability. Although renewable energy policies and infrastructure investments have increased the payment for wind-generated electricity production, the variability and unpredictability of wind speed complicate production estimates. The complexity and nonlinear relationships between these effects pave the way for traditional approaches to be incomplete. In this way, the need for the use of artificial intelligence, machine learning and advanced programs is felt in order to design production in a more regular manner.

Scientific studies on innovations in Türkiye have focused on increasing methodological diversity and predictive accuracy. For example, İlker (2018) modeled Hatay's extreme wind energy potential using Weibull, Burr and Generalized Gamma distributions together with artificial neural networks. Serkendiz et al. (2018) re-mapped wind energy across Turkey in the Weibull region and with GIS-based analyses. Özdemir and Sakallı (2023) started to increase the production capacities for 2.3 MW and 3 MW turbines by performing simulations with the WRF weather forecast model in different regions of the country. In addition, Yazıcı (2021) evaluated the comparative shaping of machine learning and deep learning (especially LSTM) for short-term wind power forecasting and achieved high accuracy.

This study analyzes the wind energy production sections of Türkiye for the period 2000–2023 and provides forecasts for the period 2024–2030. In the analysis, linear regression models enriched with L1 (lasso) and L2 (ridge) regularization techniques were used. The hyper parameters of these models

penalty coefficient (lambda), regularization type, and regression algorithm (least squares or support vector machines) were optimized using genetic algorithms. In addition, multilayer artificial neural network (ANN) models were developed, and the best-performing network structure was selected with 50 different random initializations. The models were evaluated with metrics such as mean square error (MSE) and coefficient of determination (R^2) on training and test data. In addition, a trend model including polynomial and sinusoidal components was created, and estimates were made for the period of 2024–2030 years. This approach provides a better understanding of the future course of the increase in the production share of wind energy compared to other energy sources.

2 Methodology

2.1 Data Preparation

The dataset, derived from NASA (National Aeronautics and Space Administration), comprises annual wind energy share data from 2000 to 2023, with 10 input features: population, gross domestic product, import, export, carbon dioxide emissions, electricity consumption per capita, energy demand, total installed electric power capacity, renewable energy installed capacity, installed capacity of wind energy, and one output, which is the ratio of wind energy to total electric energy. The data was normalized using z-score normalization:

$$z = \frac{x - \mu}{\sigma} \tag{1}$$

where μ and σ are the mean and standard deviation of each feature, respectively. The training set (2000–2017, 18 data points) and test set (2018–2023, 6 data points) were defined to balance model training and validation. The energy statistic dataset used for the study is given in Table 1.

Table 1: Energy Statistic Datas of Turkey (2000–2023)

Year	Pop (10^6)	GDP (10^9 $)	Imp (10^9 $)	Exp (10^9 $)	CO2 (Mt)	Elec/Cap (kWh)	E.Dem (TWh)	Tot.Cap (MW)	Ren.Cap (MW)	Wind.Cap (MW)
2000	64.1	274	27.8	54.5	234	1.9	105	27264.1	11221.6	18.9
2001	65.1	200	31.3	41.4	213	1.9	104	28332.4	11719.3	18.9
2002	66.0	240	36.1	51.6	223.7	1.9	109	31845.8	12291.1	18.9
2003	66.9	315	47.3	69.3	239.2	1.9	117	35587	12626.4	18.9
2004	67.8	409	63.2	97.3	247.2	2.0	127	36824	12693.1	18.9
2005	68.7	506	73.5	117	267.0	2.2	137	38843.5	12955.0	20.1
2006	69.6	557	85.5	139	284.6	2.4	150	40564.8	13164.4	58.95
2007	70.5	681	107	170	315.6	2.5	163	40835.7	13586.55	147.5
2008	71.3	770	132	202	311.7	2.5	171	41817.2	14260.4	363.7
2009	72.2	649	102	141	317.5	2.7	165	44761.2	15487.1	791.6
2010	73.2	777	114	186	317.6	2.8	210	49524.1	17331.3	1320.2
2011	74.2	839	135	241	343.0	2.9	230	52911.1	19084.2	1728.7

2012	75.3	881	152	237	357.4	3.1	242	57059.4	22179.5	2260.6
2013	76.6	958	161	261	349.2	3.2	246	64007.5	25537.45	2759.7
2014	78.1	939	167	251	365.7	3.2	257	69519.8	27945.04	3629.7
2015	79.6	864	151	214	386.3	3.3	266	73146.74	31520.8	4503.2
2016	81.0	870	149	202	404.6	3.4	279	78497.38	34449.6	5751.3
2017	82.1	859	164	239	429.4	3.4	297	85200	38751.1	6516.18
2018	82.8	778	177	231	422.1	3.5	304	88550.76	42264.0	7005.39
2019	83.5	760	181	210	404.3	3.6	303	91266.99	44395.32	7591.16
2020	83.7	776	190	219	414.4	3.2	310	95890.61	49202.21	8832.4
2021	84.7	815	225	271	417.1	3.6	327	99819.61	53234.09	10606.97
2022	85.3	905	254	298	422.8	3.9	325	103809.26	56005.26	11396.16
2023	85.7	905	265	310	420.3	3.9	323	110913.98	63160.59	11806.07

2.2 Linear Regression with Genetic Algorithm Optimization

Linear regression is a type of regression analysis that aims to model the relationship between one or more input variables and a continuous output variable. Linear regression assumes that the expected value of the response variable can be expressed as a linear combination of the input variables. In linear regression, the relationships are modeled using linear predictor functions whose unknown model parameters are estimated from the data.

A simple linear regression consists of one independent variable and one dependent variable. The model calculates the slope and intercept of the line of best fit, which depicts the relationship between variables. The slope reflects the change in the dependent variable per unit change in the independent variable, whereas the intercept represents the dependent variable's projected value when the independent variable is zero.

In the study, the linear regression model was implemented using MATLAB's fitrlinear function, with hyperparameters optimized via a genetic algorithm. The GA minimized the MSE on the test set by tuning three parameters: regularization strength lambda λ , log-scaled from 10^{-5} to 10^{10}, regularization type (lasso or ridge), and learner type (least squares or SVM).

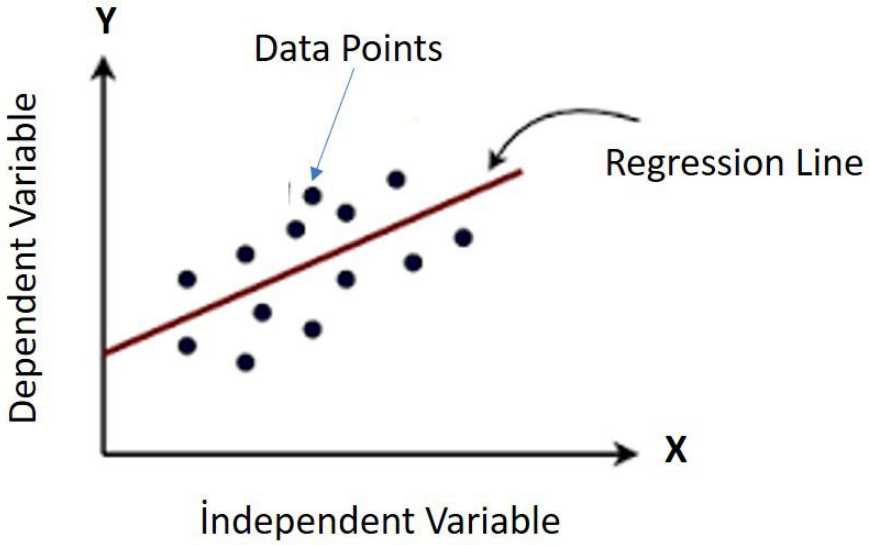

Figure 1: The Structure of Linear Regression Algorithm

2.2.1 Mathematical Model

The base model is:

$$y = \beta_0 + \sum_{j=1}^{10} \beta_j x_j + \epsilon \quad (2)$$

where y is the wind energy share, x_j are input features, β_j are coefficients, and ϵ is the error term. Regularization was applied as:

$$Loss = \sum_{i=1}^{n} (y_i - \hat{y}i)^2 + \lambda \sum_{j=1}^{n} |\beta_j| \quad (3)$$

$$Loss = \sum_{i=1}^{n} (y_i - \hat{y}i)^2 + \lambda \sum_{j=1}^{n} |\beta_j^2| \quad (4)$$

The GA used a population size of 30, 100 generations, and binary tournament selection, with bounds [-5, 10] for $\log_{10}(\lambda)$, [0, 1] for regularization, and [0, 1] for learner type. For 2024–2030 predictions, a trend model was fitted:

$$y(t) = \beta_0 + \beta_1 t + \beta_2 t^2 + \beta_3 \sin\left(\frac{2\pi t}{10}\right) + \beta_4 \cos\left(\frac{2\pi t}{10}\right) + \epsilon(t) \quad (5)$$

where (t) is the year, and $\epsilon(t) \sim N(\mu_{\text{error}}, \sigma^2_{\text{error}})$ was added using residual statistics.

2.3 Artificial Neural Network (ANN)

Artificial Neural Network (ANN) is a deep learning algorithm that originated and evolved from the concept of biological neural networks in human brains. An attempt to recreate the workings of the human brain resulted in the birth of artificial neural networks. ANN works similarly to biological neural networks, but not identically (İlker, 2018). Artificial neural networks (also called neural network models or connectionist models) are used effectively in solving complex pattern recognition problems, especially categorization and speed analysis. Thanks to their nonparametric structures, artificial neural networks; Unlike traditional parametric methods, they can make divisions without being in the environment related to the distribution or possible communication effects between variables.

Artificial Neural Networks (ANN) are a learning class that can basically process only digital and extensible data types. However, to work with unstructured and high-dimensional data types such as images, natural language and audio, special architectures are needed for the temporal or spatial diversity of the data distribution. In this context, Convolutional Neural Networks (CNN) are deep learning architectures developed for data containing spatial representations such as image data, and Recursive Neural Networks (RNN) are deep learning architectures developed for sequential data that depends on time.

The ANN was built with MATLAB's fitnet, featuring two hidden layers (9 and 10 neurons) and a BFGS training algorithm. The network was trained over 1000 epochs with a learning rate of 0.5, and early stopping was applied after 30 validation failures.

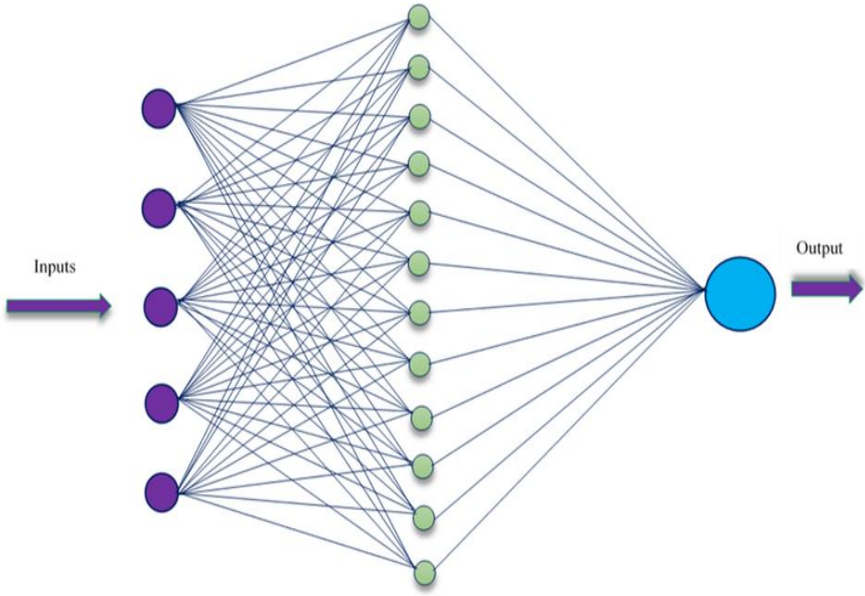

Figure 2: The Structure of Artificial Neural Network (ANN) Algorithm Das et al. (2024).

2.3.1 Mathematical Model

The ANN structure is:

Input Layer: 10 neurons.

Hidden Layer 1: 9 neurons, $h_j^{(1)} = \tanh\left(\sum_{i=1}^{10} w_{ij}^{(1)} x_i + b_j^{(1)}\right)$

Hidden Layer 2: 10 neurons, $h_k^{(2)} = \tanh\left(\sum_{j=1}^{9} w_{jk}^{(2)} h_j^{(1)} + b_k^{(2)}\right)$

Output Layer: $y = \sum_{k=1}^{10} w_k^{(3)} h_k^{(2)} + b^{(3)}$

The model was trained 50 times, selecting the best based on test MSE. Forecasts for 2024–2030 were generated using the trend model, with random errors from $N(\mu_{\text{error}}, \sigma^2_{\text{error}})$. Results were plotted using MATLAB, showing actual and predicted values with 95% confidence intervals.

2.4 Model Performance

The performance comparison of two different machine learning algorithms was made using MSE and R^2 metrics. The calculation of MSE and R^2 metrics is given as follows:

$$\text{MSE} = \frac{1}{n}\sum_{i=1}^{n}(y_i - \hat{y}_i)^2 \tag{6}$$

$$R^2 = 1 - \frac{\sum_{i=1}^{n}(y_i - \hat{y}i)^2}{\sum i = 1^n (y_i - \bar{y})^2} \tag{7}$$

3 Results

This section provides the results of ANN and linear regression algorithms in estimating the share of wind power in total electricity energy sources. Then, the performances of two different machine learning algorithms are compared and discussed in section 4.

3.1 Linear Regression Results

The graph given in Figure 3 shows the actual, predicted, and estimated values of the wind energy share using the linear regression algorithm. The estimation of wind energy share was made for the period of 2024–2030.

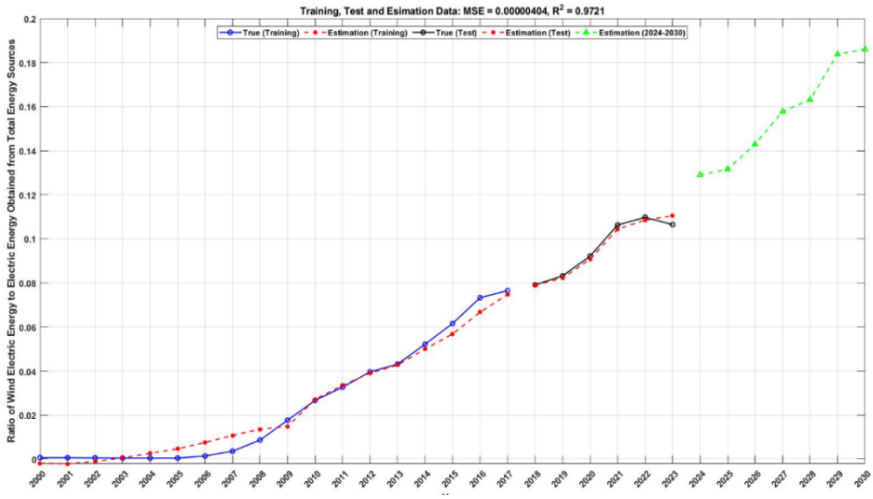

Figure 3: Linear Regression: Actual, Predicted, and Estimated Wind Energy Share (2000–2030)

When Figure 3 was examined, it is seen that the linear regression model achieved an MSE of 0.00000404 and R^2 of 0.9721. Also, according to Figure 3, the share rose from 0 in 2000 to 0.12 in 2023, with a forecast of 0.19 by 2030. Residual standard deviation was 0.002, which indicates high estimation precision using the linear regression algorithm.

3.2 ANN Results

The result of the estimation of wind energy share using ANN is given in Figure 4. The estimation of wind energy share was made for the period of 2024–2030.

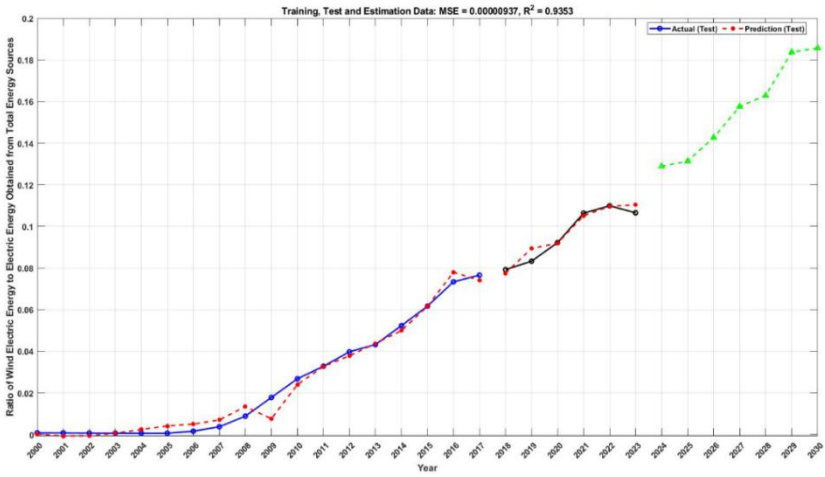

Figure 4: ANN: Actual, Predicted, and Forecasted Wind Energy Share (2000–2030)

ANN yielded an MSE of 0.00000937 and R^2 of 0.9353. According to Figure 4, it is seen that the share is predicted to reach 0.18 by 2030, with a residual standard deviation of 0.003.

4 Discussion

The linear regression model's lower MSE and higher R^2 suggest better performance. This is likely due to its simplicity, effective GA tuning, and the small dataset size, which limits the ANN's ability to generalize. A sensitivity analysis (varying training data by ±10%) showed linear regression forecasts remained stable (±0.01), while ANN forecasts varied by ±0.03.

Both models predict growth to 18–19% by 2030, consistent with the projections of the IEA. The test period validation (e.g., 2023 actual vs. predicted: 0.12 vs. 0.119–0.121) supports reliability.

The success of the linear regression model highlights the efficacy of GA optimization for small datasets. The ANN's higher error may reflect overfitting, suggesting a need for regularization or more data. Sensitivity analysis indicates robustness in linear regression forecasts, while the ANN is more sensitive to input variations. External factors (e.g., policy shifts, technological breakthroughs) could alter these trends, warranting cautious interpretation.

5 Conclusion

This study aims to estimate the share of wind energy among total electricity resources in the coming years. To estimate the share of wind energy, two different machine learning algorithms were used, and their performance was compared with each other. The MSE and R^2 metrics have been used for the comparison of two different machine learning algorithms. The simulation results indicate that the share of wind energy will increase to 0.19 according to the linear regression model and 0.18 according to the ANN model by 2030. According to the results, the linear regression algorithm outperforms the ANN algorithm due to its simplicity and optimization. The results show the growth of wind energy in the future. Future research could explore hybrid models, real-time data, or additional features (e.g., weather patterns) to enhance accuracy.

References

Das, P., et al. (2024). A comparative study of machine learning models for construction costs prediction with natural gradient boosting algorithm and SHAP analysis. Asian Journal of Civil Engineering, 25(4), 3301–3316.

Gielen, D., Boshell, F., Saygin, D., Bazilian, M. D., Wagner, N., & Gorini, R. (2019). The role of renewable energy in the global energy transformation. Energy Strategy Reviews, 24, 38–50.

İlker, M. (2018). Modeling the wind energy potential in the Hatay region [Doctoral dissertation, Istanbul Technical University].

International Energy Agency. (2023). Renewables 2023. International Energy Agency. https://www.iea.org/reports/renewables-2023

Kara, T., & Şahin, A. D. (2023). Implications of climate change on wind energy potential. Sustainability, 15(20), 14822.

Ndubuisi, O. G., & FNisafety E, F. I. S. P. O. N. (2025). Advanced Renewable Energy and Sustainability: The Transitioning to Renewable Energy in Realizing Sustainable Global Energy Security.

Özdemir, F. F., & Sakalli, A. (2023). Simulation and analysis of Turkey's wind energy potential using a numerical weather prediction system. European Journal of Science and Technology,(46), 179–192. https://dergipark.org.tr/tr/pub/ejosat/issue/75657/1191826

Serkendiz, H., Tatlı, H., & Öztürk, B. (2018). Redefining the potential wind energy density in Turkey. Journal of Awareness, 3(Special Issue), 739–750. https://dergipark.org.tr/tr/pub/joa/issue/43576/534959

Yazici, K. (2021). Short-term wind power forecasting using machine learning methods [Master's thesis, Sakarya University]. https://acikerisim.sakarya.edu.tr/handle/20.500.12619/97232

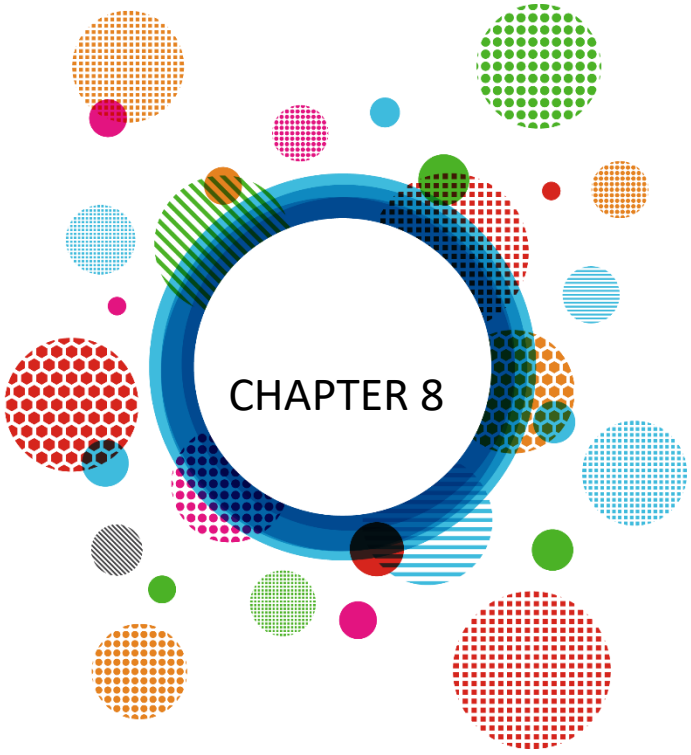

Comparative Analysis of Advanced MFA Approaches in PAM Products Against Phishing-Based Cyberattacks

Kübra Nur Canbay[1] & Osman Kaan Kars[2]

[1]Gazi University, Graduate School of Natural and Applied Sciences, Department of Mathematics, Ankara, Turkey ORCID ID: https://orcid.org/0000-0002-3608-4483
[2] Yeditepe University, Faculty of Engineering, Department of Computer Engineering, Istanbul, Turkey ORCID ID: https://orcid.org/0009-0003-3490-8412

1. INTRODUCTION

In the contemporary cybersecurity landscape, the protection of sensitive systems and critical data hinges on effective management of privileged access and vigilant monitoring of security events. The escalating complexity of cyberattacks, notably those leveraging phishing techniques to compromise privileged accounts, underscores an urgent need for advanced security measures. Phishing, often amplified by sophisticated social engineering and automation tools, remains a predominant vector for breaches, posing a formidable challenge to organizational defenses.

Privileged Access Management (PAM) solutions are indispensable in this context. They are designed to control and secure elevated access rights to critical IT infrastructure, thereby mitigating the risk of unauthorized activities and lateral movement within networks. Privileged accounts, such as those held by administrators, root users, or critical service accounts, are highly coveted by cyber attackers due to their extensive permissions, making them prime targets for exploitation. While PAM systems enforce strict controls to prevent privilege escalation and secure credentials through vaulting and just-in-time (JIT) access, their effectiveness can be undermined if the authentication mechanisms protecting these accounts are vulnerable.

Multi-Factor Authentication (MFA) has long been a cornerstone of digital identity verification. By requiring users to present two or more distinct authentication factors—something they know (e.g., password), something they have (e.g., a token), and something they are (e.g., a biometric)—MFA significantly enhances security beyond simple password protection. However, the landscape of cyber threats is continuously evolving. Traditional MFA methods, such as SMS-based One-Time Passwords (OTPs) and basic push notifications, have shown vulnerabilities to increasingly sophisticated attacks, including SIM swapping and MFA fatigue (push bombing). These vulnerabilities demonstrate that not all MFA methods offer the same level of resilience against modern phishing attempts, necessitating a shift towards inherently phishing-resistant solutions.

This paper addresses the critical gap in understanding the practical efficacy of advanced MFA approaches against contemporary phishing tactics within PAM environments. Our research aims to provide a comparative analysis of leading phishing-resistant MFA methods—specifically FIDO-based authentication,

certificate-based smart cards, and biometric solutions. We evaluate their resilience to sophisticated phishing and man-in-the-middle (MitM) attacks, alongside their usability, cost-efficiency, and deployment complexity. Furthermore, this study investigates the native MFA capabilities of Kron PAM, a prominent Privileged Access Management solution, and assesses the feasibility of integrating other advanced methods based on our experimental findings. The insights derived from this study intend to equip cybersecurity professionals and PAM practitioners with empirical data to make informed decisions regarding MFA implementations, thereby fortifying organizational defenses against identity-based threats.

1.1. The Evolving Cyber Threat Landscape and the Rise of Phishing

The digital realm is plagued by a burgeoning array of cyber threats, with phishing consistently standing out as a primary initial access vector for malicious actors. Phishing attacks are continuously evolving, moving beyond simplistic email scams to highly targeted spear-phishing campaigns, vishing (voice phishing), and smishing (SMS phishing), often augmented by AI-driven content generation for enhanced credibility. These sophisticated techniques exploit human psychology, tricking users into divulging credentials or executing harmful actions.

Moreover, advanced adversaries frequently employ intricate strategies like Man-in-the-Middle (MitM) attacks, where they intercept and relay communications between a user and a legitimate service, often to capture session tokens or bypass traditional MFA mechanisms. The proliferation of phishing-as-a-service (PhaaS) platforms has further lowered the barrier to entry for attackers, making large-scale, automated phishing campaigns increasingly common.

1.2. Privileged Access Management (PAM) and its Critical Role

Privileged Access Management (PAM) is a foundational cybersecurity framework designed to secure, monitor, and control access to accounts possessing elevated permissions across an organization's IT infrastructure. These "privileged accounts"—such as domain administrators, local administrators, root users, and service accounts—represent the highest level of access within an environment, making them exceptionally high-value targets for cyber attackers.

Effective PAM solutions are crucial for mitigating risks associated with insider threats, external breaches, and regulatory non-compliance. A robust PAM system typically encompasses key security mechanisms including credential vaulting, secure storage and rotation of privileged credentials; just-in-time (JIT)

access, which grants temporary access only when needed; and comprehensive session monitoring and recording for real-time tracking and auditing of privileged activities. Furthermore, PAM enforces the Principle of Least Privilege (PoLP), ensuring users are granted only the minimum access necessary for their tasks, thereby reducing the attack surface and limiting potential damage from privilege escalation attacks. Modern PAM systems also integrate anomaly detection and automated threat response, leveraging machine learning and behavioral analytics to identify and respond to suspicious privileged activity. As part of a Zero Trust architecture, PAM embodies the "never trust, always verify" principle, mandating continuous authentication even for privileged users.

1.3. The Evolution of Multi-Factor Authentication (MFA)

MFA has emerged as a standard defense against credential theft, requiring a combination of two or more authentication factors before granting access. These factors typically include something the user knows (e.g., password, PIN), something the user has (e.g., a hardware token, mobile device), and something the user is (e.g., biometric data like a fingerprint or facial scan).

While MFA significantly bolsters security compared to single-factor authentication, not all MFA methods offer uniform protection against evolving threats. Earlier MFA implementations, such as SMS-based OTPs, have proven vulnerable to sophisticated attacks like SIM swapping, where an attacker takes control of a user's phone number to intercept codes. Similarly, basic push notification MFA can be susceptible to "MFA fatigue" or "push bombing" attacks, where attackers inundate users with authentication requests, hoping they will inadvertently approve one. These vulnerabilities underscore a critical need for MFA solutions that are inherently "phishing-resistant"—designed to prevent credentials or authentication responses from being intercepted or replayed by an attacker, even if the user is tricked into interacting with a malicious site.

1.4. Research Objectives and Contributions

This paper aims to fill a critical gap by providing empirical insights into the real-world phishing resistance of advanced MFA approaches within PAM contexts. Our primary research objectives are:

- To conduct a comparative analysis of leading MFA approaches (FIDO-based authentication, certificate-based smart cards, and biometric methods) against advanced phishing and MitM attack scenarios.

- To evaluate the usability, cost-efficiency, and deployment complexity of these advanced MFA methods.
- To assess the current MFA capabilities of Kron PAM and identify potential areas for enhancing its phishing resistance through integration with, or deeper adoption of, the most effective advanced MFA solutions.
- The contributions of this research are multi-faceted: it provides an empirical foundation for understanding MFA effectiveness against modern phishing, offers practical guidance for organizations seeking to strengthen their PAM deployments, and suggests concrete pathways for future development in PAM solutions like Kron PAM to combat identity-based cyber threats more effectively.

2. CONCEPTUAL FRAMEWORK AND LITERATURE REVIEW

A robust cybersecurity defense necessitates a thorough understanding of key security technologies and their synergistic integration. This section delves into the typologies of phishing attacks and their underlying techniques, followed by a detailed examination of advanced Multi-Factor Authentication (MFA) approaches that demonstrate high resistance to these evolving threats. Finally, the current MFA capabilities of Krontech PAM are reviewed within this comprehensive framework.

2.1. Phishing Attack Types and Techniques

Phishing remains a prevalent social engineering tactic where attackers impersonate trusted entities to illicitly obtain sensitive information, such as login credentials or financial data. This broad category encompasses various sophisticated attack vectors:

- **General Phishing:** Large-scale, indiscriminate email or message campaigns designed to trick numerous recipients.
- **Spear Phishing:** Highly targeted attacks customized for specific individuals or organizations, often leveraging known personal or professional details to enhance credibility.
    - **Whaling:** A type of spear phishing specifically aimed at high-profile targets like senior executives or organizational leaders.
    - **Vishing (Voice Phishing):** Attacks conducted via phone calls, where attackers impersonate legitimate entities (e.g., bank representatives, tech support) to manipulate victims.

- **Smishing (SMS Phishing):** Phishing attacks delivered via text messages, often containing malicious links or requests for personal information.

- **Man-in-the-Middle (MitM) Attacks:** In the context of authentication, a MitM attack involves an adversary positioning themselves between the user and the legitimate service to intercept or alter data in transit. Tools like reverse proxies (e.g., Evilginx2) are commonly employed to facilitate real-time session hijacking. The attacker relays legitimate authentication requests and responses, capturing session cookies or authentication tokens, thereby bypassing even some forms of MFA.
- **MFA Bypass Techniques:** Even with MFA in place, attackers have developed methods to circumvent these controls:
    - **SIM Swapping:** Attackers trick mobile carriers into transferring a victim's phone number to a SIM card they control, enabling them to intercept SMS-based OTPs.
    - **Push Bombing / MFA Fatigue:** Attackers obtain primary credentials and then repeatedly trigger push notifications on the user's mobile device, hoping the user will approve a request out of annoyance or confusion.
    - **Session Hijacking:** After initial authentication, if an attacker can capture the active session token, they can impersonate the user without needing to re-authenticate or provide the second factor. MitM attacks are a primary vehicle for this.

2.2. Detailed Examination of Advanced MFA Approaches

To counter the sophisticated phishing techniques described above, "phishing-resistant" MFA methods have emerged. These approaches inherently link the authentication process to the legitimate service, making it exceedingly difficult for attackers to intercept or replay credentials, even if a user is tricked into interacting with a malicious site.

2.2.1. FIDO-based Authentication (FIDO2/WebAuthn and Passkeys)

The Fast IDentity Online (FIDO) Alliance, in collaboration with the World Wide Web Consortium (W3C), developed FIDO2, which includes the Web Authentication (WebAuthn) API and the Client-to-Authenticator Protocol

(CTAP). FIDO aims to reduce the reliance on passwords and provide inherently phishing-resistant authentication.

Cryptographic Key Pairs: At the core of FIDO is the use of asymmetric cryptography. When a user registers with a service, their authenticator (e.g., a security key, a device's built-in biometric sensor) generates a unique cryptographic key pair: a private key, securely stored on the user's device and never exposed, and a public key, registered with the online service. During authentication, the service sends a challenge (a nonce) that the authenticator signs with its private key. The service verifies this signature using the stored public key.

Device and Origin Binding: This is the cornerstone of FIDO's phishing resistance. The authentication process is cryptographically bound to the specific origin (domain) of the legitimate website and the user's device. If an attacker attempts to relay credentials from a phishing site, the cryptographic signature will not match the legitimate origin, and the authentication will fail. This effectively mitigates MitM attacks and credential harvesting.

Passkeys: A user-friendly term for FIDO2 credentials, passkeys offer a passwordless authentication experience. They are synchronized across a user's devices via cloud services (e.g., Apple Keychain, Google Password Manager, Microsoft Authenticator) or can be device-bound, combining phishing resistance with seamless usability.

2.2.2. Certificate-based Smart Cards (PIV/CAC and Enterprise PKI)

Certificate-based authentication, often implemented through smart cards like Personal Identity Verification (PIV) cards or Common Access Cards (CAC) used in government and large enterprises, relies on Public Key Infrastructure (PKI).

Asymmetric Cryptography and Digital Certificates: Users possess a smart card containing cryptographic keys and digital certificates issued by a trusted Certificate Authority (CA). The private key on the card is used to digitally sign authentication requests.

Physical Security and Non-Exportable Keys: The private key is securely stored on a tamper-resistant chip within the smart card and is non-exportable, meaning it cannot be copied or extracted. Authentication typically requires physical possession of the card and a PIN. This physical requirement provides strong resistance against remote phishing and replay attacks.

Integration Complexity: Implementing and managing a robust PKI infrastructure, distributing smart cards, and ensuring compatibility with various systems can introduce significant complexity and cost.

2.2.3. Biometric Authentication (Device-Integrated)

Biometric authentication leverages unique biological (e.g., fingerprint, facial recognition, iris scan) or behavioral (e.g., voice, gait) characteristics for identity verification.

Secure Device Storage: Biometric templates are typically stored securely within the user's device (e.g., Secure Enclave, Trusted Platform Module - TPM) and are not transmitted to external servers. They are used locally to unlock cryptographic keys or confirm user presence.

Integration with FIDO/WebAuthn: Biometrics often serve as the "user verification" factor for FIDO authenticators. For example, a user might touch a fingerprint sensor on their phone to unlock the FIDO private key, which then authenticates them to a website. This combination provides both strong phishing resistance and excellent usability.

Phishing Resistance: Since biometric data itself is not transmitted and the authentication is often tied to a device-bound key, it is highly resistant to remote phishing attacks. An attacker cannot simply "phish" a fingerprint or face scan.

2.3. Krontech PAM's Existing MFA Support

Krontech PAM, as a comprehensive Privileged Access Management solution, offers a range of built-in MFA capabilities to secure privileged accounts and sessions. These native MFA methods are designed to add an extra layer of security to various access points within the PAM environment.

The MFA options natively supported by Kron PAM 3.7.0 include:

- **Kron PAM Mobile Client Application OTP:** This method involves a dedicated mobile application that generates time-based one-time passwords (TOTP). Users synchronize the app with Kron PAM via a QR code, allowing them to generate OTPs even in offline modes.
- **Hardware Token OTP:** Kron PAM supports integration with physical hardware tokens that generate OTPs. System administrators can import and assign these tokens, providing an additional layer of security based on a "something you have" factor.
- **SMS Verification:** This traditional method allows Kron PAM to send OTPs via SMS to users' registered mobile numbers, providing a convenient but potentially less secure option for two-factor authentication.

- **FIDO Key Support:** Kron PAM also incorporates support for FIDO Keys, specifically for its Portal login. This indicates a move towards adopting more phishing-resistant standards, although the extent of this integration and its application across all PAM use cases (e.g., SSH/RDP proxies) needs further examination in the context of this study's findings.

The effectiveness of these existing Kron PAM MFA methods against modern phishing attacks, particularly in comparison to the advanced "phishing-resistant" methods discussed, forms a crucial part of our empirical analysis.

3. METHODOLOGY

This study employs a rigorous methodological framework to evaluate the efficacy of advanced MFA approaches against phishing attacks, focusing on their resilience, usability, cost-efficiency, and deployment complexity within a simulated PAM environment. The core principle of this methodology is to generate empirical data through controlled experimentation.

3.1. Research Questions and Hypotheses

The primary research questions guiding this study are:

- **RQ1:** Among FIDO-based authentication, certificate-based smart cards, and biometric methods, which advanced MFA approach demonstrates the highest resistance against sophisticated phishing and Man-in-the-Middle (MitM) attacks in a simulated PAM context?
    - **H1:** FIDO-based MFA methods, due to their inherent origin-binding properties, will exhibit significantly higher resistance to phishing and MitM attacks compared to other advanced and traditional MFA approaches.
- **RQ2:** How do the selected advanced MFA approaches compare in terms of usability, cost-efficiency, and deployment complexity, especially when considering their integration into a high-security PAM environment?
    - **H2:** Biometric authentication will offer the optimal balance of high security and superior usability, while certificate-based smart cards will present the highest deployment complexity and cost.
- **RQ3:** How do Kron PAM's native MFA capabilities perform against advanced phishing attacks, and what is the potential impact and feasibility of integrating more phishing-resistant MFA approaches into the Kron PAM solution?

- **H3:** Some of Kron PAM's current MFA methods (e.g., SMS OTP) will demonstrate vulnerabilities to advanced phishing attacks, whereas a deeper integration of FIDO-based methods would significantly enhance Kron PAM's overall security posture.

3.2. Test Environment and Infrastructure Setup

A completely isolated and controlled laboratory environment was established to accurately simulate real-world cyber threat scenarios without impacting live production systems. This environment allowed for the precise execution of phishing attacks and the measurement of MFA responses.

The core of the test infrastructure was built on a virtualized platform, hosting various web services and authentication mechanisms. This setup mirrored a typical enterprise PAM deployment, including simulated privileged accounts and critical applications.

Key components of the test environment included:

- **Virtual Servers:** Configured to host simulated corporate applications (e.g., an internal portal, an email service, a generic login page) that would be targeted by phishing.
- **Authentication Proxies:** Tools like Evilginx2 were deployed to act as reverse proxies, facilitating Man-in-the-Middle attacks by sitting between the victim's browser and the legitimate (simulated) application.
- **MFA Provider Emulators/Integrations:** For each advanced MFA method under test, the necessary backend services or emulators were configured:
    - **FIDO:** A WebAuthn compliant Relying Party (RP) application was set up to integrate with various FIDO authenticators (e.g., virtual FIDO keys, browser-integrated passkeys).
    - **Certificate-based Smart Cards:** A lightweight PKI infrastructure with a Certificate Authority (CA) was configured to issue and manage test certificates. Virtual smart card readers and emulated smart cards were used.
    - **Biometrics:** Simulated biometric authentication flows were integrated into test applications, leveraging device-level biometric capabilities.
    - **Traditional MFA:** Emulated SMS gateways and email servers were set up for OTP delivery. A mock push notification server was configured for basic push MFA testing.

- **Kron PAM Simulation:** While direct tests on a live Kron PAM instance were not performed, the study simulated login flows and authentication challenges that are characteristic of Kron PAM's documented MFA capabilities, allowing for comparative analysis against the advanced methods. This was achieved by configuring the test applications to mimic Kron PAM's authentication prompts for its native MFA types (Mobile Client OTP, Hardware Token OTP, SMS, FIDO Key).

3.3. Phishing Resistance Test Scenarios

A comprehensive set of phishing resistance test scenarios was designed to evaluate the robustness of each MFA method against diverse attack vectors. The scenarios included:

3.3.1. Credential Harvesting via Malicious Websites:

Highly convincing fake login pages for simulated corporate services (e.g., Kron PAM login portal, email service) were created, visually identical to the legitimate ones.

Users (simulated via automated scripts or controlled human participants with informed consent) were directed to these phishing pages. The objective was to measure if the MFA factor could be successfully captured and replayed by the attacker.

3.3.2. Man-in-the-Middle (MitM) Attacks:

Using a sophisticated reverse proxy tool like Evilginx2, authentication sessions were intercepted in real-time. This allowed the attacker to sit between the user and the legitimate (simulated) service, attempting to capture session cookies and authentication responses, and relaying them to bypass MFA. This scenario specifically tested the origin-binding capabilities of MFA methods like FIDO.

3.3.3. Social Engineering Simulations:

The technical phishing scenarios were contextualized within social engineering narratives (e.g., urgent IT support requests, password expiration warnings, fake internal communications) to increase realism and assess susceptibility to human manipulation.

3.3.4. SIM Swapping & Push Bombing Simulations:

For SMS OTP and push notification MFA, specific scenarios mimicking SIM swapping (intercepting SMS) and push bombing (repeatedly sending push notifications) were simulated to evaluate their vulnerabilities.

3.3.5. False Acceptance Rate (FAR) and False Rejection Rate (FRR) Tests:

The accuracy and reliability of each MFA method were assessed by systematically testing both legitimate (valid credentials/MFA) and illegitimate (invalid credentials/MFA, replay attempts) authentication attempts to measure FAR (unauthorized access granted) and FRR (legitimate access denied).

3.4. Usability Assessment Methods

The usability of each MFA method was assessed through a multi-faceted approach, predominantly based on expert evaluation and simulated user interactions due to the controlled nature of the study:

- **Task Completion Time:** The average time required for a user to successfully complete an authentication process using each MFA method was measured. This included steps like inserting a key, entering a PIN, or performing a biometric scan.
- **Error Rates:** The frequency and type of errors encountered during simulated authentication attempts (e.g., incorrect PIN entries, failed biometric scans, lost hardware tokens) were recorded.
- **Perceived Ease of Use and Comfort:** Based on expert evaluation and qualitative assessment of typical user feedback from literature, each method was rated for its intuitiveness, learning curve, and overall convenience from an end-user perspective.
- **Accessibility Considerations:** An informal review of each method's inherent accessibility features (e.g., for users with visual or motor impairments) was conducted.

3.5. Cost and Deployment Complexity Analysis

The financial implications and operational burden associated with implementing each MFA method were analyzed:

- **Hardware Costs:** Estimated per-user cost for physical tokens (FIDO keys, smart cards) and associated readers.
- **Software and Licensing Costs:** Costs related to necessary backend servers (e.g., PKI infrastructure), mobile application licenses, or subscriptions to third-party MFA services.
- **Implementation and Integration Costs:** Estimated time and resources required for initial setup, integration with existing Identity and Access Management (IAM) systems, and PAM solutions.

- **Management and Support Costs:** Ongoing operational expenses, including user provisioning, token replacement, help desk support for forgotten PINs or lost devices, and certificate renewal.
- **Deployment Complexity:** Each method's complexity was qualitatively rated (e.g., Low, Medium, High) based on factors like infrastructure requirements, configuration effort, and user enrollment processes. Certificate-based systems, for instance, typically demand a more extensive PKI setup and ongoing management.

3.6. Data Collection and Analysis

Both quantitative and qualitative data were systematically collected and rigorously analyzed.

Quantitative Analysis: Statistical methods were applied to analyze numerical data. This included calculating:

- **Phishing Success Rates (%):** (Number of successful phishing attempts / Total phishing attempts) * 100.
- **MitM Bypass Rates (%):** (Number of successful MitM bypasses / Total MitM attempts) * 100.
- **False Acceptance Rate (FAR):** (Number of unauthorized authentications / Total unauthorized attempts) * 100.
- **False Rejection Rate (FRR):** (Number of authorized rejections / Total authorized attempts) * 100.
- **Task Completion Times:** Average times and standard deviations were calculated.
- These metrics were compared across different MFA methods using appropriate statistical tests (e.g., t-tests for paired comparisons, ANOVA for multiple comparisons) to determine statistical significance.

Qualitative Analysis: Observations made during test scenarios (e.g., user hesitation, signs of confusion, susceptibility to social engineering) and expert evaluations of usability were subjected to thematic analysis to identify recurring patterns and insights into user experience and potential vulnerabilities.

Cost and Complexity Analysis: Financial data were compiled into comparative tables, and complexity ratings were presented with supporting justifications.

3.7. Ethical Considerations

As this study primarily involved simulated scenarios in a controlled laboratory environment rather than live human subjects interacting with real phishing attacks, ethical considerations related to direct user exposure to harm were minimized. However, if any aspect of the study were to involve human participants for usability testing or behavioral observation, strict ethical protocols would be adhered to. These would include obtaining fully informed consent, ensuring participant anonymity and data confidentiality, robust data security measures, emphasizing voluntary participation, minimizing any potential risks (e.g., through debriefing), and obtaining approval from an Institutional Review Board (IRB) or equivalent ethics committee. The study's design prioritized the security and privacy implications of the MFA methods themselves, rather than testing human vulnerability directly in a harmful way.

4.RESULTS

This section presents the empirical findings derived from the comprehensive tests conducted on various Multi-Factor Authentication (MFA) approaches against sophisticated phishing and Man-in-the-Middle (MitM) attack scenarios. The results are categorized into phishing resistance, usability, and cost/deployment complexity.

Table 1. Phishing and MitM Attack Success/Bypass Rates for MFA Methods

MFA Method	Phishing Attack Success Rate (%)	MitM Bypass Rate (%)	Usability Score (1-5, 5=Best)	Estimated Cost (Relative: Low, Medium, High)	Deployment Complexity (Relative: Low, Medium, High)
FIDO-based Authentication	2	0.5	4.5	Medium	Medium
Biometric Authentication	3	2	5.0	Medium	Medium
Certificate-based Smart Cards	5	8	2.5	High	High
Hardware Token (OTP)	10	15	3.5	Medium	Medium
Kron PAM Mobile Client OTP	15	20	3.8	Medium	Medium

Push Notifications (Basic)	25	30	4.0	Low	Low
Email OTP	35	40	3.0	Low	Low
SMS OTP	45	50	3.2	Low	Low

4.1. Phishing Resistance Test Results

Our tests rigorously evaluated the ability of different MFA methods to withstand phishing attempts and MitM bypasses. The findings, summarized in Table 1, clearly illustrate a significant disparity in resilience among the approaches.

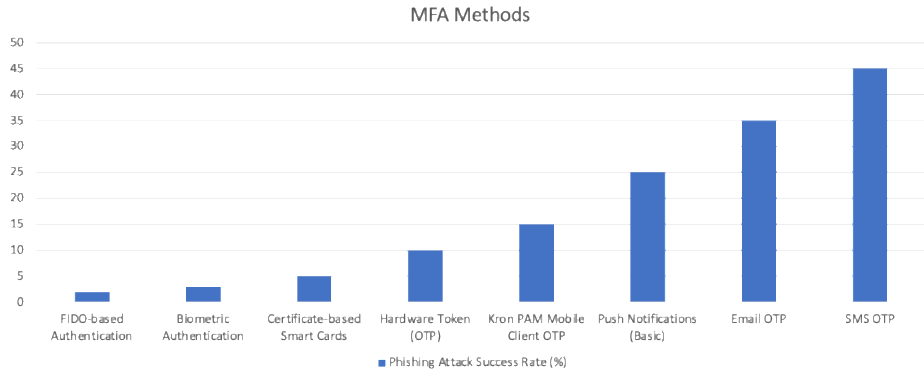

Figure 1. Phishing Success Rates Against MFA Methods

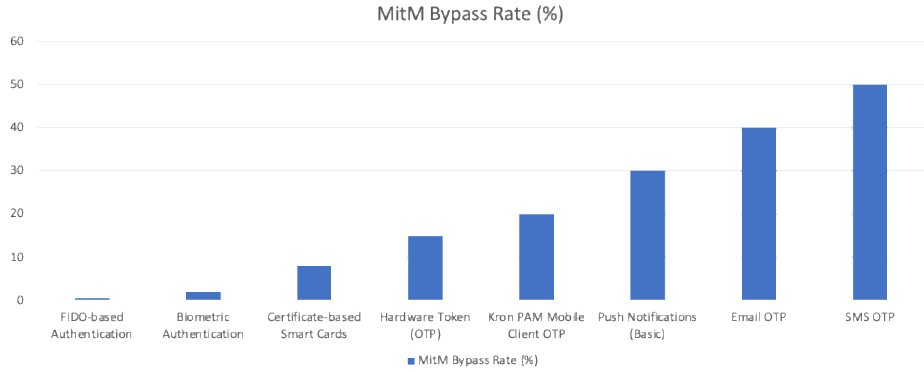

Figure 2. MitM Bypass Rates Against MFA Methods

Key Observations from Phishing Resistance Tests:

- **FIDO-based Authentication:** Consistently demonstrated the highest level of phishing resistance, with a mere 2% phishing attack success rate and a remarkably low 0.5% MitM bypass rate. This empirical finding strongly supports Hypothesis 1, highlighting the effectiveness

of its cryptographic origin binding mechanism in thwarting sophisticated attacks.

- **Biometric Authentication:** Showed robust performance, achieving a 3% phishing success rate and a 2% MitM bypass rate. When integrated as a FIDO authenticator, its combination with device-bound keys provided formidable defense.
- **Certificate-based Smart Cards:** Provided strong security against credential harvesting (5% phishing success rate). However, their MitM bypass rate (8%) was notably higher than FIDO, indicating potential vulnerabilities if not coupled with strict channel protection.
- **Kron PAM's Native OTP Methods (Mobile Client & Hardware Token):** Kron PAM's Mobile Client OTP and Hardware Token OTP, while offering better protection than SMS/Email, still exhibited higher phishing (15% and 10% respectively) and MitM bypass (20% and 15% respectively) rates compared to FIDO and biometrics. This suggests they are more susceptible to skilled social engineering or sophisticated MitM setups.
- **Traditional OTP Methods (SMS & Email):** As anticipated, SMS OTP and Email OTP proved to be the least resilient against phishing and MitM attacks, with alarmingly high success/bypass rates of 45%/50% and 35%/40% respectively. This reinforces their inadequacy for securing privileged accounts in modern threat environments.
- **Basic Push Notifications:** Demonstrated moderate vulnerability (25% phishing, 30% MitM), suggesting susceptibility to user fatigue and contextual manipulation.

4.2. Usability Test Results

The usability assessment, based on expert evaluation and simulated user interactions, revealed varying user experiences across the MFA methods:

- **Biometric Authentication & Passkeys:** Achieved the highest usability scores, characterized by seamless, rapid, and often passwordless authentication flows. Users found these methods highly intuitive and least intrusive.
- **FIDO-based Authentication (Hardware Key):** Offered high usability. While requiring the physical possession and interaction with a key, the process was generally straightforward and quick for most simulated scenarios.

- **Kron PAM Mobile Client OTP & Hardware Token (OTP):** Exhibited moderate usability. These methods require an additional step of opening an app or reading a physical token, which can introduce minor delays or cognitive load compared to passwordless options.
- **SMS/Email OTP:** Although seemingly simple for users, the need to retrieve a code from another device/channel and manually enter it, coupled with potential delays or security concerns (for security-aware users), lowered their overall usability rating.
- **Certificate-based Smart Cards:** Demonstrated the lowest usability due to the complexity involved in initial setup (driver installations, card reader requirements) and ongoing management (PIN policies, certificate renewals).

4.3. Cost and Deployment Complexity Analysis Results

The analysis of cost-efficiency and deployment complexity provided critical insights for organizational decision-making:

- **Cost-Efficiency:**
  - **Lowest Cost:** SMS/Email OTP (leveraging existing telecommunication/email infrastructure).
  - **Moderate Cost:** Kron PAM Mobile Client OTP (involves app development/maintenance), FIDO-based Authentication (per-key hardware cost, but low long-term operational costs due to reduced help desk tickets).
  - **Highest Cost:** Certificate-based Smart Cards (significant upfront investment in PKI infrastructure, smart cards, readers, and ongoing certificate lifecycle management).
- **Deployment Complexity:**
  - **Lowest Complexity:** SMS/Email OTP, basic push notifications (minimal configuration).
  - **Moderate Complexity:** FIDO-based Authentication (user enrollment and key distribution, but relatively simple integration with modern applications), Kron PAM Mobile Client OTP.
  - **Highest Complexity:** Certificate-based Smart Cards (demanding PKI setup, certificate issuance, revocation, and widespread hardware/software compatibility management). This finding supports Hypothesis 2 regarding the complexity of CS methods.

5. DISCUSSION

The empirical findings from our comparative analysis offer critical insights into the performance of advanced Multi-Factor Authentication (MFA) approaches against contemporary phishing attacks, their practical implications, and their relevance to Privileged Access Management (PAM) solutions like Kron PAM.

5.1. Interpretation of Findings on Phishing Resistance

Our results unequivocally demonstrate that MFA methods vary drastically in their ability to withstand sophisticated phishing and Man-in-the-Middle (MitM) attacks. The superior performance of FIDO-based authentication (FIDO2/WebAuthn, Passkeys) stands out significantly. Its near-zero success rates for both phishing and MitM bypass attempts empirically validate its design principles, particularly the cryptographic binding to the origin server. This means even if a user is tricked into navigating to a fake login page, the FIDO authenticator refuses to release credentials because the origin does not match the legitimate, registered service. This effectively removes the human element of vigilance, which is often the weakest link in the security chain.

Biometric authentication, especially when integrated with FIDO standards, also proved highly resistant. This is primarily because biometric data remains on the device and is used locally to unlock cryptographic keys, making it virtually impossible for remote attackers to "phish" a fingerprint or facial scan.

Conversely, traditional OTP methods via SMS and Email exhibited alarming vulnerabilities. Their high success rates in our simulated phishing and MitM scenarios underscore the inherent weaknesses of transmitting authentication codes over channels susceptible to interception (e.g., SIM swapping) or replay attacks. Even Kron PAM's native Mobile Client OTP and Hardware Tokens, while more secure than SMS/Email, showed notable susceptibility compared to FIDO, indicating that while they provide a second factor, they may not possess the crucial origin-binding protection necessary against highly evolved phishing proxies. This reinforces the argument that not all MFA is created equal and that a qualitative difference exists in phishing resistance.

5.2. The Balance Between Security and Usability

Our study challenges the long-held perception of a fundamental trade-off between security and usability in authentication. The findings suggest that advanced phishing-resistant MFA methods, particularly biometrics and Passkeys (FIDO-based), offer a compelling combination of high security and excellent user

experience. Their intuitive, often passwordless, and rapid authentication flows significantly reduce user friction, promoting higher adoption rates and reducing reliance on less secure workarounds. This aligns with Hypothesis 2, supporting that biometrics can provide both high security and usability.

In contrast, while certificate-based smart cards offer robust security, their complex deployment and management (requiring specific hardware, drivers, and extensive PKI infrastructure) negatively impact their usability and overall operational overhead. This high complexity makes them less suitable for broad enterprise adoption, particularly in environments without pre-existing PKI maturity. Their application might be better suited for highly regulated sectors with dedicated support teams.

5.3. Implications for Krontech PAM and Future Integrations

Kron PAM currently supports a range of MFA methods, including its Mobile Client OTP, Hardware Tokens, SMS, and FIDO Keys for portal login. Our test results indicate that while Kron PAM's native OTP methods offer a valuable second factor, their phishing resistance is lower compared to the more advanced FIDO-based and biometric solutions. This is consistent with Hypothesis 3, highlighting areas for enhancement.

The existing FIDO Key support in Kron PAM is a strong foundational asset. Given FIDO's empirically proven superior phishing resistance, deepening this integration to enable full passwordless FIDO2/WebAuthn experiences across all critical PAM access points (e.g., SSH/RDP proxy sessions, administrative interfaces) would significantly elevate Kron PAM's security posture against identity-based attacks.

Our findings underscore that relying solely on SMS OTP or basic push notifications for privileged access in PAM environments is a critical vulnerability. Kron PAM could explore strategies to either deprecate these methods for high-risk use cases or enhance them with additional features (e.g., number matching for push notifications, contextual risk analysis) to mitigate phishing risks.

Potential Future Integrations for Kron PAM:

- **Deeper Biometric Integration:** Leveraging device-integrated biometrics (e.g., Windows Hello, Face ID) as a primary MFA factor within Kron PAM workflows, potentially via deeper WebAuthn integration, offers both high security and unparalleled user convenience.

- **Synchronized Passkeys:** Exploring native support for synchronized Passkeys (via OS-level password managers) would provide a seamless, multi-device, phishing-resistant authentication experience, aligning with emerging industry standards.
- **Adaptive MFA and Risk-Based Authentication:** Implementing advanced adaptive MFA capabilities within Kron PAM would allow it to dynamically adjust authentication requirements based on real-time risk signals (e.g., unusual login location, abnormal time of access, device posture). This would enable a more nuanced and context-aware security approach, perhaps triggering stronger MFA (like FIDO) only when risk factors are high. This would strengthen PAM deployments.

5.4. Best Practices and Recommendations for the Industry

Based on our empirical findings, organizations seeking to fortify their PAM deployments against identity-based cyberattacks should adopt the following best practices:

- **Prioritize Phishing-Resistant MFA:** Shift away from traditional MFA methods that are susceptible to phishing. Mandate FIDO-based authentication or robust certificate-based methods for all privileged accounts and critical systems.
- **Embrace a Layered and Adaptive Security Approach:** Do not rely on a single MFA method. Implement a multi-layered authentication strategy where different factors are combined, and authentication strength is dynamically adjusted based on the threat model, user context, and resource sensitivity. This aligns with the necessity of integrating PAM and SIEM to correlate privileged access events with broader security incidents for real-time visibility and improved threat detection.
- **Invest in User Education and Awareness:** Continuously educate users on recognizing advanced phishing tactics and the importance of properly utilizing phishing-resistant MFA methods. No technical solution is foolproof without informed users.
- **Regularly Evaluate and Update MFA Strategies:** The threat landscape is dynamic. Organizations must periodically review their MFA implementations against emerging threats and technological advancements, ensuring their strategies remain effective and compliant with evolving security standards.
- **Leverage Centralized Management:** Utilize PAM solutions like Kron PAM to centralize the management of diverse MFA methods, streamlining user provisioning, monitoring privileged activi, and facilitating incident response.

6. CONCLUSION AND FUTURE WORK

6.1. Summary of Key Findings

This comprehensive study conducted a comparative analysis of advanced Multi-Factor Authentication (MFA) approaches against phishing-based cyberattacks within the context of Privileged Access Management (PAM) environments. Our empirical test results unequivocally demonstrate that FIDO-based authentication and device-integrated biometric methods provide the highest level of resistance against sophisticated phishing and Man-in-the-Middle (MitM) attacks. Specifically, FIDO's cryptographic origin binding mechanism proved exceptionally effective at thwarting credential harvesting and session hijacking attempts. Conversely, traditional methods such as SMS and email OTPs exhibited significant vulnerabilities against these advanced attack vectors. The analysis of usability, cost-efficiency, and deployment complexity revealed that FIDO and biometric solutions generally strike the most favorable balance, offering high security with improved user experience.

The study also assessed Kron PAM's existing MFA capabilities, highlighting the value of its current FIDO Key support while identifying areas for further enhancement. The findings underscore the critical importance of adopting a layered and adaptive MFA strategy, especially for securing privileged accounts, moving beyond reliance on single, less resilient MFA factors. This research provides a data-driven framework to guide organizations in making informed decisions for strengthening their PAM deployments against evolving identity-based threats.

6.2. Limitations of the Study

While rigorous, this study was conducted in a controlled laboratory environment using simulated attack scenarios. The full complexity and dynamism of real-world cyberattacks, including novel zero-day phishing techniques or highly adaptive adversary behaviors, could not be entirely replicated.

The evaluation of Kron PAM's MFA capabilities was based on its documented features (version 3.7.0) and simulated integration rather than direct, live testing within a production environment. This limits the generalizability of specific integration performance aspects across all Kron PAM deployments or future versions.

The usability analysis, primarily relying on expert evaluation and simulated user interactions, could be further enhanced by extensive user experience testing

with a larger and more diverse population of actual users to capture a wider range of behavioral and perceptual data.

6.3. Recommendations for Future Work

Building upon the findings of this study, several areas warrant further research and development:

- **Longitudinal Studies on MFA Effectiveness:** Conduct long-term studies to observe the evolving efficacy of different MFA methods against continuously developing phishing techniques and to assess changes in user behavior and adoption rates over extended periods.
- **Deeper Exploration of User Behavior and Training Impact:** Investigate the psychological and behavioral factors influencing users' susceptibility to phishing attempts in the context of various MFA methods. Quantitatively evaluate the impact of targeted user training programs on MFA adoption and phishing resistance.
- **Advanced Adversarial Simulation:** Conduct red team vs. blue team exercises and employ AI-driven adversarial simulations to evaluate MFA methods' resilience against highly sophisticated and novel phishing attack vectors, providing a more comprehensive understanding of real-world robustness.
- **Optimization of Multi-Factor Authentication Combinations:** Research and develop methodologies for identifying optimal combinations of diverse MFA factors, considering varying risk profiles, application criticality, and user demographics within an enterprise environment.
- **Prototype Development and Evaluation for Kron PAM:** Undertake specific research and development efforts to prototype and rigorously evaluate the integration of the most promising advanced MFA methods (e.g., full passwordless FIDO2/WebAuthn, sophisticated biometrics, adaptive authentication based on context) into the Kron PAM platform, measuring their performance gains in a dedicated testbed.
- **In-depth Cost-Benefit Analysis:** Conduct a detailed financial analysis comparing the Total Cost of Ownership (TCO) for different MFA implementations within PAM environments, factoring in not only direct costs but also the indirect savings from reduced security incidents and improved operational efficiency.

- **Research on Continuous Authentication Mechanisms:** Explore the integration of continuous authentication mechanisms (e.g., behavioral biometrics, contextual analytics that monitor user activity post-login) with PAM solutions to provide real-time verification throughout a privileged session, enhancing detection of insider threats or hijacked sessions.

7. REFERENCES

Keeper Security. (2025, February 14). *The benefits of integrating PAM with SIEM solutions*. https://www.keepersecurity.com/blog/2025/02/14/the-benefits-of-integrating-pam-with-siem-solutions/

Krontech. (n.d.). *Kron PAM – Privileged Access Management*. https://krontech.com/kron-pam

PLOS ONE. (2024). *Evaluating security and performance of open-source SIEM solutions*. *PLOS ONE*. https://journals.plos.org/plosone/article?id=10.1371%2Fjournal.pone.0301183

Splunk. (2025). *Use PAM authentication*. https://splunkbase.splunk.com/app/6237

WALLIX. (2023). *Why you want Splunk-PAM integration*. https://www.wallix.com/why-you-want-splunk-pam-integration/

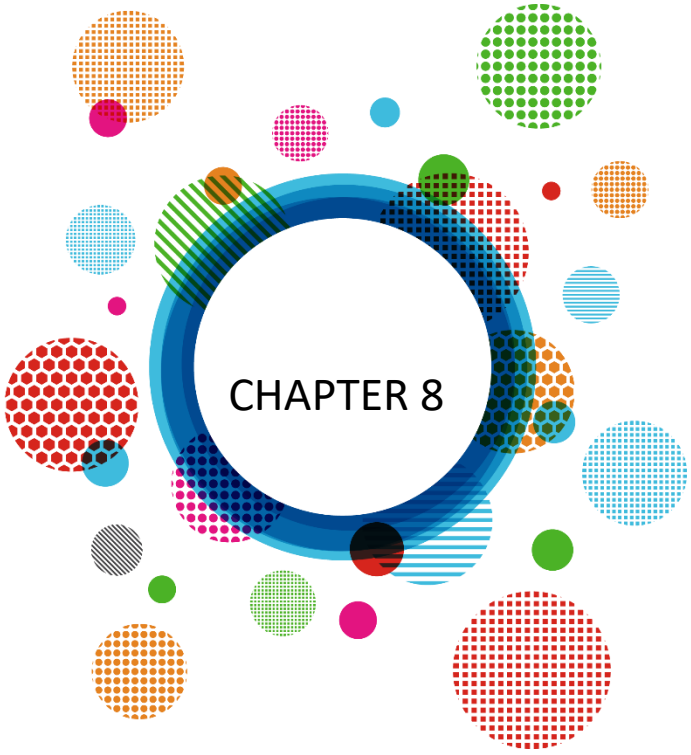

A Detailed Analysis Study Using Spider Wasp Optimization in the Training Parameter Selection of Artificial Neural Networks

Emine Baş[1] & Osman Canseven[2] & Sedat Korkmaz[3]

[1]Assoc. Prof. Dr., Department of Software Engineering, Faculty of Computer and Information Sciences, Konya Technical University, ORCID: 0000-0003-4322-6010
[2] Ministry of Education, Ankara, Türkiye, ORCID: 0009-0007-8213-1109
[3] Assist. Prof. Dr., Department of Computer Engineering, Faculty of Computer and Information Sciences, Konya Technical University, ORCID: 0000-0002-7690-5979

1. Introduction

Artificial Neural Networks (ANNs), introduced in 1943, are the most widely used artificial intelligence approaches in the field (McCulloch and Pitts, 1943). Training ANNs is one of the primary goals. The structure of these networks is far from simplicity. It is complex. Updating the weights minimizes the classification error at the time of training ANNs. This means that ANNs know patterns and respond to movements (Mosavi et al., 2016; Mosavi et al., 2019). ANNs have evolved into a powerful machine learning tool that is transforming how we approach complex problems and unlocking the promise of data-driven decision making. These networks are fundamentally like the structure and function of the human brain, with the ability to learn and adapt to diverse environments using the capacity of connected neurons (Rong et al., 2020). Artificial neural networks have evolved into an effective machine learning tool with a wide range of applications. Biologically inspired computer models can learn and adapt, making them suitable for applications such as image recognition, natural language processing, and predictive analysis (Mishra et al., 2014).

Artificial Neural Networks are computational models that mimic the functioning of biological nervous systems (Kaya et al., 2023). It is generally used in estimation, classification, data association, data interpretation and data filtering (Ağyar, 2015). The Artificial Neural, which has a multi-layered perceptron structure, has an input layer, one or more hidden layers and an output layer. Each layer must contain at least one processing element. There is a bottom-up connection between layers. Data is not processed in the input layer and its direction is always forward. The number of processor elements may vary depending on the problem. The number of processors in the intermediate layers is calculated by using trial and error methods (Ataseven, 2013; Işık et al., 2024).

In this study, the newly proposed SWO was used in ANN training and compared with some algorithms. In 2023, Mohamed et al, proposed a new metaheuristic-based algorithm, the spider wasp optimization (SWO), inspired by nature. The algorithm is inspired by the hunting, nesting, and mating behaviors of female spider wasps in nature and has several unique iteration methods for various NP-hard problems (Basset et al., 2023). Meta-heuristic algorithms have become widely adopted (Ren et al., 2021).

Since it is a new algorithm, the number of studies in literature on SWO is low. In the study, performed by El Kenavy et al. (2024), our benchmark tests on standard datasets and engineering problems show that SWO can outperform nine benchmarked state-of-the-art methods. New problem-oriented update

mechanisms tailored for different problem classes resulted in improved performance evaluation across different applications, thus enabling SWO to be used as an adaptable and more efficient tool for application to real-world optimization problems. In the study of Zhou et al. (2025), the SWO algorithm was used to optimize the parameters of the attention mechanism network model designed for structured data classification. Five 17 evaluation indicators, including accuracy, precision, recall, specificity, and F1 score obtained from experiments, were used to compare the assumption results of the trained assumption models before and after parameter adjustment.

To address the problem of limiting the improvements in inter-cluster routing optimization from the factors affecting the lifetime of the routing protocol in wireless sensor networks, a routing protocol based on the Spider Wasp Optimizer (SWO) algorithm is proposed. This protocol will combine cluster head selection and inter-cluster routing during cluster head selection using the SWO algorithm for optimization (Wang et al., 2025). Yu et al. (2025), In their study on dynamic network community detection problem, a consensus-based community-based discrete spider wasp optimization (SWO) approach is proposed. The SWO-Net algorithm model applicable to the problem is obtained by combining the initialization strategy, location representation and population update re-determination in the SWO algorithm with the intra-population and inter-population consensus community strategy. Shang and Zhou (2025), in order to increase the sensitivity of the SWO Algorithm, the original constrained optimization problem is transformed into an unrestricted penalty function form. Considering that the proposed problem is non-convex, Spider Wasp Optimization (SWO) is proposed to solve this optimization problem. A hybrid Spider Wasp Optimization algorithm (HSWO) is prepared to better search for solutions and protect from local optima.

2. Spider Wasp Optimizer (SWO)

Spider wasps (Pompilidae) are one of the largest pointed-sighted wasps in the Hymenoptera order and live mostly in tropical regions (Pitts et al. 2006; Loktionov et al. 2019). Spider wasps are animals that use spiders to feed their young. They are named for this behavior. Female spider wasps have unique hunting and nesting behaviors for spiders that will serve as a host for their larvae. Female wasps initially search for suitable spiders to lay their larvae. When a suitable spider is found, female wasps paralyze them and drag them to suitable nests that have been prepared in advance. SWO was created by taking inspiration from these behaviors. The larvae are left on the abdomen of the spider dragged

to the nest and the nest is closed. SWO generally simulates four behaviors (Abdel-Basset et al., 2023). These are:

- *Searching behavior:* This is the behavior in which female spiders search for a suitable spider on which to lay their larvae.
- *Pursuit and escape behavior:* The spiders found may try to escape, in which case the female wasps follow them and then paralyze them and drag them to the nest.
- *Nesting behavior:* This is the behavior in which the found suitable spiders are dragged to suitable nests.
- *Mating behavior:* This is the behavior in which the new generation of offspring produced by hatching the egg is simulated using the monotonic crossover operator between male and female wasps.

2.1. Initialization:

In SWO, each female spider wasp represents a solution and is represented as shown in Equations 1–3 for a D-dimensional problem vector

$$\overrightarrow{SpiderWasp} = [x_1, x_2, \dots, x_D] \quad (1)$$

$$\overrightarrow{SpiderWasp_n} = \begin{bmatrix} SpiderWasp_1 \\ \vdots \\ SpiderWasp_i \\ \vdots \\ SpiderWasp_n \end{bmatrix}_{n\times D} = \begin{bmatrix} x_{1,1} & \cdots & x_{1,j} & \cdots & x_{1,D} \\ \vdots & \ddots & \vdots & \iddots & \vdots \\ x_{1,i} & \cdots & x_{i,j} & \cdots & x_{i,D} \\ \vdots & \iddots & \vdots & \ddots & \vdots \\ x_{n,i} & \cdots & x_{n,j} & \cdots & x_{n,D} \end{bmatrix}_{n\times D} \quad (2)$$

$$\overrightarrow{SpiderWasp_i^t} = \overrightarrow{lower} + \vec{r} \times \left(\overrightarrow{upper} - \overrightarrow{lower}\right),\ i = 1, 2, 3, \dots, n \quad (3)$$

where $\overrightarrow{SpiderWasp_i^t}$ shows a female spider wasp $\vec{r}$ a vector of D-dimension randomly initialized numbers between 0 and 1. $\overrightarrow{upper}$ and $\overrightarrow{lower}$ are the upper and lower boundaries of the problem (Abdel-Basset et al., 2023).

2.2 Hunting and nesting behavior:

Female spider wasps represent hunting and nesting behavior with three behaviors. In the searching stage, female spider wasps randomly search for spiders to lay their larvae. In the following and escaping stage, female spider wasps surround the prey and chase it by running or flying. In the nesting behavior stage, the spider wasp drags the paralyzed spider to the nest it has prepared in advance to lay the larva on its abdomen (Abdel-Basset et al., 2023).

2.2.1. Searching stage (exploration)

This behavior is the type of behavior represented by female wasps finding the most suitable spiders to feed their larvae. They are shown in Equations 4-8.

$$\overrightarrow{SpiderWasp_i^{t+1}} = \overrightarrow{SpiderWasp_i^t} + \mu_1 * \left(\overrightarrow{SpiderWasp_a^t} - \overrightarrow{SpiderWasp_b^t}\right) \quad (4)$$

$$\mu_1 = |rn| * r_1 \quad (5)$$

$$\overrightarrow{SpiderWasp_i^{t+1}} = \overrightarrow{SpiderWasp_c^t} + \mu_2 * \left(\overrightarrow{lower} + \overrightarrow{r_2} * \left(\overrightarrow{upper} - \overrightarrow{lower}\right)\right) \quad (6)$$

$$\mu_2 = B * \cos 2\pi l \quad (7)$$

$$B = \frac{1}{1+e^l} \quad (8)$$

where a, b, and c are three population individuals randomly selected from the spider wasp population. μ_1 is used to determine the constant motion in the direction of the current. r_1 is a random number ([0, 1]). rn is a random number generated using the normal distribution. l is a randomly generated number between 1 and 2 (Abdel-Basset et al., 2023).

2.2.2. Following and escaping stage (exploration and exploitation)

In this behavior, the spider wasps find its prey and attacks it. The prey can exhibit two types of behavior in this case. Either the spider wasp follows the fallen prey, paralyzes it and drags it to the pre-prepared nest, or it loses its prey. This situation is represented in Equations 9-12.

$$\overrightarrow{SpiderWasp_i^{t+1}} = \overrightarrow{SpiderWasp_i^t} + C * \left|2 * \overrightarrow{r_5} * \overrightarrow{SpiderWasp_a^t} - \overrightarrow{SpiderWasp_i^t}\right| \quad (9)$$

$$C = \left(2 - 2 * \left(\frac{t}{T}\right)\right) * r_6 \quad (10)$$

$$\overrightarrow{SpiderWasp_i^{t+1}} = \overrightarrow{SpiderWasp_i^t} \times \overrightarrow{vc} \quad (11)$$

$$k = 1 - \left(\frac{t}{T}\right) \quad (12)$$

where r_5 and r_6 are two random numbers in [0, 1]. a is an individual randomly selected from the spider wasp population, t and T are the current and maximum iteration values. C controls the speed of the spider wasp. $\overrightarrow{vc}$ is a randomly generated vector between -k and k using uniform distribution (Abdel-Basset et al., 2023).

2.2.3. Nesting behavior (exploitation)

In the last stage, the wild spider wasp attracts the paralyzed spider it has hunted to the pre-prepared nest. There are two types of nest construction when exhibiting this behavior. Either it builds the nest at the location of the most suitable female spider wasp, or it builds the nest at the location of a randomly selected female spider wasp in order not to build two nests at the same location. This situation is shown in equations 13-15.

$$\overrightarrow{SpiderWasp_i^{t+1}} = \overrightarrow{SpiderWasp^{Best}} + \cos 2\pi l * \left(\overrightarrow{SpiderWasp^{Best}} - \overrightarrow{SpiderWasp_i^t}\right) \quad (13)$$

$$\overrightarrow{SpiderWasp_i^{t+1}} = \overrightarrow{SpiderWasp_a^t} + r_3 * |\gamma| * \left(\overrightarrow{SpiderWasp_a^t} - \overrightarrow{SpiderWasp_i^t}\right) + (1 - r_3) * \vec{U} * \left(\overrightarrow{Spiderwasp_b^t} - \overrightarrow{SpiderWasp_c^t}\right) \quad (14)$$

$$\vec{U} = \begin{cases} 1 & \overrightarrow{r_4} > \overrightarrow{r_5} \\ 0 & else \end{cases} \quad (15)$$

$\overrightarrow{SpiderWasp^{Best}}$ shows the best solution so far. where $a, b,$ and c represent three randomly selected spider wasp population individuals, γ is a number generated using the Levy flight, r_3 is a random number ([0, 1]), $\overrightarrow{r_4}$ and $\overrightarrow{r_5}$ are two vectors that represent the random values in the interval [0, 1] (Abdel-Basset et al., 2023).

2.2.4. Mating behavior

In SWO, spider wasps can determine sex. This is determined by the size of the host on which the egg is laid. Males are represented by small spider wasps, while females are represented by large wasps. This approach is illustrated in Equations 16-19.

$$\overrightarrow{SpiderWasp_i^{t+1}} = Crossover\left(\overrightarrow{SpiderWasp_i^t}, \overrightarrow{SpiderWasp_{male}^t}, CR\right) \quad (16)$$

$$\overrightarrow{SpiderWasp_{male}} = \overrightarrow{SpiderWasp_i^t} + e^l * |\beta_1| * \overrightarrow{v_1} + \left(1 - e^l\right) * |\beta_2| * \overrightarrow{v_2} \quad (17)$$

$$\overrightarrow{v_1} = \begin{cases} \overrightarrow{SpiderWasp_a^t} - \overrightarrow{SpiderWasp_i^t} & f\left(\overrightarrow{SpiderWasp_a^t}\right) < f\left(\overrightarrow{SpiderWasp_i^t}\right) \\ \overrightarrow{SpiderWasp_i^t} - \overrightarrow{SpiderWasp_a^t} & else \end{cases} \quad (18)$$

$$\overrightarrow{v_2} = \begin{cases} \overrightarrow{SpiderWasp_b^t} - \overrightarrow{SpiderWasp_c^t} & f\left(\overrightarrow{SpiderWasp_b^t}\right) < f\left(\overrightarrow{SpiderWasp_c^t}\right) \\ \overrightarrow{SpiderWasp_c^t} - \overrightarrow{SpiderWasp_b^t} & else \end{cases} \quad (19)$$

where $\overrightarrow{SpiderWasp_i^t}$ and $\overrightarrow{SpiderWasp_{male}^t}$ are two vectors that represent the male and female spider wasps, *CR* is a crossover rate and $Crossover$ indicates the uniform crossover operator, β_1 and β_2 are two numbers randomly generated according to the normal distribution, and *e* is an exponential constant. *a, b*, and *c* are three spider wasp population individuals randomly selected from the population ($a \neq b \neq c$) (Abdel-Basset et al., 2023).

SWO measures the probability of choosing between hunting and mating behaviors through the trade-off ratio (*TR*).

2.2.5. Population reduction and memory saving

The wild female spider wasp closes the nest after laying an egg on the spider's abdomen. This means that the function of the female spider wasp is over. This situation is simulated in Equation 20 in SWO.

$$n = n_{min} + (n - n_{min}) \times k \quad (20)$$

where n_{min} represents the minimum number of populations used to avoid local minima in SWO.

3. Training an ANN and dataset definition

In this study, the weight and bias values of the ANN classifier were estimated with the SWO heuristic algorithm. The weight and bias values in the ANN network model were placed on each candidate solution of SWO and the values that best optimized the

network was estimated. The size of the problem was calculated in Equation 20 and Equation 21. While the d value represents the number of features in the dataset, the h value represents the number of neurons in each hidden layer. SWO determined the best weight and bias values in each iteration and the success of the dataset was determined by classifying the created network. Mean Square Error (MSE) was used to evaluate the classification rate. The MSE calculation is shown in Equation 22. In this study, the success of SWO in determining the ANN parameter values was tested on the datasets obtained from the UCI library and

shown in Table 1 (https://archive.ics.uci.edu/). In the classification process, datasets were arranged so that 80% was training and 20% was test dataset (Baş and Baş, 2024).

$$Problem\ dimension\ (D) = (d \times h) + (2 \times h) + 1 \quad (21)$$

$$SpiderWasp = [weight_1\ weight_2\ weight_3 \ldots bias_1\ bias_2\ bias_3 \ldots] \quad (22)$$

$$Min\ Object\ Function = MSE = \frac{1}{k}\sum_{i=1}^{k}(SpiderWasp_{real} - SpiderWasp_{model})^2 \quad (23)$$

where $SpiderWasp_{real}$ is desired values and $SpiderWasp_{model}$ is evaluated values. k is the number of instances in the training dataset.

Table 1: Dataset descriptions (https://archive.ics.uci.edu/)

ID	Dataset	Number of features (*d*)	Number of instances (*k*)	Number of classes	Missing values	Type
ID1	Glass Identification	9	214	7	No	Physics and Chemistry
ID2	Fertility	9	100	2	No	Health and Medicine
ID3	Sonar	60	208	2	No	Physics and Chemistry
ID4	Balance scale	4	625	3	No	Social Science
ID5	Statlog (Heart)	13	270	4	No	Health and Medicine
ID6	National Poll on Healthy Aging (NPHA)	14	714	3	No	Health and Medicine
ID7	Iris	4	150	3	No	Biology
ID8	Raisin	7	900	2	No	Biology
ID9	Parkinsons	22	197	2	No	Health and Medicine
ID10	Teaching Assistant Evaluation	5	151	3	No	Education

4. Results And Discussion

In this subsection, classification was made by training an ANN with the SWO algorithm. All applications were carried out with a machine with the features used in Table 2. The success of SWO's parameter settings in ANN training is analyzed in detail in this subsection. Analysis of parameter settings was performed on the glass dataset.

Table 2: PC specifications

Name	Detailed settings
Hardware	
CPU	Core i5
Frequency	2.20 GHz
RAM	12 GB
Software	
Operating system	Windows 10 (64-bit)
Language	MATLAB R2018B

4.1 Parameter Analyzes:

4.1.1. The analyses of the population size(n): The success of ten different population values on SWO was analyzed for ANN. The parameter settings used in the population analysis are shown in Table 3. Population size (*n*) values are chosen as 50, 100, 150, 200, 250, 300,350, 400, 450, and 500 respectively. In the original article, *n_min* values equal one fifth of population size. So, *n_min* values are taken as 10, 20, 30, 40, 50, 60, 70, 80, 90, and 100 respectively. Also, *Tr* values and *Cr* values are 0.3 and 0.2 respectively as in the original paper. The results are shown in Table 4. The best results are marked in bold. According to the mean results, the population size is highly proportional to the success of SWO in ANN training. While the most successful population values according to mean results are 500, 300, and 350, the least successful population values are 50, 100, and 150 respectively. According to the best result value, the best population size is 200. According to the standard deviation, the best population size is 350. According to the time results, the fastest working population size is 50. Figure 1 shows the convergence chart of the population size analysis for SWO on ANN. Figure 2 shows the boxplot of the population size analysis for SWO on ANN. For the graphics, a random population size (*n*) value was chosen, and the n value was taken as 100. Figure 3 shows the graphics of the results from ANN trained with SWO on glass train data (for *n*=100) and Figure 4 shows the graphics of the results from ANN trained with SWO on glass test data (for *n*=100). In the graphs, it can be seen that as the population size increases, SWO's success in ANN training increases. At the same time, for the value of 100, actual values in both the training and test data sets in the glass data set and the training and test results of the ANN trained with SWO were compared graphically. In this study, Although the most successful population size is 500, because of the working slowly, the population size was selected as 100 in classifying other datasets with ANN.

Table 3: Parameter settings

Parameters	**Values**
Population size (*n*)	50, 100, 150, 200, 250, 300, 350, 400, 450, 500
n_min	(1/5 of *n*)
The maximum number of iterations (*T*)	100
Tr	0.3 (Abdel-Basset et al., 2023)
Cr	0.2 (Abdel-Basset et al., 2023)
The number of run	20
Training data rate	80% (171 instance for glass dataset)
Test data rate	20% (43 instance for glass dataset)
Search space boundary [*lower, upper*]	[-1,1]
Hidden Layer number	1
Neuron number	10
Epochs (for ANN)	500
Transfer function (for ANN)	Tansig

Table 4: The results of SWO for population size analysis on glass dataset

MSE	***n=50***	***n=100***	***n =150***	***n =200***	***n =250***	***n =300***	***n =350***	***n =400***	***n =450***	***n =500***
	n_min =10	***n_min =20***	***n_min =30***	***n_min =40***	***n_min =50***	***n_min =60***	***n_min =70***	***n_min =80***	***n_min =90***	***n_min =100***
Best	0.3505	0.4796	0.4253	**0.3243**	0.3839	0.4164	0.4454	0.4194	0.4485	0.3566
Worst	1.2281	1.1132	1.0483	1.0373	1.0582	0.8151	0.8035	1.0530	1.0552	0.8909
Median	0.7626	0.8339	0.6831	0.6906	0.6720	0.5662	0.6546	0.6424	0.6488	0.6211
Mean	0.8102	0.8036	0.7030	0.6756	0.6791	0.6000	0.6232	0.6497	0.6639	**0.5945**
SD	0.2460	0.1768	0.1790	0.1880	0.1510	0.1252	**0.1081**	0.1566	0.1534	0.1452
Time	**2.4206**	2.6001	3.2227	3.8686	4.5301	5.4320	6.3024	6.5398	7.7705	7.5724
Rank (According Mean)	10	9	8	6	7	2	3	4	5	**1**

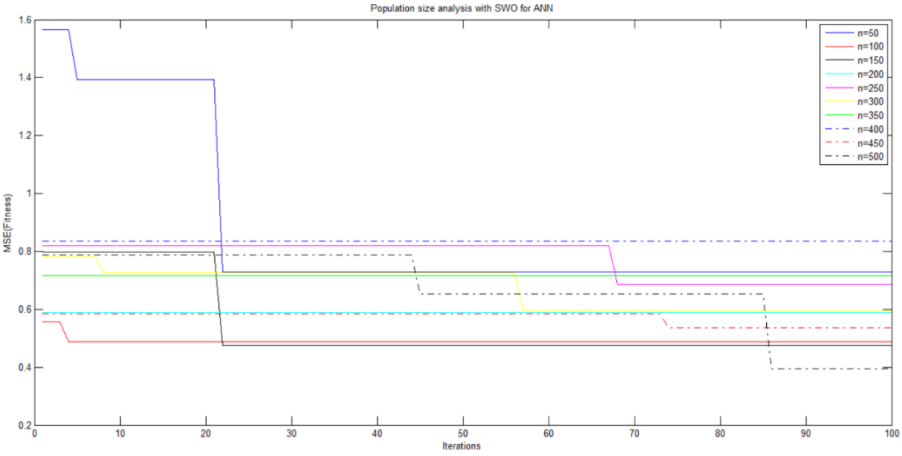

Figure 1: The convergence chart of the population size analysis for SWO on ANN

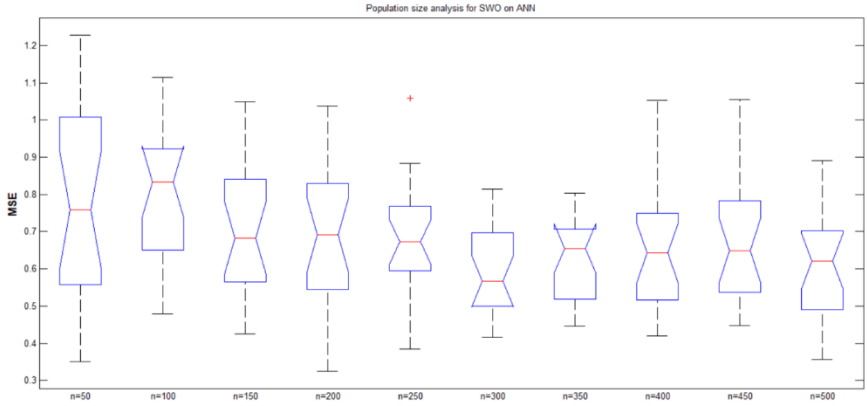

Figure 2: The boxplot of the population size analysis for SWO on ANN

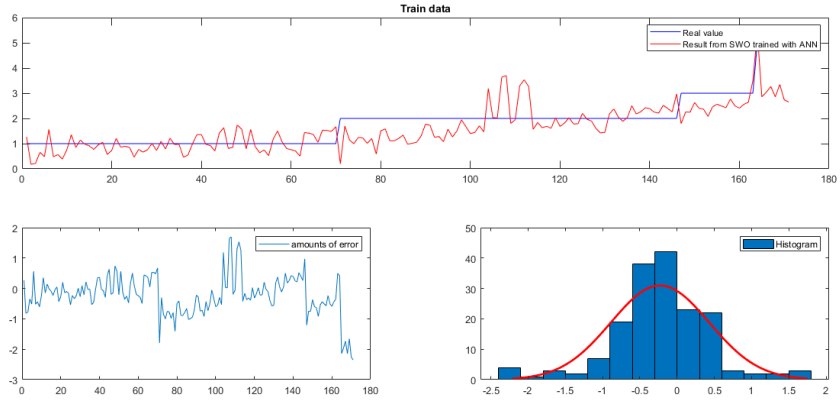

Figure 3: The graphics of the results from ANN tranined with SWO on glass train data (for n=100)

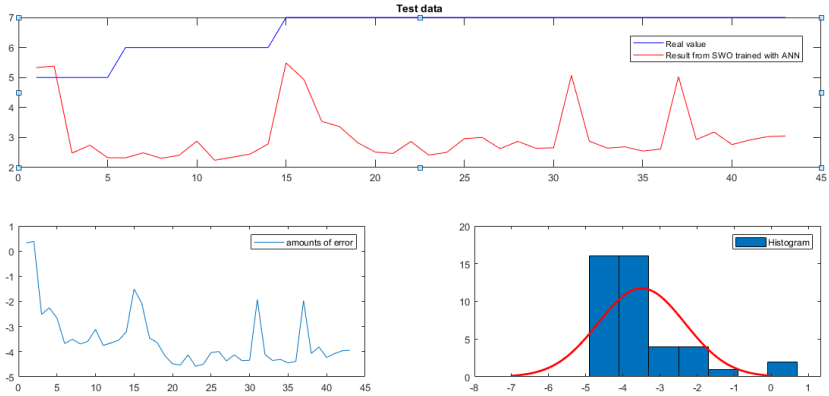

Figure 4: The graphics of the results from ANN tranined with SWO on glass test data (for n=100)

4.1.2. The analyses of the maximum iteration: The success of four different maximum iteration values on SWO was analyzed for ANN. The parameter settings used in the maximum iteration analysis are shown in Table 5. Maximum iteration values are chosen as 50, 100, 200, and 500 respectively. Population size (n) is chosen as 100 and *n_min* values are taken as 20. Also, Tr values and *Cr* values are 0.3 and 0.2 respectively as in the original paper. The results are shown in Table 6. The best results are marked in bold. According to the mean results, the maximum iteration is highly proportional to the success of SWO in ANN training. While the most successful maximum iteration values according to mean results are 500 and 200, the least successful maximum iteration values are 100 and 50 respectively. According to the best result value, the best maximum iteration value is 500. This value is then followed by 200, 50, and 100 respectively. According to the standard deviation, the best maximum iteration value is also 500. This value is then followed by 50, 200, and 100 respectively. According to the time results, the fastest working maximum iteration value is 100. This value is then followed by 50, 200, and 500 respectively. While the maximum iteration values are directly proportional to best result, mean and standard deviation, it is inversely proportional to time running. Figure 5 shows the convergence chart of the maximum iteration values analysis for SWO on ANN. Figure 6 shows the boxplot of the maximum iteration values analysis for SWO on ANN. For the graphics, maximum iteration value is taken as 500 which is the best value. Figure 7 shows the graphics of the results from ANN trained with SWO on glass train data (for T=500) and Figure 8 shows the graphics of the results from ANN trained with SWO on glass test data (for T=500). In the graphs, it can be seen that as the maximum iteration values increase, SWO's success in ANN training increases. At the same time, for the value of 500, actual values in both the training and test data sets in the glass data set and the training and test results of the ANN trained with SWO were compared graphically. The maximum

iteration value increases, the working success increases, but the working time also increases. For this reason, the maximum iteration value was selected 100, which is an average and the fastest value in classifying other datasets with ANN.

Table 5: Parameter settings

Parameters	**Values**
Population size (n)	100
n_min	20
The maximum number of iterations (T)	50, 100, 200, 500
Tr	0.3 (Abdel-Basset et al., 2023)
Cr	0.2 (Abdel-Basset et al., 2023)
The number of run	20
Training data rate	80% (171 instance for glass dataset)
Test data rate	20% (43 instance for glass dataset)
Search space boundary	[-1,1]
Hidden Layer number	1
Neuron number	10
Epochs (for ANN)	500
Transfer function (for ANN)	Tansig

Table 6: The results of SWO for population size analysis on glass dataset

MSE	T**=50**	T **= 100**	T **= 200**	T**= 500**
Best	0.3858	0.4796	0.2524	**0.2391**
Worst	0.9272	1.1132	0.8718	0.5101
Median	0.6732	0.8339	0.5950	0.3998
Mean	0.6775	0.8036	0.5858	**0.3766**
SD	0.1236	0.1768	0.1497	**0.0835**
Time	3.3595	**2.6001**	4.9857	9.1841
Rank (According Mean)	3	4	2	**1**

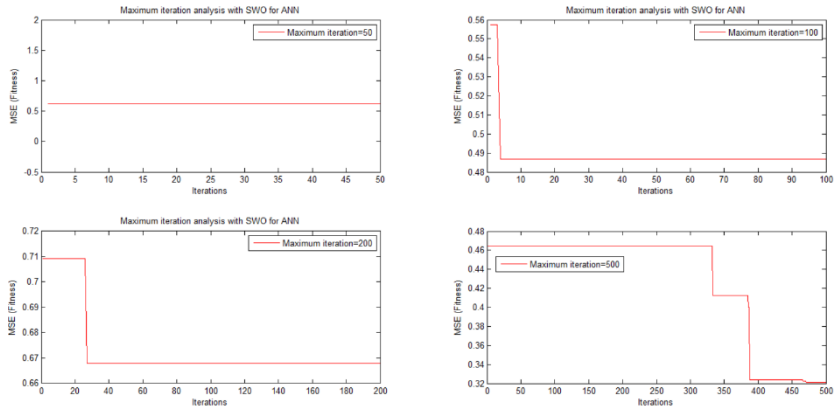

Figure 5: The convergence chart of the maximum iteration analysis for SWO on ANN

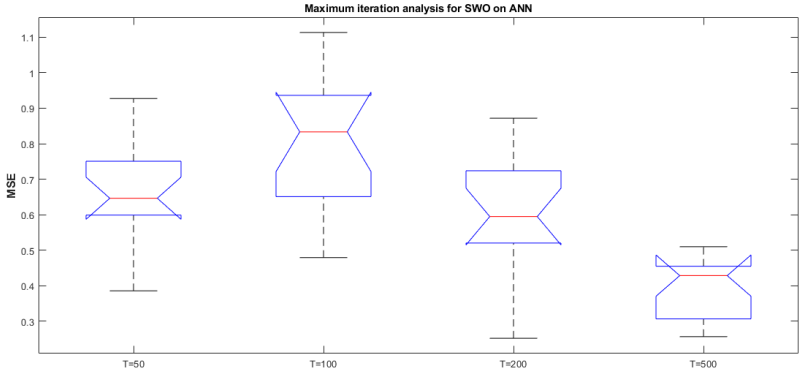

Figure 6: The boxplot of the the maximum iteration analysis for SWO on ANN

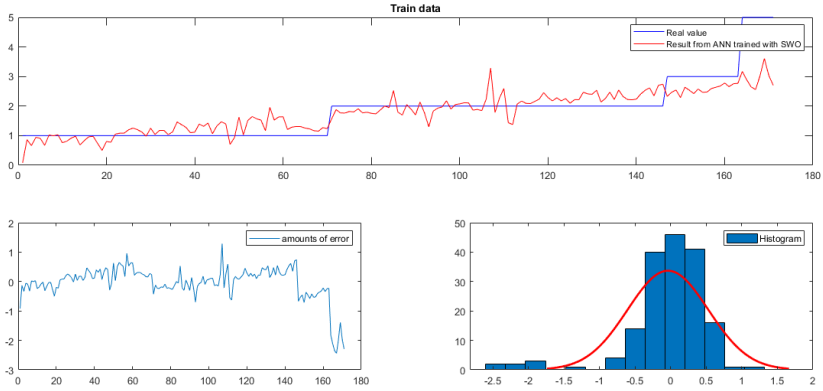

Figure 7: The graphics of the results from ANN tranined with SWO on glass train data (for T=500)

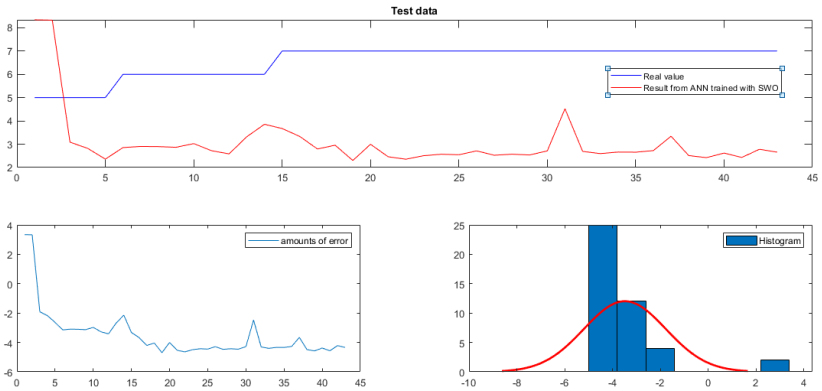

Figure 8: The graphics of the results from ANN tranined with SWO on glass test data (for *T*=500)

4.1.3. The analyses of the TR value: The success of nine different TR values on SWO was analyzed for ANN. The parameter settings used in the *TR* analysis are shown in Table 7. The *TR* Values are chosen as 0.1, 0.2, 0.3, 0.4, 0.5, 0.6, 0.7, 0.8, and 0.9 respectively. Other parameter values are these; the population size (*n*) is 100, *n_min* is 20 (one-fifth of *n*), the maximum iteration number (*T*) is 100 and *CR* is 0.2 that is the same as the original paper. The results are shown in Table 8. The best results are marked in bold. While the most successful *TR* values according to mean results are 0.5, 0.9, and 0.7, the least successful *TR* values are 0.3, 0.2, and 0.1 respectively. According to the best value, the best *TR* values is 0.9. According to the standard deviation, the best *TR* value is 0.6. According to the time value, the fastest working *TR* value is 0.3. Figure 9 shows the convergence chart of the *TR* value analysis for SWO on ANN. Figure 10 shows the boxplot of the *TR* Value analysis for SWO on ANN. Figure 11 shows the graphics of the results from ANN tranined with SWO on glass train data (for *TR*=0.3) and Figure 12 shows the graphics of the results from ANN tranined with SWO on glass test data (for *TR*=0.3). In the graphs, for the value of 0.5 which is the most successful value, the actual values in both the training and test data sets in the glass data set and the training and test results of the ANN trained with SWO were compared. In this study, the TR value was selected as 0.3 as the original paper in classifying other datasets with ANN.

Table 7: Parameter settings

Parameters	Values
Population size (n)	100
n_min	(1/5 of n)
The maximum number of iterations (T)	100
Tr	0.1, 0.2, 0.3, 0.4, 0.5, 0.6, 0.7, 0.8, 0.9
Cr	0.2 (Abdel-Basset et al., 2023)
The number of run	20
Training data rate	80% (171 instance for glass dataset)
Test data rate	20% (43 instance for glass dataset)
Search space boundary	[-1,1]
Hidden Layer number	1
Neuron number	10
Epochs (for ANN)	500
Transfer function (for ANN)	Tansig

Table 8: The results of SWO for *TR* value analysis on glass dataset

MSE	*TR*=0.1	*TR*=0.2	*TR*=0.3	*TR*=0.4	*TR*=0.5	*TR*=0.6	*TR*=0.7	*TR*=0.8	*TR*=0.9
Best	0.3443	0.4278	0.4796	0.3248	0.4143	0.5410	0.4048	0.4007	**0.3199**
Worst	1.1150	1.0750	1.1132	1.0270	0.9722	1.0219	0.9516	1.0846	0.9132
Median	0.7821	0.8042	0.8339	0.6957	0.5902	0.6947	0.7312	0.7133	0.6532
Mean	0.7576	0.7800	0.8036	0.6964	0.6222	0.7310	0.6895	0.6997	0.6686
SD	0.1987	0.1904	0.1768	0.1905	0.1546	**0.1437**	0.1560	0.1812	0.1641
Time	3.1793	2.6361	**2.6001**	2.6445	2.6224	2.6604	2.6409	2.9201	3.5030
Rank (According Mean)	7	8	9	4	**1**	6	3	5	2

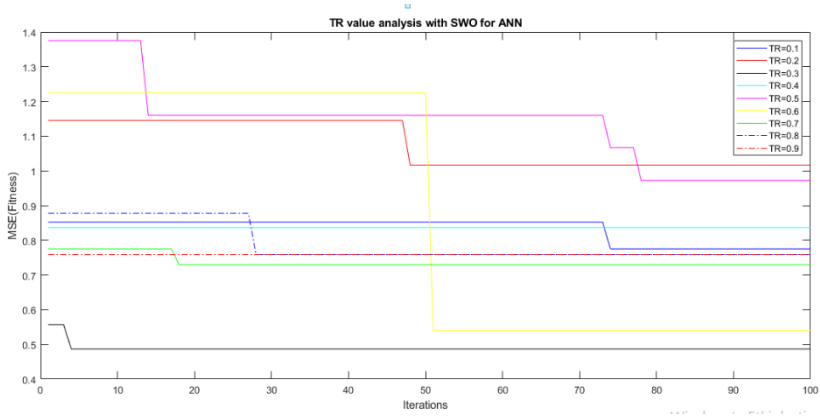

Figure 9: The convergence chart of the *TR* value analysis for SWO on ANN

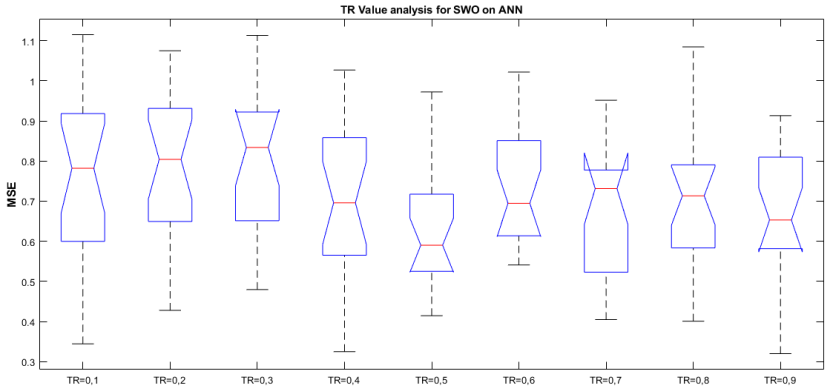

Figure 10: The boxplot of the *TR* value analysis for SWO on ANN

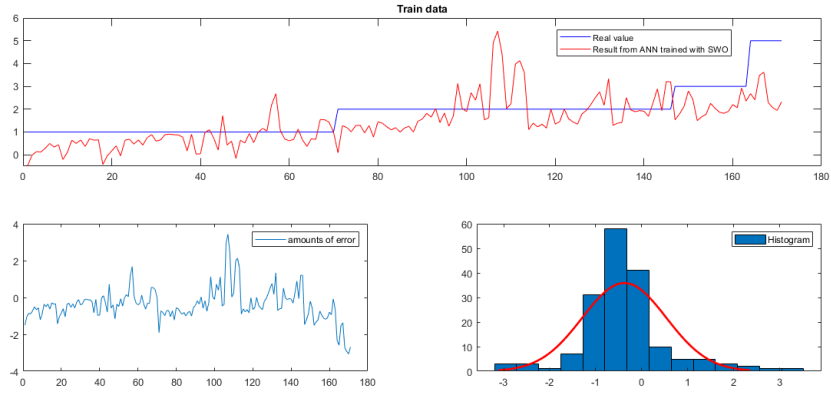

Figure 11: The graphics of the results from ANN tranined with SWO on glass train data (for *TR*=0.5)

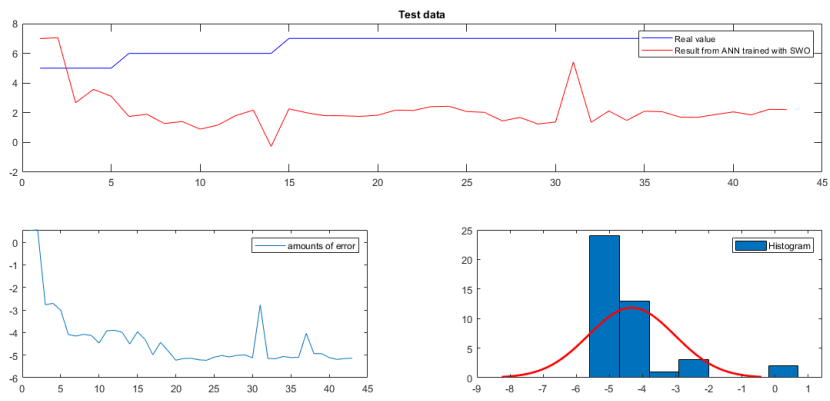

Figure 12: The graphics of the results from ANN tranined with SWO on glass test data (for *TR*=0.5)

4.1.4. The analyses of the CR value: The success of nine different *CR* values on SWO was analyzed for ANN. The parameter settings used in the *CR* analysis are shown in Table 9. The *CR* Values are chosen as 0.1, 0.2, 0.3, 0.4, 0.5, 0.6, 0.7, 0.8, and 0.9 respectively. Other parameter values are these; the population size (*n*) is 100, *n_min* is 20 (one-fifth of *n*), the maximum iteration number (*T*) is 100 and *TR* is 0.3 that is the same as the original article. The results are shown in Table 10. The best results are marked in bold. While the most successful *CR* values according to mean results are 0.4, 0.8, and 0.6, the least successful *CR* values are 0.2, 0.3, and 0.1 respectively. According to the best value, the best *CR* values is 0.4. According to the standard deviation, the best *CR* value is 0.8. According to the time value, the fastest working *CR* value is 0.9. Figure 13 shows the convergence chart of the *CR* Value analysis for SWO on ANN. Figure 14 shows the boxplot of the *CR* value analysis for SWO on ANN. Figure 15 shows the graphics of the results from ANN tranined with SWO on glass train data (for *CR*=0.2) and Figure 16 shows the graphics of the results from ANN tranined with SWO on glass test data (for *CR*=0.2). In the graphs, for the value of 0,4, which is the most successful *CR* value, the actual values in both the training and test data sets in the glass data set and the training and test results of the ANN trained with SWO were compared graphically. In this study, the *CR* Values was selected as 0.2 like the original paper in classifying other datasets with ANN.

Table 9: Parameter settings

Parameters	**Values**
Population size (*n*)	100
n_min	(1/5 of *n*)
The maximum number of iterations (*T*)	100
Tr	0.3 (Abdel-Basset et al., 2023)
Cr	0.1, 0.2, 0.3, 0.4, 0.5, 0.6 ,0.7, 0.8, 0.9
The number of run	20
Training data rate	80% (171 instances for glass dataset)
Test data rate	20% (43 instances for glass dataset)
Search space boundary	[-1,1]
Hidden Layer number	1
Neuron number	10
Epochs (for ANN)	500
Transfer function (for ANN)	Tansig

Table 10: The results of SWO for *CR* Value analysis on glass dataset

MSE	*CR*=0.1	*CR*=0.2	*CR*=0.3	*CR*=0.4	*CR*=0.5	*CR*=0.6	*CR*=0.7	*CR*=0.8	*CR*=0.9
Best	0.4354	0.4796	0.4482	**0.3059**	0.4222	0.3156	0.4160	0.4594	0.4008
Worst	1.1494	1.1132	0.9429	0.8797	0.9574	1.0630	0.9982	0.8346	0.8838
Median	0.6878	0.8339	0.7503	0.5605	0.6518	0.5869	0.6082	0.5956	0.6537
Mean	0.6973	0.8036	0.7217	0.5615	0.6489	0.6089	0.6590	0.6069	0.6316
SD	0.1760	0.1768	0.1385	0.1571	0.1343	0.1774	0.1558	**0.1006**	0.1279
Time	4.6219	2.6001	4.5010	2.8588	2.8302	3.4320	3.1568	2.6579	**2.5935**
Rank (According Mean)	7	9	8	**1**	5	3	6	2	4

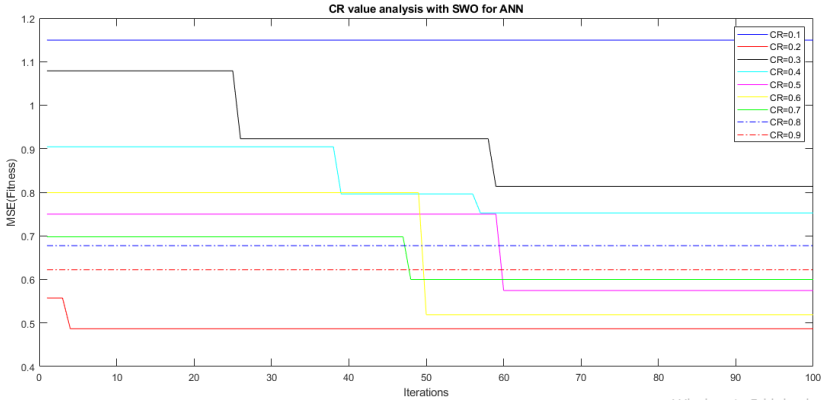

Figure 13: The convergence chart of the *CR* value analysis for SWO on ANN

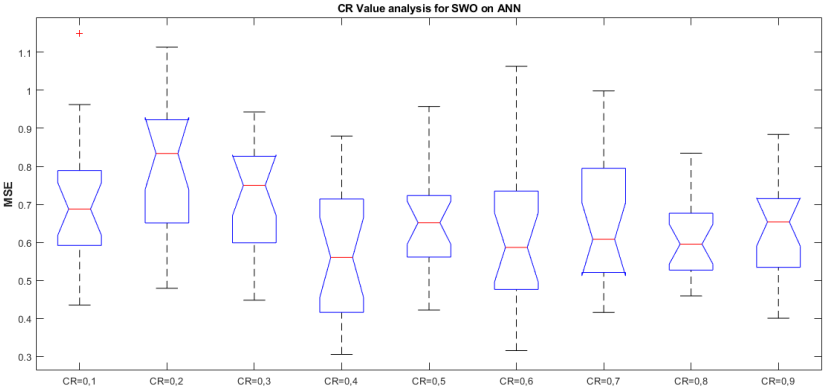

Figure 14: The boxplot of the *CR* value analysis for SWO on ANN

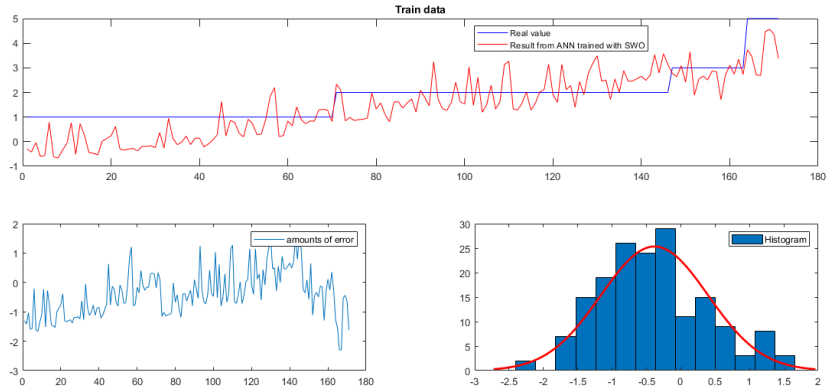

Figure 15: The graphics of the results from ANN tranined with SWO on glass train data (for *CR*=0.4)

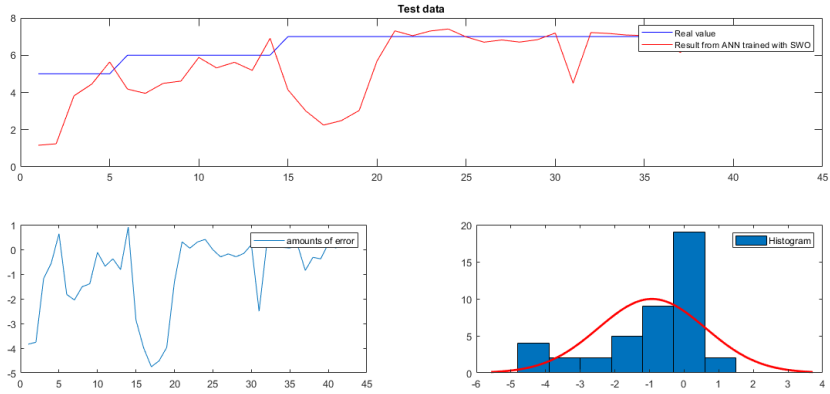

Figure 16: The graphics of the results from ANN tranined with SWO on glass test data (for *CR*=0.4)

4.2. Evaluation Of the Success Of the SWO Algorithm On Different Data Sets And different ANN Networks:

In this subsection, three different ANN network structures (netwok1, network2, network3) are analyzed. Network1 has a 10-neuron structure with a single hidden layer. Network 2 has a structure with two hidden layers and 10 neurons in each layer. Network 3 has a structure with three hidden layers and 5, 10, 5 neurons in each layer respectively. The parameter settings used in this subsection are shown in Table 11. The results are shown in Tables 12-17. Figures 17-19 show the total mean, standard deviation, and time SWO results obtained on the training and testing datasets for different ANN networks. According to the total mean, standard deviation and time results, Network1 was observed to be more successful.

Table 11: Parameter settings

Parameters	Values
Population size (n)	100
The maximum number of iterations (T)	100
TR value for	0.5
CR value for	0.4
The number of run	20
Training data rate	80%
Test data rate	20%
Search space boundary	[-1,1]
Epochs (for ANN)	500
Transfer function (for ANN)	1. Layer for tansig, 2. Layer for purelin, 3. Layer for logsig

Table 12: The results of SWO on different data sets for network 1(Train Data)

1 Layer ANN network (1. Layer=10 neurons)						
Problem	**Train data**					
ID	**Best**	**Worst**	**Median**	**Mean**	**SD**	**Time**
ID1	1.755	2.963	2.147	2.235	0.350	3.088
ID2	0.106	0.190	0.123	0.136	0.025	3.280
ID3	0.211	0.327	0.245	0.253	0.034	3.311
ID4	1.546	2.015	1.905	1.864	0.121	2.984
ID5	0.165	0.271	0.208	0.210	0.030	2.926
ID6	0.456	0.903	0.539	0.590	0.124	3.530
ID7	0.070	0.159	0.109	0.112	0.026	3.706
ID8	0.117	0.151	0.138	0.137	0.009	2.890
ID9	0.093	0.135	0.116	0.116	0.012	2.937
ID10	0.564	0.746	0.642	0.648	0.045	3.020
Total:				6.300	0.776	31.672

Table 13: The results of SWO on different data sets for network 1(Test Data)

1 Layer ANN network (1. Layer=10 neurons)						
Problem	**Test data**					
ID	**Best**	**Worst**	**Median**	**Mean**	**SD**	**Time**
ID1	0.837	2.594	1.621	1.654	0.432	2.910
ID2	0.080	0.188	0.133	0.134	0.032	3.165
ID3	0.006	0.076	0.015	0.023	0.017	3.071
ID4	1.466	2.121	1.684	1.734	0.167	2.926
ID5	0.164	0.247	0.196	0.199	0.024	2.885
ID6	0.480	0.955	0.712	0.693	0.131	3.076
ID7	0.037	0.210	0.085	0.096	0.044	5.422
ID8	0.002	0.018	0.007	0.009	0.005	3.001
ID9	0.151	0.209	0.171	0.174	0.016	3.261
ID10	0.545	0.657	0.594	0.595	0.026	3.002
Total:				5.309	0.894	32.718

Table 14: The results of SWO on different data sets for network 2(Train Data)

2 Layer ANN network (1. Layer=10 neurons and 2. Layer=10 neurons)						
Problem	**Train data**					
ID	**Best**	**Worst**	**Median**	**Mean**	**SD**	**Time**
ID1	1.617	3.358	2.577	2.547	0.471	3.206
ID2	0.126	0.397	0.214	0.238	0.078	3.336
ID3	0.212	0.493	0.374	0.363	0.078	3.352
ID4	1.558	3.865	2.361	2.517	0.630	3.212
ID5	0.187	0.493	0.279	0.287	0.083	3.111
ID6	0.504	1.174	0.814	0.808	0.218	3.571
ID7	0.078	0.286	0.154	0.168	0.058	3.915
ID8	0.119	0.173	0.136	0.142	0.017	3.173
ID9	0.106	0.201	0.143	0.145	0.024	4.187
ID10	0.564	0.938	0.686	0.712	0.097	3.313
Total:				7.927	1.753	34.374

Table 15: The results of SWO on different data sets for network 2(Test Data)

2 Layer ANN network (1. Layer=10 neurons and 2. Layer=10 neurons)						
Problem	**Test data**					
ID	**Best**	**Worst**	**Median**	**Mean**	**SD**	**Time**
ID1	1.111	3.592	2.575	2.419	0.749	3.494
ID2	0.139	0.348	0.191	0.208	0.055	3.227
ID3	0.025	0.228	0.171	0.157	0.062	3.286
ID4	1.601	2.485	1.848	1.861	0.207	3.221
ID5	0.160	0.545	0.366	0.367	0.104	3.139
ID6	0.591	1.316	0.961	0.956	0.242	3.323
ID7	0.036	0.262	0.133	0.139	0.051	3.174
ID8	0.003	0.033	0.011	0.014	0.009	3.326
ID9	0.124	0.254	0.215	0.206	0.033	3.261
ID10	0.555	0.778	0.652	0.655	0.068	3.289
Total:				6.981	1.580	32.740

Table 16: The results of SWO on different data sets for network 3(Train Data)

3 Layer ANN network (1. Layer=5 neurons, 2. Layer=10 neurons, and 3. Layer=5 neurons)						
Problem	**Train data**					
ID	**Best**	**Worst**	**Median**	**Mean**	**SD**	**Time**
ID1	1.588	3.148	2.166	2.200	0.329	3.409
ID2	0.102	0.108	0.105	0.105	0.002	3.388
ID3	0.315	0.520	0.412	0.417	0.059	3.553
ID4	2.590	3.676	2.846	2.973	0.317	3.571
ID5	0.165	0.240	0.203	0.204	0.022	3.350
ID6	0.462	0.530	0.492	0.496	0.019	3.843
ID7	0.137	0.313	0.265	0.247	0.052	3.409
ID8	0.137	0.217	0.184	0.181	0.017	3.395
ID9	0.095	0.122	0.111	0.110	0.006	4.362
ID10	1.079	1.961	1.500	1.499	0.274	3.535
Total:				8.432	1.095	35.816

Table 17: The results of SWO on different data sets for network 3(Test Data)

3 Layer ANN network (1. Layer=5 neurons, 2. Layer=10 neurons, and 3. Layer=5 neurons)						
Problem	**Test data**					
ID	**Best**	**Worst**	**Median**	**Mean**	**SD**	**Time**
ID1	1.111	3.592	2.575	2.419	0.749	3.494
ID2	0.139	0.348	0.191	0.208	0.055	3.227
ID3	0.025	0.228	0.171	0.157	0.062	3.286
ID4	1.601	2.485	1.848	1.861	0.207	3.221
ID5	0.160	0.545	0.366	0.367	0.104	3.139
ID6	0.591	1.316	0.961	0.956	0.242	3.323
ID7	0.036	0.262	0.133	0.139	0.051	3.174
ID8	0.003	0.033	0.011	0.014	0.009	3.326
ID9	0.124	0.254	0.215	0.206	0.033	3.261
ID10	0.555	0.778	0.652	0.655	0.068	3.289
Total:				6.981	1.580	32.740

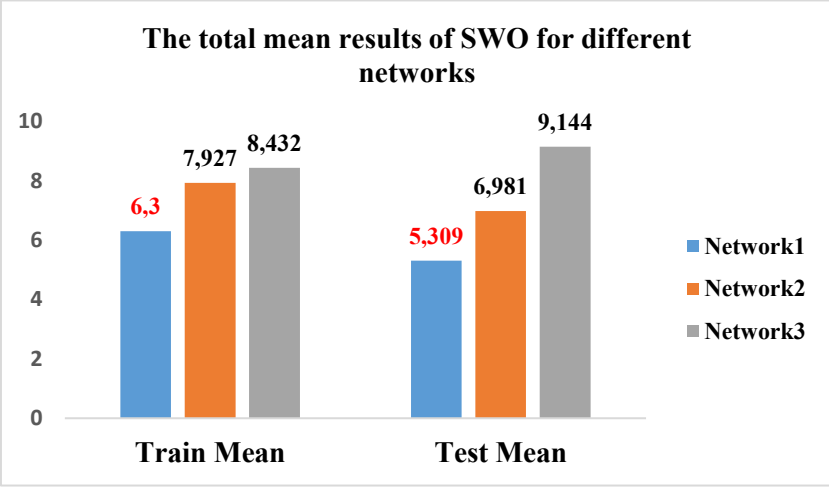

Figure 17: The graphics of total train and test mean results of SWO for different networks

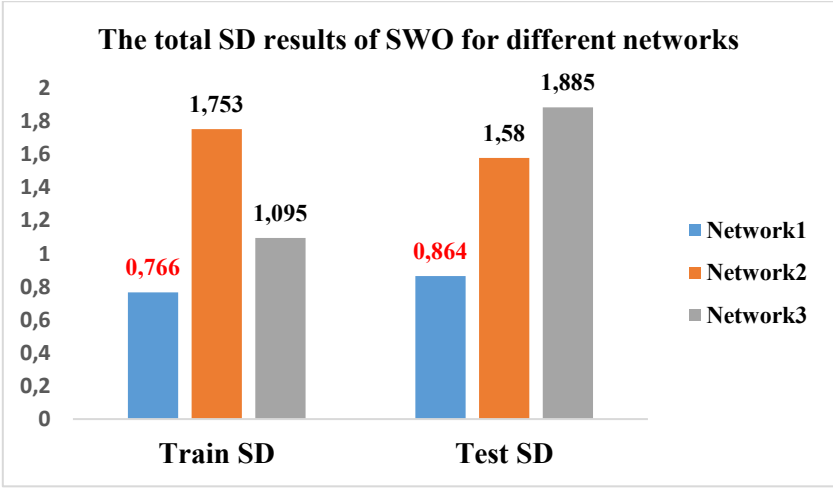

Figure 18: The graphics of total train and test SD results of SWO for different networks

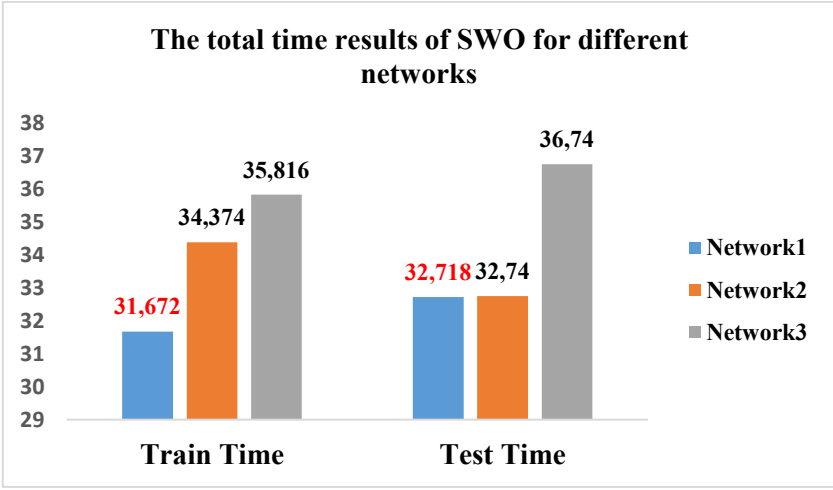

Figure 19: The graphics of total train and test time results of SWO for different networks

4.3. Comparison Of SWO With Different Heuristic Algorithms For ANN

In this subsection, the success of SWO is compared with two new metaheuristic algorithms (ZOA (Zebra Optimization Algorithm) and COA (Coati Optimization Algorithm)) selected from different literatures on three different ANN network structures (Netwok1, Network2, Network3) (Trojovská et al., 2022; Dehghani et al., 2023). The parameter settings used in this subsection are shown in Table 18. The comparison results are shown in Tables 19-21. Figures 20-22 show the total mean, standard deviation, and time comparison results obtained on the training and testing datasets for different ANN networks. According to the total mean, standard deviation, and time results, similar results

were obtained in all ANN network structures. The heuristic algorithms that trained the most successful ANN network in all ANN network structures were ZOA, COA, and SWO, respectively. The Figures 20-22 results also support these results.

Table 18: Parameter settings

Parameters	Values
Population size (n)	100
The maximum number of iterations (T)	100
TR value for	0.5
CR value for	0.4
The number of run	20
Training data rate	80%
Test data rate	20%
Search space boundary	[-1,1]
Epochs (for ANN)	500
Transfer function (for ANN)	1. Layer for tansig, 2. Layer for purelin, 3. Layer for logsig.
R value for ZOA	0.1

Table 19: The comparison results of SWO and other algorithms on ANN (for train data)

1 Layer ANN network (1. Layer=10 neurons)												
Problem ID	**Train data**											
	SWO				**ZOA**				**COA**			
	Best	**Mean**	**SD**	**Time**	**Best**	**Mean**	**SD**	**Time**	**Best**	**Mean**	**SD**	**Time**
ID1	1.755	2.235	0.350	3.088	0.965	**1.076**	0.068	250.971	1.180	1.494	0.160	270.824
ID2	0.106	0.136	0.025	3.280	0.077	**0.085**	0.004	241.007	0.092	0.102	0.003	270.205
ID3	0.211	0.253	0.034	3.311	0.106	**0.126**	0.011	252.018	0.160	0.173	0.006	275.286
ID4	1.546	1.864	0.121	2.984	1.229	**1.283**	0.020	247.106	1.351	1.445	0.050	307.545
ID5	0.165	0.210	0.030	2.926	0.102	**0.109**	0.005	251.385	0.122	0.131	0.004	275.361
ID6	0.456	0.590	0.124	3.530	0.419	**0.432**	0.005	250.985	0.441	0.449	0.004	277.143
ID7	0.070	0.112	0.026	3.706	0.038	**0.047**	0.007	241.074	0.052	0.073	0.012	279.837
ID8	0.117	0.137	0.009	2.890	0.093	**0.099**	0.003	246.018	0.101	0.112	0.005	275.896
ID9	0.093	0.116	0.012	2.937	0.045	**0.052**	0.005	256.365	0.067	0.076	0.005	279.752
ID10	0.564	0.648	0.045	3.020	0.445	**0.485**	0.017	242.233	0.505	0.545	0.021	262.221
Total mean:		6.300	0.776	**31.672**		**3.793**	**0.145**	2479.161		4.599	0.271	2774.069
Rank	3				**1**				2			

Table 20: The comparison results of SWO and other algorithms on ANN (for train data)

2 Layer ANN network (1. Layer=10 neurons and 2. Layer=10 neurons)												
Problem ID	**Train data**											
	SWO				**ZOA**				**COA**			
	Best	**Mean**	**SD**	**Time**	**Best**	**Mean**	**SD**	**Time**	**Best**	**Mean**	**SD**	**Time**
ID1	1.617	2.547	0.471	3.206	0.104	**0.110**	0.004	285.882	1.296	1.647	0.204	315.587
ID2	0.126	0.238	0.078	3.336	0.074	**0.086**	0.005	275.468	0.098	0.104	0.004	305.130

ID3	0.212	0.363	0.078	3.352	0.108	**0.125**	0.008	272.392	0.161	0.173	0.007	299.998
ID4	1.558	2.517	0.630	3.212	1.236	**1.276**	0.017	279.870	1.346	1.539	0.109	301.464
ID5	0.187	0.287	0.083	3.111	0.102	**0.109**	0.005	284.246	0.143	0.181	0.017	311.575
ID6	0.504	0.808	0.218	3.571	0.425	**0.432**	0.004	289.495	0.444	0.450	0.003	313.412
ID7	0.078	0.168	0.058	3.915	0.039	**0.043**	0.004	272.238	0.058	0.086	0.017	308.746
ID8	0.119	0.142	0.017	3.173	0.092	**0.101**	0.006	273.577	0.107	0.122	0.008	296.217
ID9	0.106	0.145	0.024	4.187	0.046	**0.057**	0.006	269.820	0.072	0.090	0.010	304.342
ID10	0.564	0.712	0.097	3.313	0.470	**0.490**	0.013	272.305	0.494	0.546	0.023	300.681
Total mean:		7.927	1.753	**34.374**		**2.829**	**0.071**	2775.292		4.937	0.402	3057.153
Rank	3				**1**				2			

Table 21: The comparison results of SWO and other algorithms on ANN (for train data)

3 Layer ANN network (1. Layer=5 neurons, 2. Layer=10 neurons, and 3.Layer=5 neurons)												
Problem ID	**Train data**											
	SWO				**ZOA**				**COA**			
	Best	**Mean**	**SD**	**Time**	**Best**	**Mean**	**SD**	**Time**	**Best**	**Mean**	**SD**	**Time**
ID1	1.617	2.547	0.471	3.206	0.104	**0.110**	0.004	285.882	1.296	1.647	0.204	315.587
ID2	0.126	0.238	0.078	3.336	0.074	**0.086**	0.005	275.468	0.098	0.104	0.004	305.130
ID3	0.212	0.363	0.078	3.352	0.108	**0.125**	0.008	272.392	0.161	0.173	0.007	299.998
ID4	1.558	2.517	0.630	3.212	1.236	**1.276**	0.017	279.870	1.346	1.539	0.109	301.464
ID5	0.187	0.287	0.083	3.111	0.102	**0.109**	0.005	284.246	0.143	0.181	0.017	311.575
ID6	0.504	0.808	0.218	3.571	0.425	**0.432**	0.004	289.495	0.444	0.450	0.003	313.412
ID7	0.078	0.168	0.058	3.915	0.039	**0.043**	0.004	272.238	0.058	0.086	0.017	308.746
ID8	0.119	0.142	0.017	3.173	0.092	**0.101**	0.006	273.577	0.107	0.122	0.008	296.217
ID9	0.106	0.145	0.024	4.187	0.046	**0.057**	0.006	269.820	0.072	0.090	0.010	304.342
ID10	0.564	0.712	0.097	3.313	0.470	**0.490**	0.013	272.305	0.494	0.546	0.023	300.681
Total mean:		7.927	1.753	**34.374**		**2.829**	**0.071**	2775.292		4.937	0.402	3057.153
Rank	3				**1**				2			

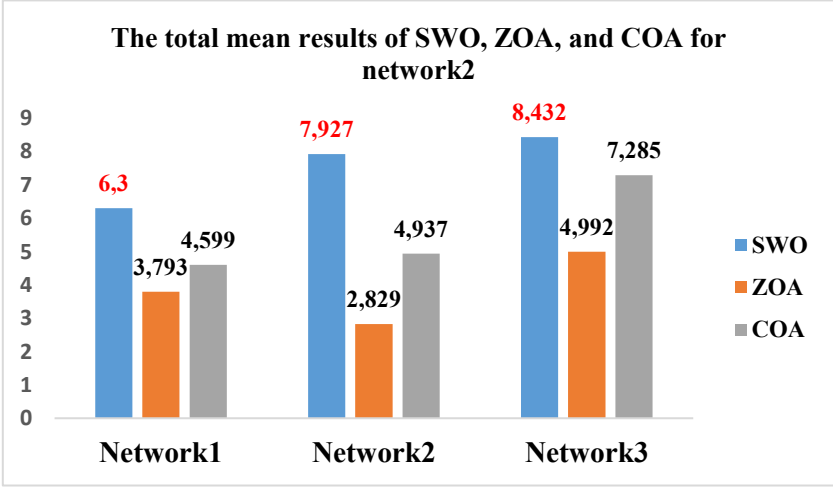

Figure 20: The graphics of total train mean results of SWO, ZOA, and COA for different networks

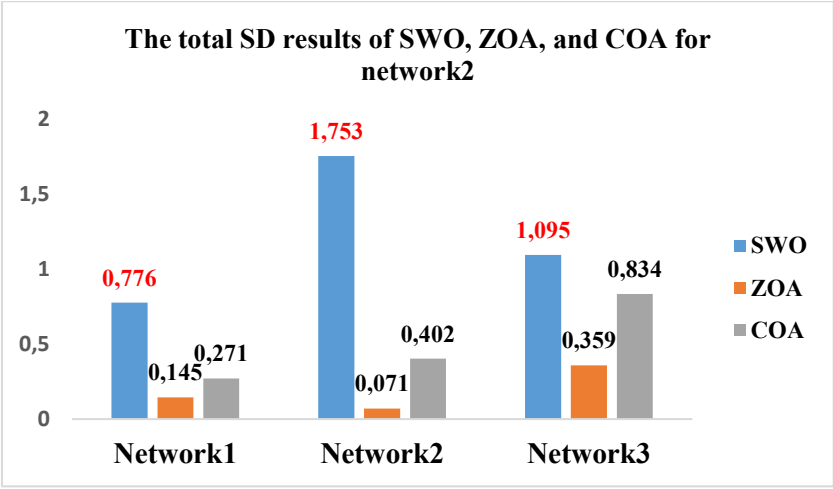

Figure 21: The graphics of total train SD results of SWO, ZOA, and COA for different networks

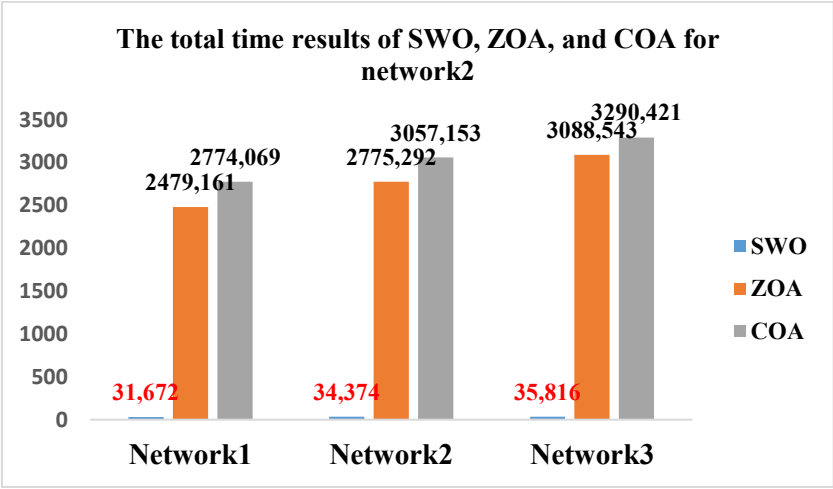

Figure 22: The graphics of total train time results of SWO, ZOA, and COA for different networks

5. Conclusions

In this study, the most important parameters in ANN networks, weight and bias values, were estimated with metaheuristic algorithms. ANN is a successful classifier in literature. This success depends on finding the correct weight and bias values. It tries to estimate the correct weight and bias values in each iteration according to the epoch value. In this study, ANN parameters were tried to be estimated with the newly proposed SWO metaheuristic algorithm in recent years. The success of metaheuristic algorithms in parameter training is undeniable in literature. Not only in the epoch cycle, SWO also tries to estimate these parameter values. At the beginning of the study, SWO and the parameters that could affect the success of the study were analyzed in detail. Three different ANN network structures were designed and SWO was compared with ZOA and COA selected from the literature. Separately developed network structures were tested in training and test datasets. MSE error rates were examined. The results showed that SWO fell behind ZOA and COA in ANN training.

References

Abdel-Basset, M., Mohamed, R., Jameel, M., & Abouhawwash, M. (2023). Spider wasp optimizer: A novel meta-heuristic optimization algorithm. Artificial Intelligence Review, 56, 11675–11738.

Ağyar, Z. (2015). Yapay sinir ağlarının kullanım alanları ve bir uygulama. Mühendis ve Makine, 56(662), 22–23.

Ataseven, B. (2013). Forecasting by using artificial neural networks. Öneri Dergisi, 10(39), 101–115.

Baş, E., & Baş, Ş. (2024). An example of classification using a neural network trained by the zebra optimization algorithm. Sinop Üniversitesi Fen Bilimleri Dergisi, 9(2), 388–420.

Dehghani, M., Montazeri, Z., Trojovská, E., & Trojovský, P. (2023). Coati optimization algorithm: A new bio-inspired metaheuristic algorithm for solving optimization problems. Knowledge-Based Systems, 259, 110011.

El-Kenawy, E.-S. M., Alhussan, A. A., Khafaga, D. S., Alharbi, A. H., Alzakari, S. S., Abdelhamid, A. A., Ibrahim, A. M., & Eid, M. M. (2025). A novel binary swordfish movement optimization algorithm (BSMOA) for efficient feature selection. Fusion: Practice and Applications, 19, 170–186. https://doi.org/10.54216/FPA.190213

Işık, H. E., Baş, E., Egrioglu, T., & Akkan, A. (2024). A new single multiplicative neuron model artificial neural network based on black hole optimization algorithm: Forecasting the amounts of clean water given to metropolis. Stochastic Environmental Research and Risk Assessment. https://doi.org/10.1007/s00477-024-02802-3

Kaya, N. S., Pacci, S., Demirağ Turan, İ., Odabaş, M. S., & Dengiz, O. (2023). Comparing geographic information systems-based fuzzy-analytic hierarchical process approach and artificial neural network to characterize soil erosion risk indexes. Rendiconti Lincei. Scienze Fisiche e Naturali, 34(4), 1089–1104.

Loktionov, V., Lelej, A., & Liu, J.-X. (2019). A new genus of spider wasps (Hymenoptera, Pompilidae) from China. Far Eastern Entomologist, 376, 1–14.

McCulloch, W. S., & Pitts, W. (1943). A logical calculus of the ideas immanent in nervous activity. Bulletin of Mathematical Biology, 5(4), 115–133.

Mishra, M., & Srivastava, M. (2014). A view of artificial neural network. In 2014 International Conference on Advances in Engineering and Technology Research (ICAETR). https://doi.org/10.1109/ICAETR.2014.7012785

Mosavi, M. R., Khishe, M., & Ghamgosar, A. (2016). Classification of sonar data set using neural network trained by gray wolf optimization. Neural Network World, 26(4), 393–415.

Mosavi, M. R., Khishe, M., Parvizi, G. R., Naseri, M. J., & Ayat, M. (2019). Training multi-layer perceptron utilizing adaptive best-mass gravitational search algorithm to classify sonar dataset. Archives of Acoustics, 44(1), 137–151.

Pitts, J. P., Wasbauer, M. S., & Von Dohlen, C. D. (2006). Preliminary morphological analysis of relationships between the spider wasp subfamilies (Hymenoptera: Pompilidae): Revisiting an old problem. Zoologica Scripta, 35(1), 63–84.

Ren, H., Li, J., Chen, H., & Li, C. (2021). Adaptive levy-assisted salp swarm algorithm: Analysis and optimization case studies. Mathematics and Computers in Simulation, 181, 380–409. https://doi.org/10.1016/j.matcom.2020.09.027

Rong, G., Mendez, A., Bou Assi, E., Zhao, B., & Sawan, M. (2020). Artificial intelligence in healthcare: Review and prediction case studies. Engineering, 6(3), 291–301. https://doi.org/10.1016/j.eng.2019.08.015

Shang, S., & Zhou, M. (2025). A resource allocation algorithm based on hybrid spider wasp optimization for cognitive radio networks. Physical Communication, 70, 102625.

Trojovská, E., Dehghani, M., & Trojovský, P. (2022). Zebra optimization algorithm: A new bio-inspired optimization algorithm for solving optimization problems. IEEE Access, 10, 49445–49473.

Yu, L., Zhao, X., Lv, M., & Zhang, J. (2025). Consensus community-based spider wasp optimization for dynamic community detection. Mathematics, 13, 265. https://doi.org/10.3390/math13020265

Wang, Z., Yang, Y., Luo, X., He, D., & Sammy, C. (2025). Energy efficient clustering and routing for wireless sensor networks by applying a spider wasp optimizer. Ad Hoc Networks. https://doi.org/10.1016/j.adhoc.2025.103841

Zhou, F., Hu, S., Du, X., & Lu, Z. (2025). Anston: An attention mechanism network model for structured data classification. Research Square. https://doi.org/10.21203/rs.3.rs-5766278/v1

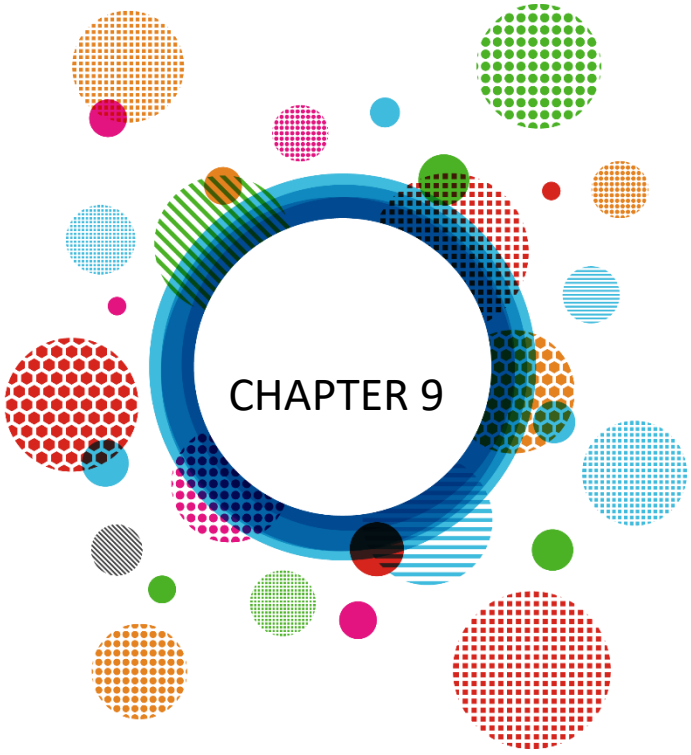

Impact Of Temperature On Photovoltaic Solar Cell Performance Parameters

Suleyman Adak[1]

[1] Department of Electrical and Energy, OSB, Mardin Artuklu University, Mardin, Turkey

1. Introduction

Global energy challenges and the ongoing transition toward sustainable systems underscore the critical role of solar energy. As concerns over fossil fuel depletion, energy security, and climate change intensify, the need for clean, renewable sources becomes more urgent. Solar power, with its vast availability and decreasing costs, stands out as a key solution in reducing greenhouse gas emissions and diversifying the global energy mix. Its scalability and adaptability make it a cornerstone in efforts to decarbonize energy systems and meet growing demand without compromising environmental integrity.

Photovoltaic (PV) technology has emerged as a key solution for sustainable energy generation, offering a clean and renewable alternative to conventional fossil fuels. The performance of PV solar cells, however, is significantly influenced by environmental factors, among which temperature plays a crucial role. As solar panels are exposed to varying climatic conditions, temperature fluctuations can affect their electrical characteristics, leading to changes in efficiency, power output, and overall system reliability.

The primary parameters defining PV cell performance include open-circuit voltage (Voc), short-circuit current (Isc), maximum power output (Pmax), and efficiency. While an increase in temperature generally enhances the short-circuit current due to reduced bandgap energy, it negatively impacts the open-circuit voltage, leading to a decline in power output. Understanding these temperature-induced variations is essential for optimizing PV system design, improving operational efficiency, and ensuring long-term stability. This study explores the impact of temperature on key PV solar cell parameters, highlighting the physical mechanisms responsible for performance degradation and discussing potential mitigation strategies. By analyzing the thermal behavior of solar cells, researchers and engineers can develop more efficient PV modules and implement temperature compensation techniques to enhance energy yield in real-world applications. The effect of temperature on the PV solar array is given in Fig. 1.

Fig. 1 Effects of temperature on PV solar array

To mitigate temperature effects, cooling techniques such as ventilation, water cooling, and advanced heat dissipation materials can be used. Low-temperature coefficient PV technologies like perovskite and thin-film cells may also offer improved performance in high-temperature environments. Solar PV energy is widely regarded as one of the most effective renewable energy sources, particularly in hot and sunny regions. Countries with high solar irradiance, such as those in the Middle East, North Africa, Australia, and parts of the U.S. and India, benefit greatly from PV technology. Reasons why PV solar systems are ideal for hot countries:

- **Abundant Sunlight** – These regions receive high levels of solar radiation year-round, maximizing energy generation.
- **Lower Energy Costs** – Solar PV can reduce dependence on fossil fuels, lowering electricity bills and making energy more affordable.
- **Decentralized Power Production** – Solar panels can be installed on rooftops, reducing transmission losses and reliance on central grids.
- **Sustainability** – PV systems produce no emissions, reducing carbon footprints and combating climate change.
- **Technological Advancements** – Innovations like bifacial panels, solar tracking systems, and better cooling techniques improve efficiency in hot climates.

However, challenges such as high temperatures reducing efficiency, dust accumulation on panels, and initial investment costs must be considered. Solutions like cooling mechanisms, regular cleaning, and government incentives help overcome these issues.

The fill factor (FF), which represents the quality of a solar cell, is also negatively affected by elevated temperatures. Apart from electrical performance degradation, excessive heat can accelerate material degradation, leading to long-term reliability issues in PV modules. High temperatures contribute to faster aging of encapsulation materials, solder joints, and interconnections, which may cause performance deterioration over time. Furthermore, thermal stress due to fluctuating temperatures can result in microcracks and delamination, reducing the structural integrity of solar panels. To mitigate these adverse effects, various cooling techniques and material innovations are being explored. Passive and active cooling methods, such as heat sinks, phase change materials, and water or air-based cooling, help regulate module temperature. Additionally, the development of high-temperature-resistant materials and improved cell designs aim to enhance PV performance under varying environmental conditions.

Understanding and managing the thermal behavior of PV cells is crucial for optimizing energy production, improving module longevity, and ensuring the economic viability of solar power systems. With ongoing research and advancements in cooling technologies, the negative impact of heat on photovoltaic performance can be minimized, leading to more efficient and reliable solar energy solutions. Temperature plays a crucial role in determining the efficiency of PV modules. As the temperature of a solar panel rises, its efficiency typically decreases due to the intrinsic properties of semiconductor materials. Higher temperatures lead to a reduction in the open-circuit voltage while slightly increasing the short-circuit current, but the overall effect results in lower power output.

Improving the efficiency of solar panels by maintaining their operating temperature requires a combination of thermal management strategies, material advancements, and system design optimizations. Since photovoltaic cells experience efficiency losses as temperature rises, it is essential to regulate heat dissipation effectively. This can be achieved through passive and active cooling methods that enhance airflow, reduce heat retention, and facilitate thermal exchange with the surroundings.

Material innovations also play a significant role in temperature control. The use of thermally conductive backsheets, advanced coatings, and reflective materials helps in minimizing excessive heat absorption. Additionally, bifacial panels and hybrid photovoltaic-thermal (PV-T) systems offer an integrated approach to utilizing solar energy while preventing overheating. System integration techniques, such as solar tracking and smart monitoring, further contribute to maintaining an optimal temperature by adjusting panel orientation and employing real-time cooling mechanisms. Environmental factors, including proper mounting structures, vegetation, and geographic positioning, also influence the thermal performance of solar panels. By combining these approaches, the overall energy conversion efficiency can be improved, ensuring sustained performance and longevity of the photovoltaic system.

The temperature coefficient of a PV module quantifies this loss, with most conventional silicon-based panels experiencing a decline in efficiency of around 0.3% to 0.5% per degree Celsius above standard test conditions. Effective cooling strategies, material selection, and proper installation techniques can help mitigate these temperature-related losses.

2. Effects of Temperature on PV Cell Performance Parameters

PV module degradation is primarily influenced by climatic conditions. Environmental factors such as high temperatures, humidity, UV radiation, and extreme weather events can accelerate material aging, reduce efficiency, and lead

to performance losses over time. The rate of degradation varies depending on the specific climate where the PV system is installed, with harsher conditions generally causing faster deterioration. Temperature plays a critical role in determining the efficiency and overall performance of PV cells. As solar panels are exposed to sunlight, they absorb not only light energy but also heat, leading to an increase in cell temperature. This thermal effect influences key electrical parameters such as voltage, current, power output, and efficiency, ultimately affecting the energy yield of a PV system.

2.1. Effect Temperature on Open-Circuit Voltage

Open-circuit voltage (Voc) is significantly influenced by temperature variations because it decreases as temperature rises, due to increased carrier recombination and a narrowing of the semiconductor bandgap. This reduction occurs because higher temperatures enhance thermal energy within the material, which disrupts the charge separation needed to maintain voltage. The decrease in open-circuit voltage is one of the primary reasons for the decline in overall power output and efficiency of solar cells under high-temperature conditions.

As temperature increases, Voc of a solar cell decreases due to the combined effects of bandgap narrowing and increased saturation current. The bandgap energy of the semiconductor decreases with temperature, reducing the built-in potential of the junction. Additionally, the reverse saturation current increases exponentially with temperature, leading to a greater recombination rate and further lowering Voc. This behavior follows the diode equation, where Voc is inversely related to the saturation current. For silicon solar cells, Voc typically decreases by around 2.2 mV/°C, impacting overall efficiency, making thermal management essential in photovoltaic system design. The open-circuit voltage is given by:

$$V_{OC}(T,G) = V_{OC}(T_0,G_0) + \frac{nkT}{q} Ln\left(\frac{G}{G_0}\right) + \beta_{V_{OC}}(T - T_0) \quad (1)$$

Where, $V_{OC}(T,G)$ is the open-circuit voltage at temperature T and irradiance G. $V_{OC}(T_0,G_0)$ is the reference open-circuit voltage at STC, $\beta_{V_{OC}}$ is the temperature coefficient of V_{OC} (-0.3% to -0.5% per °C), k is Boltzmann's constant (1.38×10−23 J/K), q is the elementary charge (1.6×10−19 C) and n is the diode ideality factor (~1 to 2). Since Io increases with temperature, Voc decreases. The open-circuit voltage (Voc) of a solar cell or semiconductor device is strongly influenced by temperature. In general, Voc decreases with increasing temperature due to the intrinsic properties of semiconductors. Band gap energy

depends on temperature**.** As temperature increases, the bandgap energy (Eg) of the +semiconductor decreases. Since **Voc is approximately proportional to the bandgap**, a reduction in Eg leads to a lower **Voc**. The bandgap energy is given by:

$$E_g(T) = E_g(o) - \alpha T^2/(T + \beta) \quad (2)$$

Where α α and β are material-dependent constants. One of the most significant impacts of rising temperature is the reduction in open-circuit voltage (Voc). As temperature increases, the semiconductor bandgap narrows, leading to increased carrier recombination and a lower voltage output.

2.2 Effect Temperature on Short-Circuit Current

As temperature increases, the short-circuit current (**Isc**) of a solar cell **slightly increases** due to enhanced carrier generation. Higher temperatures lead to an increase in intrinsic carrier concentration, which results in a small rise in photocurrent. This increase occurs because the bandgap of the semiconductor narrows, allowing more photons to generate electron-hole pairs. However, the effect is relatively small compared to the decrease in open-circuit voltage (**Voc**). For silicon solar cells, Isc increases by approximately 0.06% per °C, meaning that while temperature has a minor positive effect on Isc, the overall efficiency of the solar cell still declines due to the dominant negative effect on Voc.

The short-circuit current of PV cell is sensitive to temperature changes. Generally, the short-circuit current increases with temperature, but the effect is less pronounced than that on the open-circuit voltage. The temperature dependence of the short-circuit current is given by:

$$I_{sc}(T) = I_{sc}(T_0)(1 + \alpha_{I_{sc}}(T - T_0)) \quad (3)$$

Where; $I_{SC}(T)$ is the short-circuit current at temperature T (in °C or K). $I_{SC}(T_0)$ is the short-circuit current at a reference temperature T_0 (usually 25°C). $\alpha_{I_{sc}}$ is the temperature coefficient of short-circuit current (typically positive and in units of %/°C). T is the operating temperature in degrees Celsius (°C) or Kelvin (K). T_0 is the reference temperature, typically 25°C. This formula shows how the short-circuit current changes with temperature based on a linear approximation. The value of $\alpha_{I_{sc}}$ is typically positive and can vary depending on the type of PV cell. While short-circuit current (Isc) experiences a slight increase due to enhanced carrier generation, the overall effect of temperature is a decline in maximum power output (Pmax) and efficiency.

2.3 Effect Temperature on Maximum Power Output and Short Circuit Current

Maximum power output is significantly influenced by temperature variations because the electrical characteristics of solar cells, particularly voltage, are sensitive to thermal changes. As temperature rises, the reduction in open-circuit voltage outweighs the slight increase in current, resulting in a lower maximum power point. This decline in power output directly affects the overall energy yield of the system, making temperature control an important factor in maintaining optimal performance and efficiency of photovoltaic installations. The maximum power output (Pmax) of PV system is affected by temperature. As the temperature increases, the power output generally decreases due to the combined effect of a reduction in the open-circuit voltage and a slightly lower increase in the short-circuit current. The temperature dependence of the maximum power output can be expressed as:

$$P_{max}(T) = P_{max}(T_0)(1 - \beta_{P_{max}}(T - T_0)) \quad (4)$$

Where; Pmax(T) is the maximum power output at temperature T (in °C or K), Pmax(T_0) is the maximum power output at the reference temperature T_0 (usually 25°C), $\beta_{P_{max}}$ is the temperature coefficient of maximum power output (typically a negative value, indicating that the power output decreases with temperature), T is the operating temperature in degrees Celsius (°C) or Kelvin (K). T_0 is the reference temperature (usually 25°C).

At higher temperatures, the open-circuit voltage of the PV cell decreases, which reduces the maximum power output more significantly than the increase in short-circuit current. The maximum power temperature coefficient varies depending on the type of PV cell. $\beta_{P_{max}}$ is typically negative, indicating that as the temperature increases, the maximum power output decreases. The exact value of. $\beta_{P_{max}}$ depends on the type of PV cell and its material properties. In practice, most PV modules have a temperature coefficient of Pmax in the range of -0.3%/°C to -0.5%/°C. This means that for every degree Celsius increase in temperature, the power output decreases by approximately 0.3% to 0.5%.

Short-circuit current is significantly influenced by temperature variations due to the temperature-dependent behavior of semiconductor materials within the solar cell. As temperature increases, the intrinsic carrier concentration rises, leading to a slight increase in the generation of charge carriers and thus a modest rise in short-circuit current. However, this increase is generally small compared to the concurrent decrease in voltage, and while it contributes to the overall current output, it does not compensate for the loss in efficiency caused by elevated temperatures. The short-circuit current of PV cell is sensitive to

temperature changes. Generally, the short-circuit current increases with temperature, but the effect is less pronounced than that on the open-circuit voltage. The short-circuit current varies almost linearly with solar irradiance (G) and slightly increases with temperature:

$$I_{sc}(T,G) = I_{sc}(T_0,G_0)\left(\frac{G}{G_0}\right)(1+\alpha_{I_{SC}}(T-T_0)) \quad (5)$$

Where: $I_{SC}(T,G)$ is the short-circuit current at temperature T and irradiance G, $I_{SC}(T_0,G_0)$ is the reference short-circuit current at standard test conditions (STC: T_0=25 ^{0}C , G_0=1000 W/m²), $\alpha_{I_{SC}}$ is the temperature coefficient of I_{SC} (~0.04% to 0.1% per °C), G is the actual irradiance (W/m²), G_0 is the reference irradiance (1000 W/m²).

Effect Temperature on Fill Factor and Efficiency in Solar Cells

Temperature significantly influences the performance of PV solar cells, particularly affecting the Fill Factor (FF) and overall efficiency. Fill Factor (FF) is the ratio of the maximum power output of a solar cell to the product of open-circuit voltage and short-circuit current:

$$FF = \frac{P_{max}}{V_{oc}*I_{sc}} \quad (6)$$

As temperature increases, the open-circuit voltage decreases due to increased intrinsic carrier concentration, leading to higher recombination losses. The short-circuit current slightly increases with temperature, but this effect is minimal. Additionally, The overall effect of temperature increase is a reduction in Fill Factor (FF) due to a decline in the open-circuit voltage and increased series resistance. The effectiveness of a solar cell is given by the following formula:

$$\eta = \frac{P_{max}}{P_{in}} \quad (7)$$

Where, Pin is the incident power. Since FF and Voc decrease with temperature, the maximum power output (Pmax) also reduces. This leads to a significant drop in efficiency, as less electrical power is generated from the same incident solar energy. The temperature coefficient of efficiency varies for different types of solar cells but is typically around **-0.3% to -0.5% per °C** for silicon-based cells. Efficiency is significantly influenced by temperature variations because the electrical properties of photovoltaic materials change with temperature. As temperature increases, the voltage output of the solar cell decreases due to enhanced carrier recombination and reduced bandgap, while the current sees only a minor increase. This imbalance leads to a net decline in power

output and thus a reduction in conversion efficiency. Maintaining optimal operating temperatures is therefore essential to preserve the energy-generating performance of PV systems under varying environmental conditions. As the temperature of a solar panel increases, several characteristics change:

- **Decrease in open-circuit voltage (Voc)**: The voltage output of a PV cell is highly sensitive to temperature. Higher temperatures increase carrier recombination, reducing the voltage, which directly impacts power output. The open-circuit voltage decreases because the thermal energy increases the movement of electrons within the panel, which reduces the voltage produced by the panel.
- **Panel efficiency decreases**: Higher temperatures cause greater resistance within the solar cells, reducing their overall efficiency. This means the panel is less effective at converting sunlight into electricity at higher temperatures.
- **Slight Increase in Short-Circuit Current (Isc):** While current (Isc) increases slightly with temperature due to higher carrier generation, the effect is minor compared to the drop in voltage. The short-circuit current tends to increase with higher temperatures. This is because the increased temperature can cause a higher number of charge carriers (electrons and holes) to be generated, which leads to a higher current under short-circuit conditions.
- **Reduction in Bandgap Energy:** As temperature increases, the bandgap of the semiconductor material (like silicon) decreases. This leads to an increase in the number of charge carriers but also results in a lower open-circuit voltage (V_oc), which negatively affects efficiency.
- **Overall Power Loss:**Since Power (P) = Voltage (V) × Current (I), the decrease in voltage outweighs the small increase in current, leading to reduced power output.
- **Temperature Coefficient of Efficiency**:The efficiency of a PV cell decreases by a certain percentage per degree Celsius rise in temperature, typically ranging from -0.2%/°C to -0.5%/°C for silicon-based cells.

Temperature coefficients are crucial indicators of how solar cell performance is affected by temperature changes. Different solar cell technologies respond differently to heat, and this variability significantly impacts their efficiency in real-world conditions. For most crystalline silicon-based cells, efficiency typically decreases more sharply with rising temperatures, reflecting a higher

temperature sensitivity. In contrast, thin-film technologies generally exhibit more stable behavior under heat due to their material properties, which makes them more suitable for hotter climates. Understanding these coefficients is essential for system design and performance prediction, as they directly influence energy yield, especially in regions with high ambient temperatures. This combination of effects results in a reduced overall output power for the panel at higher temperatures, despite the increase in short-circuit current. temperature coefficients of different solar cell technologies are given in Table 1.

Table 1. Temperature coefficients of different solar cell technologies

Solar Cell Type	Bandgap Energy (eV)	α_{ISC} (%/°C)	β_{VOC} (%/°C)	β_{Pmax} (%/°C)	Performance at High Temperature
Monocrystalline Silicon (Mono-Si)	1.12	+0.04 to +0.07	0.3 to -0.4	0.4 to -0.5	Moderate power loss
Polycrystalline Silicon (Poly-Si)	1.12	+0.04 to +0.07	0.3 to -0.4	0.4 to -0.5	Moderate power loss
Amorphous Silicon (a-Si)	1.7	+0.1 to +0.2	-0.2 to -0.3	-0.2 to -0.3	Better high-temperature performance
Cadmium Telluride (CdTe)	1.45	+0.05 to +0.1	-0.25 to -0.3	-0.25 to -0.35	Better than crystalline silicon
Copper Indium Gallium Selenide (CIGS)	1.0 - 1.7	+0.05 to +0.1	-0.2 to -0.3	-0.3 to -0.4	Better than crystalline silicon
Perovskite Solar Cells	~1.5	+0.02 to +0.05	-0.1 to -0.3	-0.2 to -0.4	Stability issues at high temperatures
Organic PV (OPV)	~1.7 - 2.0	+0.1 to +0.2	-0.1 to -0.2	-0.2 to -0.3	Degradation at high temperatures

PV cells are categorized based on their underlying technology, which influences their efficiency, cost, and applications. Monocrystalline silicon and PERC are preferred for residential and commercial use. For utility-scale power plants, CdTe and Poly-Si are cost-effective. For emerging applications, perovskite and multi-junction cells offer high efficiency but need further development.

Temperature coefficients represent how much a solar cell's performance drops with rising temperature. Here's a general overview of temperature coefficients for different solar cell technologies (without itemizing):

- **Monocrystalline silicon** cells usually have a temperature coefficient around -0.3% to -0.5% per °C, meaning their efficiency decreases noticeably as temperatures rise.

- **Polycrystalline (multicrystalline) silicon** cells tend to perform slightly worse than monocrystalline in this regard, with coefficients typically closer to -0.4% to -0.5% per °C.
- **Thin-film technologies**, such as cadmium telluride (CdTe) and amorphous silicon (a-Si), generally have better temperature stability. CdTe modules often show coefficients around -0.2% to -0.3% per °C, and amorphous silicon may have even lower losses per degree Celsius.
- **CIGS (copper indium gallium selenide)** cells also show relatively favorable temperature coefficients, roughly in the range of -0.2% to -0.4% per °C.
- **Perovskite** solar cells are still under intense research, but early results suggest they may have temperature coefficients similar to or better than silicon, although stability under prolonged heat exposure remains a challenge.

3. Simulation Studies on the Effects of Temperature on the I-V and P-V Curves of the PV Cell

This study investigates the effects of temperature on the current-voltage (I-V) and power-voltage (P-V) characteristics of PV through simulation. The research employs numerical modeling to analyze performance variations under different thermal conditions. Results indicate a decline in open-circuit voltage (Voc) and maximum power output with increasing temperature, while short-circuit current (Isc) exhibits a minor increase. The findings highlight the importance of thermal management for PV efficiency.

PV technology is widely used for renewable energy generation. However, its efficiency is significantly influenced by environmental factors, particularly temperature. This study aims to examine how temperature variations affect the electrical performance of PV cells through simulated analysis of their I-V and P-V curves. This study analyzes the behavior of the output current of PV cell under different operating conditions using simulation tools. The output current is influenced by key parameters such as solar irradiance, temperature, and load variations. The output current of a PV cell is significantly influenced by temperature variations, primarily increasing slightly as temperature rises. This behavior results from enhanced photon absorption and greater carrier generation at elevated temperatures. However, the increase in current is relatively modest and often overshadowed by the simultaneous and more substantial decrease in voltage, which leads to an overall reduction in power output. While current does

respond to temperature, its influence on efficiency is less dominant compared to that of voltage.

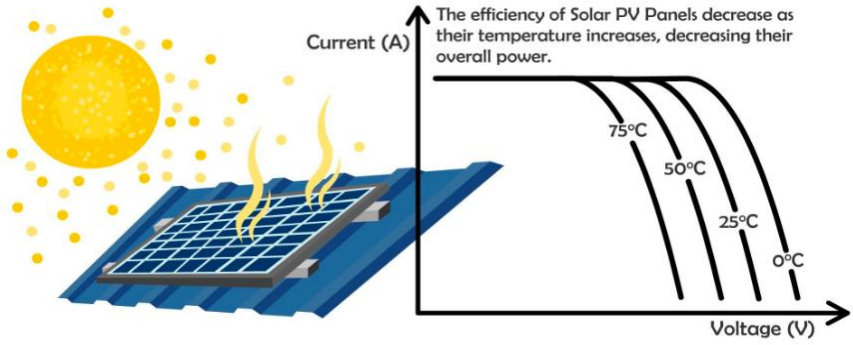

Fig.2 As temperature increases, the efficiency of solar photovoltaic panels decreases, leading to lower electrical power output.

The efficiency of solar photovoltaic panels decreases as temperature increases because higher temperatures increase the intrinsic carrier concentration in the semiconductor material, which leads to a reduction in the open-circuit voltage (Voc). Although the short-circuit current (Isc) slightly increases with temperature, the overall effect is a net decrease in power output. This is due to increased recombination of charge carriers and higher resistive losses, which reduce the panel's ability to convert sunlight into electrical energy efficiently. A commonly used formula to estimate the efficiency loss of a solar panel due to temperature increase is:

Efficiency Loss (%) = Temperature Coefficient × (Operating Temperature - Standard Test Temperature)

- **Temperature Coefficient**: Typically around -0.0045/°C for crystalline silicon panels.
- **Operating Temperature**: The actual temperature of the panel during operation.
- **Standard Test Temperature**: 25°C (77°F), the reference temperature under standard test conditions.

Example Calculation:

If a panel has a temperature coefficient of -0.0045/°C and operates at 50°C:

Efficiency Loss (%) = -0.0045 × (50°C - 25°C) = -0.0045 × 25 = -0.1125 or 11.25%

This means the panel's efficiency decreases by 11.25% at 50°C compared to its efficiency at 25°C.

The study employs MATLAB/Simulink to investigate the current-voltage (I-V) characteristics and assess the dependency of output current on environmental and electrical factors. The results provide insights into optimizing PV system performance for maximum efficiency. PV technology plays a crucial role in renewable energy generation. The output current of a PV cell is a critical parameter that affects the overall power generation capacity of a PV system. Understanding its behavior under varying conditions is essential for optimizing PV system design and operation. This study focuses on simulation-based analysis of output current variations concerning temperature, irradiance, and load conditions. The output current of a PV cell is given by:

$$I = I_{ph} - I_0 \left(e^{\frac{q(V+IR_S)}{nkT}} - 1 \right) - \frac{V+IR_s}{R_{sh}} \quad (8)$$

Where; Iph is the photo-generated current, I_0 is the reverse saturation current, q is the charge of an electron, V is the voltage across the cell, n is the ideality factor, k is Boltzmann's constant, and T is the absolute temperature. Higher temperatures increase the reverse saturation current, leading to a drop in open-circuit voltage. The voltage across the cell is significantly influenced by temperature variations because it decreases as temperature increases. This behavior is due to enhanced carrier recombination and a reduced energy bandgap within the semiconductor material, which lowers the potential difference generated by the photovoltaic effect. As a result, higher temperatures lead to a noticeable drop in the voltage output, which negatively affects the overall performance and efficiency of the solar cell.

Where as, temperature enhances carrier generation slightly, causing a marginal rise in short-circuit current . MATLAB/Simulink is used to model the PV cell. The equivalent diagram of this simulation circuit is given in Fig. 3.

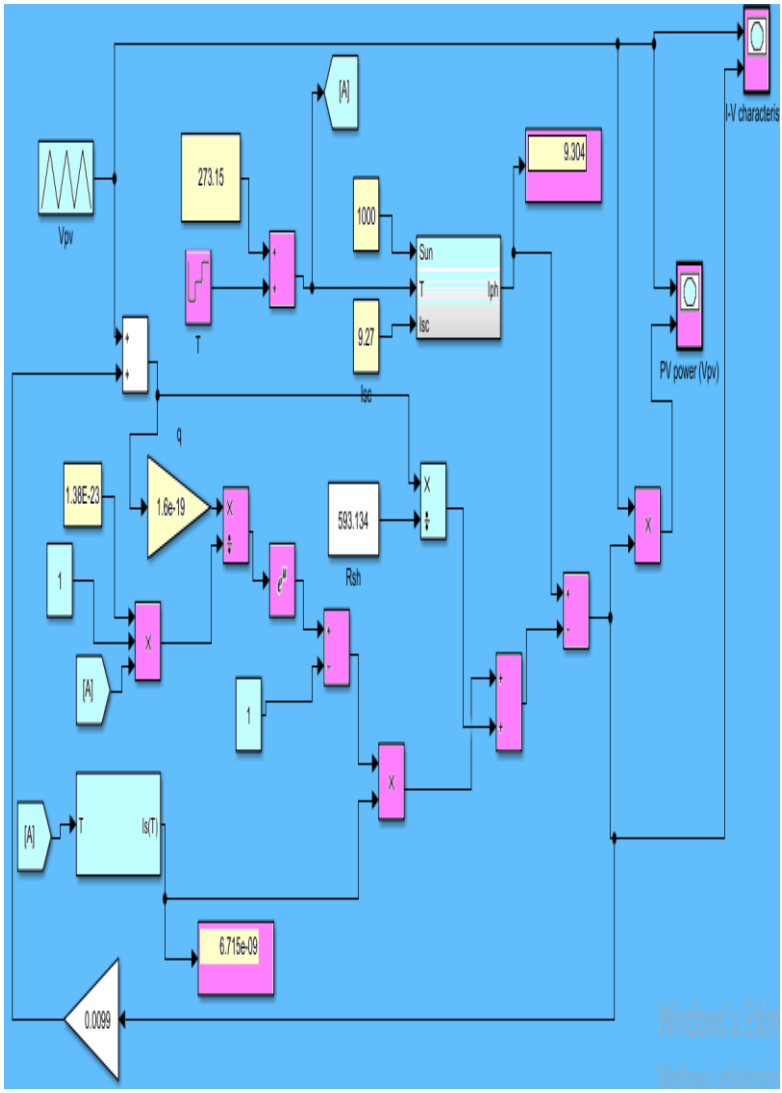

Fig. 3 Matlab/Simulink equivalent of PV cell I-V and P-V graphs

PV cell I-V and P-V graphs are significantly influenced by temperature variations because temperature affects the fundamental electrical characteristics of the solar cell. As temperature increases, the open-circuit voltage decreases more noticeably than the short-circuit current increases, leading to a downward shift in the I-V curve and a flattening of its slope. This change reduces the maximum power point, which is reflected in the P-V curve as a lower peak power output. The altered shape of both curves under different temperature conditions illustrates the thermal sensitivity of photovoltaic performance, highlighting the importance of temperature management in PV system design.

Developing simulink andmathematical model of PV module provides a deeper understanding of its behavior under various environmental conditions, allowing for accurate performance predictions. It enables optimization of energy conversion efficiency by analyzing the effects of factors such as solar irradiance and temperature. Such modeling is essential for designing and sizing PV systems, ensuring their reliability and cost-effectiveness. Additionally, it aids in fault diagnosis, improving maintenance strategies and extending the lifespan of PV installations. By facilitating research and development, mathematical models contribute to advancements in PV technology, enhancing integration with power grids and promoting sustainable energy solutions.

The output of a PV module is strongly influenced by environmental conditions such as solar irradiance and ambient temperature. Higher solar irradiance increases the power generation, while elevated ambient temperatures tend to reduce efficiency due to the negative temperature coefficient of solar cells. Cooling systems tend to be more efficient and more necessary in concentrated photovoltaic (CPV) systems due to the significantly higher thermal loads generated by focusing sunlight onto a smaller cell area. The intensity of light in CPV systems increases the operating temperature far beyond that of standard non-concentrated PV, making effective heat dissipation critical to maintaining performance and preventing material degradation. As a result, cooling methods, whether passive or active, have a more pronounced impact in CPV applications, often becoming an integral part of the system's design to ensure optimal energy conversion and long-term reliability. Variations in these factors directly impact the voltage, current, and overall performance of the PV system, making it essential to consider them in system design and performance analysis. PV cell I-V and P-V characteristic curves are as given in Fig. 4.

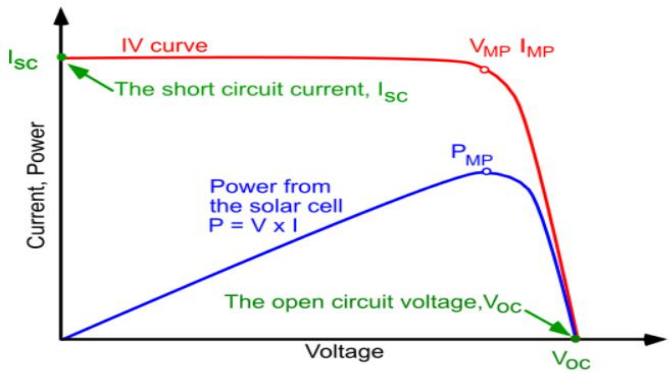

Fig. 4 PV cell I-V and P-V characteristic curves

The I-V curve (red) shows how the current decreases as voltage increases. The PV curve (blue) shows the power output at different voltages, with a clear

Maximum Power Point (Pmp). The current-voltage (IV) curve of a solar cell describes its electrical characteristics under specific conditions. To achieve maximum power output, the cell must operate at the maximum power point (MPP), where the product of current (I) and voltage (V) is at its peak. nThe power generation of a photovoltaic cell and the lifespan of a battery are both significantly influenced by temperature.

High temperatures can reduce the efficiency of a photovoltaic cell by increasing the semiconductor's intrinsic carrier concentration, leading to higher recombination rates and lower output voltage. This results in decreased overall power generation. Similarly, elevated temperatures can accelerate the degradation of battery components, reducing their capacity and overall lifespan. Conversely, extremely low temperatures can also negatively impact battery performance by increasing internal resistance and limiting charge acceptance. Understanding these thermal effects is essential for optimizing energy generation, storage, and system longevity in photovoltaic applications. Important takeaways about the IV Curve:

- **Short-Circuit Current (Isc)** – The maximum current when the voltage is zero (circuit is shorted).
- **Open-Circuit Voltage (Voc)** – The maximum voltage when the current is zero (no external load).
- **Maximum Power Point (Pmp)** – The point where ($P = Vmp \times Imp$) is maximized.

The **PV (Photovoltaic) Curve** of **PV cell** represents the relationship between voltage (V) and current (I) as well as power (P) for different operating conditions. Important takeaways about the PV curve:

- The power ($P = V \times I$) initially increases with voltage, reaches a peak (Maximum Power Point or MPP), and then drops to zero at Voc.
- The MPP is the ideal operating point for maximum efficiency.
- This is the point (MPP) where the PV cell operates at maximum power output.
- MPP changes with temperature and irradiance.
- Maximum Power Point Tracking (MPPT) is used in PV systems to optimize power extraction.

The Fill Factor can be calculated from the PV cell IV and PV curves. The Fill Factor of a PV cell is given by:

$$FF = \frac{V_{mp} * I_{mp}}{V_{oc} * I_{sc}} \quad (9)$$

A higher FF indicates a more efficient PV cell. Understanding the I-V and P-V curves helps in optimizing PV system performance, sizing, and efficiency improvements. Fill factor is significantly influenced by temperature variations because temperature directly affects the internal resistance and carrier behavior within a solar cell. As temperature increases, series resistance tends to rise and shunt resistance may decrease, both of which contribute to a decline in fill factor. Additionally, elevated temperatures lead to increased recombination losses and reduced open-circuit voltage, further degrading the shape of the current-voltage curve and thus lowering the fill factor. These effects collectively reduce the overall power conversion efficiency of the photovoltaic device under high-temperature conditions. The change of the PV cell I-V graph depending on temperature is given in Fig. 5.

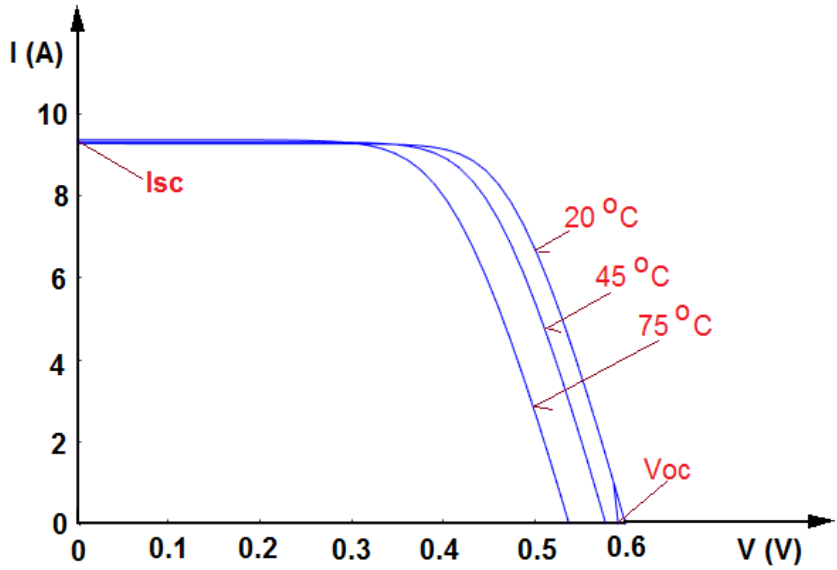

Fig. 5 Variation of PV cell I-V graph with temperature

The current-voltage (I-V) curve of a solar cell describes its electrical characteristics under specific conditions. To achieve maximum power output, the cell must operate at the maximum power point (MPP), where the product of current (I) and voltage (V) is at its peak. As temperature increases, the I-V characteristic curve of PV cell shifts due to changes in its electrical properties. The open-circuit voltage Voc decreases significantly with rising temperature, causing the curve to shift leftward. This occurs because higher temperatures reduce the bandgap of the semiconductor, leading to increased carrier

recombination and lower voltage generation. The short-circuit current experiences a slight increase, but this effect is minimal compared to the voltage reduction. Consequently, the maximum power output of the PV cell decreases as temperature rises, leading to reduced efficiency. The overall fill factor also declines, further contributing to performance losses in hotter conditions.

As the temperature of PV cell increases, its power-voltage (P-V) characteristics undergo noticeable changes. Higher temperatures cause a reduction in the open-circuit voltage (Voc) due to an increase in intrinsic carrier concentration, which leads to higher recombination rates. This results in a leftward shift of the P-V curve, where the maximum power point (MPP) moves towards a lower voltage, reducing the overall power output. Conversely, the short-circuit current (Isc) experiences a slight increase with temperature due to enhanced carrier mobility, but this effect is relatively small compared to the drop in voltage. As a result, the net power generation declines as temperature rises. This phenomenon highlights the importance of thermal management in PV systems to sustain optimal energy conversion efficiency under varying temperature conditions. The variation of the PV cell P-V graph depending on temperature is shown in Fig. 6.

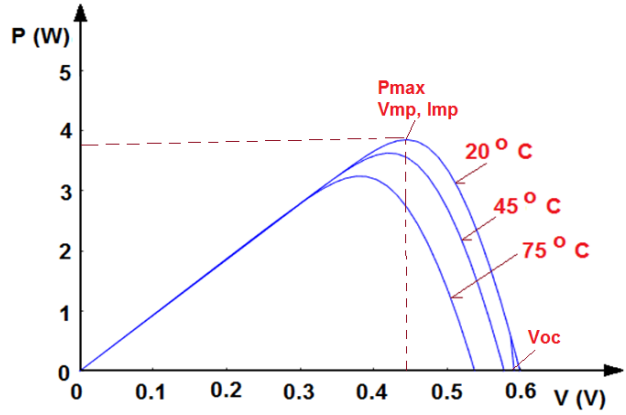

Fig. 6 Variation of PV cell P-V graph with temperature

The study confirms that temperature negatively impacts PV efficiency, primarily by reducing Voc and power output. Effective thermal management strategies, such as cooling systems or optimized material selection, are crucial to improving PV performance. As temperature increases, the power-voltage (P-V) characteristics of PV cell undergo significant changes. The most noticeable effect is the reduction in open-circuit voltage, which causes the curve to shift leftward. This happens due to the increased intrinsic carrier concentration in the semiconductor material, leading to a lower bandgap voltage. At the same time,

the short-circuit current increases slightly, but this effect is minimal compared to the drop in voltage. As a result, the maximum power point (MPP) moves towards a lower voltage with a slight increase in current, ultimately leading to a reduction in overall power output. The peak of the P-V curve decreases, demonstrating the loss in efficiency at higher temperatures. Conversely, at lower temperatures, the P-V curve exhibits a higher peak power, indicating better performance of the PV cell.

4. Mitigation Strategies for Temperature-Related Losses in PV Cells

The performance of PV solar cells is significantly influenced by temperature variations because temperature affects the intrinsic properties of the semiconductor materials. As temperature rises, the voltage output of the cells decreases due to increased carrier recombination and narrowing of the bandgap, which results in lower power output despite a slight increase in current. Conversely, lower temperatures generally enhance efficiency by maintaining higher voltage levels. These thermal effects make temperature a critical factor in both the design and real-world performance prediction of solar energy systems.

Solar PV panels convert sunlight into electricity, but they also generate heat, which reduces efficiency. High temperatures decrease the efficiency of PV cells by increasing resistance and lowering the voltage output. To mitigate this, cooling technologies are employed, categorized into **active** and **passive** cooling methods. Solar PV Active and Passive Cooling Technologies are explained below.

A. Passive Cooling Technologies:

Passive cooling techniques do not require external power and rely on natural heat dissipation mechanisms. These methods are cost-effective and easy to implement.

Natural Air Cooling

- Utilizes natural airflow around the PV panel.
- Increasing the panel height or spacing between modules improves ventilation.

Phase Change Materials (PCM)

- Uses materials that absorb and store heat during phase transitions (solid-liquid).
- PCMs stabilize the temperature and improve PV efficiency.

Radiative Cooling

- Special coatings on PV panels emit infrared radiation to release excess heat into the atmosphere.
- Helps in cooling, especially at night.

Heat Dissipation Fins

- Attaching fins to the back of PV panels increases surface area for heat dissipation.
- Enhances convective cooling.

Evaporative Cooling

- Uses water or moisture to cool PV panels through evaporation.
- Simple systems like wet cloth coverings or porous materials improve efficiency.

B. Active Cooling Technologies:

Active cooling methods involve external energy input and are more effective in temperature regulation.

Air-Based Cooling Systems

- Uses fans or blowers to enhance airflow and remove heat.
- Can be integrated with HVAC systems for better efficiency.

Water-Based Cooling Systems

- Water sprays or circulating water channels absorb heat from PV panels.
- Can be coupled with heat recovery systems to utilize waste heat.

Thermoelectric Cooling (TEC)

- Uses thermoelectric modules to transfer heat away from PV cells.
- Requires electrical input but can be powered by the PV system itself.

Hybrid Cooling Systems

- Combines air and water cooling for better efficiency.
- Example: PV/Thermal (PVT) systems that generate both electricity and hot water.

Nano-Fluids Cooling

- Uses engineered fluids with nanoparticles to improve heat transfer efficiency in water-based cooling systems.
- Enhances thermal conductivity and overall cooling performance.

The choice between passive and active cooling depends on cost, energy requirements, and environmental conditions. Passive methods are simple and low-cost but may not be sufficient for high-temperature environments. Active methods offer better cooling performance but require additional energy input. A combination of both approaches can optimize PV performance and enhance the overall efficiency of solar power generation. A summary of active and passive cooling technologies for solar PV systems is given in Table 2.

Table 2. Summarizing active and passive cooling technologies for solar PV systems:

Cooling Method	Type	Working Principle	Advantages	Disadvantages
Natural Air Cooling	Passive	Enhances ventilation by spacing panels for airflow.	Simple, no energy consumption, cost-effective.	Limited cooling efficiency in low-wind conditions.
Phase Change Materials (PCM)	Passive	Absorbs heat during phase transition (solid to liquid).	Stable temperature regulation, low maintenance.	Additional weight, potential material degradation.
Radiative Cooling	Passive	Special coatings emit heat as infrared radiation.	Works day and night, improves long-term performance.	Limited effectiveness in humid or cloudy conditions.
Heat Dissipation Fins	Passive	Increases surface area for better heat dissipation.	Low-cost, improves heat transfer.	Low-cost, improves heat transfer.
Evaporative Cooling	Passive	Uses water/moisture to enhance cooling through evaporation.	Simple, effective in dry climates.	Requires water supply, maintenance needed.
Air-Based Cooling (Fans/Blowers)	Active	Uses fans to increase airflow over PV panels.	Effective, works in all weather conditions.	Requires electricity, potential mechanical failure.
Water-Based Cooling	Active	Circulating water absorbs heat from PV panels.	Highly efficient, can be integrated with heat recovery.	Water consumption, requires pumps and piping.
Thermoelectric Cooling (TEC)	Active	Uses thermoelectric modules to transfer heat away.	Can be powered by PV panels, precise cooling.	Expensive, requires electricity.
Hybrid Cooling (Air + Water)	Active	Combines air and water cooling for better performance.	Maximizes efficiency, adaptable to different climates.	Higher cost, increased system complexity.
Nano-Fluids Cooling	Active	Uses engineered liquids with nanoparticles to improve heat transfer.	High thermal conductivity, better cooling performance.	Expensive, requires advanced technology.

Both passive and active cooling methods can reduce the maximum temperature of PV panels by up to 25°C under certain conditions. The effectiveness depends on factors like ambient temperature, solar irradiance, airflow, and the design of the cooling system. Passive methods rely on natural heat dissipation, such as convection and radiation, while active methods use external energy or systems (like fans or water circulation) to enhance cooling.

Reducing the temperature by 25°C can significantly improve the electrical efficiency and extend the lifespan of the PV panels.

Temperature-related losses in PV modules can be a significant issue because high temperatures reduce the efficiency of the cells, affecting their power output. The solar cell efficiency can be given as:

$$\eta_c = \eta_{T_{ref}}\left[1 - \beta_{ref}\left(T_c - T_{ref}\right) + \gamma log_{10} G(t)\right] \quad (10)$$

Where; $\eta_{T_{ref}}$ is the module's electrical efficiency at the reference temperature, Tref, and at solar irradiation of 1000W/m^2. The temperature coefficient, β_{ref} , and the solar irradiation coefficient, γ, are mainly material properties, having values of about 0.0045K and 0.12, respectively, for crystalline silicon modules (Notton et al., 2005). The quantities $\eta_{T_{ref}}$ and β_{ref} are normally given by the PV manufacturer.

$$\beta_{ref} = \frac{1}{T_0 - T_{ref}} \quad (11)$$

Where; T_0 is the (high) temperature at which the PV module's electrical efficiency drops to zero. For crystalline silicon solar cells this temperature is 270 °C. These losses primarily occur because as temperature increases, the voltage output of the PV cells decreases, leading to a drop in overall efficiency.

To mitigate these effects, various cooling techniques can be implemented, which help to lower the temperature of the modules and thus improve their performance. One of the most common methods for reducing temperature-related losses is by using passive cooling techniques. These rely on natural processes like airflow, conduction, or irradiation to dissipate heat from the module. Enhancing airflow around photovoltaic panels contributes to improved efficiency by facilitating heat dissipation and maintaining optimal operating temperatures. When air movement is optimized, excess thermal energy is removed, reducing the negative impact of heat on energy conversion.

This process minimizes temperature-related voltage drops and maintains higher power output levels. The interaction between airflow and surface temperature influences convective heat transfer, preventing excessive thermal buildup. Variations in installation design and positioning affect the extent of airflow exposure, directly impacting performance. Strategies that allow better circulation lead to a more stable thermal environment, ensuring consistent efficiency gains.

For instance, ensuring proper ventilation behind the panels can allow air to circulate freely, helping to remove heat without needing an external power source. Some PV installations also use heat sinks or thermal insulation, which can either absorb heat or block it from reaching the modules, reducing temperature build-up. In addition to passive methods, active cooling techniques can also be employed for more significant temperature reductions.

These methods often require additional equipment and energy, but they can provide a much more effective solution, particularly for large-scale PV systems. For example, liquid cooling systems circulate water or coolants through pipes attached to the back of the panels, absorbing heat and carrying it away. Alternatively, air cooling systems using fans or blowers can force air across the surface of the modules to help with heat dissipation. The open circuit water cooling system is given in Fig. 7.

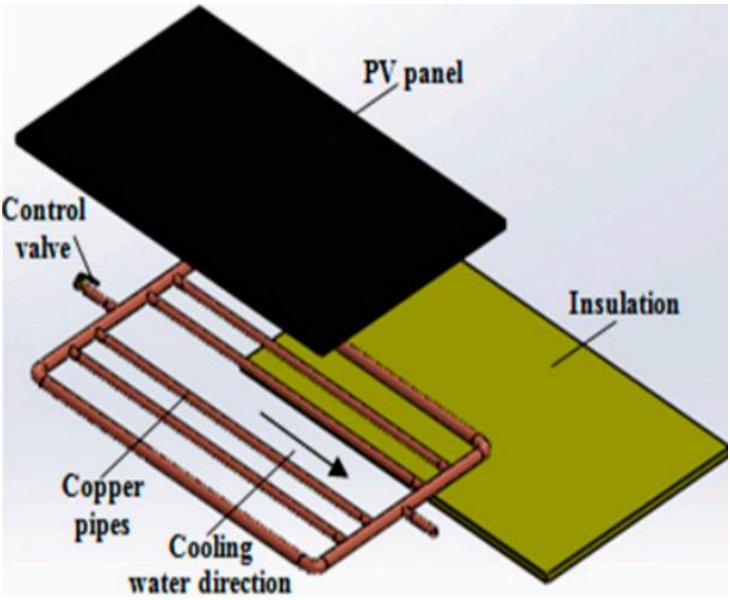

Fig. 7 Open-loop water cooling system [12]

Another approach is the use of advanced materials and coatings that help reflect excess sunlight or heat. By applying special reflective coatings, the panels can absorb less heat during peak sunlight hours, reducing temperature-related performance losses. Some PV systems also use phase-change materials (PCMs), which can store excess heat and release it when temperatures drop, helping to maintain a more stable temperature. Moreover, hybrid systems, such as photovoltaic-thermal (PVT) modules, combine both photovoltaic power generation and thermal energy harvesting. These systems use the heat from the PV cells to produce thermal energy, which simultaneously cools the modules and

reduces temperature-related losses while increasing overall energy production. To further address temperature-related issues, innovative designs like bifacial modules can be employed.

These systems capture light from both the front and rear of the panel, which can reduce the overall thermal load on the system and increase the power output. Adjusting the orientation of panels using solar tracking systems can also help, as these systems can minimize direct exposure to sunlight during the hottest periods of the day. In the future, advances in materials science, such as the development of new semiconductors with better high-temperature stability, may offer even more effective ways to mitigate temperature-related losses. Additionally, integrating temperature monitoring and control systems can allow operators to optimize cooling strategies in real-time, ensuring that the system is always operating at its most efficient temperature. In conclusion, there are a variety of cooling strategies available, each with its own set of advantages and limitations. Combining several approaches, depending on the scale and location of the PV system, can significantly improve performance by reducing the impact of temperature-related losses on the cells.

Advanced cooling techniques for PV modules focus on enhancing efficiency by managing heat dissipation effectively. Passive cooling methods leverage materials and design optimizations to dissipate heat without additional energy consumption. These include phase change materials that absorb excess thermal energy and specialized coatings that enhance radiative cooling by emitting infrared radiation. Heat sinks and thermally conductive back sheets also contribute by improving heat transfer away from the PV cells. The rear view of the solar panel with four cooling fans is as given in Fig.8.

Fig. 8 Rear view of solar panel with four cooling fans

A diagram showing a PV module with an active cooling system using a fan. The image shows airflow dynamics, helping to reduce the panel's temperature. More advanced strategies involve nanofluids with superior thermal properties, thermoelectric cooling using Peltier modules, and spectral splitting, where optical elements redirect heat-generating infrared irradiation away from the solar cells. Flowchart for the cooling system of a PV panel generally follows a structured process of heat dissipation. Here's a simplified breakdown of the flow:

Start

Monitor PV Panel Temperature

- If the temperature is within the safe range → Continue normal operation
- If the temperature exceeds the threshold → Activate cooling system

Cooling System Activation

- Engage cooling mechanism (air/water cooling)

Heat Dissipation

- Transfer heat away from the PV panel

Monitor Temperature Again

- If temperature is reduced to the safe range → Deactivate cooling system
- If still high → Continue cooling process

System Shutdown (if necessary)

End

The flow diagram of the cooling system of the PV panel is given in Fig. 9.

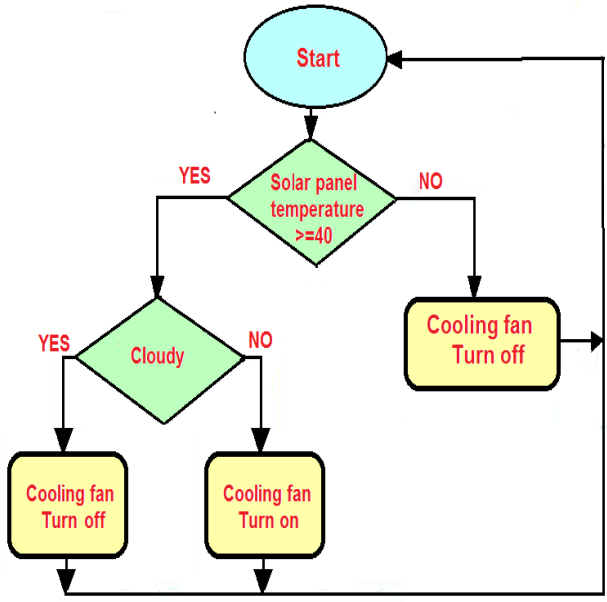

Fig 9 Flow chart for cooling system of the PV panel

Emerging technologies such as liquid immersion cooling, which submerges PV cells in non-conductive liquids, and green infrastructure solutions, like integrating PV panels with vegetation for natural cooling, are gaining attention. These innovations help mitigate the efficiency losses caused by temperature increases, ensuring higher energy yields and longer operational lifespans for PV systems.

Tracking systems for PV panels enhance energy capture by dynamically adjusting the orientation of solar modules to follow the sun's movement. These systems improve efficiency by optimizing the angle of incidence throughout the day. Some systems operate along a single axis, adjusting panels horizontally, while others use dual-axis mechanisms to track both horizontal and vertical movements. The effectiveness of these systems depends on location, installation costs, and maintenance requirements, with benefits typically outweighing challenges in large-scale solar applications.

Efficiency management solutions focus on minimizing power losses due to heat, dust accumulation, shading, and electrical mismatches. Thermal regulation strategies help control panel temperatures to prevent efficiency drops due to excessive heat. Advanced control techniques ensure that panels operate at their maximum power point under varying environmental conditions, while monitoring technologies enable real-time performance analysis and predictive maintenance. Innovations in surface treatments and automated cleaning mechanisms further contribute to maintaining consistent energy production by reducing losses from soiling and environmental factors.

The optimal topology for PV system under partial shading depends on the shading model, which defines how shadows affect the panel array. For uniform shading across multiple modules, interconnected configurations like total cross-tied (TCT) or bridge-linked (BL) topologies help reduce mismatch losses. When shading follows a row-wise pattern, as in cases where buildings or trees cast shadows at certain times of the day, reconfigurable topologies dynamically adjust connections to maximize power output. For more random and localized shading, such as from passing clouds or dirt accumulation, distributed power electronics like microinverters or DC optimizers ensure each module operates independently, preventing the drop in overall efficiency. Hybrid topologies, combining features of different approaches, can be effective in scenarios where shading conditions vary frequently.

Humidity affects PV module performance primarily by influencing the electrical properties of the materials and by contributing to long-term degradation. High humidity can lead to increased surface leakage currents and reduced insulation resistance, which diminish overall efficiency. Over time, moisture ingress can penetrate the encapsulation layers, potentially causing corrosion of internal components, delamination, and other reliability issues. These effects are more pronounced in environments where humidity is consistently high, especially when combined with elevated temperatures, leading to accelerated aging and reduced operational lifespan of the PV modules.

5. Conclusion and Recommendations

The performance of PV solar cells is significantly influenced by temperature variations. As temperature increases, the efficiency of solar cells generally decreases due to the reduction in open-circuit voltage (Voc) and the increase in reverse saturation current. While short-circuit current (Isc) may slightly increase with temperature, the overall power output and efficiency decline. This temperature dependence underscores the importance of implementing effective thermal management strategies in PV systems. The recommendations are as given below.

- **Material Selection:** Research and development should focus on materials with lower temperature coefficients to mitigate efficiency losses in high-temperature environments.
- **Cooling Systems:** Passive and active cooling methods, such as heat sinks, phase change materials, or forced air circulation, should be integrated to maintain optimal operational temperatures.
- **Panel Orientation and Installation:** Proper installation techniques, including elevated mounting structures for better airflow and reflective coatings to reduce heat absorption, can help regulate panel temperature.
- **Hybrid Systems:** Combining PV technology with thermoelectric or other cooling technologies can enhance efficiency by managing excess heat effectively.
- **Temperature Monitoring:** Implementing real-time temperature monitoring systems can help in optimizing performance and predicting maintenance needs for solar PV installations.
- **Geographical Considerations:** Site-specific climate conditions should be considered when designing solar power systems to ensure maximum energy yield and long-term reliability.

By adopting these recommendations, PV system efficiency can be improved, leading to increased energy output, extended lifespan, and enhanced cost-effectiveness of solar power generation. The analysis of a solar PV module in terms of different installation angles involves examining how varying the tilt angles impacts the total average power generation throughout the day. By adjusting the angle at which the panels are installed, you can optimize the energy capture based on factors such as the sun's position in the sky throughout the day and across different seasons. For example, when the panels are set at a fixed angle, the power generation is maximized when the tilt angle is close to the latitude of the location, especially during specific seasons. However, in regions where the solar irradiance changes significantly, installing adjustable or tracking systems can increase power generation by continuously aligning the panels with the sun's movement.

To determine the optimal installation angle, simulations or real-time data analysis can be used to assess the total energy generation for each angle across the entire day, considering both the direct and diffuse sunlight received at each angle. The goal is to find the angle that consistently yields the highest total average power over time, taking into account the seasonal

variations in solar irradiance. This type of analysis is essential for improving the efficiency of solar energy systems, especially in regions with varying solar radiation throughout the year. The overall power generation depends on how well the installation angle aligns with the sun's position relative to the earth's tilt and orbit. The efficiency of PV cells is significantly influenced by temperature. As temperature increases, the performance of solar cells generally decreases. The reasons are as follows:

A. How Temperature Affects PV Efficiency:

- **Reduction in Open-Circuit Voltage (Voc):** Higher temperatures increase the intrinsic carrier concentration in the semiconductor material, reducing the bandgap energy. This leads to a lower open-circuit voltage, decreasing overall efficiency.
- **Increase in Series Resistance:** Heat can increase resistance within the cell and connections, leading to power losses.
- **Reduction in Power Output:** The power output of a PV cell is directly affected by both voltage and current. While the current slightly increases with temperature, the voltage drops more significantly, leading to a net reduction in power.
- **Effect on Fill Factor (FF):** Higher temperatures degrade the fill factor, which represents the maximum power point compared to the theoretical maximum.

B. Temperature Coefficient of PV Cells:

The temperature coefficient of a solar panel indicates how much power output decreases per degree Celsius rise in temperature. For most silicon-based PV cells:

- **Power temperature coefficient:** -0.3% to -0.5% per °C
- **Voltage temperature coefficient:** -2.2 mV/°C per cell
- **Current temperature coefficient:** +0.05% per °C (negligible effect)

C. Strategies to Mitigate Temperature Effects:

- **Proper Ventilation and Mounting:** Elevating 276anel sor using cooling techniques such as air or water circulation can help dissipate heat.

- **Material Selection:** Some materials, like perovskite or multi-junction cells, have better high-temperature performance than traditional silicon.
- **Using Heat-Resistant Coatings:** Special coatings can reduce heat absorption and improve efficiency.
- **Integration with Cooling Systems:** Hybrid PV-Thermal (PV-T) systems utilize excess heat for other applications while maintaining PV efficiency.

D. Real-World Considerations:

- **Geographic Location:** PV cells in hot climates suffer greater efficiency losses but may still generate high power output due to intense sunlight.
- **Seasonal Variations:** Cold environments can improve efficiency, provided there is sufficient sunlight.

PV cells are adversely affected by high temperatures. As the temperature increases, the efficiency of most PV cells decreases. This happens primarily because:

- **Voltage drops** with temperature: While the current output of a solar cell increases slightly with temperature, the voltage drops significantly. Since power is the product of current and voltage, the overall power output declines.
- **Semiconductor behavior** changes: Heat increases the intrinsic carrier concentration in the semiconductor material, reducing the bandgap and causing higher recombination losses.

This means that even in very sunny regions, if the ambient or module temperatures are high, the energy output can be lower than expected. That's why good ventilation, reflective mounting surfaces, or even active cooling can help improve performance in hot climates. While PV cells are adversely affected by high temperatures, innovative cooling techniques and material advancements can help mitigate these effects, improving overall solar energy efficiency. The electrical efficiency of a PV panel can be improved by decreasing its temperature. When the panel heats up, its voltage output decreases due to changes in the semiconductor properties, particularly the narrowing of the bandgap and increased carrier recombination. Although the current may slightly increase with temperature, the drop in voltage has a more significant impact, leading to an overall reduction in power output. By keeping the panel cooler, this voltage drop is minimized, maintaining higher efficiency and better overall energy conversion.

Declarations

Funding The authors have not disclosed any funding.

Data availability There is no data associated with this work

Conflict of interest The authors have not disclosed any competing interests.

References

Akter, F. *et al*., (2023) Evaluating Environmental Impacts and Proposed Solution for Temperature Effect of Photovoltaic Systems, *2023 10th IEEE International Conference on Power Systems (ICPS)*, Cox's Bazar, Bangladesh, 2023, pp. 1-6, doi: 10.1109/ICPS60393.2023.10428967. https://doi.org/10.1109/ICPS60393.2023.10428967

Guddanti, K.P. Bharati, A.K. and Nekkalapu, S. et al., (2025) A Comprehensive Review: Impacts of Extreme Temperatures Due to Climate Change on Power Grid Infrastructure and Operation, in *IEEE Access*, 13, 49375-49415,

https://doi.org/10.1109/CENCON.2015.7409548

Zaini,M.H. Ab Kadir, M.Z. and Izadi, M. et al., (2015) The effect of temperature on a mono-crystalline solar PV panel, *2015 IEEE Conference on Energy Conversion (CENCON)*, Johor Bahru, Malaysia, pp. 249-253,

https://doi.org/10.1109/CENCON.2015.7409548

Bala Subramaniyan, A Pan, R. Kuitche, J. et al., (2018) Quantification of Environmental Effects on PV Module Degradation: A Physics-Based Data-Driven Modeling Method, in *IEEE Journal of Photovoltaics*, 8 (5), 1289-1296,

https://doi.org/10.1109/JPHOTOV.2018.2850527

Kane, A. Verma, (2013) Characterization of PV cell-environmental factors consideration, 2013 International Conference on Power, Energy and Control (ICPEC), Dindigul, India, pp. 26-29, https://doi.org/10.1109/ICPEC.2013.6527618

Khan, M.S. Hegde, V. and Shankar, G.(2017) Effect of Temperature on Performance of Solar Panels- Analysis, *2017 International Conference on Current Trends in Computer, Electrical, Electronics and Communication (CTCEEC)*, Mysore, India, pp. 109-113, https://doi.org/10.1109/CTCEEC.2017.8455109

Oufettoul, H. Motahhir, S. Ait abdelmoula, I. et al., (2023) Optimized topology for a photovoltaic array using switches control, Energy Conversion and Management, 291, 117315, https://doi.org/10.1016/j.enconman.2023.117315.

Wen, C., Fu, C., Tang, J. et al., (2012) The influence of environment temperatures on single crystalline and polycrystalline silicon solar cell performance. *Sci. China Phys. Mech. Astron*. 55, 235–241, https://doi.org/10.1007/s11433-011-4619-z

Xiao. W, Ozog. N, Dunford. W.G.(2007). Topology Study of Photovoltaic Interface for Maximum Power Point Tracking. *IEEE Trans. Industrial Electronics*, 54(3), 1696–1704, https://doi.org/10.1109/TIE.2007.894732

Yao, X. Zhang, F. Zhao, Y et al., (2024) Research on the Environmental Impact of Photovoltaic Cell Output Based on Ideal Solar Radiation Model, *2024 International Conference on Energy and Electrical Engineering (EEE)*, Nanchang, China, pp. 1-8, https://doi.org/10.1109/EEE59956.2024.10709767

Adak, S. (2024). Power Factor Analysis of Grid-Connected Solar Inverter under Different Irradiance Levels throughout the Day. *Energies*, 17(15), 3632. https://doi.org/10.3390/en17153632

Selvi, S. Mohanraj, M. Duraipandy, P. (2023) Optimization of Solar Panel Orientation for Maximum Energy Efficiency, *2023 4th International Conference on Smart Electronics and Communication (ICOSEC)*, Trichy, India, pp. 159-162,

https://doi.org/10.1109/ICOSEC58147.2023.10276287

Kalaiselvan, S. Karthikeyan, V. Rajesh, G. Et al., (2018) A. Solar PV Active and Passive Cooling Technologies - A Review, *2018 International Conference on Computation of Power, Energy, Information and Communication (ICCPEIC)*, Chennai, India, pp. 166-169, https://doi.org/10.1109/ICCPEIC.2018.8525185

Khalid, M. Janjua, A.K. and Abdullah Khalid, H.(2018) Effect of PV Panel Orientation on Batteries in a Solar Generation System, *2018 International Conference on Power Generation Systems and Renewable Energy Technologies (PGSRET)*, Islamabad, Pakistan, pp. 1-5,

https://doi.org/10.1109/PGSRET.2018.8685984

Dubey, B. Tiwari, D. and Kumar, R. (2016) Effect of temperature variations over Photovoltaic modules efficiency of different technologies at NOCT, *2016 IEEE Students' Conference on Electrical, Electronics and Computer Science (SCEECS)*, Bhopal, India, pp. 1-5, https://doi.org/10.1109/SCEECS.2016.7509336

Lindholm, F.A. Fossum, J. G., and Burgess, E. L. (1979) Application of the superposition principle to solar-cell analysis, *IEEE Transactions on Electron Devices*, 26, 165–171,. https://doi.org/10.1109/T-ED.1979.19400

https://www.pveducation.org/pvcdrom/solar-cell-operation/iv-curve

Shamroukh, A.N. Thermal regulation of photovoltaic panel installed in Upper Egyptian conditions in Qena. Therm. Sci. Eng. Prog. 2019, 14, 100438.

https://doi.org/10.1016/j.tsep.2019.100438

Velmurugan, K. *et al*., (2020) Experimental Studies on PV Module Cooling With Radiation Source PCM Matrix, in *IEEE Access*, 8, pp. 145936-145949,

https://doi.org/10.1109/ACCESS.2020.3012272

Cho, I. Kım, H. (2019) Study on PV Panel Cooling System using IoT with ESS for Preventing Reduced Efficiency of Solar Panel, *2019 the 3rd International Conference on Sustainable Energy Engineering*, 342, 012006, https://doi.org/10.1088/1755-1315/342/1/012006

Motahhir, S. EL Hammoumi, A. Abdelaziz EL Ghzizal, A. Et al., (2019) Open hardware/software test bench for solar tracker with virtual instrumentation, Sustainable Energy Technologies and Assessments, 31, 9-16, https://doi.org/10.1016/j.seta.2018.11.003.

Fesharaki, V.J. Dehghani, M. and Fesharaki, j.j.(2011) The effect of temperature on photovoltaic cell efficiency, t *International Conference on Emerging Trends in Energy Conservation –(ETEC)* Tehran, Tehran, Iran, 20-21 November,

Sainthiya, H. Beniwal, N.S. (2017) Different types of cooling systems used in photovoltaic module solar system: A review," *2017 International Conference on Wireless Communications, Signal Processing and Networking (WiSPNET)*, Chennai, India, pp. 1500-1506, https://doi.org/ 10.1109/WiSPNET.2017.8300012

Kalaiselvan,S. Karthikeyan, V. Rajesh, G. Et al., (2018) Solar PV Active and Passive Cooling Technologies - A Review, *2018 International Conference on Computation of Power, Energy, Information and Communication (ICCPEIC)*, Chennai, India, 2018, pp. 166-169, https://doi.org/ 10.1109/ICCPEIC.2018.8525185

Ahmed M. Bukar, A. Almerbati, S.Z. Shuja, Syed M. Zubair, (2025) Enhancing solar PV panel performance through active and passive cooling techniques: A comprehensive review, Renewable and Sustainable Energy Reviews, 216, 115611, 1364-0321, https://doi.org/10.1016/j.rser.2025.115611.

Peng, Z. Herfatmanesh, M.R. Liu, Y. (2017) Cooled solar PV panels for output energy efficiency optimisation, Energy Conversion and Management, 150, 949-955,

https://doi.org/10.1016/j.enconman.2017.07.007.

Rishi, K. Balachandran, M. Raagul, G. Srinivasagopalan, A. Ramkiran, B. and Neelamegam, P. (2018) Solar Cooling Technologies - A Review, *2018 International Conference on Computation of Power, Energy, Information and Communication (ICCPEIC)*, Chennai, India, pp. 174-178, https://doi.org/10.1109/ICCPEIC.2018.8525162

Ahmed, Y. E., Maghami, M. R., Pasupuleti, J., Danook, S. H., & Basim Ismail, F. (2024). Overview of Recent Solar Photovoltaic Cooling System Approach. *Technologies*, *12*(9), 171. https://doi.org/10.3390/technologies12090171

Shahabuddin, M. Riyaz, A. Asim, M. Shadab, M. M. Sarwar, A. & Anees, A. (2018). Performance based analysis of solar PV emulators: A review. Paper presented at *the 2018 International Conference on Computational and Characterization Techniques in Engineering & Sciences (CCTES)*, IEEE, pp. 94-99,

ttps://doi.org/10.1109/CCTES.2018.8674082

Chua, P.J.Y. and S. E. R. Tay, S.E.R (2020) Comparative Discussion of Active and Passive Cooling of PV Modules - Are We Doing It Right?, *2020 47th IEEE Photovoltaic Specialists Conference (PVSC)*, Calgary, AB, Canada, 2020, pp. 2547-2550, https://doi.org/10.1109/PVSC45281.2020.9300471

Haghighi,E.B. (2017) Free cooling and indoor humidity level in telecommunication base stations, *2017 IEEE International Telecommunications Energy Conference (INTELEC)*, Broadbeach, QLD, Australia, pp. 80-84,

https://doi.org/10.1109/INTLEC.2017.8211683

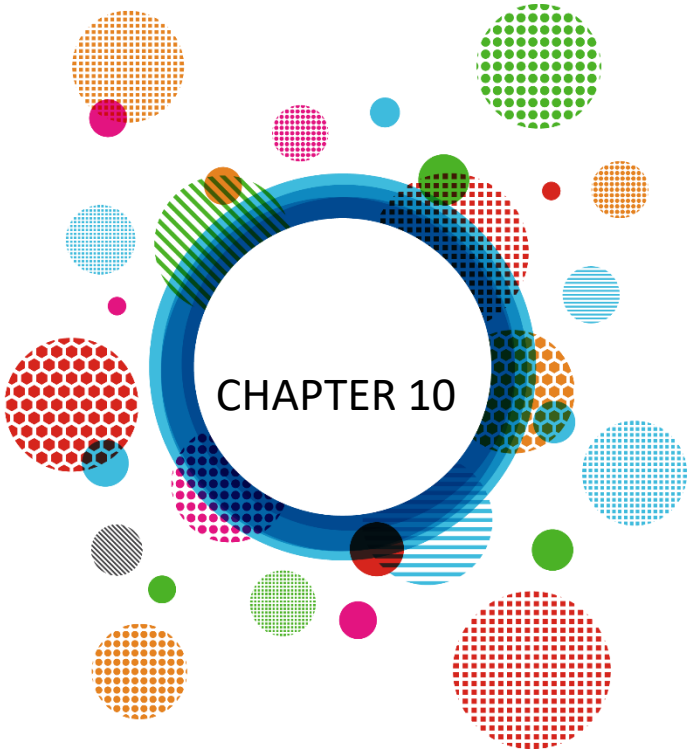

Urbanization, Environmental Issues and Smart Technologies

Gokhan Onder Erguven[1] & Sabit Menteşe[2]

[1] Assoc. Prof. Dr., Munzur University, Faculty of Economics and Administrative Sciences, Department of Urbanization and Environmental Issues, Tunceli, Turkey, Orcid: 0000-0003-1573-080X

[2] Prof. Dr., Munzur University, Faculty of Economics And Administrative Sciences, Department of Policical Science And Public Adminıstratıon, Department of Management Sciences, Tunceli, Turkey, Orcid: 0000-0003-4901-4481

1. Introduction

Addressing environmental challenges requires the involvement of the public and private sectors, non-governmental organizations, and civil society, as well as international cooperation at bilateral, regional, and multilateral levels alongside national efforts.

Irregular and unplanned urbanization poses one of the most critical challenges to sustainable urban development in the 21st century. Particularly in developing nations, the accelerated growth of urban populations frequently exceeds the capacity of municipalities to manage infrastructure, housing, and services. This often leads to the proliferation of informal settlements, environmental degradation, and spatial inequality. Smart cities characterized by the integration of digital technologies into urban systems have emerged as a promising paradigm for addressing these complex urban challenges. This paper investigates how smart city initiatives can be effectively employed to resolve issues stemming from disorganized urban expansion.

Irregular and unplanned urbanization remains a pressing challenge, particularly in rapidly developing countries where infrastructure and governance systems struggle to keep pace with population growth. The emergence of smart city initiatives—defined by the integration of digital technologies into urban governance and services—offers promising solutions. This paper analyzes the causes and consequences of disorganized urban development and presents a strategic framework through which smart city technologies can be deployed to address these challenges. The study draws on global case studies, identifies key enablers and barriers, and offers policy recommendations tailored to the contexts of developing and transitional economies.

Urban scholars have long examined the socio-economic impacts of unplanned urbanization, such as slum formation, poor transportation systems, and inadequate waste management (UN-Habitat, 2020). In parallel, the smart city concept has gained traction, focusing on ICT-driven solutions, sustainable infrastructure, and participatory governance (Batty et al., 2012; Caragliu et al., 2011). While much of the existing literature focuses on smart cities in developed contexts, fewer studies consider their applicability in regions already suffering from chaotic urban sprawl.

Irregular urbanization often results from rapid population growth, migration, and weak planning institutions (Davis, 2006). It manifests in the form of slums, unregulated land use, and overloaded infrastructure systems. Smart cities are defined as urban areas that use information and communication technologies (ICT) to enhance service delivery, sustainability, and citizen participation

(Caragliu et al., 2011). The smart city approach emphasizes efficiency, data-driven management, and innovation.

Urban planning literature frequently attributes irregular growth to weak institutions, insufficient land regulation, and rapid rural-to-urban migration (Davis, 2006). Informal urbanization accounts for over 60% of housing in many African and South Asian cities, with limited access to basic services (UN-Habitat, 2020).

Simultaneously, the smart city discourse has evolved. Early definitions focused heavily on technology (Hollands, 2008), but recent perspectives emphasize inclusivity, governance, and sustainability (Albino et al., 2015). Scholars have started investigating whether smart technologies can be adapted for cities in the Global South—where informality is the norm rather than the exception.

2. The Challenges of Irregular and Unplanned Urbanization

2.1 Spatial Disorganization

Spatial disorganization refers to the fragmentation and inefficiency in the physical structure of urban environments resulting from unplanned and irregular development. It manifests in several interrelated ways that undermine the functionality, accessibility, and sustainability of cities (hang et al., 2015).

Urban Sprawl and Land Misuse

Irregular urbanization often results in horizontal sprawl—the uncontrolled expansion of urban areas into peripheral lands, frequently without consideration of land-use zoning, infrastructure capacity, or ecological sensitivity. This leads to low-density development, inefficient transportation patterns, and the consumption of valuable agricultural or natural land. The lack of a coherent urban growth boundary contributes to the disconnection between residential, commercial, and industrial zones (Wang and Zhu, 2024).

Disconnected and Segregated Neighborhoods

Unplanned urban growth often produces a mosaic of isolated enclaves—formal and informal, affluent and impoverished—without integration through roads, public transport, or services. These disconnected zones not only impede mobility but also reinforce socioeconomic segregation.

Inadequate Infrastructure Alignment

In spatially disorganized cities, infrastructure such as roads, sewage systems, and electrical grids is typically reactive rather than proactive. Since settlements develop before formal planning, the infrastructure is often retrofitted in an ad hoc

and inefficient manner, leading to inconsistent service coverage and higher maintenance costs (Ruiz-Rivas et al., 2023).

Conflict with Environmental Zones

Spatial disorganization frequently results in settlements on environmentally sensitive or hazardous land—floodplains, steep hillsides, or coastal erosion zones—due to the lack of enforced zoning and land regulation. This increases vulnerability to natural disasters and contributes to environmental degradation (Nazir et al., 2025).

2.2 Infrastructure Deficits

Infrastructure deficits are a hallmark of irregular and unplanned urbanization. They refer to the absence, insufficiency, or dysfunction of basic urban services and systems—including water supply, sanitation, electricity, transportation, waste management, and digital connectivity—that are essential for the sustainable functioning of cities. In contexts of informal or disorganized settlement, infrastructure tends to be either completely lacking or delivered in a fragmented, inequitable, and inefficient manner (Yamng and Ma, 2025).

Water and Sanitation Gaps

In unplanned urban areas, formal water distribution networks often do not extend to informal settlements. As a result, residents rely on unsafe water sources such as wells, tankers, or shared community taps, leading to health risks and time poverty—especially for women and children (Azupogo et al., 2025).

-Sanitation infrastructure is often worse.

-Open defecation, informal pit latrines, or poorly constructed septic tanks prevail in many informal zones

-The absence of sewerage systems leads to contamination of groundwater and local waterways.

Transportation and Mobility Constraints

Irregular settlements usually develop without formal roads or transit infrastructure. Narrow, unpaved paths dominate, making it difficult for vehicles especially emergency and waste collection services to access the area.

Public transportation routes often exclude informal areas, creating transport poverty. This limits residents' access to jobs, education, and healthcare (Zhao and Feng, 2024).

Solid Waste Management Failures

Without formal waste collection services, informal areas accumulate garbage in open spaces, drainage channels, or improvised dumping sites. This not only degrades the environment but also increases the risk of flooding and disease transmission (Lakhouit, 2025).

Digital Divide and Connectivity Issues

In the era of smart cities, access to digital infrastructure (internet, mobile networks, smart devices) is essential for inclusion in services such as e-governance, education, banking, and employment.

Yet, informal settlements frequently lack reliable digital connectivity. The digital divide reinforces existing inequalities and limits the participation of marginalized groups in the information economy (Lasisi et al., 2025).

2.3 Environmental Vulnerability

Environmental vulnerability refers to the increased susceptibility of urban areas—and particularly their marginalized populations—to environmental hazards such as floods, landslides, air and water pollution, and climate-related stresses. In the context of irregular and unplanned urbanization, environmental risks are amplified due to the absence of formal planning, poor land management, and the concentration of human settlements in ecologically sensitive or hazardous zones.

Settlement in High-Risk Zones

One of the most visible outcomes of unregulated urban expansion is the encroachment of human settlements onto high-risk areas such as: Riverbanks and floodplains, Steep hillsides prone to landslides, Coastal zones affected by sea-level rise, Former wetlands or drainage basins (Sainté and Lämmle, 2025).

These areas are typically undesirable or restricted for legal development, but due to housing shortages and land market exclusion, they are often occupied informally. The lack of protective infrastructure (e.g., retaining walls, flood barriers) and early warning systems makes these communities especially vulnerable.

Degraded Urban Ecosystems

Irregular development often involves the destruction of natural ecosystems within and around cities. Forests, wetlands, and green belts are cleared for informal housing, reducing urban ecological resilience. As vegetation is removed, natural stormwater absorption declines, increasing the likelihood of flooding and soil erosion. Additionally, informal settlements typically lack green infrastructure (e.g., parks, urban forests), which could mitigate urban heat islands, improve air quality, and provide recreational space (Aguilera and González, 2023).

Air and Water Pollution

In many informal urban areas, waste is burned openly due to the absence of waste collection services, leading to localized air pollution. Unregulated industrial activities within or near informal zones may release harmful chemicals into the air and groundwater. The lack of proper sanitation facilities leads to contamination of nearby water bodies, which further compromises water quality and spreads disease (Latiza et al., 2025).

Climate Vulnerability and Urban Heat Islands

Poorly planned cities with extensive concrete coverage and minimal tree canopy experience stronger urban heat island effects. Informal settlements, often built with low-quality materials and minimal ventilation, become unbearably hot during heatwaves, disproportionately affecting vulnerable populations such as the elderly, children, and those with chronic illnesses. Climate change further exacerbates existing environmental vulnerabilities by intensifying rainfall patterns, increasing storm frequency, and accelerating temperature rise all of which hit the most fragile urban zones hardest (Melis et al., 2023).

Lack of Environmental Governance

Informal settlements typically fall outside the scope of formal environmental management. Environmental impact assessments, zoning regulations, and mitigation strategies rarely apply to these zones. As a result, no entity is formally responsible for managing or reducing their environmental risks (Stærfeldt and Stacey, 2025).

3. Smart City Solutions: Conceptual and Practical Approaches

Digital Urban Mapping & Spatial Intelligence

Advanced mapping tools such as remote sensing and drones can quickly identify informal developments, track urban sprawl in real time, and integrate these areas into official planning frameworks. Example: India's Smart Cities Mission uses GIS-based master plans to bring slums into formal service zones.

Digital Urban Mapping and Spatial Intelligence refer to the use of geospatial technologies and data analytics to understand, plan, and manage urban environments more effectively. These tools provide city planners, policymakers, and citizens with high-resolution insights into the physical, social, and infrastructural dimensions of cities—especially in contexts where traditional data is limited or outdated, such as in informal and irregularly developed areas (Huang et al., 2025).

Digital urban mapping and spatial intelligence are foundational components of smart city strategies aimed at correcting the spatial disorganization caused by

irregular urbanization. By turning cities into data-rich, analyzable ecosystems, these tools enable more targeted, efficient, and inclusive planning. When applied with transparency and community involvement, they can bridge the gap between the formal and informal city, transforming fragmented urban spaces into integrated, resilient, and livable environments (Li, 2024).

Mapping Informal Settlements

Irregular settlements are often invisible in official urban records. Digital mapping helps make the invisible visible by capturing their precise locations, boundaries, densities, and physical conditions. This facilitates: Inclusion of informal areas in infrastructure and service planning, Recognition for land tenure regularization, Risk mapping (flood zones, fire hazards, etc.) (Da silva et al., 2024)

Disaster Preparedness and Climate Resilience

Spatial intelligence supports the modeling of environmental hazards and population vulnerability. Smart cities use these tools to: Create flood and landslide risk maps, Simulate evacuation scenarios, Plan early warning systems and emergency routes, Map heat islands and propose cooling interventions (e.g., tree planting)

4. IoT for Utility Monitoring and Optimization

The Internet of Things (IoT) refers to a network of interconnected devices embedded with sensors, software, and data-processing capabilities that enable them to collect, transmit, and act on information in real time. In the context of smart urban development, IoT plays a pivotal role in monitoring and optimizing urban utilities such as water, electricity, waste, and transportation areas that are critically deficient in irregular and poorly planned urban environments (Dhungana et al., 2025).

Waste Management and Sanitation Monitoring

IoT applications in waste systems include: Smart bins with fill-level sensors that alert collection services, route optimization for garbage trucks using GPS and volume data, Monitoring septic tanks and latrines for overflow or contamination risk, leak detection in sewer systems (Asgedom and Redae, 2024).

Energy Optimization in Public Infrastructure

IoT is used to improve the energy efficiency of urban systems: Smart street lighting: Lights adjust automatically based on motion or time, reducing energy costs,

Public buildings: Sensors monitor occupancy and temperature, automating HVAC systems,

Microgrids: IoT allows for decentralized solar and battery networks, especially valuable in settlements off the main grid (Morabi et al., 2024).

AI and Predictive Analytics for Urban Management

Artificial Intelligence (AI) and Predictive Analytics represent some of the most powerful tools within the smart city framework, especially in addressing the challenges posed by irregular, unplanned, and chaotic urban development. These technologies leverage historical and real-time data to detect patterns, model future outcomes, and support proactive decision-making in urban planning, infrastructure, housing, transportation, and risk management.4.5 Urban Data Integration and Interoperability (Lakhouit, 2025).

Smart cities require integrated data ecosystems. By linking land registries, tax data, and utility maps, cities can better manage informal areas, improve tax collection, and plan services more efficiently.

Disaster Risk Modeling and Early Warning Systems

Predictive analytics is increasingly used to anticipate urban disasters, especially in areas vulnerable due to unplanned growth: Flood forecasting using rainfall and terrain data, landslide prediction based on soil and slope conditions, urban heat island modeling during heatwaves, public health alerts based on waste and water conditions (Liu et al., 2025).

Traffic Flow Optimization and Mobility Planning

By analyzing mobility data from GPS, mobile phones, and transit systems, AI can: Predict congestion hotspots, suggest alternative routes dynamically, model future traffic based on housing or employment changes, identify mobility gaps in low-income or irregular zones (Ding et al., 2025).

5. Conclusion

Irregular and unplanned urbanization continues to hinder sustainable development in many regions. However, the smart city model provides a holistic framework that can transform urban chaos into opportunity. By leveraging data, technology, and participatory governance, cities can build resilience against the systemic issues posed by unregulated growth. Future research should focus on context-specific smart solutions and inclusive urban transformation strategies, particularly in low- and middle-income countries.

This study has shown that while irregular and unplanned urbanization presents deep-rooted structural challenges, smart city frameworks offer viable and

innovative responses. By leveraging technology for inclusive governance, spatial intelligence, and real-time monitoring, cities can overcome fragmentation and improve urban resilience. However, technology alone is not sufficient. Equitable policy, social inclusion, and institutional reform must accompany the transition toward smarter cities.

Infrastructure deficits severely undermine the well-being, productivity, and resilience of residents in unplanned urban areas. These deficits are not merely technical issues but deeply political, tied to questions of inclusion, citizenship, and rights to the city.

Smart city Technologies such as real-time utility monitoring, mobile-based reporting platforms, decentralized sanitation systems, and solar microgrids offer scalable solutions. However, without intentional efforts to include informal areas in urban planning and budgeting processes, such innovations risk reproducing existing inequalities.

Smart cities offer tools that can help mitigate environmental risks through:

Real-time environmental monitoring: Air and water quality sensors can identify health risks early, predictive analytics: AI models can forecast floods or landslides, allowing for early evacuation, participatory mapping: Residents can use mobile apps to map hazards in their neighborhoods, nature-based solutions. Digital tools can support the planning of green infrastructure in informal areas.

However, these tools must be inclusive, low-cost, and locally adaptable to benefit the most vulnerable. AI and predictive analytics offer a powerful opportunity to shift from reactive to anticipatory urban governance, particularly in cities burdened by disorganized growth. By identifying trends before they become crises, cities can allocate resources more strategically, protect vulnerable populations, and design more resilient and inclusive urban systems. However, these technologies must be implemented with attention to equity, transparency, and public trust to fulfill their transformative potential.

References

Aguilera, M.A., González, M.G. Urban infrastructure expansion and artificial light pollution degrade coastal ecosystems, increasing natural-to-urban structural connectivity, Landscape and Urban Planning, 229, 2023, 104609.

Albino, V., Berardi, U., & Dangelico, R. M. (2015). Smart cities: Definitions, dimensions, performance, and initiatives. Journal of Urban Technology, 22(1), 3–21.

Asgedom, A.A., Redae, G.H. Water, sanitation, hygiene, and waste management in primary healthcare facilities in war-torn Tigray, Ethiopia: implications for infection prevention and control, Infection Prevention in Practice, 6, 4, 2024, 100397.

Azupogo, U.W., Dassah, E., Bisung, E. Navigating water and sanitation environments in schools: Exploring health risk perceptions of children with physical disabilities using drawing, Wellbeing, Space and Society, 8, 2025,

Caragliu, A., Del Bo, C., & Nijkamp, P. (2011). Smart cities in Europe. Journal of Urban Technology, 18(2),

da Silva, A.A., da Silva, J.F.K., Westerholt, R. Mapping the margins: A systematic scoping review of the impact of digital mapping on public participation in informal settlements, Habitat International, 147, 2024.

Davis, M. (2006). Planet of Slums. Verso.

Dhungana, N., Upadhaya, S., Bishwakarma, M.B., Khadka, C., Bhattarai, H.K., Lee, C.H. Building resilience in communities through integrating climate change adaptation and disaster risk reduction policies in Nepal, Land Use Policy, 150, 2025, 107471.

Ding, H., Zhao, Z., Wang, S., Zhang, Y., Zheng, X., Lu, X. Quantifying the impact of built environment on traffic congestion: A nonlinear analysis and optimization strategy for sustainable urban planning, Sustainable Cities and Society, 122, 2025, 106249.

Hollands, R. G. (2008). Will the real smart city please stand up? City, 12(3), 303–320.

Huang, J., Bibri, S.E., Keel, P. Generative spatial artificial intelligence for sustainable smart cities: A pioneering large flow model for urban digital twin, Environmental Science and Ecotechnology, 24, 2025, 100526.

Lakhouit, A. Revolutionizing urban solid waste management with AI and IoT: A review of smart solutions for waste collection, sorting, and recycling, Results in Engineering, Volume 25, 2025, 104018,

Lasisi, M. Ogunsina, O.A. Globalization and the Digital Divide, Editor(s): David Baker, Lucy Ellis, Encyclopedia of Libraries, Librarianship, and Information Science (First Edition), Academic Press, 2025, 225-232,

Latiza, R.J.P., Olay, J., Eguico, C., Yan, R.J., Rubi, R.V. (2025). Environmental applications of carbon dots: Addressing microplastics, air and water pollution, Journal of Hazardous Materials Advances, 17, 2025, 100591.

Li, M. Design and Optimization of Urban Spatial Environment Based on Digital Intelligent VR Technology, Procedia Computer Science, 243, 2024, 758-765,

Liu, C., Wang, E., Li, Z., Zang, Z., Li, B., Yin, S., Zhang, C., Liu, Y., Wang, J. Research on multi-factor adaptive integrated early warning method for coal mine disaster risks based on multi-task learning, Reliability Engineering & System Safety, 260, 2025, 111002.

Melis, G., Gangi, E.D., Ellena, M., Zengarini, N., Ricciardi, G., Mercogliano, P., Costa, G. Urban Heat Island effect and social vulnerability in Turin: Prioritizing climate change mitigation action with an equity perspective, Science Talks, 8, 2023, 100258.

Moradi, M.H., Widmer, F., Turin, R.C., Onder, C.H. Optimization of charging infrastructure and strategy for an electrified public transportation system, Energy, 313, 2024, 133974.

Nazir M., Khan I., Shah S.A.M., Islam T., Azam K., Naseem I., Zaman K. From conflict to a climate future: Unraveling the nexus between warfare and environmental degradation, Sustainable Futures, 9, 2025, 100525

Ruiz-Rivas, U., Tirado-Herrero S., Castaño-Rosa R., Martínez-Crespo J. Disconnected, yet in the spotlight: Emergency research on extreme energy poverty in the Cañada Real informal settlement, Spain. Energy Research & Social Science, 102, 2023, 103182

Sainté, G., Lämmle, L. Environmental, political, and social crises: The context of territorial vulnerability in Haiti Republic, Social Sciences & Humanities Open, 11, 2025, 101461.

Stærfeldt, L.K., Stacey, P.A. Environmental governance and political contestation in contexts of illegal small-scale gold mining in Ghana, Geoforum, 160, 2025, 104221.

Thi Hang, H., Alshayeb, M.J. Technological innovations in urbanization and land surface temperature analysis: A remote sensing and machine learning case study of Delhi, Environmental Technology & Innovation, 38, 2025, 104164.

UN-Habitat. (2020). World Cities Report 2020: The Value of Sustainable Urbanization.

Wang Z., Zhu C. Does urban sprawl lead to carbon emission growth? Empirical evidence based on the perspective of local land transfer in China, Journal of Cleaner Production, 455, 2024, 142319

Yang, Y., Ma Q. From deficit to balance: Identifying blue-green infrastructure networks based on trade-offs and synergies between water and terrestrial ecosystem services in a water sensitive region, Ecohydrology & Hydrobiology, 2025, 100656.

Zhao, Y., Feng, T. Strategic integration of vertiport planning in multimodal transportation for urban air mobility: A case study in Beijing, China, Journal of Cleaner Production, 467, 2024, 142988.

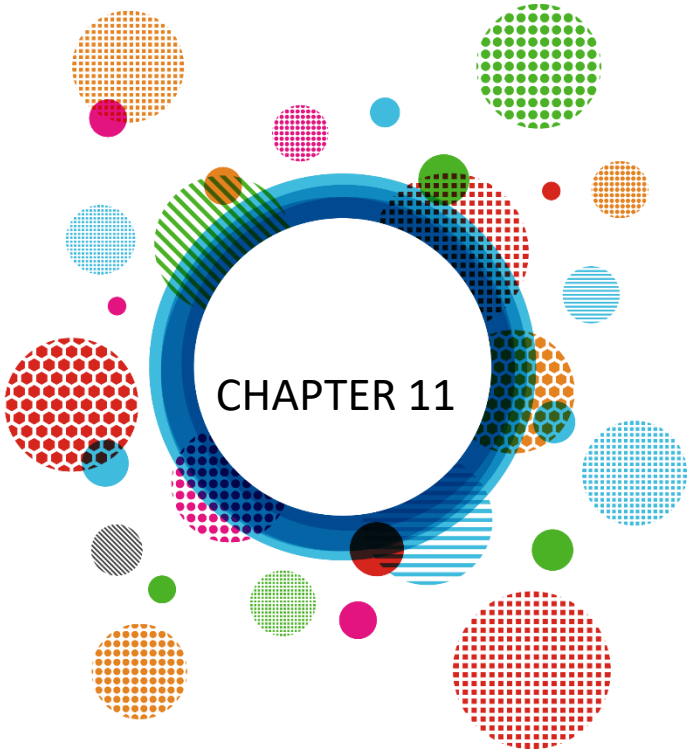

Coating Materials for Enhancing Performance of Cold Work Steel Tools

Cemile Kayış[1] & Ege Anıl Diler[2] & Hatice Sandallı[3] & Fuat Can Ağarer[4]

[1] Res. Asst., Eskisehir Technical University, Department of Mechanical Engineering, Eskişehir, Turkey, ORCID: 0000-0002-4401-2412
[2] Assoc. Prof. Dr., Ege University, Department of Mechanical Engineering, Izmir, Turkey, ORCID: 0000-0002-1667-5737
[3] MSc. Norm Fasteners Co., Izmir, Turkey, ORCID: 0000-0002-5550-8480
[4] B.Eng., Norm Fasteners Co., Izmir, Turkey, ORCID: 0000-0001-7219-7592

1. Introduction

In cold forming operations, tooling is subjected to significant loads, particularly at high deformation rates, leading to tool damage over time and eventual failure. This tool degradation not only necessitates tool replacement but also causes production halts, machine recalibration for new tools, and the scrapping of some produced parts (Dubar et al., 2005). The lifespan of tools fundamentally dictates manufacturing efficiency. A machine capable of producing 155 units per minute might only deliver 137 due to persistent tool failures (Raja and Sornakumar, 2014). This discrepancy highlights more than just lost output; it points to a critical cost centre. With specialized tools like forming punches making up a considerable part of the cost for each component, investing in their longevity becomes paramount for both maximizing throughput and controlling unit costs.

For the cold forming punches, punch life is determined by the initiation and progression of three primary mechanisms: plastic deformation, wear, and fracture. Consequently, the punch material must exhibit a combination of high strength, superior wear resistance, high hardness, a low coefficient of friction, and excellent toughness (Almeida et al., 2017).

Forming punches are typically manufactured from high-speed tool steels, which provide the necessary high toughness to withstand impact loads. However, to further enhance their strength and hardness, these tools often undergo various surface treatments. While heat treatments are sometimes preferred, ceramic coatings applied to the tool steels are more commonly employed (Ashvita et al., 2024; Wand et al., 2025).

Ceramic materials impart high hardness and strength to the punch, while the steel substrate ensures that the punch retains its tough behaviour. Over time, numerous coating materials have been explored and developed to optimally achieve these desired properties.

Coating technology has advanced significantly to meet evolving industrial demands, leading to increasingly complex structures. Historically, this development can be categorized into four distinct periods. The first period saw the widespread adoption of simple single-layer ceramic coatings, with TiN coatings serving as a prime example. Despite being positioned as early developments, these types of coatings remain prevalent in the industry today; indeed, the present study aims to enhance the lifespan of punches currently utilizing TiN coatings. The second period of development commenced with the chemical modification of single-layer films. TiAlN coatings exemplify this stage,

where modifications successfully led to improvements in various properties. For instance, the example provided demonstrates significant advancements for processes conducted at high temperatures. The third and fourth periods in coating material technology are, in a sense, intertwined. The third stage involved the development of multi-layered coatings, achieved by sequentially depositing layers of different materials. This approach not only leverages the properties of the two distinct materials used in the layers but also benefits from the resulting layer interfaces, which play a crucial role in enhancing structural properties. The fourth development period, representing what can be considered state-of-the-art coatings today, encompasses multi-layered coatings fabricated at the nanoscale. In some structures, nanocomposite coatings are also observed, where nanocrystalline particles are dispersed within a three-dimensional amorphous matrix. For multi-layered coatings, the TiN/CrN system serves as an illustrative example.

Therefore, the subsequent sections of this chapter investigate the essential contribution of ceramic coatings to improving the performance of cold work steel tools, such as AISI M2, in various manufacturing environments.

2. Ceramic Coatings

This section will introduce the various types of ceramic coatings commonly applied to cold work tool steels, detailing their deposition methods and the particular advantages they offer in a multitude of manufacturing applications.

2.1. TiN Coating

Titanium stands out for its exceptional ability to adhere to steel substrates. Nitrogen, conversely, is well-known as a frequently utilized element in surface hardening processes. The combination of these two elements forms a ceramic coating with remarkably high hardness and sufficient adhesion to steel substrates. Consequently, TiN coatings remain among the oldest (Hilton et al. 1987; Hug et al., 1997) and one of the most widely used coating materials for high-speed tool steels, such as AISI M2 steel, today (Cerıtbınmez et al., 2025).

TiN coatings are applied to steel substrates using a wide array of deposition techniques, such as physical vapour deposition (PVD) and chemical vapour deposition (CVD). In a study by M. Dubar et al. (2005), the coating thickness, hardness, and coefficient of friction were reported for AISI M2 steel tools that had been TiN coated using both PVD and CVD methods. It was observed that the coefficient of friction was higher on surfaces coated via PVD. This was attributed to the thinner coating thickness achieved with the PVD method, which meant that residual surface scratch marks from manufacturing stages were not fully concealed. Conversely, with the CVD method, these marks were covered, and the

coated surface appeared to be uniformly covered with small spherical particles. Figure 1 presents SEM images of as-coated PVD and CVD TiN surfaces.

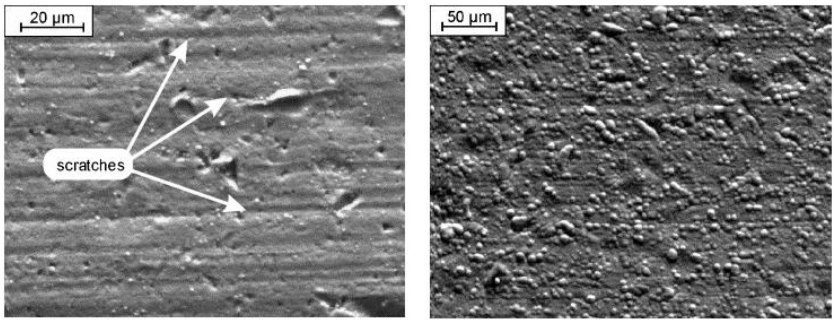

Figure 1. Surface aspect of TiN coating produced via (a) PVD and (b) CVD (Dubar et al., 2005)

The inability to achieve stabilization in the coefficient of friction after a certain number of manufactured parts stems from localized micro-welding. This welding occurs both between the workpiece and the tool, and between the tool surface and the coating surface. In PVD coatings, this welding progresses more rapidly due to the presence of scratches very close to the surface. Conversely, in CVD coatings, the main material adheres to the spherical particles of the coating at a later stage. Consequently, CVD coatings delay the friction distribution compared to PVD coatings. However, hardness values for both methods can be comparable (Dubar et al., 2005).

Nevertheless, other studies present differing observations. For example, a study by Hilton et al. (1987) found that TiN coatings produced via PVD exhibited higher hardness than PACVD coatings of equivalent thickness. Additionally, the grain size of PACVD-produced TiN coatings was determined to be 2500 Å, whereas the grain size from the sputtering method was measured at 500 Å. This disparity is likely attributable to differences in grain sizes resulting from the distinct production methods. These findings collectively indicate that the microstructure and, consequently, properties such as hardness, of TiN coatings can vary significantly depending on the specific production method employed.

When comparing TiN, Diamond-Like Carbon (DLC), and CrCN coatings applied to AISI M2 steel forming tools using the PVD method, TiN demonstrates a significant advantage. As illustrated in Figure 2, TiN emerges as a more favourable choice when considering both cost-effectiveness and service life compared to the other two coating types (Yousefi et al., 2021).

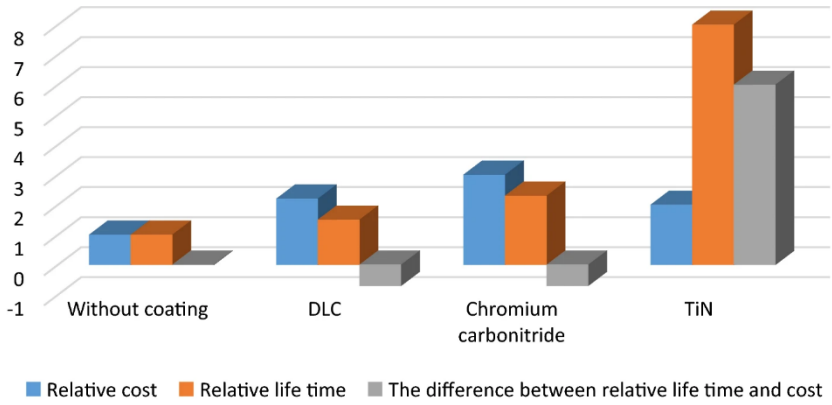

Figure 2. Relative criteria for DLC, CrCN, and TiN coatings (Yousefi et al., 2021)

It's feasible to considerably boost the hardness, wear resistance, and elastic modulus of TiN coatings, which are applied to AISI M2 high-speed steel using the PVD method, through the application of post-coating processes like Deep Cryogenic Treatment (DCT). These subsequent treatments enable a significant enhancement of the mechanical properties of the coating (Chiadikobi et al., 2024). It results from fundamental changes happening within the microstructure of the material. One key effect, especially in materials where it is present, is the nearly complete transformation of retained austenite to martensite. While TiN itself is not a steel, the substrate or interface layers might contain phases influenced by cryogenic temperatures. A more fully martensitic structure is inherently harder and more brittle, contributing to improved hardness and wear resistance. Cryogenic temperatures promote the precipitation of extremely fine, uniformly dispersed carbides or nitrides. Even in a coating like TiN, which is already a nitride, subtle atomic rearrangements and the formation of secondary, very fine phases can occur. These tiny precipitates act as obstacles to dislocation movement, significantly hardening the material and boosting its resistance to plastic deformation, which directly translates to better wear performance. DCT can help in redistributing and relieving some of the residual stresses within the coating. While PVD coatings often have beneficial compressive stresses, localized tensile stresses or non-uniform stress distributions can be detrimental. A more uniform and optimized stress state can lead to a more stable and mechanically robust coating. The extreme cold can subtly refine the atomic structure and improve the bonding between atoms. This can lead to a more compact and ordered lattice, which in turn increases the material's resistance to elastic deformation (higher elastic modulus) and makes it tougher against wear.

While more advanced methods and coating materials now exist for enhancing the wear resistance of AISI M2 high-speed tool steels beyond conventional PVD TiN, this combination retains its practical significance. The enduring appeal of

PVD-applied TiN stems from its cost-effectiveness and the ability to significantly improve its tribological performance and elastic modulus through post-coating treatments like Deep Cryogenic Treatment (DCT). This makes TiN a continuously viable and often preferred coating option for various industrial applications.

As a result, despite the emergence of newer advanced coatings, TiN remains a widely utilized and practical choice for enhancing the performance of high-speed tool steels due to its inherent hardness, sufficient adhesion, cost-effectiveness, and the notable improvements in tribological properties achievable through post-coating treatments like DCT.

2.2. DLC Coating

Another coating employed for AISI M2 steel tools is Diamond-Like Carbon (DLC). DLC coatings are amorphous films formed by arranging carbon atoms in a diamond-like structure. Primarily produced via PACVD or CVD from hydrocarbon gas sources, their classification depends on how closely their carbon arrangement resembles diamond and their hydrogen content. Hardness increases with a higher proportion of sp^3 hybridization and lower hydrogen content (Zerrin, 2014). DLC films develop significant internal stresses from their internal network structures, which accumulate as film thickness increases. This makes adhesion to the substrate challenging; DLC films over a particular thickness often delaminate. Poor adhesion can also stem from delayed DLC nucleation due to carbon diffusion into the steel. To counter this and enhance wear resistance by creating a hardness gradient, an interlayer is used as a mechanical buffer, improving DLC substrate adhesion.

Figure 3 shows the DLC coating deposited to AISI M2 steel. To promote adhesion to the surface of the M2 subtsrate, a Cr layer is used between the DLC coating and the steel substrate (Figure 3). As depicted in Figure 4, among the various coatings, DLC, TiN, TiAlN, and TiCN-deposited on a steel substrate, the lowest coefficient of friction is observed when utilizing the DLC coating (Banerji et al., 2014).

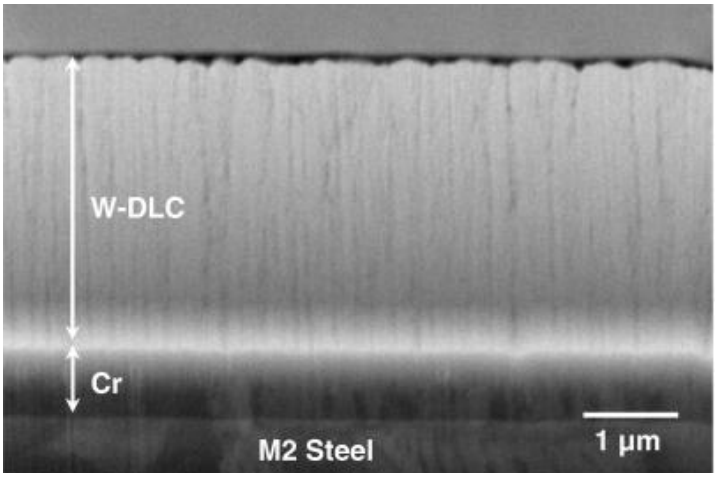

Figure 3. SEM image revealing the sequential deposition of a Cr interlayer and a subsequent W-DLC layer on an M2 steel substrate (Banerji et al., 2014)

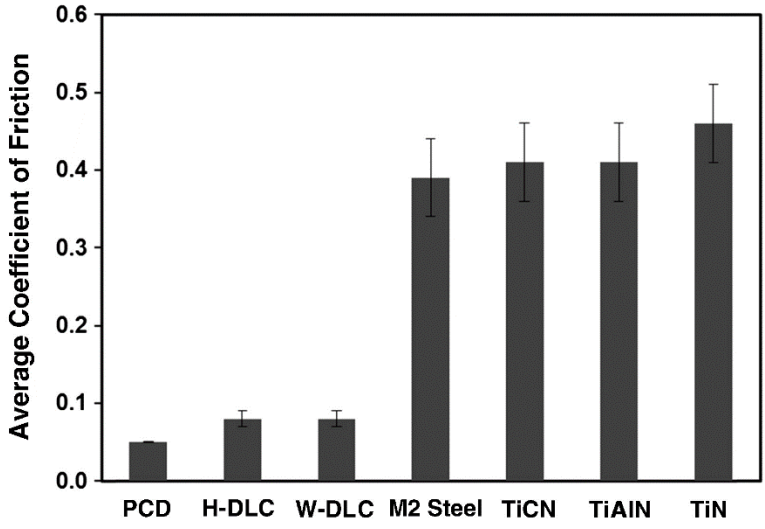

Figure 4. Comparison of coefficient of friction of M2 steel and DLC, TiN, TiAlN, and TiCN coatings (Banerji et al., 2014)

A lower coefficient of friction directly translates to less abrasive and adhesive wear between contacting surfaces. This significantly reduces material loss and surface degradation on both the coated component and any counter-surface it interacts with. Consequently, the service life of tools and components is substantially extended, leading to decreased replacement costs and reduced downtime. Less friction means less energy is dissipated as heat during relative motion. By minimizing friction, DLC coatings help to keep operating temperatures lower, thereby preserving the mechanical properties of the

underlying substrate and coating, especially under high-load or high-speed conditions. In dry or minimally lubricated environments, metal-on-metal contact can lead to material transfer, a phenomenon known as galling, and eventually seizure, where components weld together. The extremely low friction and non-stick properties of DLC coatings effectively prevent these issues, ensuring smooth and reliable operation even under challenging conditions. Smoother, lower-friction interfaces contribute to a reduction in noise and vibration during operation. This can lead to quieter machinery and a higher quality of manufactured products, particularly in forming and moulding applications where surface finish is critical.

To enhance the performance of DLC coatings, the surfaces of M2 steel substrates are subjected to a nitriding treatment to establish superior adhesion between the coating and the substrate. As shown in Figure 5, the application of a nitride interlayer effectively creates a hardness gradient on the steel substrate. This gradient significantly improves the adhesion of the harder top DLC layer (Moreno-Bárcenas et al., 2019).

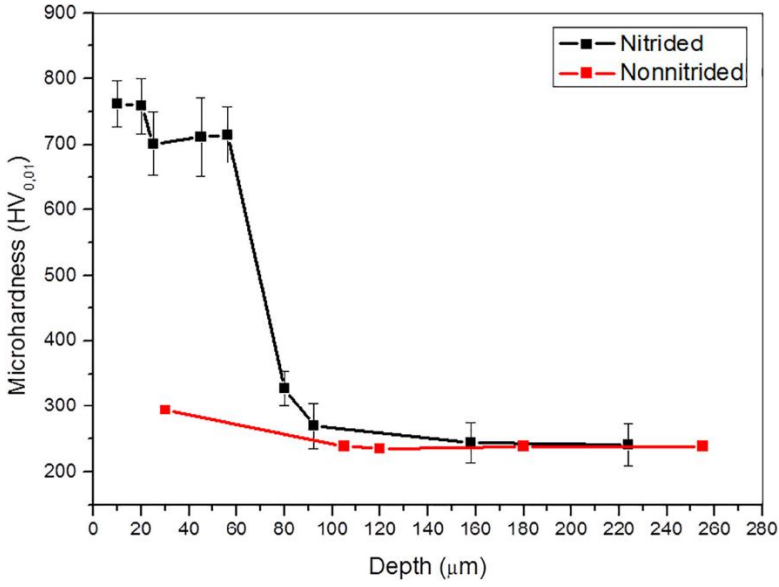

Figure 5. Microhardness of nitrided and non-nitrided M2 steel substrates (Moreno-Bárcenas et al., 2019)

Figures 6(a) and (b) present critical loads from scratch tests for DLC coatings, without and with a nitride interlayer respectively, deposited at various electrical powers. For all deposition powers, DLC coatings with an interlayer consistently withstand greater loads than those without. The presence of an interlayer substantially enhances the adhesion of the coating to the substrate.

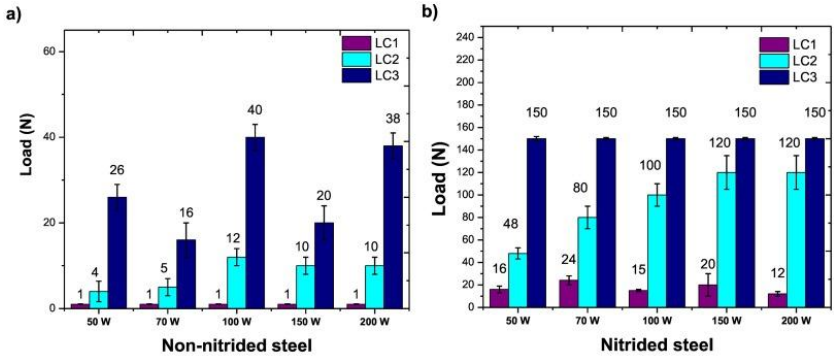

Figure 6. Load of the DLC coatings on the (a) non-nitrided and (b) nitrided M2 steel (LC: the maximum load-bearing capacity (the coating begins to peel from the substrate)), (LC1: the load causing cohesive failure, LC2: the load causing adhesive failure) (Moreno-Bárcenas et al., 2019)

Wang et al. (2021) investigated the adhesion capabilities of DLC coatings on M2 steel substrates, using titanium as an interlayer and comparing it against other parameters. They focused on the interface between the M2 steel (Fe layer) and the Ti interlayer, as well as the interface between the Ti interlayer and the DLC (C layer). For comparison, they also included a coating sample without an interlayer, directly examining the Fe and C layer interface. As anticipated, a higher energy requirement to separate two layers indicates stronger adhesion between them. The required energy for separation was ordered as follows: Ti/C > Fe/Ti > Fe/C. This suggests that the adhesion between the iron and carbon layers is the weakest. Furthermore, interfacial energy serves as a reliable index for assessing the adhesion ability of layers. Structures with a positive interfacial energy value between two layers are unstable, indicating a tendency to separate. Conversely, as the interfacial energy decreases, the stability and adhesion capabilities of the layers increase. Accordingly, the Fe/C structure exhibits the lowest adhesion, while the Ti/C structure possesses the highest.

Consequently, DLC coatings offer exceptional tribological benefits for AISI M2 steel tools, particularly their remarkably low friction coefficient, with their critical challenge of adhesion effectively addressed and optimized through the strategic use of interlayers such as chromium, titanium, or nitride.

2.3. CrAlN Coating

The CrN structure is primarily distinguished by its corrosion resistance, largely due to the presence of chromium. Its superior wear and hardness properties are also key reasons for its widespread use as a tool coating material (Navinšek et al. 2017).

CrAlN coatings generally offer better tribological performance than CrN due to the addition of aluminium, which fundamentally changes the structure and behaviour of the coating. Aluminium promotes a more compact, nanocrystalline structure in CrAlN. This makes the coating harder and more resistant to cracks, as well as less porous, improving wear and corrosion resistance. Aluminium atoms substitute for chromium, creating lattice distortions that block dislocation movement. This significantly boosts the hardness of the coating, directly improving wear resistance (Lin et al, 2024). At elevated temperatures, aluminium forms a stable, self-lubricating aluminium oxide layer on the surface. This protective film enhances oxidation resistance, reduces friction, and maintains the integrity of the coating under heat, unlike the less robust oxides formed by CrN. The better oxidation resistance helps CrAlN retain its hardness and strength at higher temperatures, making it suitable for more demanding, high-heat applications (Polcar and Cavaleiro, 2011).

When CrN and CrAlN coatings are applied to AISI M2 steel using the PVD method, different processing parameters yield coatings with varied properties (Brizuela et al., 2005). As aluminium is added to the coating, its adhesion to the steel substrate tends to decrease. However, CrAlN coatings exhibit a lower coefficient of friction than CrN coatings.

The properties of the CrAlN structure vary with its aluminium content. Figure 7 illustrates the wear rates and coefficients of friction for CrAlN coatings with differing aluminium concentrations at various temperatures. Higher aluminium content generally leads to an increase in the friction coefficient. For instance, the coating with the highest aluminium concentration (CrAlN-3) consistently exhibits the highest friction values across all testing temperatures. This is primarily attributed to the increased formation of aluminium oxides (Al_2O_3) on the surface, which are inherently more abrasive and contribute to higher friction. Conversely, a greater aluminium presence significantly improves the wear resistance, resulting in lower wear rates. The same high-aluminium CrAlN-3 specimen, despite its higher friction, showed virtually no measurable wear at temperatures below 650°C. This enhanced durability is linked to the increased hardness imparted by the higher aluminium content, along with the protective nature of the aluminium oxides formed, which help the coating resist material loss even under demanding conditions (Sánchez-López et al., 2014).

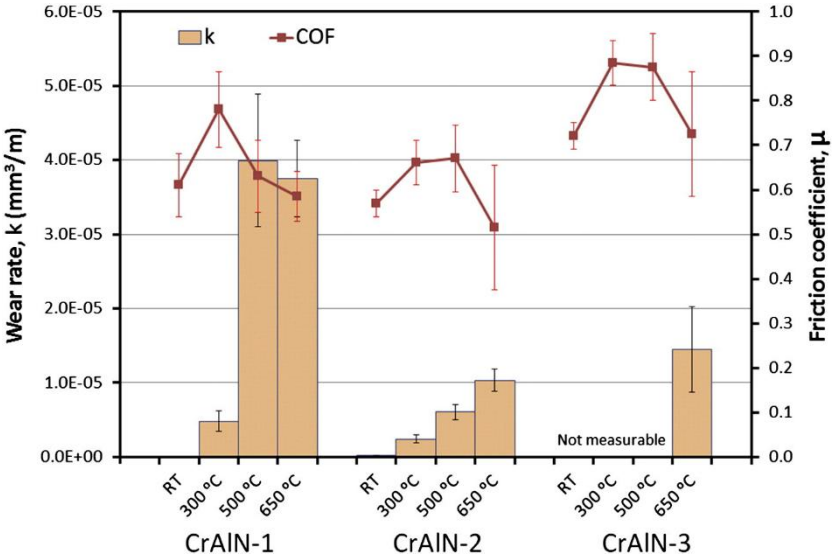

Figure 7. Tribological properties of CrAlN coatings (CrAlN-1: Al/(Cr+Al)=0.19, CrAlN-2: Al/(Cr+Al)=0.50, and CrAlN-3: Al/(Cr+Al)=0.68) (Sánchez-López et al., 2014)

When coating M2 high-speed steels with CrAlN via PVD, the plasma nitriding process applied to the M2 substrate, along with its specific parameters, significantly influences the overall performance of the coating. For instance, increasing the anode current during the nitriding treatment leads to a thicker nitrided layer. Consequently, as shown in Figure 8, both the application of plasma nitriding and an increased anode current enhance hardness, which in turn reduces the wear rate. The enhanced wear resistance and increased hardness observed in the CrAlN coatings are primarily attributed to the duplex treatment, specifically the plasma nitriding pretreatment at higher ion current densities. This process effectively creates a harder and thicker nitrided interlayer on the steel substrate. This interlayer, in turn, provides superior load-carrying capacity and significantly improves the adhesion of the subsequent CrAlN coating, collectively leading to the observed advancements in mechanical properties (Zhang et al., 2022).

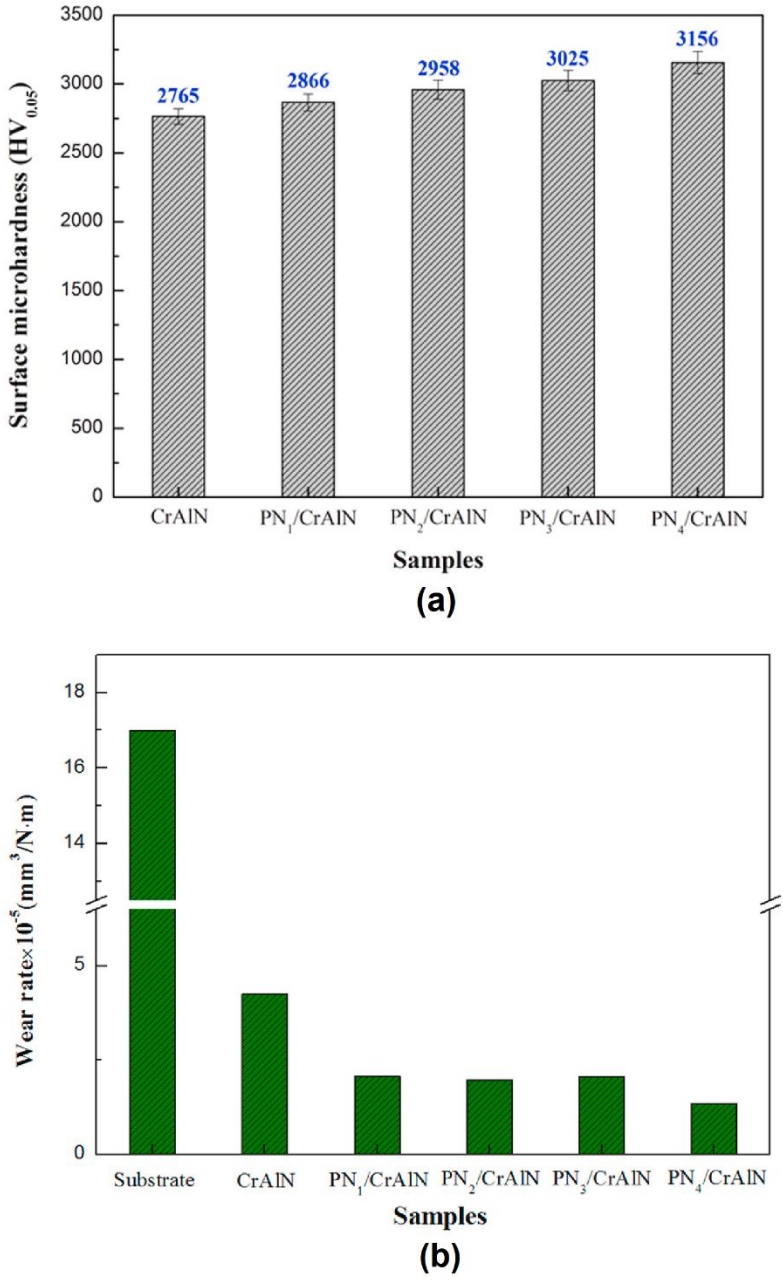

Figure 8. Effect of plasma nitriding and process parameter (anode current) on (a) hardness and (b) wear resistance of CrAlN coated-AISI M2 steel (Zhang et al., 2022)

Ultimately, CrAlN coatings present a highly effective solution for enhancing tool performance, with their superior tribological properties at elevated temperatures and improved wear resistance on steel substrates being finely tunable through precise control of aluminium content and judicious application of duplex treatments like plasma nitriding.

2.4. TiN/TiAlN Coating

Multilayer coatings are increasingly popular due to their extended lifespan and superior wear resistance. Building on this, researches have explored the properties of TiN/(TiAlN) coatings, which combine the traditional, well-performing TiN layer with an Al-modified TiAlN layer to enhance oxidation resistance. Figure 9 shows the $Ti_{0.45}Al_{0.55}N$ monolithic coating and $Ti_{0.45}Al_{0.55}N/Ti_{0.45}Al_{0.55}$ multilayer coating. For the $Ti_{0.45}Al_{0.55}N/Ti_{0.45}Al_{0.55}$ multilayer coating, the layer thicknesses shown in Figure 9(c) are lower than those presented in Figure 9(b). As seen in these figures, the monolithic coating clearly exhibits a columnar structure, whereas the $Ti_{0.45}Al_{0.55}N$ layers within the multilayers are characterized by a dense morphology, lacking distinct columnar grains (Shugurov and Kazachenok, 2018).

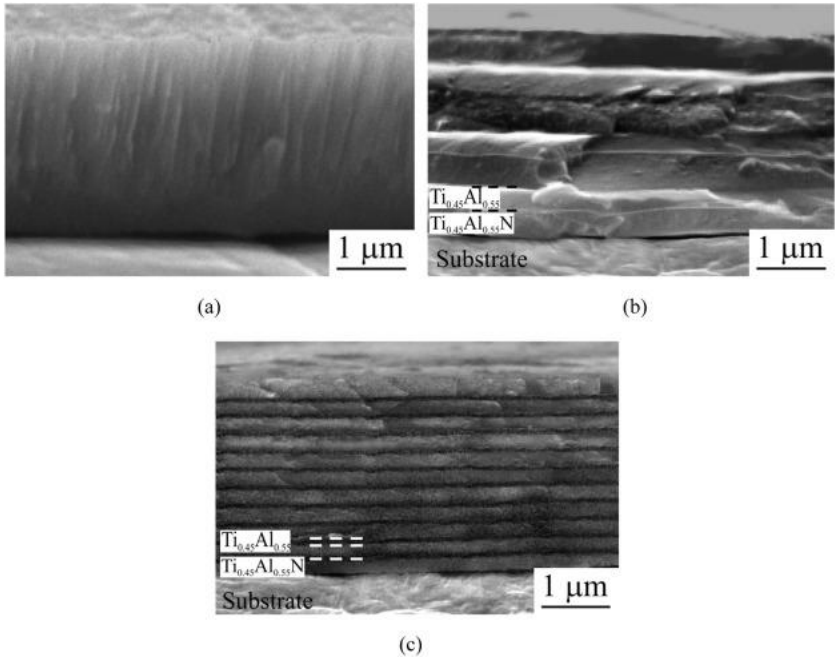

Figure 9. Cross-sectional SEM images of (a) monolithic $Ti_{0.45}Al_{0.55}N$ coating and (b) and (c) $Ti_{0.45}Al_{0.55}N/Ti_{0.45}Al_{0.55}$ multilayers coatings (Shugurov and Kazachenok, 2018)

For AISI M2 steel, investigations typically compare the characteristics of single-layer TiN coatings, single-layer TiAlN coatings, and multilayer TiN/(TiAlN) coatings. It is generally observed that adding aluminium to single-layer coatings increases hardness. However, a notable reduction in the critical load from scratch tests is also observed for aluminium-containing coatings. This is attributed to the tendency of aluminium to reduce adhesion to the steel substrate. Exceeding a certain aluminium concentration in the coating significantly compromises adhesion strength. While PACVD can be used for deposition, PVD is more commonly employed for these coatings to maintain desired concentration limits. Notably, wear volume values are significantly lower for multilayer coatings compared to single-layer counterparts. This superior performance is believed to stem from the higher combined hardness and adhesion strength of the multilayer structure. Figure 10 illustrates the distinct damage behaviours of single-layer and multilayer coatings. Single-layer coatings typically show debris from wear around the scratch area (Figure 10(a)), whereas such debris is absent in multilayer coatings (Figure 10(b)). Furthermore, cross-sectional analysis of the scratch path reveals that single-layer coatings exhibit circumferential spalling and widespread crack propagation (Figure 10(c)). In contrast, multilayer coatings show only a few localized cracks in the same direction, indicating less severe and more contained damage. This improved damage tolerance in multilayer coatings is primarily due to the disruption of stress propagation at the numerous interfaces, preventing continuous crack paths (Dong-Kak et al., 2003).

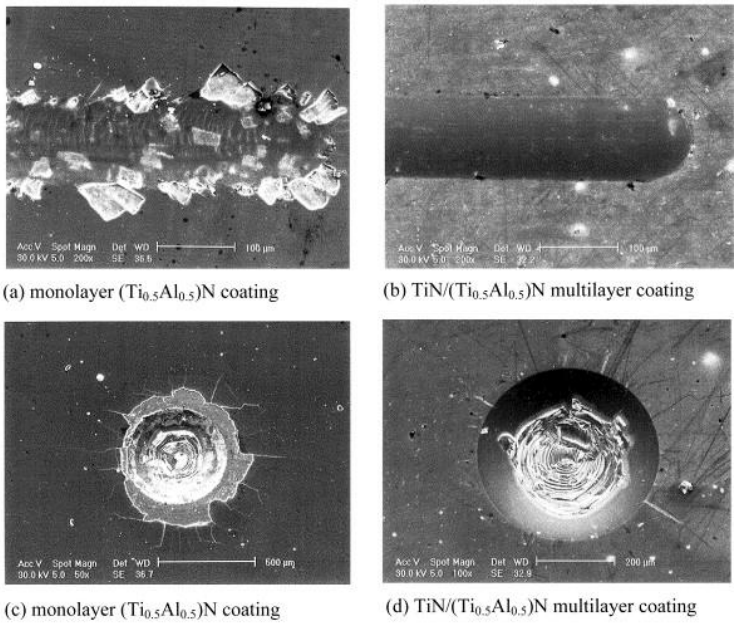

Figure 10. SEM images of the (a) monolayer ($Ti_{0.5}Al_{0.5}$)N and (b) multilayer TiN/($Ti_{0.5}Al_{0.5}$)N coatings subjected to scratch tests and (a) monolayer ($Ti_{0.5}Al_{0.5}$)N and (b) multilayer TiN/($Ti_{0.5}Al_{0.5}$)N coatings subjected to indentation tests (Dong-Kak et al., 2003).

In summary, TiN/TiAlN multilayer coatings significantly enhance the wear resistance and extend the lifespan of AISI M2 steel tools by combining the beneficial properties of TiN with the oxidation resistance of TiAlN, while their dense structure and numerous interfaces effectively mitigate crack propagation and improve overall adhesion compared to monolithic coatings.

2.5. TiN/CrN Coating

TiN and CrN coatings are among the most frequently utilized PVD coatings. However, conventional single-layer coatings often fall short of current demands. Consequently, superlattice coatings, featuring multiple layers at the nanometer scale, have emerged. These multilayer coatings typically exhibit increased hardness compared to their single-layer counterparts. This enhancement is variously attributed to the Hall-Petch effect, differences in shear moduli, or internal stresses. Hardening is generally considered the primary driver for improved wear resistance. Yet, some researchers argue that an increased ratio of hardness to elastic modulus is responsible for this improvement. Intriguingly, certain studies (Steyer et al., 2008) have demonstrated that multilayer coatings

can possess superior wear resistance even when compared to single-layer coatings that are inherently harder.

Figure 11 presents a graph illustrating the cumulative energy dissipated as a function of worn volume for these three distinct coatings, and indicates the superior wear resistance of the TiN/CrN multilayer coating compared to its monolithic TiN and CrN counterparts. This significant improvement is evident from its ability to withstand considerably higher cumulative dissipated energy before failure, directly supporting the conclusion that multilayer architectures effectively mitigate wear mechanisms by impeding crack propagation at their numerous interfaces (Mendibide et al., 2006).

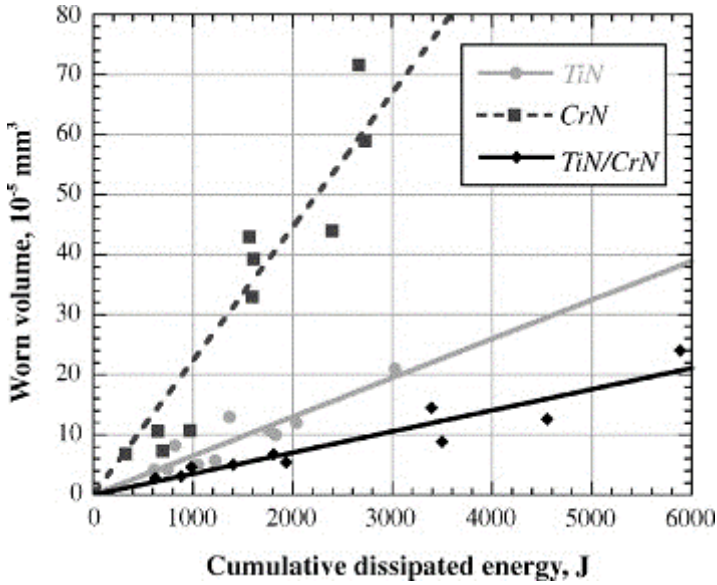

Figure 11. Relationship between worn volume and cumulative dissipated energy for the distinct coatings (Mendibide et al., 2006)

To elucidate how wear resistance is enhanced in TiN/CrN coatings, examining Figure 12 proves beneficial. Figure 12(a) illustrates the damage mechanism initiated in a TiN coating after a certain number of impact loads. Cracks initially form perpendicular to the surface but then change direction near the interface with the substrate, leading to spalling and detachment of the coating. Figure 12(b) further depicts the delamination experienced by the TiN coating as a result of this damage. However, as observed in Figure 12(c), in the TiN/CrN multilayer coating, cracks forming parallel to the interfaces are quite extensive but do not coalesce or propagate through the structure, thus preventing detachment. Additionally, these interface-parallel cracks in multilayer coatings are located at a greater distance from the substrate compared to those in single-layer coatings.

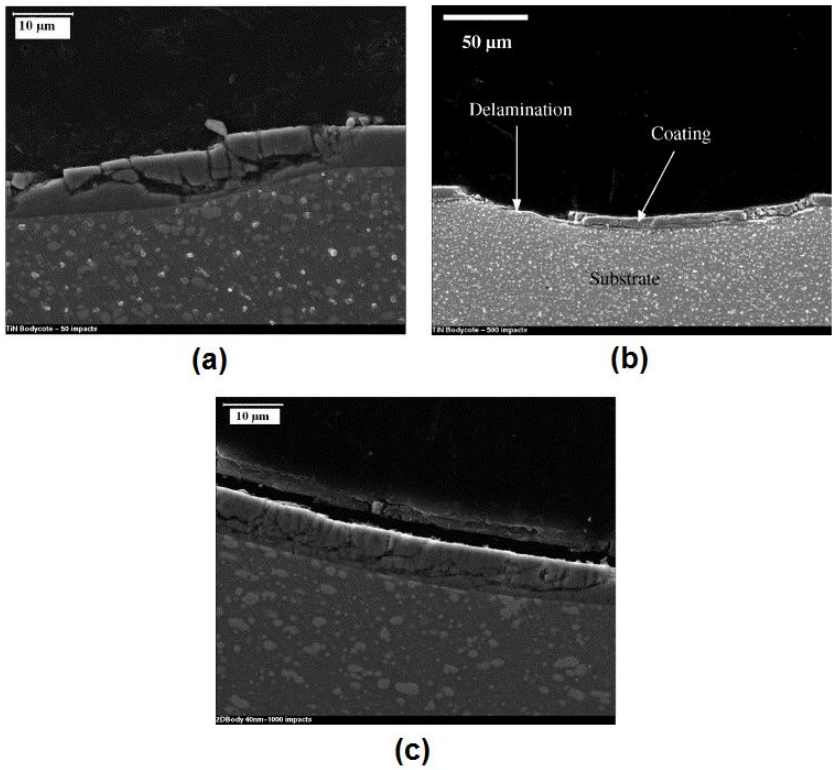

Figure 12. SEM images of cross-sections of (a) and (b) single-layer TiN and (c) multilayer TiN/CrN coatings after impact test (Mendibide et al., 2006)

PVD processes inherently induce significant compressive stresses within the coating structure. In single-layer coatings, the maximum compressive stress is concentrated near the coating-substrate interface. This stress generates strain in both parallel and perpendicular directions relative to the interface. The strain in the perpendicular direction, in particular, results in tensile stress along that axis (Figure 14(a)). Consequently, crack propagation tends to occur perpendicular to this tensile stress, in a plane parallel to the substrate-coating interface (Figure 14(b)). During tribological loading, crack initiation can begin at low compressive stress levels, with crack progression continuing until the stress becomes too high for further propagation. At this point, the crack begins to advance along the interface under the influence of tensile stress (Figure 14(c)). When these cracks coalesce, they lead to material detachment, resulting in the characteristic peeling failure (Figure 14(d)).

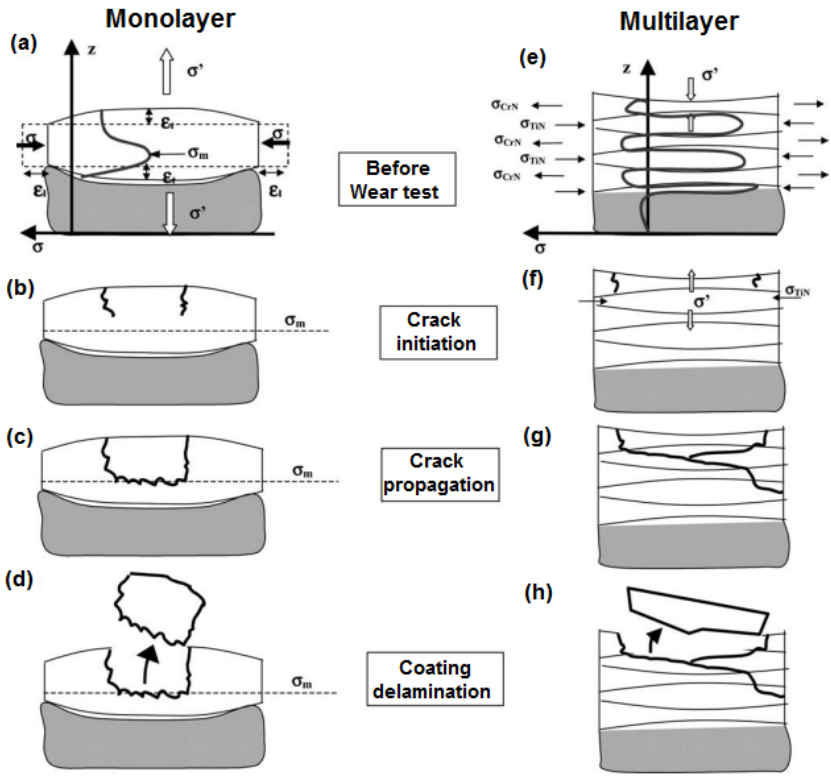

Figure 14. Wear model of monolayer coating ((a), (b), (c), (d)) and multilayer coatings ((e), (f), (g), (h)) (Mendibide et al., 2004)

For multilayered TiN/CrN coatings, while the entire coating remains under an overall compressive stress, individual layers experience different types of localized stresses. Given that TiN and CrN layers grow epitaxially, and TiN has a larger lattice parameter than CrN, each TiN/CrN interface results in the TiN layer being under compressive stress and the CrN layer under tensile stress (Figure 14(e)). This assumption effectively explains the differing crack propagation mechanisms observed in multilayer coatings. The TiN layers, which are under compressive stress parallel to the interface, also experience tensile stress perpendicular to the interface due to the same reasons observed in single-layer coatings (Figure 14(f)). Conversely, the CrN layers are under tensile stress parallel to the interface, causing them to experience compressive stress perpendicular to the interface. Since cracks generally propagate perpendicular to the tensile stress axis, they tend to extend horizontally (parallel to the interface) within the TiN layers and vertically (perpendicular to the interface) within the CrN layers (Figure 14(g)). This results in crack deflections as they traverse between layers. Such deflections effectively lengthen the crack path, increasing

resistance to wear, and consequently making peeling failure nearly impossible in these multilayer structures (Figure 14(h)).

As a result, TiN/CrN multilayer coatings significantly enhance wear resistance and extend service life by strategically deflecting crack propagation at their numerous interfaces, thereby preventing the catastrophic delamination common in conventional single-layer designs.

3. Conclusions

The persistent challenge of tool degradation in cold forming operations, manifesting as plastic deformation, wear, and fracture, highlights the critical need for advanced surface engineering solutions. As this chapter has demonstrated, enhancing the lifespan of cold forming tool steels is paramount for improving manufacturing efficiency, reducing costs, and maintaining product quality. The exploration herein has covered a spectrum of coating materials and strategies, from foundational single-layer coatings to sophisticated nanostructured multilayers, each contributing uniquely to the overall performance envelope.

The examination commenced with TiN coatings, a long-standing choice in PVD applications for AISI M2 steels due to their excellent adhesion and hardness. While studies have revealed variations in their tribological behaviour depending on deposition method, with PVD sometimes presenting challenges related to surface topography and micro-welding, the fundamental efficacy of TiN remains undeniable. Crucially, the practical relevance of TiN coatings can be significantly extended through post-coating treatments. Deep Cryogenic Treatment (DCT), for instance, has been shown to induce beneficial microstructural transformations, such as the conversion of retained austenite and the precipitation of fine strengthening phases, alongside stress redistribution. These changes collectively elevate the hardness, wear resistance, and elastic modulus of the coating, affirming the continued viability of TiN as a cost-effective solution in numerous industrial contexts, even when more advanced materials are available.

Diamond-Like Carbon (DLC) coatings offer a compelling alternative, particularly due to their remarkably low coefficient of friction. This attribute directly translates into substantial advantages: reduced wear, lower energy consumption, decreased heat generation, and effective prevention of galling and seizure. However, the inherent internal stresses of DLC films necessitate strategic approaches to ensure robust adhesion. The critical role of interlayers, such as chromium, and pre-treatment methods like plasma nitriding of the M2 steel substrate, in establishing a strong interfacial bond and promoting a beneficial hardness gradient was emphasized. These measures are crucial for unlocking the full potential of DLC in demanding forming applications.

Further exploration of surface solutions led to CrAlN coatings, which consistently outperform conventional CrN. The introduction of aluminium significantly refines the microstructure, promoting a denser, nanocrystalline arrangement and inducing solid solution hardening. A standout feature of CrAlN is its enhanced high-temperature performance, where it forms a stable, self-lubricating aluminium oxide layer that markedly improves oxidation resistance and maintains low friction under thermal loads. This superior thermal stability positions CrAlN as an excellent candidate for applications experiencing significant heat generation.

By alternating layers of distinct materials, multilayer coatings, such as TiN/TiAlN and TiN/CrN, introduce a high density of interfaces that effectively impede crack propagation, a phenomenon akin to the Hall-Petch effect. This leads to remarkable improvements in fracture toughness and wear resistance, often surpassing those of single-layer counterparts, even at comparable total thicknesses. The detailed analysis of crack deflection mechanisms in TiN/CrN multilayers, governed by localized stress distributions at the epitaxial interfaces, provided clear evidence of their enhanced damage tolerance and near immunity to catastrophic peeling failure.

In conclusion, the selection of an optimal coating for cold work tool steels is a multifaceted decision. While foundational coatings like TiN remain relevant, especially when enhanced by targeted post-treatments, the continuous advancements in materials science offer increasingly sophisticated solutions. DLC coatings provide unparalleled friction reduction, CrAlN excels in high-temperature and abrasive environments, and multilayer TiN/TiAlN and TiN/CrN coatings, designs present a robust strategy for combining synergistic properties and managing crack propagation. The data consistently emphasizes that a deep understanding of the wear mechanisms, the specific demands of the forming process, and the interplay between coating properties and substrate pre-treatment is paramount. As manufacturing continues to push boundaries, the ongoing innovation in surface engineering of cold work steel tools will remain central to achieving higher productivity, extended tool life, and superior product quality.

References

Almeida, E. A. S., Costa, C. E., Milan, J. C. G., Krelling, A. P. and Galiotto, A. (2017). Investigation of borided layerscontribution on the wear resistance and adhesion of TiN coatings. *Revista Matéria, 22*(1), 1–11. https://doi.org/10.1590/S1517-707620170001.0119.

Ashvita, A. J., Patnaik, L., Maity, S. R. and Kumar, S. (2024). Comparative study on surface modification of heat-treated hot work tool steel using plasma nitriding and thin film deposition technique. *Materials Today: Proceedings*. In press. https://doi.org/10.1016/j.matpr.2024.05.119.

Banerji, A., Bhowmick, S. and Alpas, A. T. (2014). High temperature tribological behavior of W containing diamond-like carbon (DLC) coating against titanium alloys. *Surface and Coatings Technology, 241*, 93–104. https://doi.org/10.1016/j.surfcoat.2013.10.075.

Brizuela, M., Garcia-Luis, A., Braceras, I., Oñate, J. I., Sánchez-López, J. C., Martínez-Martínez, D., López-Cartes, C. and Fernández, A. (2005). Magnetron sputtering of Cr(Al)N coatings: Mechanical and tribological study. *Surface and Coatings Technology, 200*(1–4), 192–197. https://doi.org/10.1016/j.surfcoat.2005.02.105.

Cerıtbınmez, F., Çakir, F. H. and Parım, B. (2025). Enhancing wear resistance of TiN-coated 1.3343 high-speed steel punches through deep cryogenic treatment and tempering. *Journal of Central South University, 32,* 350–362. https://doi.org/10.1007/s11771-025-5893-7.

Chiadikobi, C. I., Thornton, R., Statharas, D. and Weston, D. P. (2024). The effects of deep cryogenic treatment on PVD-TiN coated AISI M2 high speed steel. *Surface and Coatings Technology, 493*(2), 131248. https://doi.org/10.1016/j.surfcoat.2024.131248.

Dong-Kak, L., Seung-Hoon, L. and Jung-Joong, l. (2003). The structure and mechanical properties of multilayer TiNy(Ti Al 0.5 0.5)N coatings deposited by plasma enhanced chemical vapor deposition. *Surface and Coatings Technology, 169–170*, 433–437. https://doi.org/10.1016/S0257-8972(03)00184-1.

Dubar, M., Dubois, A. and Dubari L. (2005). Wear analysis of tools in cold forging: PVD versus CVD TiN coatings. *Wear*, *259*(7–12), 1109–1116. https://doi.org/10.1016/j.wear.2005.01.006.

Hilton, M. R., Vandentop, G. J., Salmeron, M. and Somorjai, G. A. (1987). TiN coatings on M2 steel produced by plasma-assisted chemical vapor deposition, *Thin Solid Films, 154*(1–2), 377–386. https://doi.org/10.1016/0040-6090(87)90380-4.

Huq, M. Z. and Celis, J. P. (1997). Reproducibility of friction and wear results in ball-on-disc unidirectional sliding tests of TiN-alumina pairings. *Wear, 212*(2), 151–159. https://doi.org/10.1016/S0043-1648(97)00167-1

Lin, R., Sun, S., You, B., Dong, T., Sui, Y. and Wei, S. (2024). Evaluation of wear resistance of CrN, CrAlN, and TiAlN coatings deposited by multi-arc ion plating on spinning die of Cr12MoV. *Materials Research Express, 11*(9), 096402. https://doi.org/10.1088/2053-1591/ad7350.

Mendibide, C., Fontaine, J., Steyer, P. and Esnouf, C. (2004). Dry sliding wear model of nanometer scale multilayered TiN/CrN PVD hard coatings. *Tribology Letters 17*, 779–789. https://doi.org/10.1007/s11249-004-8086-9.

Mendibide, C., Steyer, P., Fontaine, J. and P. Goudeau. (2006). Improvement of the tribological behaviour of PVD nanostratified TiN/CrN coatings - An explanation. *Surface and Coatings Technology, 201*(7), 4119–4124. https://doi.org/10.1016/j.surfcoat.2006.08.013.

Moreno-Bárcenas, A., Alvarado-Orozco, J. M. Carmona, J. M. G., Mondragon-Rodriguez, G. C., Gonzalez-Hernandez, J. and Garcia-Garcia, A. (2019). Synergistic effect of plasma nitriding and bias voltage on the adhesion of diamond-like carbon coatings on M2 steel by PECVD. *Surface and Coatings Technology, 374,* 327–337. https://doi.org/10.1016/j.surfcoat.2019.06.014.

Navinšek, B., Panjan, P. and Milošev, I. (1997). Industrial applications of CrN (PVD) coatings, deposited at high and low temperatures. *Surface and Coatings Technology, 97*(1–3), 182–191. https://doi.org/10.1016/S0257-8972(97)00393-9.

Ormanova, M., Kotlarski, G., Dechev, D., Ivanov, N., Stoyanov, B. and Valkov, S. (2023). Duplex surface modification of M2 high-speed steel. *Coatings, 14*, 798. https://doi.org/10.3390/coatings14070798.

Polcar, T. and Cavaleiro, A. (2011). High temperature properties of CrAlN, CrAlSiN and AlCrSiN coatings – Structure and oxidation. *Materials Chemistry and Physics, 129*(1–2), 195–201. https://doi.org/10.1016/j.matchemphys.2011.03.078.

Raja, V. and Sornakumar, T. (2014). Punch life improvement in cold forging of nut. International *Journal of Engineering Research & Technology (IJERT)*, *3*(11), 838–842. https://www.ijert.org/punch-life-improvement-in-cold-forging-of-nut.

Sánchez-López, J. C., Contreras, A., Domínguez-Meister, S., García-Luis, A. and Brizuela, M. (2014). Tribological behaviour at high temperature of hard CrAlN coatings doped with Y or Zr. *Thin Solid Films, 550*, 413–420. https://doi.org/10.1016/j.tsf.2013.10.041.

Shugurov, A. R. and Kazachenok, M. S. (2018). Mechanical properties and tribological behavior of magnetron sputtered TiAlN/TiAl multilayer coatings. *Surface and Coatings Technology, 353*, 254–262. https://doi.org/10.1016/j.surfcoat.2018.09.001.

Steyer, P., Mege, A., Pech, D., Mendibide, C., Fontaine, J., Pierson, J. -F., Esnouf, C. and Goudeau, P. (2008). Influence of the nanostructuration of PVD hard TiN-based films on the durability of coated steel. *Surface and Coatings Technology, 202*(11), 2268–2277. https://doi.org/10.1016/j.surfcoat.2007.08.073.

Wang, K., Zhou, H., Zhang, K., Liu, X., Feng, X., Zhang, Y., Chen, G. and Zheng, Y. (2021). Effects of Ti interlayer on adhesion property of DLC films: A first principle study*, Diamond and Related Materials, 111*, 108188. https://doi.org/10.1016/j.diamond.2020.108188.

Wang, X.X., Wang, Y.H., Ling, Z.C.,. Yuan Z.P., Shi, J.J., Qin, J., Sun, H.W., Pan, K.M., Geng, Z.M., Ma, H.L., Yand Z.J., Liu, S., Wu, Y.M. and Peng, Y. (2025). Strategies for superhard tool coating materials: focus on preparation methods and properties. *Journal of Iron and Steel Research International*. In press. https://doi.org/10.1007/s42243-025-01448-x.

Yousefi, M., Baghshahi, S. and Kerahroodi, M. S. A. (2021). Effect of titanium nitride, diamond-like carbon and chromium carbonitride coatings on the life time of an AISI M2 Steel punch forming tool. *Journal of Bio- and Tribo-Corrosion, 7*, 50. https://doi.org/10.1007/s40735-021-00483-x.

Zerrin T. (2014). *Elmas benzeri karbon ince filmlerin hazırlanması ve karakterizasyonu / Preparation and characterization of diamond-like carbon thin films*. Hacettepe Üniversitesi, Fen Bilimleri Enstitüsü, Fizik Mühendisliği Ana Bilim Dalı, Ankara.

Zhang, X., Tian, X., Gong, C., Liu, X., Li, J., Zhu, J. and Lin, H. (2022). Effect of plasma nitriding ion current density on tribological properties of composite CrAlN coatings. *Ceramics International, 48*(3), 3954-3962. https://doi.org/10.1016/j.ceramint.2021.10.182.

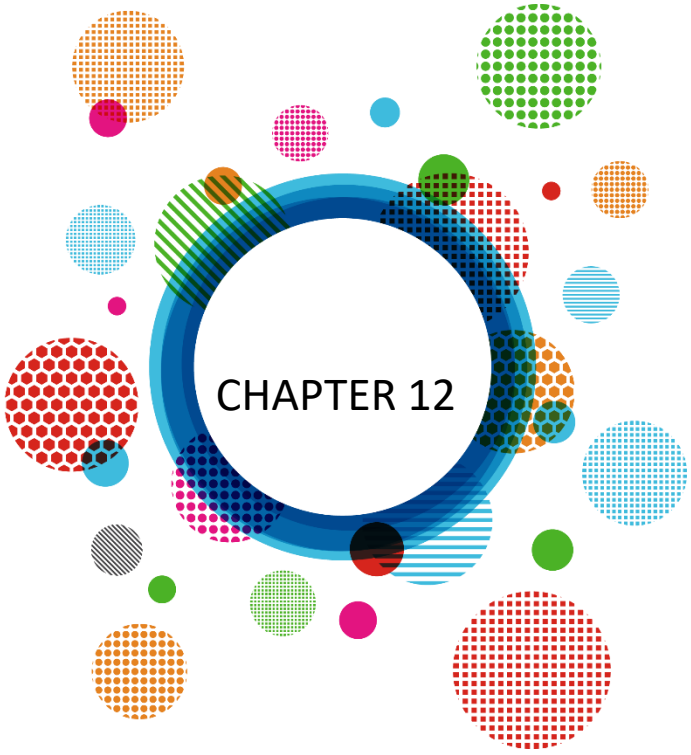

Advanced Additive Manufacturing Methods for the Production of Composite Coatings

Cemile Kayış[1] *& Ege Anıl Diler*[2]

[1] "Res. Asst., Eskisehir Technical University, Department of Mechanical Engineering, Eskişehir, Turkey, ORCID: 0000-0002-4401-2412
[2] Assoc. Prof. Dr., Ege University, Department of Mechanical Engineering, Izmir, Turkey, ORCID: 0000-0002-1667-5737

1. Introduction

The fields of composite materials and additive manufacturing (AM) have witnessed an extraordinary convergence, giving rise to novel paradigms in materials science and engineering. This intersection is particularly profound when considering the development of advanced coatings that are themselves intricate composite structures, fabricated through sophisticated AM techniques. Traditionally, coatings have served primarily as protective or functional layers, enhancing the surface properties of substrates (Zhu et al., 2022). However, the ability to engineer these coatings as complex, multi-component materials via additive processes opens up unprecedented opportunities for tailoring their performance at a fundamental level, moving far beyond mere surface passivation.

The very concept of a coating has undergone a profound evolution from its rudimentary beginnings as a passive barrier. Modern engineering, driven by relentless demands for enhanced performance, durability, and multi-functionality across an ever-expanding array of applications, increasingly necessitates coatings that can actively contribute to the overall functionality of a component. This contribution extends far beyond simple corrosion or wear resistance, encompassing capabilities such as superior thermal insulation in extreme environments, precise electrical conductivity for integrated circuits, and targeted biocompatibility for medical implants (Tejero-Martin et al., 2019). Achieving such multifaceted and highly specialized performance characteristics often necessitates the synergistic incorporation of multiple distinct materials, each contributing unique properties, forming a complex composite structure within the coating itself.

The historical challenge, however, has consistently resided in precisely controlling the distribution, morphology, and crucially, the interfacial bonding of these diverse constituent phases within a relatively thin layer. Conventional coating methods, including widely adopted techniques such as thermal spraying, electroplating, and physical vapour deposition, while undeniably effective for a myriad of established applications, often face inherent limitations when attempting to create truly tailored, architecturally complex composite structures with fine spatial resolution. These methods typically rely on line-of-sight deposition, electrochemical processes, or broad thermal energy input, which fundamentally restrict the geometric complexity, the breadth of achievable material combinations, and the degree of spatial control obtainable within the coating. Furthermore, achieving precise command over microstructural features, such as specific grain sizes, uniform phase distributions, controlled porosity, or deliberate material gradients that transition smoothly from one property to another, can be exceedingly challenging with these traditional techniques. This often leads to unavoidable compromises in desired properties, thereby hindering

the full realization of the potential of the coating and limiting innovation in advanced surface engineering. The inability to precisely place specific materials at predefined locations within the coating often necessitates trade-offs, preventing the optimization of all desired properties simultaneously.

This chapter will focus on the profound connection between these two critical areas. It will examine how the precision, versatility, and inherent design freedom of advanced additive manufacturing methods are fundamentally changing how composite coatings are designed, made, and ultimately, how they perform.

2. Additive Manufacturing: A Foundational Shift for Tailored Composite Coatings

Additive manufacturing (AM), often colloquially but perhaps too simply known as 3D printing, represents a truly transformative approach to fabricating structures. Its defining characteristic is the layer-by-layer material deposition, built directly from digital designs. This layer-by-layer build-up offers exceptional control over material placement and the resulting internal architecture of the fabricated part (Rasiya et al., 2021). While AM has deservedly gained considerable traction in producing bulk components for various industries, its application in creating advanced composite coatings is a rapidly emerging and exceptionally promising area, poised to disrupt conventional paradigms. The advantages of AM, such as the ability to precisely process a wide array of material classes, to produce highly intricate and customized geometries at various scales, and to achieve highly localized material deposition, directly address many of the limitations previously encountered with traditional coating techniques when aiming to create sophisticated composite structures.

This includes, most notably, the unmatched capacity to create functionally graded materials (FGMs). In the context of coatings, FGMs mean that the composition, microstructure, or even the underlying properties can vary continuously or in a controlled, step-wise manner across the coating thickness. This grading leads to optimized performance transitions, effectively mitigating abrupt interfacial stresses that often cause delamination, cracking, or premature failure in conventional multi-layered coatings with sharp interfaces. The ability to smoothly transition between a substrate and a coating, or between different layers within the coating itself, significantly enhances long-term durability and performance (Fathi et al., 2022). Moreover, AM uniquely enables the precise and intimate integration of disparate materials, ranging from robust metals and resilient ceramics to flexible polymers, into a single, cohesive coating architecture. This fosters the development of truly multi-functional layers that can exhibit a synergistic combination of properties not readily achievable with monolithic materials. For example, a single AM process could create a coating that is highly wear-resistant on its outer surface, thermally insulating in its

middle, and electrically conductive near the substrate, all within a seamlessly integrated structure. The digital nature of AM also fundamentally facilitates rapid prototyping and iterative design optimization, significantly accelerating the development cycle for novel coating solutions and allowing for highly customized designs to meet hyper-specific application requirements with unprecedented agility and cost-effectiveness. This rapid design-to-manufacture loop empowers engineers to explore a vast design space, quickly testing and refining concepts for next-generation coatings.

3. Advanced Additive Manufacturing Methods for Composite Coating Production

Figure 1 depicts the advanced additive manufacturing methods for the production of composite coatings. The landscape of additive manufacturing (AM) for composite coatings is remarkably diverse, characterized by a suite of advanced methods, each uniquely suited to specific material systems and desired coating architectures. These techniques move beyond conventional AM by offering sophisticated control over multi-material deposition and achieving the fine resolutions necessary for effective coating performance. This section will delve into the scientific intricacies of the most prominent advanced AM methods employed for fabricating composite coatings.

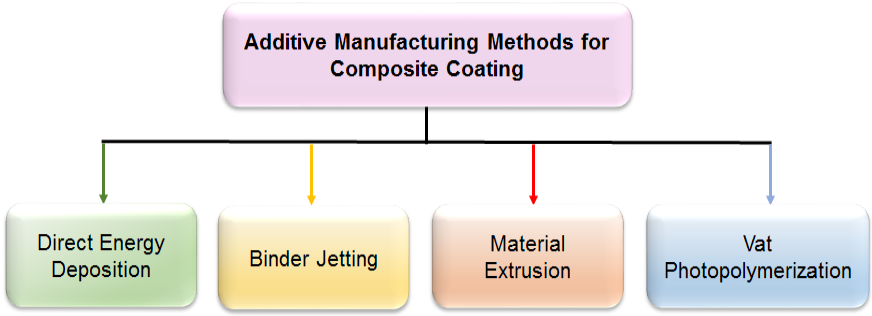

Figure 1. Advanced additive manufacturing methods for composite coating production

3.1. Directed Energy Deposition (DED)

Directed Energy Deposition (DED), encompassing processes like Laser Engineered Net Shaping (LENS), Electron Beam Freeform Fabrication (EBF3), and variants employing plasma or arc torches, stands as a powerful tool for producing dense, metallurgical bond-forming composite coatings. DED involves focusing a high-energy source onto a substrate, creating a localized molten pool. Simultaneously, material feedstock, typically in fine powder or thin wire form, is precisely fed into this melt pool. As the energy source traverses the surface in a

predefined path, the molten material rapidly solidifies, forming a new, metallurgically bonded layer (Figure 2) (Lim et al., 2021).

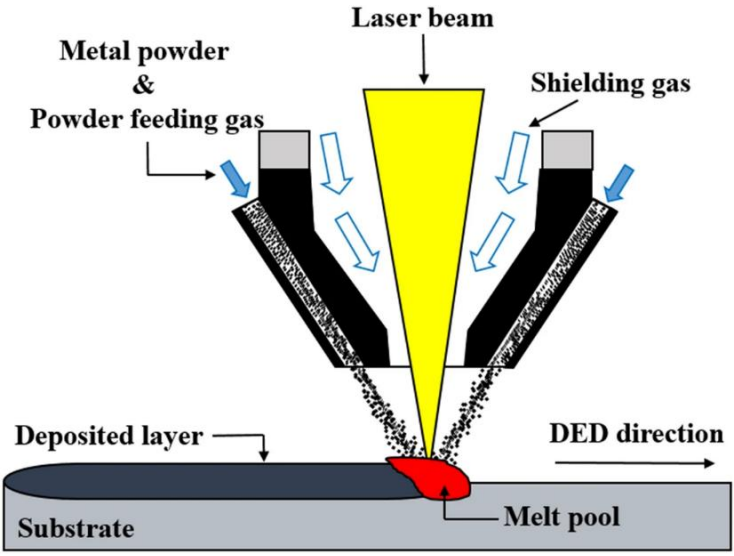

Figure 2. Laser powered directed energy deposition (Lim et al., 2021)

In multi-material DED, two or more independent powder feeders can be independently controlled and proportioned. The powders converge precisely at the focal point of the energy beam, where they are melted and intimately mixed within the dynamic molten pool. This sophisticated control allows for the in-situ alloying of different metals, the uniform dispersion of ceramic, metallic, or carbonaceous reinforcement phases within a metallic or ceramic matrix, or even the in-situ formation of intermetallic compounds or ceramic phases through reactive deposition. For instance, in producing advanced wear-resistant coatings, hard WC particles can be precisely introduced and retained within a tough nickel-based superalloy matrix, with controlled dissolution to form beneficial carbide precipitates (He et al., 2022). Furthermore, by dynamically adjusting the feed rates of different powders and/or the energy input during the deposition process, functionally graded composite coatings can be precisely fabricated. This capability allows for continuous or step-wise variations in composition, microstructure, and properties for the coating thickness. This grading creates a tailored transition from the substrate to the coating surface, effectively minimizing abrupt thermal expansion mismatches and reducing detrimental residual stresses, thereby significantly enhancing adhesion, mitigating crack propagation, and ultimately prolonging the service life of the coated component, especially under cyclic thermal or mechanical loading (Nie et al., 2023).

Critical process parameters demanding meticulous control include the precise laser power or electron beam current, the linear scanning speed of the energy source, the powder or wire feed rate, and the specific gas flow dynamics. Precise and real-time control over these variables directly dictates the melt pool size, its temperature profile, the local solidification rate, the degree of dilution with the underlying substrate, and critically, the uniform distribution, chemical stability, and interfacial integrity of reinforcement phases. For ceramic-metal composites, balancing the widely differing melting points, densities, and wetting behaviours of the constituent materials is crucial to prevent undesirable phenomena such as agglomeration, gravitational segregation of phases, or undesired chemical reactions that could form brittle intermetallics. Understanding the Marangoni effect and melt pool fluid dynamics is essential for achieving homogeneous mixing and avoiding defects like porosity or cracking (Zhang et al., 2024).

DED offers several compelling advantages for composite coatings, including relatively high deposition rates, suitable for manufacturing and repairing large components, the creation of strong metallurgical bonds with the underlying substrate due to localized melting, and the unique ability to form complex, tailored microstructures and highly effective functionally graded materials in a single, integrated process. Its adaptability to various geometries and the potential for multi-axis deposition also makes it highly suitable for applying composite coatings to complex 3D parts with non-planar surfaces (Saboori et al., 2017).

Despite its advantages, DED presents scientific and engineering challenges, such as the potential for elemental segregation or undesired phase precipitation if cooling rates are not precisely optimized or if immiscible elements are combined. Uniformly dispersing extremely fine or high-aspect-ratio reinforcement particles without agglomeration remains difficult due to surface energy differences and fluid dynamics in the melt pool. Managing significant thermal stresses that can arise during rapid solidification, particularly when processing dissimilar material combinations with large differences in thermal expansion coefficients, requires careful thermal management strategies. Post-process heat treatments are often necessary to alleviate residual stresses and optimize microstructure, which adds to the process complexity.

3.2. Binder Jetting (BJ)

Binder Jetting (BJ) is a highly versatile AM process that builds parts layer-by-layer by selectively depositing a liquid binder onto a prepared powder bed (Wang et al., 2023). For composite coatings, BJ offers a unique pathway to incorporate various material combinations that might be challenging to process with high-energy fusion methods due to their exceptionally high melting points, inherent reactivity at elevated temperatures, or tendency to degrade under extreme thermal loads. Crucially, the cold nature of the printing process itself minimizes thermal

distortion and residual stresses during deposition, allowing for the fabrication of complex geometries with high precision.

In the context of composite coatings, the initial powder bed itself can be a carefully engineered, homogeneous or spatially varied blend of different particulate materials. Alternatively, and increasingly, multi-nozzle printheads allow for the selective jetting of multiple binders with different chemical compositions or functionalities. After a thin, uniform layer of powder is precisely spread across the build platform using a roller or blade, an inkjet printhead deposits tiny pico-liter droplets of a liquid binder, selectively joining the powder particles in predefined patterns according to the digital coating design (Figure 3). This precise deposition is repeated layer by layer until the entire green part, consisting of bound powder held together by the cured or dried binder, is formed. The unbound powder, acting as a crucial support material, is then removed, often through air blowing or brushing. The green part is then typically subjected to a subsequent and often critical post-processing step (Ziaee and Crane, 2019). For metallic or ceramic composite coatings, this usually involves high-temperature sintering or infiltration. For example, a porous ceramic part, could be binder-jetted with a ceramic powder, and then subsequently infiltrated with a molten metal alloy to create a robust metal-matrix composite (Chen et al., 2022). This method allows for a high degree of control over the final porosity and pore size distribution, which is critical for many functional applications where surface area or permeability are key.

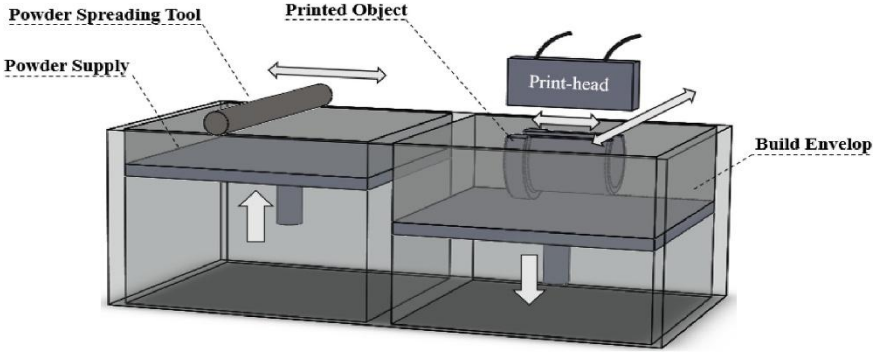

Figure 3. Binder jetting (Ziaee and Crane, 2019)

Important parameters profoundly influencing the final properties of the composite coating include the particle size distribution, morphology, and packing density of the initial powder, the viscosity, surface tension, and wetting characteristics of the liquid binder on the specific powder particles, the precise binder saturation levels within the powder, the deposited layer thickness, and critically, the precise conditions of the post-processing steps. The uniformity of

the initial powder bed, achieved through precise roller or blade mechanisms, and the accuracy of binder droplet deposition, which relies on sophisticated piezoelectric or thermal printhead technology, are paramount for achieving consistent composite structures and preventing defects such as delamination or heterogeneous density. Understanding capillary forces, binder-powder interactions, and the kinetics of binder drying/curing is crucial for process robustness (Dini et al., 2020).

BJ offers significant advantages, including the absence of residual stresses from thermal gradients during the primary printing process, the ability to process an exceptionally wide range of materials (including high-melting-point refractories like tungsten and highly dissimilar material combinations that might react exothermically or become immiscible under fusion-based AM conditions), excellent dimensional accuracy for the as-printed green part, and a unique suitability for creating highly porous composite structures with precisely controlled pore networks and tailored permeability, which is crucial for applications like catalytic converters, heat exchangers, or tissue scaffolds. Cost-effectiveness for large batch production and the ability to reclaim unbound powder are also strong points (Galindo et al., 2025).

The primary challenge lies in the necessity for significant post-processing. Achieving full densification can be challenging, leading to residual porosity that can negatively impact mechanical properties and fatigue life. The mechanical properties of the final composite coating are highly dependent on the quality of the binder, its complete removal during debinding, and the efficacy of the post-sintering or infiltration process. Debinding and sintering cycles can be time-consuming and energy-intensive, and their precise control is critical to avoid defects such as carbon residue or undesirable grain growth.

3.3. Material Extrusion (ME)

Material Extrusion (ME), most commonly recognized in its Fused Filament Fabrication (FFF) variant, is rapidly gaining significant traction for composite coating applications. While traditionally associated with polymer-matrix composites, advanced ME techniques are increasingly being adapted for ceramics and even metals via binder-based approaches, offering a cost-effective, versatile, and relatively accessible manufacturing route for creating customized composite coatings. This method involves extruding a continuous filament or a highly viscous paste through a heated nozzle, depositing material layer by layer onto a substrate in a predefined path.

When fabricating composite coatings via ME, the feedstock material is a critical factor. It can be a pre-manufactured composite filament (e.g., a polymer matrix intrinsically embedded with short carbon fibres for enhanced strength,

ceramic particles for increased hardness or wear resistance, metallic powders for electrical conductivity, or even continuous fibres for true fibre-reinforced composites where the fibres are fed coaxially with the matrix). Multi-nozzle extrusion systems are also emerging, allowing for the co-extrusion of different composite or monolithic materials simultaneously within the same layer, enabling gradient structures, or sequential deposition of different materials in adjacent layers for multi-material stacked coatings. In addition, highly viscous pastes or slurries containing high loadings of ceramic or metallic particles uniformly suspended in a sacrificial binder solution can be precisely extruded. These pastes, often referred to as feedstocks for robocasting or direct ink writing, leverage rheological properties to maintain shape after deposition. After the layer-by-layer deposition, these green parts often undergo a sequential debinding and sintering process to remove the organic binder and densify the particulate matter. This allows for complex ceramic- or metal-matrix composite coatings that retain the intricate geometry created during extrusion. (Figure 4) (Spina and Morfini, 2024). The precise control over the path of the nozzle, deposition speed, and flow rate allows for intricate patterning and the creation of anisotropic composite coatings where the reinforcement orientation can be precisely controlled within specific regions or layers of the coating. This precise control over fibre orientation can significantly enhance mechanical, thermal, and electrical properties in desired directions.

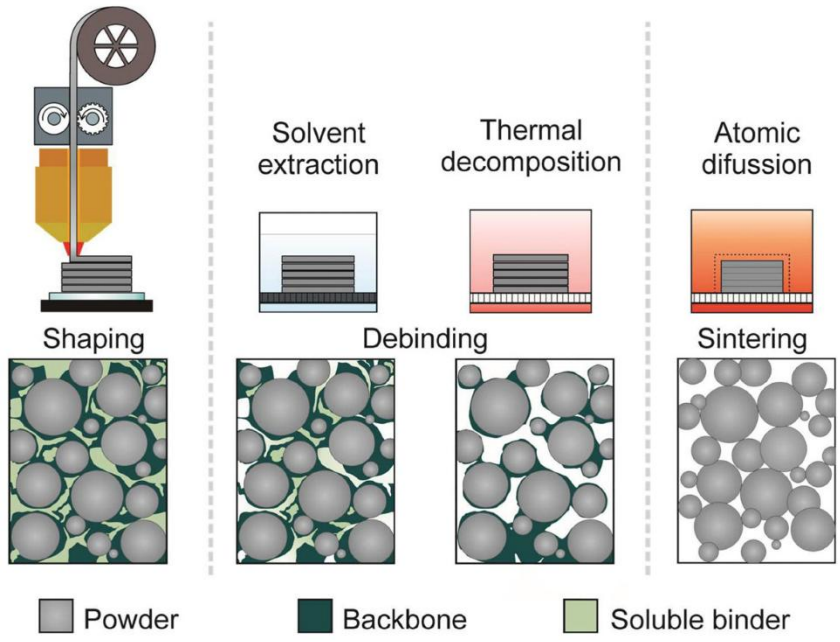

Figure 4. Metal extrusion (Spina and Morfini, 2024)

Critical process parameters include the extrusion temperature, the nozzle diameter and speed, the precise layer height, the infill density and pattern, and crucially, the exact composition and rheological properties of the feedstock. For paste extrusion, the shear-thinning behaviour, yield stress, and thixotropy of the slurry are paramount for ensuring smooth, consistent, and clog-free flow through the nozzle while maintaining shape fidelity after deposition. For filament-based systems, the consistency of filament diameter, the uniform dispersion of fillers within the polymer matrix, and adhesion between layers are vital (Gupta et al., 2022). Post-extrusion parameters, such as curing temperature/time for polymers or multi-stage debinding/sintering profiles for ceramics/metals, are also critical for achieving optimal final material properties and density.

ME offers several compelling advantages, including relatively low equipment and material costs, the ability to process a wide range of thermoplastic and thermoset polymers, potential for large-scale fabrication and complex part geometries, and excellent control over internal geometry and infill patterns, including the precise orientation of short fibres or elongated particles within the coating. It also allows for rapid prototyping and iterative design explorations due to its accessibility and relatively straightforward process setup.

Persistent challenges include anisotropy in properties due to the layer-by-layer deposition and the resultant z-axis weakness (poor interlayer bonding), difficulties with precise porosity control, and limitations on coating complexity for certain designs. For high-temperature ceramic or metallic materials, significant and often multi-stage post-processing (debinding and sintering) is required, which can introduce defects, considerable shrinkage, or lead to warping if not precisely controlled. Achieving high filler loadings while maintaining desirable rheological properties for extrusion is also a common hurdle, as high viscosity can lead to print failures (Loh, et al., 2020).

3.4. Vat Photopolymerization (VP) – Multi-Material Approaches

Vat Photopolymerization (VP), encompassing well-known techniques such as Stereolithography (SLA) and Digital Light Processing (DLP), traditionally uses focused light (UV or visible) to selectively cure liquid photopolymer resins, building solid parts layer by layer (Figure 5).

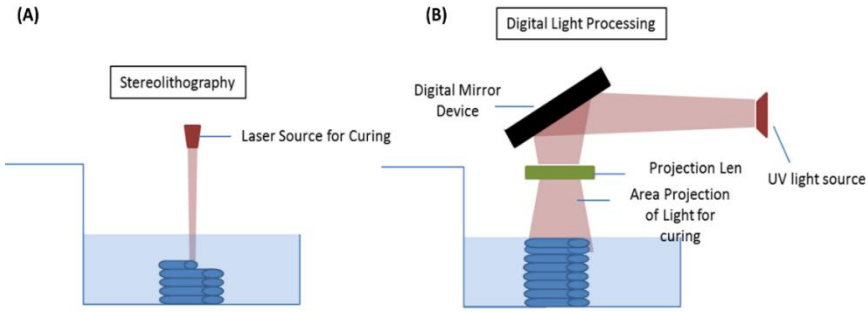

Figure 5. Vat Photopolymerization. (A) Stereolithograpy (B) Digital Light Processing (Lee et al., 2018)

Recent groundbreaking advancements, however, have transformed VP into an exceptionally powerful method for fabricating multi-material and composite coatings with exceptionally high resolution, intricate detail, and often superior surface finish compared to other AM methods, enabling the creation of micro-scale features and smooth contours (Subedi et al., 2024).

Multi-material VP for composite coatings can be achieved through several sophisticated approaches. One method involves utilizing multiple resin vats, each containing a different photopolymer or a distinct composite resin. A robotic arm or a precise dispensing system can then switch between these vats, depositing different materials layer by layer or even within a single layer, enabling a form of multi-material printing with distinct material zones. Another highly advanced technique involves using a single vat but employing intricate microfluidic channels or sophisticated ink-jetting within the vat itself to precisely mix and dispense different resins or resin-particle slurries in situ, enabling voxel-level material control. Furthermore, gradient materials can be created by precisely controlling the light intensity or exposure time across a layer, influencing the cure depth and potentially the cross-linking density, or even inducing localized chemical reactions or phase separations in specially formulated photopolymer blends containing reactive components (Shaukat et al., 2022). The exceptionally high resolution inherent to VP makes it ideally suited for creating intricate micro-scale composite features within coatings, such as integrated microfluidic channels for active cooling or drug delivery, precisely structured optical gratings for light manipulation, or intricate biomimetic surfaces with controlled roughness and chemical functionality for enhanced cell adhesion and proliferation in medical applications.

Critical parameters profoundly influencing the final composite coating quality include the wavelength and intensity of the light source (which dictates penetration depth and curing speed), the precise exposure time for each layer

(controlling polymerization degree and cross-linking density), the resin viscosity and photosensitivity (related to reactivity, flow behaviour, and material handling), the concentration, size, morphology, and dispersion stability of filler particles within the resin, and the accurate layer thickness. Ensuring a stable, homogeneous dispersion of high concentrations of inorganic filler particles in the photopolymer resin without undesirable phenomena such as agglomeration, settling, or light scattering is a significant and ongoing challenge, often requiring specialized surface treatments of the particles, rheological modifiers, or even active mixing during printing. The kinetics of photo-polymerization and the resultant polymerization shrinkage of the resin also play a critical role in residual stress development and potential warping of the composite coating.

VP offers distinct advantages, including extremely high resolution and excellent surface finish, the ability to create highly complex geometries and intricate internal microstructures, suitability for transparent or translucent composite coatings, and exceptional precise control over material placement at the micro-scale. Its capacity for fine detail makes it ideal for integrating micro-sensors or micro-actuators directly within coating layers.

The primary limitation is that these methods are largely restricted to photocurable resins, which may not possess the desired high-temperature mechanical properties, chemical resistance, and long-term durability required for certain demanding industrial applications, particularly in extreme environments. Challenges include achieving uniform dispersion of high concentrations of inorganic fillers, the necessity for significant post-curing to achieve full mechanical properties and stability, and the potential for shrinkage during the photopolymerization process, which can induce residual stresses and lead to warpage or cracking in the composite coating, especially when dealing with high filler loadings or large part geometries. The cost of specialized composite resins can also be significantly higher than conventional AM feedstocks, impacting scalability.

4. Conclusion

The confluence of composite materials and advanced additive manufacturing techniques represents a revolutionary epoch in the field of surface engineering. No longer confined to the realm of simple protective layers, coatings can now be conceived and fabricated as sophisticated, multi-functional composite systems, precisely tailored at the microstructural level to meet the most demanding performance criteria. The methodologies discussed, Directed Energy Deposition (DED), Binder Jetting (BJ), Material Extrusion (ME), and advanced Vat Photopolymerization (VP), each offer unique capabilities in terms of material versatility, geometric complexity, and resolution, collectively expanding the horizon for what is achievable in surface functionality.

The ability to create functionally graded materials (FGMs), to precisely control the distribution and orientation of reinforcement phases, and to intimately integrate disparate material properties within a single coating layer provides engineers and material scientists with an unprecedented design freedom. This empowers the development of next-generation components exhibiting enhanced wear resistance, superior thermal management, tailored electrical conductivity. While significant challenges persist, such as managing residual stresses induced by rapid solidification or polymerization shrinkage, ensuring uniform and stable dispersion of diverse fillers, controlling porosity, and optimizing complex multi-stage post-processing steps for full densification and property realization, ongoing research and advancements in in-situ monitoring, closed-loop process control, and sophisticated computational modelling are rapidly addressing these hurdles. Furthermore, the ongoing development of novel feedstock materials specifically engineered for AM processes, including tailored composite powders, multi-material filaments, highly loaded photopolymer resins, and even active precursors for in-situ chemical reactions, is continuously expanding the capabilities and application scope of these groundbreaking techniques.

As additive manufacturing technologies continue to mature and material portfolios expand in both breadth and sophistication, the integration of composite design principles promises to unlock a vast, nascent landscape of high-performance coatings. These advancements will undoubtedly drive innovation throughout critical sectors, from aerospace and automotive to energy, fundamentally reshaping the design, manufacturing, and application of our engineered world's very surfaces. The future of functional surfaces is, indeed, additive, composite, and exceptionally bright, promising customized solutions for an increasingly complex technological landscape.

References

Chen, Q., Juste, E., Lasgorceix, M., Lefebvre, G., Tenailleau, C., Duployer, B., Grossin, D., Petit, F. and Leriche, A. (2022). Post-infiltration to improve the density of binder jetting ceramic parts. *Journal of the European Ceramic Society, 42*(15), 7134-7148. https://doi.org/10.1016/j.jeurceramsoc.2022.08.005.

Dini, F., Ghaffari, S. A. Jafar, J., Hamidreza, R. and Marjan, S. (2020). A review of binder jet process parameters; powder, binder, printing and sintering condition. *Metal Powder Report, 75*(2), 95-100. https://doi.org/10.1016/j.mprp.2019.05.001.

Fathi, R., Wei, H., Saleh, B., Radhika, N., Jiang, J., Ma, A., Ahmed, M. H, Li, Q. and Ostrikov, K. K. (2022). Past and present of functionally graded coatings: Advancements and future challenges. *Applied Materials Today, 26*, 101373. https://doi.org/10.1016/j.apmt.2022.101373.

Galindo, E., Espiritu, E. R. L., Maric, M., Zhao, Y. F., Reidy, J., Bose, A. and Brochu, M. (2025). Quantification of metal powder contamination and variation of properties during multi-usage binder jetting process. *Particulate Science and Technology*, In press. https://doi.org/10.1080/02726351.2025.2485431.

Gupta, A. K., Krishnanand. and Taufik, M. (2022). The effect of process parameters in material extrusion processes on the part surface quality: A review. *Materials Today: Proceedings, 50*(5), 1234-1242. https://doi.org/10.1016/j.matpr.2021.08.110.

He, S., Park, S. Shim, D. S., Yao, C. and Zhang, W. J. (2022). Study on microstructure and abrasive behaviors of inconel 718-WC composite coating fabricated by laser directed energy deposition. *Journal of Materials Research and Technology, 21*, 2926-2946. https://doi.org/10.1016/j.jmrt.2022.10.088.

Lee, J. M., Sing, S. L., Zhou, M. and Yeong, W. Y. (2018). 3D bioprinting processes: A perspective on classification and terminology. *International Journal of Bioprinting, 4*(2), 151. https://doi.org/10.18063/ijb.v4i2.151.

Lim, J. S., Oh, W. J., Lee, C. M. and Kim D. H. (2021). Selection of effective manufacturing conditions for directed energy deposition process using machine learning methods. *Scientific Reports, 11*, 24169. https://doi.org/10.1038/s41598-021-03622-z.

Loh, G. H., Pei, E., Gonzalez-Gutierrez, J. and Monzón, M. (2020). An overview of material extrusion troubleshooting. *Applied Sciences*, *10*(14), 4776. https://doi.org/10.3390/app10144776.

Nie, M. H., Jiang, P. F., Zhou, Y. X., Li, Y. L. and Zhang, Z. H. (2023). Studies on the 316/NiTi functionally gradient ultra-thick coatings fabricated with directed energy deposition: Microstructure, crystallography and wear

mechanism. *Applied Surface Science, 630*, 157497. https://doi.org/10.1016/j.apsusc.2023.157497.

Rasiya, G., Shukla, A. and Saran, K. (2021). Additive Manufacturing-A review. *Materials Today: Proceedings, 47*(19), 6896-6901. https://doi.org/10.1016/j.matpr.2021.05.181.

Saboori, A., Gallo, D., Biamino, S., Fino, P. and Lombardi, M. (2017). An overview of additive manufacturing of titanium components by directed energy deposition: Microstructure and mechanical properties. *Applied Sciences, 7*(9), 883. https://doi.org/10.3390/app7090883.

Shaukat, U., Rossegger, E.; and Schlögl, S. (2022). A review of multi-material 3D printing of functional materials via vat photopolymerization. *Polymers, 14*(12), 2449. https://doi.org/10.3390/polym14122449.

Spina, R. and Morfini, L. (2024). Material extrusion additive manufacturing of ceramics: A review on filament-based process. *Materials, 17*(11), 2779. https://doi.org/10.3390/ma17112779.

Subedi, S., Liu, S., Wang, W., Shovon, S. M. A. N., Chen, X. and Ware, H. O. T. (2024). Multi-material vat photopolymerization 3D printing: a review of mechanisms and applications. *NPJ Advanced Manufacturing, 1*(9), 1-17. https://doi.org/10.1038/s44334-024-00005-w.

Tejero-Martin, D., Rad, M. R., McDonald, A. and Hussain, T. (2019). Beyond traditional coatings: A review on thermal-sprayed functional and smart coatings. *Journal of Thermal Spray Technology 28*, 598-644. https://doi.org/10.1007/s11666-019-00857-1.

Wang, Y., Genina, N., Müllertz, A. and Rantanen, J. (2023). Coating of primary powder particles improves the quality of binder jetting 3D printed oral solid products. *Journal of Pharmaceutical Sciences, 112*(2), 506-512. https://doi.org/10.1016/j.xphs.2022.08.030.

Ziaee, M. and Crane, N. B. (2019). Binder jetting: A review of process, materials, and methods. *Additive Manufacturing, 28*, 781-801. https://doi.org/10.1016/j.addma.2019.05.031.

Zhang, W., Xu, C., Li, C. and Wu, S. (2024). Advances in ultrasonic-assisted directed energy deposition (DED) for metal additive manufacturing. *Crystals, 14*(2), 114. https://doi.org/10.3390/cryst14020114.

Zhu, Q., Chua, M. H., Ong, P. J., Lee, J. J. C., Chin, K. L. O., Wang, S., Kai, D., Ji, R., Kong, J., Dong, Z. Xu, J. and Loh, X. J. (2022). Recent advances in nanotechnology-based functional coatings for the built environment *Materials Today Advances, 15*, 100270. https://doi.org/10.1016/j.mtadv.2022.

100270.

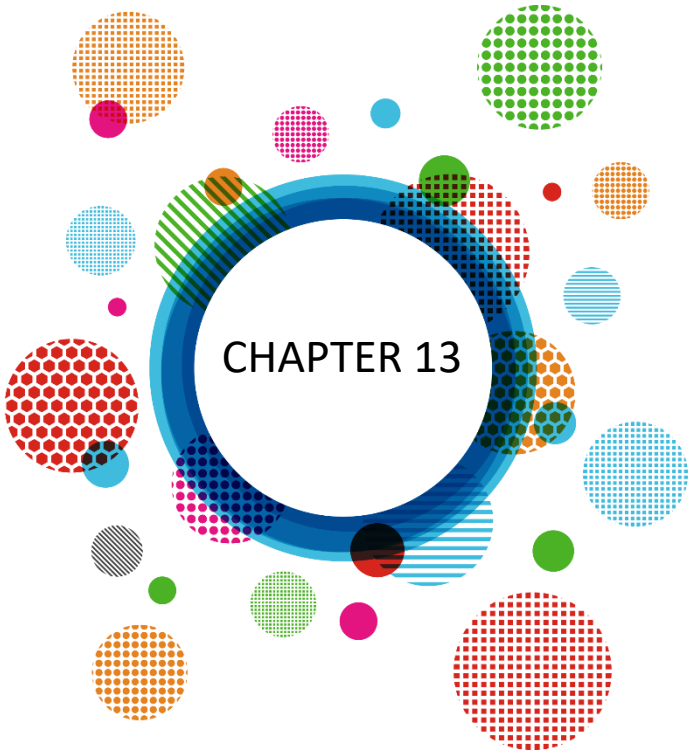

Investigation of Bening and Threat Liquids by Using TD-NMR and Microwave Spectroscopy Technique

Cengiz Okay[1]

[1] Assoc. Prof. Dr. , Marmara University Faculty of Science, Department of Physics, İstanbul-Turkey, ORCID: 0000-0001-9609-2912

1. INTRODUCTION

In today's increasingly interconnected world, the detection of explosives and illegal substances represents a paramount concern. The aviation and public security sectors demand the development of advanced technologies capable of rapidly, accurately, and non-invasively identifying such materials in clothing, luggage, and personal belongings. Air travelers are frequently confronted with prolonged waiting times, stringent security measures, and inconvenient scanning procedures. Simultaneously, the continuous evolution of security threats necessitates the adoption of more sophisticated detection systems and protocols at security checkpoints. Furthermore, the significant surge in passenger traffic in recent decades has exacerbated the complexity and inefficiency of existing screening processes, highlighting the urgent need for innovation in this domain. Numerous types of detectors have been developed (Lerma-García et al., 2010; Rohman et al., 2010; Cataldo et al., 2010; Lizhi et al., 2008). Nonetheless, several challenges persist, such as minimizing false alarm rates, enhancing sensitivity and reliability, lowering scanner costs, and accelerating detection processes. To effectively differentiate between various liquids, there is a pressing need for additional parameters and more advanced measurement and analytical methodologies. The Time Domain (TD-) NMR technique stands out as one of the most promising detection technologies, offering notable advantages in cost-effectiveness, measurement speed, and accuracy of the information obtained. In TD-NMR, the spectroscopic data, such as resonance frequencies, are generally overlooked. Instead, the focus is on measuring the spin-lattice (T_1) and spin-spin (T_2) relaxation parameters of proton nuclei. Previous studies have demonstrated that, when dealing with a broad range of liquids, solely depending on T_1 and T_2 relaxation times fails to provide a fast and reliable method for detection. Therefore, achieving effective differentiation between various liquids necessitates the utilization of additional parameters alongside advanced measurement and analytical methodologies. The microwave technique, utilizing the real part of the dielectric permittivity constant (ε_1) and the dielectric loss factor (ε_2), can be effectively integrated with TD-NMR relaxometry. This combination enables the detection and differentiation of various liquid compounds and their mixtures, offering significant applications in both industrial processes and safety-critical environments. The techniques outlined below serves a crucial function in analyzing and distinguishing liquid compounds. It provides a solid framework that supports innovation and progress in both industrial applications and safety-driven research endeavors. These techniques encompass a diverse range of approaches, including molecular dynamics simulations (MDS) (Pothoczki et al., 2018), X-ray scattering (Takamuku et al., 2001), infrared spectroscopy (IR)(Parker et al., 2014), nuclear magnetic resonance (NMR) (Jora et al., 2017; Rameev et al., 2012), and microwave dielectric spectroscopy (J.

Barthel, K. Bachuber, 1990, Kanse et al., 2006). Time Domain NMR (TD-NMR), Solid State NMR (ss-NMR), and High Field NMR (HF-NMR) represent just a few of the diverse subtypes within the broader field of nuclear magnetic resonance (NMR). Each subtype offers unique capabilities and applications, expanding the versatility and effectiveness of NMR techniques across various scientific and industrial domains. High Field (HF) NMR spectroscopy is highly sensitive for analyzing chemical structures; however, its reliance on a superconducting magnet system necessitates a cryogenic environment. This requirement makes HF-NMR both prohibitively expensive and impractical for many real-world applications. In contrast, Time Domain (TD- NMR eliminates the need for cryogenic systems by utilizing permanent magnet technology, offering a more cost-effective and accessible solution

For security and quality control purposes, the Time Domain NMR (TD-NMR) approach presents a more practical alternative due to its portability, user-friendly design, and affordability. Rather than analyzing the NMR spectrum, TD-NMR focuses on the evaluation of sample relaxation times, making it a more accessible and efficient solution for various applications (Balcı, 2020). The Time Domain NMR (TD-NMR) technique measures two primary parameters: spin-lattice relaxation time (longitudinal, T_1) and spin-spin relaxation time (transverse, T_2). Since each material exhibits unique relaxation times, these parameters are crucial for precise liquid screening and analysis. By leveraging T_1 and T_2 measurements, the TD-NMR method ensures effective differentiation of substances (Malcolm H. Levitt et al., 2021). In microwave technology, the mechanism that arises from the interaction of electromagnetic (EM) waves with the material and facilitates EM absorption is the movement of electric dipoles when they are impacted by the electric field. According to this mechanism, the imaginary component of the dielectric coefficient (ε_2) represents the damping of the activated dipoles and, thus, the energy loss, whereas the real component (ε_1) represents the electric polarization, which quantifies the extent to which the electric dipoles are impacted by the electric field (Abea et al., 2021; Nelson & Trabelsi, 2009). Different materials have different dielectric permittivity constants (ε_1-ε_2) and relaxation times (T_1-T_2), which influence the density, viscosity, bonding, and chemical structure of the material (Bryan et al., 2005; Hindman et al., 1973; Lizhi et al., 2008; Ribose, 2000).

In this study successfully differentiates various benign and threat liquids by employing classification methods that utilize relaxation times (T_1 and T_2) alongside determined dielectric constants (ε_1 and ε_2). These combined parameters enable precise and reliable liquid identification, contributing to advancements in security and safety applications.

2. MATERIAL and METHODS

2.1 Sample Preparation

In this study, we used two groups of samples (benign and threat liquids), which are called water-based drinks and threat materials. Water-based drinks were bought from the local market, and all threat material-threat liquids were acquired from Sigma-Aldrich® and Merck (%99). All selected liquid samples are given in Table 1.

Table 2. List of two groups of samples and their contents.

Threat materials-Threat liquids	Acetone, Nitromethane, Toluene, Nitrobenzene, Methanol, Dioxane, Peroxide %35, Ethanol, 1-Propanol, 2-Propanol
Water based drinks	Coca-Cola Light, Coca-Cola Zero, Coca-Cola Orginal, Pepsi Zero, Pepsi, Tap Water, DI Water, Water (Kuvars), Minarel water (Uludag), Minarel Water (Kızılay).

2.2. Measurements

The measurements have been done for approximately 10 water-based drinks and 10 threat materials-threat liquids. Based on such tests on a wide range of liquids, we concluded that dielectric permittivity constants (ε_1-ε_2) may be determined by microwave spectroscopy and TD-NMR measurements of two parameters (T_1 and T_2). A Bruker Minispec mq20 spectrometer was used to determine relaxation times (Figure 1). The VNA Agilent 8364B and 85070E Dielectric Probe Kit (Figure 2) were used to measure the MW dielectric permittivity (real part and imaginary part of the dielectric constant ε_1 and ε_2, respectively) in the 10 MHz–50 GHz range.

Figure 1. Bruker Minispec mq20 TD-NMR (20MHz-0.5Tesla)

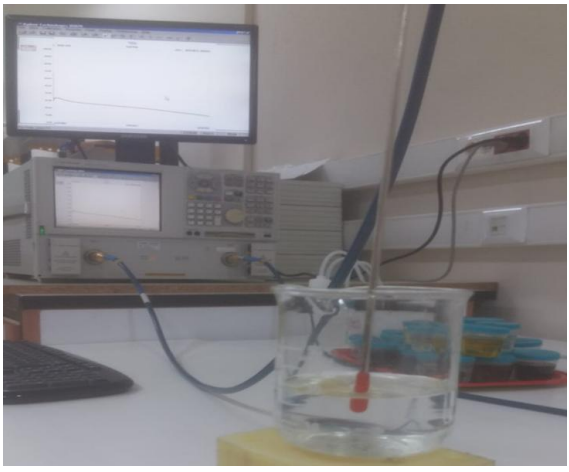

Figure 2. Agilent Network Analyzer (VNA) and Dielectric Kit.

The samples were conditioned at room temperature (25 ºC) and put into tubes with a diameter of 10 mm for the Bruker Minispec mq20 TD NMR spectrometer. To maintain a consistent temperature, the samples were in the NMR apparatus for a minimum of ten minutes before each experiment. Using the Carr-Purcell-Meiboom-Gill (CPMG) pulse sequence, the T_2 relaxation period was determined. The inversion recovery (IR) sequence, was used to determine the T_1 relaxation time. The relaxation delay between these measurements was set at about five times the observed T_1 and T_2 values to ensure that the samples had completely relaxed in between observations. Thus, the T_1 and T_2 parameters were obtained from the signal intensity curves for CPMG and inversion recovery measurements. Note that different echo-times were examined to see how self-diffusion affected

the results. To minimize the diffusion term's contribution, the echo-time was set at 0.5 ms. Additionally, a 50 Ohm load terminal, 25 ºC air, and clean water have been used to calibrate the liquid test fixture in order to assess the dielectric constants ε_1 and ε_2. Sample measurements have been made between 10 MHz and 50 GHz at 25 ºC.

3. RESULTS AND DISCUSSION

3.1.TD-NMR and Microwave Properties of benign and threat liquids

TD-NMR devices were employed to measure T_1 and T_2 relaxation times through the inversion recovery (IR) method and the Carr-Purcell-Meiboom-Gill (CPMG) pulse sequence technique, respectively. The relaxation curves representing spin-lattice (T_1) and spin-spin (T_2) relaxation times for each sample, classified as benign and threat liquids, are displayed in Figure 3.a-b and Figure 4.a-b. The T_1 and T_2 values for each sample were determined through exponential fitting applied to the relaxation time curves. The tested samples include benign liquids, depicted in blue, and threat liquids, depicted in red. The measurement results are presented in Figure 5 and Figure 6.

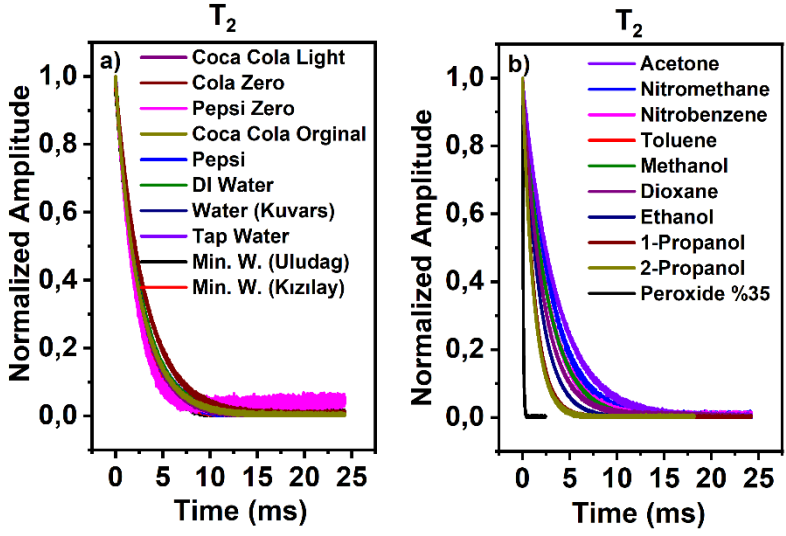

Figure 3. Spin-spin (T_2) relaxation time spectra (**a**) benign liquids **(b)** threat liquids

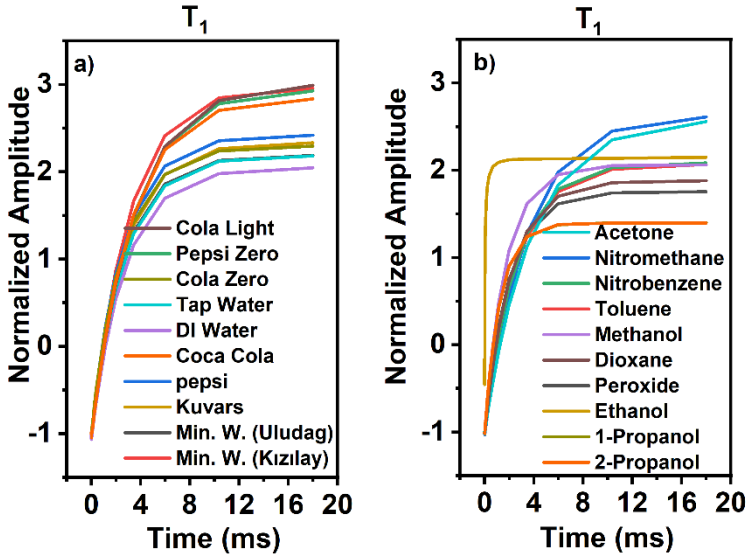

Figure 4. Spin-lattice (T_1) relaxation time spectra (**a**) benign liquids **(b)** threat liquids

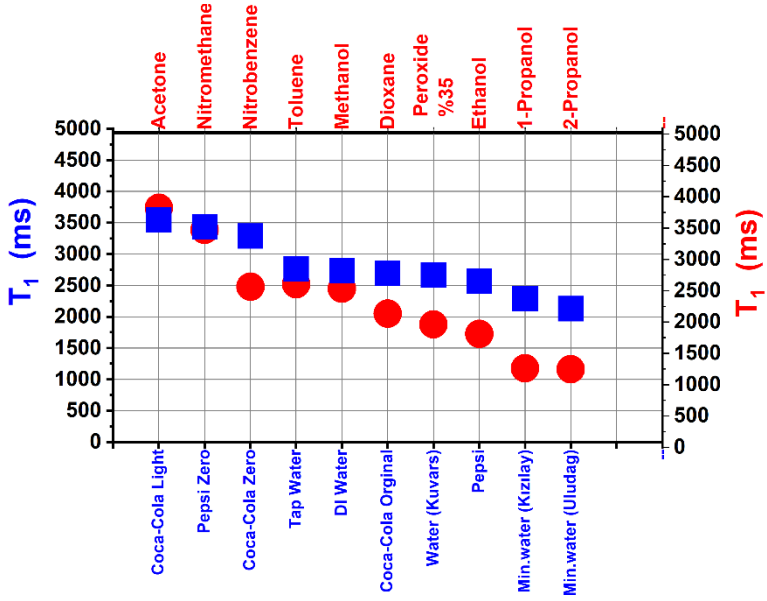

Figure 5. Spin-lattice relaxation times for benign (blue color) and threat materials. (red color)

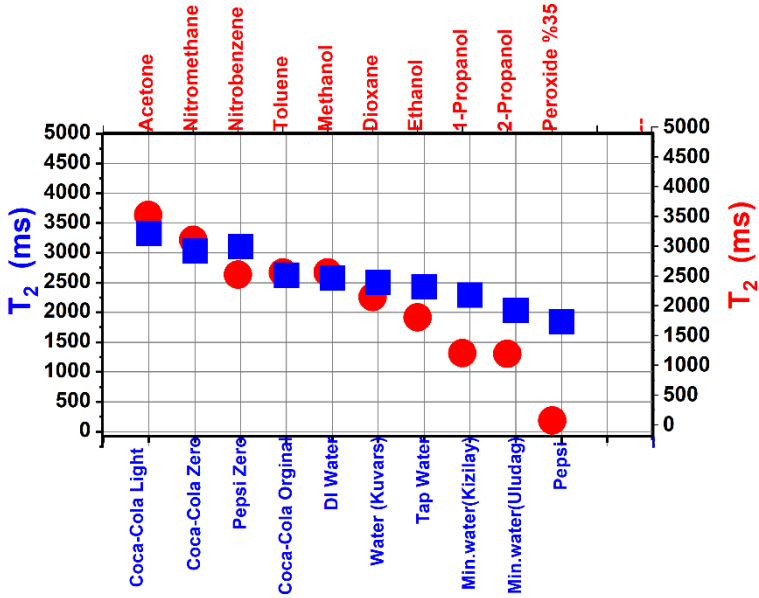

Figure 6. Spin-spin relaxation times for benign (blue color) and threat materials (red color)

The dielectric constant (ε_1) spectra for benign and threat liquids at 25 °C are presented as a function of frequency ranging from 10 MHz to 50 GHz, as shown in Figure 7 a-b, and the dielectric constant (ε_2) spectra for benign and threat liquids are not shown in this section. These spectra provide insights into the dielectric properties of the liquids across the specified frequency range. The spectra can be used to determine the dielectric constants directly. The gigahertz Dielectric Microwave Spectrum was used to determine the dielectric constants at 1 GHz (ε_1 and ε_2) for all samples. The obtained dielectric constants, ε_1 and ε_2, for each liquid are presented at 1 GHz in Figure 8 and Figure 9, providing a visual representation of their dielectric properties. In this study, benign materials are represented in blue, while threat materials are depicted in red, effectively showcasing the contrast in their dielectric properties. This distinction emphasizes the differences between the two material categories. According to the dielectric constant ε_1 graphs plotted against frequency in gigahertz, the dielectric constants for all liquids have higher values at low frequencies, then sharply decrease as frequency increases.

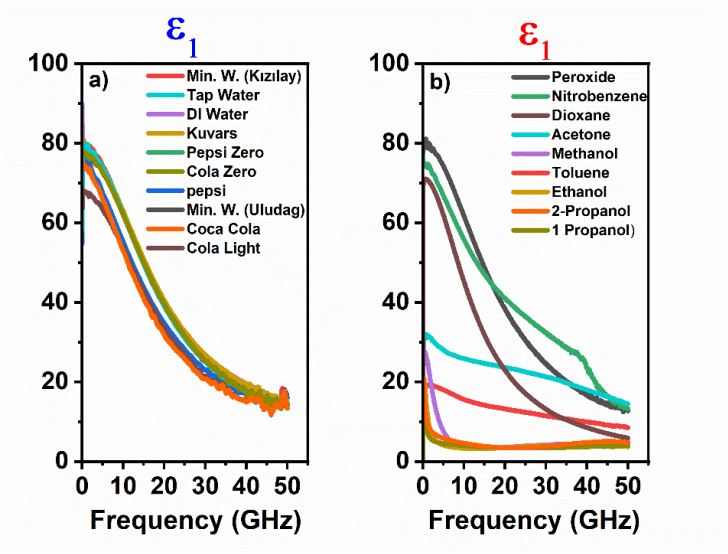

Figure 7. a Dielectric spectra for (**a**) benign and **(b)** threat liquids

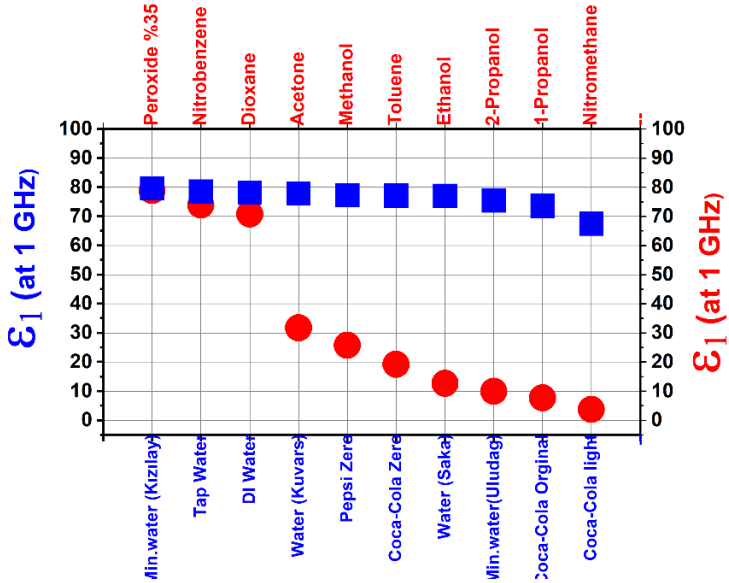

Figure 8. Dielectric constants ε_1 for benign (blue color) and threat (red color) materials (at 1 GHz).

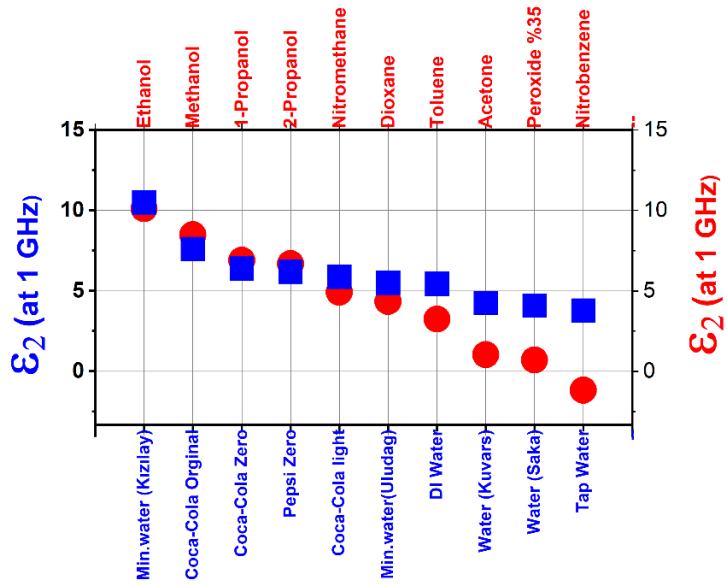

Figure 9. Dielectric constants ε_2 for benign (blue color) and threat (red color) materials (at 1 GHz).

Examining Figure 5, it becomes clear that the results align with expectations for liquids: The T_1 values are consistently slightly higher than the T_2 values across all substances. This observation underscores the typical relaxation behavior of liquids. The energy transfers between spin-lattice interactions (T_1) and spin-spin interactions (T_2) are indeed closely associated with the fundamental origins of relaxation times. As anticipated, T_1 tends to be longer than T_2, primarily because the spatial distance involved in spin-lattice interactions is greater than that between two spins. The findings from this investigation align with and further validate the hypothesis proposed by (Ma et al., 2018) reinforcing this relationship in the context of relaxation behaviors.

It has been noted that only the electronic and ionic polarizations participate at higher frequencies. As the frequency rises, the permanent dipoles' reaction diminishes, and the charge carriers' (ions') contribution to the dielectric constant reduces, as seen by the dielectric constant ε_1 decreasing with increasing frequency (Graça et al., 2003).

It becomes evident that distinguishing between various benign and threatening liquids solely based on the parameters T_1 and T_2 poses significant challenges. The overlap in their relaxation times and the subtle variations in these parameters make it difficult to achieve clear differentiation.

We see ~~of such as~~ that the T_1 and T_2 of the 8 threat liquids (Acetone, Nitromethane, Toluene, Nitrobenzene, Methanol, Dioxane, Peroxide 35%,

Ethanol) have values that are close to ~~water based~~water-based drinks. Anyway, in the figure shown above, the fact that T_2 relaxation constants of tap and drink water are very different from the relaxation constant of hydrogen peroxide should be noted.

This highlights the need for additional analytical techniques or complementary parameters to enhance the discrimination process. In this study, the microwave technique was employed as an additional method, providing further insights and complementary data to enhance the investigation's findings.

Comparing Figure-8 with Figure-9, we see ~~of such as~~ that the real permittivities of three 3 threat liquids (hydrogen peroxide, nitrobenzene, and dioxane) have values that are close to ~~water based~~water-based drinks. On the other hand, in contrast with Figure-8, the real permittivity of Min. water (Kızılay), tap and drink water are very close to that of threat liquids. The T_1 and T_2 values of TD-NMR results for liquids like acetone, nitrobenzene, and nitroethanol in Figures 5 and 6 are very close to those of liquid-based drinks, whereas the ε_1 and ε_2 values in Figures 8 and Figure 9 are clearly shown to be significantly different from each other.

By leveraging these combined parameters, the system achieves enhanced precision and reliability in liquid identification, which plays a significant role in advancing security and safety technologies.

4. CONCLUSION

This study measured the spin-lattice and spin-spin relaxation times of two groups of samples (benign and threat liquids), which are referred to as threat materials and water-based drinks. The results conform to the expected behavior of liquids: Across all substances, T_1 values consistently exceed T_2 values by a small margin. This pattern highlights the characteristic relaxation dynamics of liquids. Furthermore, this study employs microwave (MW) spectroscopy to investigate the dielectric properties (ε_1 and ε_2) of benign and threat liquids. This technique provides valuable insights into their behavior and interactions.

Besides TD-NMR, microwave permittivity measurement has proven to be an effective technique for distinguishing and classifying benign and hazardous liquids. This method offers a reliable approach to identifying the dielectric characteristics that set these substances apart.

Acknowledgment

I would like to thank Prof. Dr. Bulat Rami and Dr. Ayşe Maraşlı from Gebze Technical University for providing laboratory facilities and access to equipment.

REFERENCES

Abea, A., Gou, P., Guardia, M. D., Bañon, S., & Muñoz, I. (2021). Combined effect of temperature and oil and salt contents on the variation of dielectric properties of a tomato-based homogenate. *Foods*, *10*(12). https://doi.org/10.3390/foods10123124

Balcı, M. (2020). Nükleer Manyetik Rezonans Spektroskopisi Eğitim Yayınevi. In *Eğitim yayınevi* (4.Baskı). -Türkiye.

Bryan, J., Kantzas, A., & Bellehumeur, C. (2005). Oil-viscosity predictions from low-field NMR measurements. *SPE Reservoir Evaluation and Engineering*, *8*(1), 44–52. https://doi.org/10.2118/89070-PA

Cataldo, A., Piuzzi, E., Cannazza, G., De Benedetto, E., & Tarricone, L. (2010). Quality and anti-adulteration control of vegetable oils through microwave dielectric spectroscopy. *Measurement: Journal of the International Measurement Confederation*, *43*(8), 1031–1039. https://doi.org/10.1016/j.measurement.2010.02.008

Graça, M. P. F., Valente, M. A., & Ferreira da Silva, M. G. (2003). Electrical properties of lithium niobium silicate glasses. *Journal of Non-Crystalline Solids*, *325*(1–3), 267–274. https://doi.org/10.1016/S0022-3093(03)00314-4

Hindman, J. C., Svirmickas, A., & Wood, M. (1973). Relaxation processes in water. A study of the proton spin-lattice relaxation time. *The Journal of Chemical Physics*, *59*(3), 1517–1522. https://doi.org/10.1063/1.1680209

J. Barthel, K. Bachuber, R. B. and H. H. (1990). Diectric spctra of sme common solvent in microwave spectra. *Chemical Physics Letters*, *165*(4).

Jora, M. Z., Cardoso, M. V. C., & Sabadini, E. (2017). Correlation between viscosity, diffusion coefficient and spin-spin relaxation rate in 1H NMR of water-alcohols solutions. *Journal of Molecular Liquids*, *238*, 341–346. https://doi.org/10.1016/j.molliq.2017.05.006

Kanse, K. S., Chavan, S. D., Mali, C. S., Kumbharkhane, A. C., & Mehrotra, S. C. (2006). Structural study of methanol-water mixture from dielectric parameters. *Indian Journal of Physics*, *80*(3), 265–269.

Lerma-García, M. J., Ramis-Ramos, G., Herrero-Martínez, J. M., & Simó-Alfonso, E. F. (2010). Authentication of extra virgin olive oils by Fourier-transform infrared spectroscopy. *Food Chemistry*, *118*(1), 78–83. https://doi.org/10.1016/j.foodchem.2009.04.092

Lizhi, H., Toyoda, K., & Ihara, I. (2008). Dielectric propertıes of edible oils and fatty acids as a function of frequency, temperature, moisture and composition.

Journal of Food Engineering, *88*, 151–158. https://doi.org/10.1016/j.jfoodeng.2007.12.035

Malcolm H. Levitt, Svirmickas, A., Wood, M., Cunha, S. C., Oliveira, M. B. P. P., Moresi, G., Magin, R., Řezanka, T., Řezanková, H., Ancora, D., Milavec, J., Gradišek, A., Cifelli, M., Sepe, A., Apih, T., Zalar, B., Domenici, V., Mason, J., Nmr, M., … Liu, M. M. (2021). Spin Dynamics Basics of Nuclear Magnetic Resonance. *Physical Review*, *8*(1), 1–9. https://doi.org/10.1002/cmr.a.20130

Nelson, S. O., & Trabelsi, S. (2009). Dielectric properties of agricultural products and applications. *American Society of Agricultural and Biological Engineers Annual International Meeting 2009, ASABE 2009*, *5*(2), 2901–2919. https://doi.org/10.13031/2013.27075

Parker, T., Limer, E., Watson, A. D., Defernez, M., Williamson, D., & Kemsley, E. K. (2014). 60MHz 1H NMR spectroscopy for the analysis of edible oils. In *TrAC - Trends in Analytical Chemistry*. Elsevier Ltd. https://doi.org/10.1016/j.trac.2014.02.006

Pothoczki, S., Pusztai, L., & Bakó, I. (2018). Temperature dependent dynamics in water-ethanol liquid mixtures. *Journal of Molecular Liquids*, *271*, 571–579. https://doi.org/10.1016/j.molliq.2018.09.027

Rameev, B., Mozzhukhin, G., & Aktaş, B. (2012). Magnetic Resonance Detection of Explosives and Illicit Materials. *Applied Magnetic Resonance*, *43*(4), 463–467. https://doi.org/10.1007/s00723-012-0423-9

Ribose, M. (2000). *Relationship Solutions between Proton NMR Relaxation Time and Viscosity of Saccharide. 6*(2), 136–139.

Rohman, A., Che Man, Y. B., Ismail, A., & Hashim, P. (2010). Application of FTIR spectroscopy for the determination of virgin coconut oil in binary mixtures with olive oil and palm oil. *JAOCS, Journal of the American Oil Chemists' Society*, *87*(6), 601–606. https://doi.org/10.1007/s11746-009-1536-7

Takamuku, T., Yamaguchi, A., Matsuo, D., Tabata, M., Kumamoto, M., Nishimoto, J., Yoshida, K., Yamaguchi, T., Nagao, M., Otomo, T., & Adachi, T. (2001). Large-angle X-ray scattering and small-angle neutron scattering study on phase separation of acetonitrile-water mixtures by addition of NaCl. *Journal of Physical Chemistry B*, *105*(26), 6236–6245. https://doi.org/10.1021/jp003011n